Local Moments and Itinerant Electrons: Gaining New Insights through Investigating Electronic and Dynamical Properties

A Dissertation Presented for the
Doctor of Philosophy
Degree
The University of Tennessee, Knoxville

Nicholas Steven Sirica
August 2017

Abstract

Magnetic materials are often categorized in terms of either a purely local or a purely itinerant picture despite the fact that the vast majority actually fall within a spectrum that ranges between these two extremes. It is from such a starting point that this thesis aims at developing an understanding of how the complex interplay between local moments and itinerant electrons ultimately affects the electronic and dynamical properties. Such ideas are explored in greater detail using two materials as case studies: the chiral helimagnet $Cr_{1/3}NbS_2$ [Cr intercalated Niobium Disulfide] and YFe_2Ge_2 [Yttrium Iron Germanide] a Pauli paramagnet believed to be near a magnetic quantum critical point. From this investigation, new microscopic insights into macroscopic phenomena such as the intriguing magneto-transport properties of $Cr_{1/3}NbS_2$ and the presence large longitudinal fluctuations in the moment of YFe_2Ge_2 were gained. Focusing on $Cr_{1/3}NbS_2$ it was found that both Cr- and Nb-derived states participate in the formation of the Fermi surface. Based on this finding, it is evident that the same states responsible for magnetism are likewise those responsible for transport. Consequently, a clear separation between the magnetic and itinerant degrees of freedom is not evident; a finding that is most clearly illustrated by the increase in spectral weight observed at E_F as the temperature is lowered below the magnetic transition temperature. Extending this work to include real-time measurements of the electron, lattice and spin dynamics, an anonymously long demagnetization dynamic was observed in the magnetic phase of $Cr_{1/3}NbS_2$. However, rather implying the spins to be thermally insulated from the electronic degrees of freedom, such a finding may simply imply that spin flips occurring via Elliot-Yafet mechanism are inefficient due to an imbalance in the spin polarized density-of-state in the ferromagnetic state. Finally, after expressing the limitations of single color optical pump-optical probe experiments, the design, construction and commissioning of a time-resolved ARPES system is presented with particular interest in laying out future plans enabling this system to resonantly excite collective modes in strongly correlated systems.

Table of Contents

Chapter 1: Overview 1

Chapter 2: Background and Motivation for Studying the Electronic Structure of the Chiral Helimagnet $Cr_{1/3}NbS_2$ 7
2.1 Chiral Helimagnetism 7
2.2 Skyrmions 9
2.3 The Chiral Soliton Lattice in $Cr_{1/3}NbS_2$ 13
2.4 Motivation for Measuring Electronic Structure 17
2.5 Electronic Structure of Intercalated TMDCs 18
2.6 Relating the Electronic Structure to the Exchange Interaction 24

Chapter 3: Experimental Techniques 26
3.1 Photoemission Spectroscopy 26
3.1.1 Corel Level Photoemission 28
3.1.2 Angle Resolved Photoemission Spectroscopy 33
3.1.3 Soft X-ray ARPES 39
3.1.4 Resonant Photoemission Spectroscopy 53
3.2 Static and Ultrafast Optical Spectroscopy 59
3.2.1 Optical Pump-Probe Spectroscopy 59
3.2.2 Magneto-Optical Kerr Effect 65

Chapter 4: Experimental Apparatus 70
4.1 The ARPES Spectrometer 70
4.1.1 Ultra-high Vacuum 70
4.1.2 Electron Energy Analyzer 73
4.1.3 Electrostatic Lens 76
4.1.4 Sample Manipulator 78
4.1.5 Helium Gas Discharge Lamp 83
4.2 Ultrafast Laser System 85
4.2.1 Modelocking 85
4.2.2 Pulse Compensation 93
4.2.3 Chirped Regenerative Amplification 94

Chapter 5: Investigation into the Electronic Structure of $Cr_{1/3}NbS_2$ 98
5.1 Surface Characterization 98
5.2 Comparison of $Cr_{1/3}NbS2$ and NbS_2 113
5.3 Polarization Dependence 120
5.4 Temperature dependence 123
5.5 Insights from *ab initio* Calculations 132

Chapter 6: Spectroscopic Evidence for Strong Quantum Spin Fluctuations with Itinerant Character in YFe_2Ge_2 137
6.1 Introduction 137
6.2 Fe 2p and $L_{3,2}$ 139
6.3 Valence Band 141
6.4 Fe 3s 141

Chapter 7: Disentangling the Electronic, Lattice and Spin Dynamics in the Chiral Helimagnet $Cr_{1/3}NbS_2$ 148
7.1 Static MOKE 150
7.2 Transient Reflectivity 152
7.3 Time-Resolved MOKE 159

Chapter 8: Time-Resolved ARPES: Current Status and Future Directions 163
8.1 Non-linear Optics 164
8.2 Optical Layout 167
8.3 Time-Resolved ARPES 170
8.4 Future Directions 174

References 177

Vita 187

List of Tables

Table 4.1: Calculated energy resolutions for the R4000 spectrometer given specific choice of pass energy and slit width 77

List of Figures

Figure 2.1: Small angle neutron scattering (SANS) performed on MnSi in (a) the helical and (b) the A-phase [1]. Signature of helimagnetic ordering along the 111 direction is given by the presence of satellite peaks at +/- Q = 0.036 $Å^{-1}$. SANS data collected in the A-phase shows superposition of three helical spin structures. Theoretical models showed this to be a signature of the Bloch Skyrmion 10

Figure 2.2: Schematic illustration of the topological Hall effect [2]. Effective Lorentz force experienced by the electron is a direct consequence of the type of strong interactions that exists between itinerant electron and Skyrmions 12

Figure 2.3: Schematic illustration of (a) crystal structure, (b) and (c) the CHM ground state and (d) the CSL phase taken from [3]. Note that the CSL comes about when field is applied in the easy plane perpendicular to the helical axis.....14

Figure 2.4: Normalized inter-layer magnetoresistance measured for $T < T_C$ and plotted as a function normalized field. As pointed out in [4] the inter-layer magnetoresistance is found to track the soliton kink density remarkably well. 16

Figure 2.5: Intra-layer (a) transport and (b) magnetotransport measurements taken from [5]. Note the sharp drop in resistivity and large negative magnetoresistance occurring at T_C. Given these measurements to be taken in the ab-plane, such results cannot be rationalized on basis of Bragg scattering by soliton kinks.....16

Figure 2.6: Schematic illustration of the valence band for (a) NbS_2 and (b) $Cr_{1/3}NbS_2$ under the supposition of a rigid band interpretation. Note that in the rigid band picture, the intercalant serves to donate electrons so as to fill d_z^2 sub-band 20

Figure 2.7: Fermi surface ARPES map of $NbSe_2$ taken from [6]. Note presence of small Se derived hole pocket at Γ and bilayer split Nd-derived hole pockets at Γ and K.....22

Figure 2.8: Effects of Rb intercalation on the electronic structure of TaS_2 taken from [7]. Here, Rb deposition alters the CDW periodicity as can be seen from LEED images in (a) and affects both the local electronic environment of the Ta 4f (b) and the size of the Mott-Peierls gap in the electronic structure (c) 23

Figure 3.1: Core level PES spectra of (a) the Carbon 1s for ethyl trifluoroacetate and (b) the Nitrogen 1s of sodium azide. Note from the spectra the sensitivity of the core level binding energy to its particular chemical environment. Taken from [8] 30

Figure 3.2: For the ARPES geometry shown in (a), (b) illustrates the electronic band dispersion and corresponding single particle removal spectral function for a non-interacting system characterized by a momentum distribution function $n(k) = \theta(k-k_F)$. In contrast (c) demonstrates the effect that electron correlations will have on an ARPES spectrum. Notably, the single particle removal spectrum takes on a characteristic peak-dip-hump structure with the coherent

quasi-particle peak showing a broadening in accordance with $(E-E_F)^2$. Additionally, note how the momentum distribution function changes as compared to the non-interacting case. Here the magnitude of the step at k_F is defined by the quasiparticle renormalization factor Z_k. Taken from [9] 38

Figure 3.3: Dependence of ARPES intensity on (a) photon polarization and (b) photon energy, which manifests in (c) as the corresponding photoelectron cross-sections for a particular atomic sub-shell. Such dependencies comprise what is commonly referred to as matrix element effects in an ARPES spectrum. Taken from [9] 40

Figure 3.4: Schematic illustration of the experimental geometry for PES. Noting that the sampling depth is given here by $z = l/sin\theta$, it is evident that a greater bulk sensitivity will be gained at normal emission, where $\theta = \pi/2$. Taken from [10] 42

Figure 3.5: The so-called "universal curve" that phenomenologically describes the dependence of electron inelastic mean free path, λ, on kinetic energy. Taken from [11] 44

Figure 3.6: Schematic illustration of the experimental geometry of Beamline 7.0.2 at the Advanced Light Source. As compared to conventional ARPES, consideration of the angle at which the light impinges on the sample must be noted as the corresponding *k*-conversion will need to correct for the contribution coming from photon momentum..... 50

Figure 3.7: Fermi surface maps of $Na_{0.75}CoO_2$, $Na_{0.8}CoO_2$, and $Na_{0.9}CoO_2$, obtained as a function of increasing photon energy into the soft X-ray regime, where a correction for photon momentum has been applied..... 51

Figure 3.8: Schematic illustration of (a) valence and (b) core-level PES as well as (c) the non-resonant Auger decay of a core hole. With a resonant excitation, such as that shown in (d), the corresponding (e) participator and (f) spectator auto-ionization channels can then open up. Note how the final state in (e) and (a) are identical leading to a resonant enhancement of the valence band PES. Taken from [12] 55

Figure 3.9: Illustration of the photon energy dependence of a resonant Raman Auger measured by tuning the photon energy across the Ni L_3 and L_2 edges. Taken from [13]..... 57

Figure 3.10: Respective time and energy scales of the various processes that can be found in strongly correlated systems. Taken from [14] 60

Figure 3.11: Schematic illustration of the effective temperature model used in the description of relaxation dynamics for an optical pump-probe experiment. Taken from [14]..... 62

Figure 3.12: Illustration of the coherently excited collective modes that can arise from (a) an impulsively stimulated Raman process or (b) a displacive excitation. For both cases, the driving terms shown in (c) and (d) will yield different phases of the respective oscillations providing a means by which these two excitations can be distinguished. Taken from [15]..... 64

Figure 3.13: Schematic illustration of the relevant geometries for a MOKE experiment. Depending upon the direction of the magnetization relative to the scattering plane, the effect will be to vary the intensity and/or rotate the plane of polarization of the reflected light. Taken from [16] 68

Figure 4.1: Sketch of the ARPES pumping configuration 72

Figure 4.2: Mass spectrum of residual gas in ARPES chamber taken when the chamber base pressure is better than 6.0×10^{-11} Torr. Main peaks can be ascribed to H_2, C, H_2O, CO, and CO_2. Note that at such a pressure $P_{H2O} < P_{CO}$ indicative of a good bake-out 74

Figure 4.3: Ray tracing diagrams for an electrostatic lens working in (a) transmission and (b) angular mode. Taken from [17] 79

Figure 4.4: Schematic illustration of the trajectory taken by an electron emitted from the sample with a given E_K and θ_K as it passes through the CHA and strikes a 2D spatial detector. Figure reproduced here from NM 80

Figure 4.5: Energy level diagram taken from [10] showing the difference in work function that comes about from grounding the sample to the spectrometer 82

Figure 4.6: Intensity of photoelectron secondaries as a function of monochromator reading. Main lines are labeled with the zero order peak denoting specular reflection. Counts measured by sweeping monochromator in both a forward and backward direction for determination of backlash 84

Figure 4.7: Illustration of a Fabry-Perot interferometer showing in (a) the attenuation of an incident E_0 by subsequent reflection and transmission through the etalon and (b) the difference in path length taken between two transmitted beams 87

Figure 4.8: (a) The total number of longitudinal modes that can be stained in a laser cavity juxtaposed to the gain bandwidth of the active medium. Note in (b) how only the modes that fall in the gain bandwidth become amplified 89

Figure 4.9: (a) incoherent and (b) coherent sum of N = 4 cavity modes. Note in (b) how even with relatively few number of modes a pulse starts to take shape 91

Figure 4.10: Schematic diagram of the Coherent Micra oscillator reproduced here from [18] 92

Figure 4.11: Normal dispersion curves of (a) UV used silica and (b) borosilicate glass plotted from data provided by Thorlabs website. Such glass is commonly used in optics and will introduce a positive chirp into an ultrashort pulse passing through the optic 95

Figure 4.12: Simple illustration of a prism compressor reproduced here from [19]. In addition to prisms, pulse compensation can also be accomplished by use of other dispersive elements such as gratings. 95

Figure 4.13: Schematic diagram of the Coherent RegA 9050 chirped regenerative amplifier reproduced here from [20]. 97

Figure 5.1: (a) S 2p core level spectrum taken at normal emission from *in situ* cleaved $Cr_{1/3}NbS_2$ with hν = 918 eV. The BE separation between the doublet originating from the surface (solid line) and the deeper layers (dashed line) amounts to ~1 eV. (b) Cr 2p core level recorded at normal emission with hν = 918eV. Key features include a spin orbit split doublet (A, B), and a loss feature (C). The arrows indicate kinks in the line shape of features A and B 100

Figure 5.2: (a) STM image of *in situ* cleaved $Cr_{1/3}NbS_2$ single crystals taken with a bias voltage of -0.4V illustrating the large-scale surface morphology. (b) Line profile along the broken line in a) reveals a terrace step height of 0.61 nm with high corrugation near the step edge. (c,d) Atomic resolution images of the (c) "smooth" and (d) "rough" areas denoted by s and r respectively. ..102

Figure 5.3: (a) Unit cell of $Cr_{1/3}NbS_2$ taken from [5]. (b) Representative LEED image obtained from $Cr_{1/3}NbS_2$ with an electron beam energy of 215 eV. The unit cell of the 1×1 (solid) and $(\sqrt{3}\times\sqrt{3})R30°$ (dotted) reciprocal lattice are indicated 104

Figure 5.4: High resolution ARPES spectra taken from $Cr_{1/3}NbS_2$ with σ-polarized photons of energy hν = 48eV. Non-dispersive surface states are indicated by arrows in both the (a) image plot and (b) stacked EDCs 106

Figure 5.5: ResPES measured from $Cr_{1/3}NbS_2$ across the Cr L_3 absorption edge with photon polarization contained entirely in the sample plane. (a) Cr L_3 XAS measured in total electron yield. (b) ResPES image plot and (c) representative line profiles extracted at the corresponding photon energies labeled in (a) 107

Figure 5.6: ARPES spectra of $Cr_{1/3}NbS_2$ measured along the ΓK direction over a wide (a_1-a_4) and narrower (b_1-b_4) binding energy range using photon energies hν = 40 eV (a_1, b_1), hν = 196 eV (a_2, b_2), hν = 401eV (a_3, b_3) and hν = 736 eV (a_4, b_4). Spectra at hν = 40 eV has been symmetrized with respect to the Γ point.....109

Figure 5.7: Stacked EDCs (a_1-a_4) and MDCs (b_1-b_4) along the ΓK direction extracted from the corresponding image plots depicted in Figure 5.6 b_1-b_4. Tick marks tracing the dispersion of the two bands in proximity to E_F have been added to the EDC stacks in a_1-a_4 as a guide to the eye. In the MDC stacks, the MDC at E_F is denoted with a thicker line 111

Figure 5.8: Direct comparison of MDCs extracted at E_F for hν =40 eV, 196 eV, 401 eV and 736 eV depicting k_F crossings about Γ. Features from the hν = 40eV spectra are labeled α, β_1, and β_2 for the purpose of comparisons. For a description of this notation, see text 112

Figure 5.9: Comparison of (a) valence band and (b) Nb 3d PES spectra for NbS_2 (top) and $Cr_{1/3}NbS_2$ (bottom) as measured at normal emission with hν = 750 eV. From (a), a comparison of similar features in the VB as well as the shallow S 3s core level demonstrates a 0.4 eV shift towards higher binding energy. The suppression of the higher BE peaks of the Nb 3d doublet (solid line) observed in $Cr_{1/3}NbS_2$ is visible in (b).....115

Figure 5.10: Band dispersion of ((a_1),(a_2)) NbS_2 and ((b_1),(b_2)) $Cr_{1/3}NbS_2$ measured along the ΓK direction over a wide BE range using hν = 40eV photons having a polarization horizontal ((a_1), (b_1)) or vertical ((a_2),(b_2)) with respect to the scattering plane.....116

Figure 5.11: Stacked EDCs of the corresponding image plots in Figure 5.10 shown within ~ 1 eV from E_F. Tick marks tracing the dispersion of the "bonding" (red) and "anti-bonding" (black) bilayer split Nb-bands have been added as a guide to the eye. The Nb-derived "bonding" band is found to sink ~ 200 meV below E_F (b).....117

Figure 5.12: Direct comparison of MDCs at E_F extracted from the data shown in Figure 5.10. In the fit of the MDCs, shown in (a_1) and (b_1), the broken lines denote spectral weight originating from the background. The main features of the MDCs in $Cr_{1/3}NbS_2$ ((b_1), (b_2)) are likewise denoted in NbS_2 (a_1). In (a_1), peak S (red) sinks below E_F in $Cr_{1/3}NbS_2$. A slight misalignment of the sample is responsible for an asymmetry with respect to Γ of the MDCs in (a_2) and (b_2) .119

Figure 5.13: Band dispersion measured along the ((a_1), (b_1)) ΓK and ((a_2), (b_2)) ΓM direction using π-polarized ((a_1), (a_2)) and σ-polarized ((b_1), (b_2)) photons of energy hν = 40eV 121

Figure 5.14: Fermi surfaces of $Cr_{1/3}NbS_2$ measured along the ((a_1), (b_1)) ΓK and ((a_2), (b_2)) ΓM direction using π-polarized ((a_1), (a_2)) and σ-polarized ((b_1), (b_2)) photons of energy hν = 40eV. Solid and broken lines denote the 1×1 and √3×√3 BZ, respectively.....122

Figure 5.15: Temperature dependent ARPES image plots obtained along the ΓM direction using π-polarized photons of hν = 48 eV. Here, all band crossing points are denoted by white arrows 124

Figure 5.16: MDCs extracted at E_F for spectra measured along the ΓM direction with photon energy hν = 48 eV. Note the emergence of the exchange split $\beta_{1,2}$ bands for T < 120K, and the loss of spectral weight for T > T_C.....125

Figure 5.17: ResPES spectra obtained using a linear horizontal photon polarization. Here, photon energy was tuned across the Cr L_3 absorption edge where the corresponding x-ray absorption spectrum is shown as an inset in panel (b). Symbols on the XAS are used to denote the particular photon energy of the VB traces shown in (b). The spectra excited with different photon energies are compared to the spectrum excited off-resonance with photon energy hν = 570 eV. Note the clear indication of Cr resonance at E_F as hν is tuned to the peak of the XAS spectrum. This result clearly indicates that Cr-derived states participate in the FS of $Cr_{1/3}NbS_2$ 126

Figure 5.18: (a) EDC spectra integrated from $k_{\Gamma M}$ = 0.24 $Å^{-1}$ to 0.8 $Å^{-1}$ and normalized to photon flux. This data reveals an increase of spectral weight in proximity of E_F occurring for T < T_C. Similarly, (b) shows EDCs extracted at k_F of the α band as a function of temperature in which spectra have been normalized in a region absent of any dispersive features (1.4 eV). Note the monotonic increase of spectral weight as T is lowered below T_C. This behavior is more clearly

highlighted by the inset in (b) showing the changes in spectral weight occurring within 150 meV from E_F 128

Figure 5.19: Symmetrized EDCs of the α-band displayed over +/- 200 meV binding energy range and stacked as a function of increasing temperature 130

Figure 5.20: MDCs extracted at E_F along the ΓK direction using (a) π-polarized and (b) σ-polarized photons. The photon energy was varied from hν = 40eV to hν = 60eV in steps of 1 eV (a), or 2 eV (b) 134

Figure 5.21: (a) Sketch of the 1×1 Brillouin zone illustrating how the hole-like band at K folds due to a √3×√3 super-lattice potential. (b) Band dispersion taken along the ΓK direction with σ-polarized photons of hν = 40eV. Superimposed on the image plot is a trace of the MDC peak positions of the band at K (solid) translated by a √3×√3 lattice vector (broken line). (c) MDC stacks having a negative offset taken from 300 meV to E_F from the image plot in (b). Broken lines have been translated by a √3×√3 lattice vector and rescaled so as to directly compare the dispersion. (d) Band dispersion measured along the ΓK direction with LV polarized photons of energy hν = 196 eV 135

Figure 6.1: (a) Fe 2*p* core level PES spectrum excited with photon energy hν = 907.5 eV. (b) Fe L_{23} XAS spectrum. Note the marked similarities with corresponding spectra excited in Fe-based high temperature superconductors 140

Figure 6.2: Valence band measured with photon energy hν = 907.5 eV. Note the high DOS at E_F, denoted with the vertical dashed line. Also shown are the calculated total DOS, and the Fe 3d, Ge 4s and Ge 4p partial DOS 142

Figure 6.3: (a) Fe 3s and (b) Ge 3s core level PES spectra excited with photon energy hν = 907.5 eV. The value of the energy separation of the multiplet is ΔE_{3s} = 3.15 eV 144

Figure 6.4: (a) Snapshot of a distribution of longitudinal spin fluctuations taken on a timescale that ranges between the electron hopping and spin procession lifetime. (b) The resultant M-SP 3s spectrum illustrating the wide Gaussian envelope of the higher BE component which is indicative of fluctuations in the magnitude of the magnetic moment 145

Figure 7.1: Decomposition of the magnetization along (a) transverse/longitudinal and (b) polar directions as measured by MOKE. A direct comparison of the transverse and longitudinal MOKE signal shown in the inset of (a) reveals that the magnetization predominately aligns parallel to the applied field direction within the ab-plane 151

Figure 7.2: Transient reflectivity spectra of NbS_2 ((a) and (b)) and $Cr_{1/3}NbS_2$ ((c) and (d)) measured over short- and long-time delays. Spectra have been measured using an amplified Ti:Sapphire laser system operating a 1 kHz repetition rate 153

Figure 7.3: Summary of results from a room temperature fluence dependence comparing the fit parameters of NbS_2 (open circles) with $Cr_{1/3}NbS_2$ (open squares). Here, parameters for (a) the

amplitude of the transient reflectivity, (b) electron relaxation time, (c) amplitude of low frequency coherent mode, and (d) period of low frequency coherent mode are plotted as function of pump power 155

Figure 7.4: Transient reflectivity spectrum of $Cr_{1/3}NbS_2$ taken with a 50 fs step size over a 10 ps delay so as to better study the behavior of the high frequency coherent phonon mode. Fourier transform shown in inset reveals a single mode at ~5.5 THz, which is found from fitting of the real time dynamic to have a long dampening lifetime 157

Figure 7.5: Comparison of (a) room temperature (300K) and (b) low temperature (77K) transient reflectivity spectra over a 50 ps delay. Note the presence of the long demagnetization dynamic in (b).....158

Figure 7.6: (a) Transient reflectivity and (b) time-resolved MOKE measurements made on $Cr_{1/3}NbS_2$ in the magnetic phase using a NOPA having an output centered at 680 nm 160

Figure 7.7: Calculated spin-polarized density-of-states of $Cr_{1/3}NbS_2$ in units of eV^{-1} per unit cell. Note the lower values of the DOS for the spin down channel for energies of ca. ± 250 meV from E_F.....162

Figure 8.1: Schematic diagram of the optical layout for transient reflectivity and time-resolved ARPES 168

Figure 8.2: Electronic band dispersion of $Bi_2Sr_2CaCu_2O_{8+\delta}$ measured along the nodal direction using a laser excitation source ($h\nu$ = 6.34 eV). Spectra were obtained using a pass energy E_p = 5.0 eV for an electrostatic lens table optimized for (a) He gas discharge lamp and (b) laser source 172

Figure 8.3: Snapshots of the time evolution of the transiently populated topological surface states in Sb_2Te_3 taken at (a) t = -2.0 ps, (b) t = 0 ps, (c) t = 2.5 ps and (d) t = 5.0 ps.....173

Figure 8.4: Schematic diagram of a visible/near IR non-collinear optical parametric amplifier 175

Chapter 1: Overview

In the description of magnetism, one often encounters two extremes: the local picture of Curie-Weiss and the itinerant picture of the Stoner model. However, for most magnetic materials, neither description turns out to be entirely applicable, as magnetism most often falls somewhere on a spectrum between these two extremes. Thus, in starting from this point, much of the work found within this thesis aims at developing an understanding of how the complex interplay that develops between local moments and itinerant electrons affects the electronic and dynamical properties within a material. Chiefly, when the same electrons responsible for forming the moment are also those that participate in transport, it is no longer possible to clearly separate these two degrees of freedom (DOF). Thus, it is within this thesis that these ideas are explored in greater detail using two materials as a case study: the chiral helimagnet $Cr_{1/3}NbS_2$ and YFe_2Ge_2 a Pauli paramagnet believed to be near a magnetic quantum critical point.

This thesis is organized into eight chapters, beginning with a review of the relevant literature that motivates our investigation into the electronic structure of the chiral helimagnet and 3d intercalated transition metal dichalcogenide, $Cr_{1/3}NbS_2$. As a non-centrosymmetric magnet, $Cr_{1/3}NbS_2$ is a member of a broader class of materials that have attracted significant interest due to the interplay that develops between their magnetic and transport degrees of freedom. Within this class of compounds, the most widely studied are those known to host a topologically protected, 2D spin texture known as a Skyrmion. Here, much of the interest surrounding Skyrmions stems from the fact that the relatively long length scale of these spin textures allows for the possibility of manipulating them at the nano or even the mesoscale level through use of externally applied field or current. It is then due to the detailed interaction that arises between itinerant electrons and Skyrmions that a number of interesting and potentially technologically relevant phenomena, including the topological Hall and spin transfer torque effect, emerge.

While not conclusively shown to host a Skyrmion phase, a renewed interest in $Cr_{1/3}NbS_2$ has developed thanks to the discovery of a unique, one-dimensional solitonic excitation in this

material known as a chiral soliton lattice (CSL). Briefly stated, the CSL is a non-linear magnetic superstructure consisting of forced ferromagnetic domains that are periodically partitioned by 360° domain walls. Much like Skyrmions, the CSL is a topological object that can be manipulated by way of an external magnetic field. Namely, for a modest $H > 0.2$ T magnetic field applied perpendicular to the helical (c-) axis, it has been shown that the size of the ferromagnetic domains in the CSL phase can be continuously tuned. From a technological viewpoint, this finding is particularly significant as the CSL can act as a tunable effective potential for itinerant electron spins, allowing for one to exercise precise control over the transport properties of itinerant spin carriers.

Based upon this tunability, it has been proposed that a possible origin for the inter-layer magnetoresistance (MR) as measured with the field applied parallel to the *ab*-plane could result from Bragg scattering of conduction electrons by the chiral soliton kinks. Experimental evidence in support of this claim comes from a measurement of the inter-layer MR, which shows a direct correlation between the magneto-transport properties and the soliton lattice density. Specifically, it was found that the inter-layer MR will track the soliton lattice density remarkably well, producing a drop in the resistivity that occurs with stronger applied field. However, recent intra-layer transport and magnetotransport experiments indicate that the strong coupling that exists between the magnetic and transport DOF in this material could arise from more than what can be rationalized by the spin ordering argument described above.

Not surprisingly, the interpretation into the microscopic origin of the negative MR within $Cr_{1/3}NbS_2$ is fundamentally rooted in its electronic structure. In assuming spin ordering provides the sole origin for the negative MR within this material, an implicit assumption regarding the electronic structure is made. This is that the Cr intercalant acts as a charge reservoir donating electronic charge, with the effect of raising the chemical potential, without altering the overall Fermi surface (FS) or band topology of NbS_2. Thus, within the so-called rigid band interpretation, following donation of electrons to Nb-derived bands, the remaining electrons on the Cr site will simply serve to form local spin moments that couple to one another through conduction electrons. Given the findings from intra-layer MR to indicate that spin-ordering arguments alone cannot completely describe all the magneto-transport properties observed within this material, it is suggested that the electronic structure then plays a non-trivial role. Therefore, we present in Chapter 5 a detailed investigation into the electronic structure of $Cr_{1/3}NbS_2$ using

the experimental techniques outlined in Chapter 3 on the experimental apparatus discussed in Chapter 4.

In Chapter 5, our investigation necessarily begins with a characterization of the freshly exposed surface of *in-situ* cleaved $Cr_{1/3}NbS_2$. Generally speaking, it cannot be assumed that a surface cleaved *in-situ* will be representative of bulk. This can be attributed to the fact that surfaces will often relax or reconstruct so as to lower their free energy. Even without such processes, thanks to the fact that Cr atoms intercalate within the van der Waals gaps of NbS_2, through cleaving it is entirely possible that both the ordering and stoichiometry of the remaining Cr atoms at the surface will be different from those found in bulk. Such a difference has important consequences on the electronic structure, as it would imply a unique Brillouin zone or even doping for the topmost NbS_2 layer. Ultimately, through the course of our surface characterization, it was found that the remaining Cr adatoms randomly distributed on the surface following sample cleave will simply give rise to non-dispersive states in the angle-resolved-photoemission spectra (ARPES). Based upon this finding, we conclude that electronic structure measurements of *in-situ* cleaved $Cr_{1/3}NbS_2$ can in fact be used to reliably measure how intercalation serves to modify the host NbS_2 compound.

As expected, the introduction of a Cr intercalant serves to donate electronic charge to the NbS_2 bands, resulting in a raise of the chemical potential by ~0.4 eV. However, in addition to effectively donating charge, two additional bands at Γ (β_1, β_2), and one additional band at K (δ) are likewise found to emerge. Seeing as these additional features cannot be rationalized on the basis of a rigid band picture, it was initially speculated and subsequently shown that they must arise as a direct consequence of Cr intercalation. Most notably, from a temperature dependent ARPES investigation, the β_1, and β_2 bands centered at Γ were shown to be magnetic exchange split bands. Interestingly enough, a closer inspection of the data reveals a progressive decrease of the spectral weight occurring for these bands as temperature is raised above the helimagnetic ordering temperature. Such a finding is intriguing as this type of behavior is not typical for itinerant ferromagnetic systems.

Following this line of inquiry, resonant photoemission spectroscopy (ResPES) was used to determine the elemental character of the states comprising the valence band. From such measurements it found that both Cr- and Nb-derived states are hybridized, and that both participate in the formation of the FS. As it turns out, the presence of Cr-derived states at E_F has

significant implications for a microscopic description of magnetism and its interplay with the transport degrees of freedom. Based on these findings, it is evident that the same states responsible for magnetism are likewise those present at the Fermi level. Consequently, a clear separation between the magnetic and itinerant DOF does not occur, and the motion of the itinerant electrons and the local spin moments can be influenced reciprocally in a self-consistent fashion. In the end, the result of such interplay is most clearly illustrated by the increase in spectral weight observed at E_F as the temperature is lowered below the helimagnetic transition temperature. Such a finding then supports the notion that the electronic structure plays a non-trivial role in the magneto-transport properties of this material.

At this point there are then two directions worth exploring. The first entails an investigation of other 3d intercalated transition metal dichalcogenides following the same line of study as was used for $Cr_{1/3}NbS_2$. In such a case, the underlying motivation for doing so lies in the fact that the microscopic origin of magnetic excitations like Skyrmions, and CSL kinks is found in the fundamental interactions allowed in a crystalline lattice lacking inversion symmetry. More specifically, it is through the Dzyaloshinskii-Moriya interaction, which is ultimately spin-orbit derived, that many of the properties that underscore the functionality of non-centrosymmetric magnets originate. In this way, the 3d intercalated transition metal dichalcogenides are ideal systems to study as they represent a potential workbench for tuning the strength of the spin-orbit interaction through substitution of either heavier or lighter transition metal elements.

As an alternative line of investigation, our interest was directed more towards examining the dynamical properties of $Cr_{1/3}NbS_2$ with the possibility of using ultrashort laser pulses to manipulate magnetic order. In this way, there are then two means of capturing ultrafast dynamics presented in this thesis. The first, discussed in Chapter 6, takes advantage of the extremely short time scales involved in the photoemission process (10^{-17}s to 10^{-16}s). From this variation of core hole clock spectroscopy, in which the intrinsic lifetime of the core-hole sets a natural timescales for the dynamical process, the occurrence of large fluctuations in the spin moment were found on the Fe site of YFe_2Ge_2. Such a material was shown to have many of the same spectroscopic signatures as the Fe-pnictide superconductors, including exchange multiplets appearing in the Fe 3s core level photoemission spectra that reveals a magnitude for the magnetic moment that is significantly larger than that deduced from conventional, static measurements.

Such a discrepancy is particularly noteworthy in YFe_2Ge_2, as this material only exhibits Pauli paramagnetism. Therefore, this compound represents another example of a strong interplay that develops between magnetic and transport DOF as the fluctuations in the magnitude of the local moments found on a Fe site is intimately linked with the itinerancy in the system.

Compared to core-hole clock spectroscopy, the recent development of turn-key femtosecond (fs) laser systems has opened up the possibility of measuring temporal dynamics in real time. Specifically, given the ultrashort duration of these light pulses, a temporal resolution on the order of the characteristic time-scales of electronic and atomic motion can now be achieved. Among other things, this then allows for possibility of measuring coherently excited collective modes. Such a prospect is especially appealing for $Cr_{1/3}NbS_2$ as this not only includes a measure of coherently excited phonon modes, but magnon modes that are unique to helimagnetic systems as well. Furthermore, through optomagnetic processes like the inverse Faraday effect, there is the additional possibility of manipulating magnetic order on time-scales much shorter than that of the precessional timescale of spins. In this way, it may even be possible to induce the CSL transition within $Cr_{1/3}NbS_2$ using ultrashort light pulses as opposed to an externally applied magnetic field.

Given such exciting prospects, a detailed characterization of the static and transient magneto-optical properties of $Cr_{1/3}NbS_2$ is presented in Chapter 7. In such a case, the measurements reported within this chapter were carried out so as to disentangle the relevant contributions arising from electron, lattice and spin to the overall relaxation dynamics. It was confirmed that $Cr_{1/3}NbS_2$ possesses a magnetic easy plane, while single color optical pump-probe experiments reveal significant differences in the dynamics of NbS_2 and $Cr_{1/3}NbS_2$. Chief among these is the excitation of a high frequency coherent phonon mode that is unique to $Cr_{1/3}NbS_2$. Lastly, a long demagnetization dynamic was observed in the magnetic phase of $Cr_{1/3}NbS_2$ suggesting that the spins are thermally insulated from the electronic degrees of freedom. However, rather than being indicative of two decoupled DOF, the fact that the magnetic dynamic is not directly affected by optical excitations may simply imply spin flips occurring via Elliot-Yafet mechanism are inefficient due to an imbalance in the spin polarized DOS in the ferromagnetic state.

Finally, despite gaining insights into the various interactions that exist between electron, lattice, and spin degrees of freedom through the measure of real-time relaxation dynamics using

optical pump and probe spectroscopy, the fact that these experiments are performed using just the fundamental frequency of a Ti:Sapphire implies that only a temporal resolution can be achieved. In this way, a single color optical pump-optical probe experiment simply serves as a means of capturing the time evolution of the reflectivity, without providing any additional spectroscopic insights. With the initial stages of laser excitation serving to create a non-equilibrium distribution of photo-excited electrons, without having any means of characterizing this transiently excited non-equilibrium state, there is a certain degree of ambiguity associated with what physically gives rise to a change in the transient reflectivity.

For this reason, a direct probe of the changes that occur within the electronic structure is needed so as to elucidate the role that an intense, optical pump pulse has particularly in the generation of photo-induced phase transitions or the creation of hidden states inaccessible by equilibrium processes. In such a case, the ability of ARPES to not only provide a measure of the electronic structure with both an energy and momentum resolution, but also its capability of gaining valuable insights into the many-body interactions by way of the single particle spectral function makes this technique a premier tool for studying the time evolution of the electronic structure. Therefore as is discussed in Chapter 8, the design, construction and commissioning of a time-resolved ARPES system is presented with particular interest in laying out future plans enabling this system to resonantly excite collective modes in strongly correlated systems such as the manganites.

Chapter 2: Background and Motivation for Studying the Electronic Structure of the Chiral Helimagnet $Cr_{1/3}NbS_2$

2.1 Chiral Helimagnetism

The development of next generation electronic devices relies on the ability to precisely control intrinsic degrees of freedom (DOF) beyond that of charge. One such promising avenue involves the manipulation of individual, or average spin angular momentum of itinerant carriers, in what is commonly referred to as spintronics [21]. Here, one of the main technological appeals lies in the fact that the electron spin is an example of a two state quantum system, making it ideal for use in defining a binary pair for digital electronics [22]. While not as ubiquitous as the electronic transistor, spintronic devices have managed to find use in some specific technological applications, with the most well known example being that of the giant magnetoresistive (GMR) sensors used for magnetic storage devices [23]. Ultimately, the utility of a GMR device stems from the profound effect application of even a slight external magnetic field has on transport. This can be attributed to the fact that the relative magnetization between magnetic multi-layers changes the conditions for ballistic transport based on the spin of the itinerant electron. In this regard, a new class of materials known as chiral helimagnets (CHMs) has emerged, and just as for GMRs, the particular magnetic state of these materials is found to profoundly influence electronic transport. As will be discussed in greater detail below, it is ultimately this interplay between magnetic and transport degrees of freedom that makes CHMs promising materials for future spintronic and other information technology applications.

To understand the origin of the many unique properties hosted by CHM materials, it is necessary to first define the concept of chirality and what the resultant magnetic ground state for local spin moments distributed on the chiral framework of a lattice will be. Simply stated, chirality is characterized by a reflection asymmetry manifesting itself as either a left- or right-handedness. This property is universally found throughout the natural world, covering a wide range of disciplines and length scales [24]. For a lattice, chirality is often discussed in the context

of crystal structure. One of the simplest definitions for structural chirality is that an object be non-superimposable with its mirror image. Using the language of group theory, this implies that a structure lacks both a center of inversion as well as a mirror plane [25]. More precisely, this definition is a generalization of the fact that improper rotations, that is a rotation followed by a reflection, cannot be a symmetry operations of the crystallographic space group.

When local magnetic moments are distributed about a lattice lacking inversion symmetry, two competing exchange interactions develop. These include the usual symmetric exchange interaction, which favors a parallel, or ferromagnetic, ordering of spins, and an anti-symmetric exchange interaction known as the Dzyaloshinskii-Moriya interaction (DMI) [26,27]. The DMI originates as a first order correction to the energy of the super-exchange Hamiltonian with spin-orbit coupling being treated as a perturbation [26,27,28]. Typically, for crystals with a high degree of symmetry, this correction is often small. However, when inversion symmetry is broken, as it is for CHMs, the correction of the DMI will become leading order, resulting in an effective spin Hamiltonian that is given by [29,30]

$$\widehat{H} = -J \sum_{i,j} \vec{S}_i \cdot \vec{S}_j + \vec{D} \cdot \sum_{i,j} \vec{S}_i \times \vec{S}_j - g\mu_B \vec{H} \cdot \sum_i \vec{S}_i \qquad (2.1)$$

Here, $J > 0$ denotes the ferromagnetic exchange integral, $\vec{S}_i$ the spin on the i^{th} lattice site, g the Lande g-factor, μ_B a Bohr magneton, $\vec{H}$ an externally applied magnetic field, and lastly, $\vec{D}$ the DMI vector. Seeing as the DMI favors a perpendicular orientation of spins, a competition between the symmetric, ferromagnetic exchange and the much weaker, anti-symmetric DMI develops. The result of this competition is a twisting of the magnetization into an incommensurate helix having a long periodicity and a well-defined handedness determined by the DMI vector [29,31,32,33,34,35]. That is, in contrast to other helical antiferromagnets, such as the rare earth metals Holmium (Ho) and Dysprosium (Dy), the fundamental origin of the CHM magnetic ground state is entirely unique to crystals lacking in inversion symmetry [36].

While the interactions that lead to the formation of the CHM ground state are intimately tied to the symmetry of the lattice, the long length scale of the helical spin structure implies that the spin degrees of freedom can be essentially decoupled from that of the lattice. For this reason, part of the technological appeal generated by these materials originates from the possibility that the spin degrees of freedom can be manipulated at the nano or even mesoscale level, independent of the details of the lattice. This is an especially relevant fact given that CHMs are known to support extremely stable solitons, or non-linear excitations that maintain their shape and energy

as they propagate [37,38]. In other words, thanks to the long length scale of the spin structures, externally applied fields or current can be used to manipulate these solitonic excitations without altering their fundamental spin textures. Perhaps the best-known example of this can be found in the manipulation of magnetic Skyrmions.

2.2 Skyrmions

In condensed matter physics, magnetic Skyrmions are topologically protected spin textures that can be stabilized by thermal fluctuations in chiral magnets [39,40]. The root of this name originally comes from particle physics, where Tony Skyrme proposed that the stability of particles, such as hadrons, can be ultimately attributed to these being topologically protected entities [41]. For magnetic skyrmions, this topological protection manifests in a stable two dimensional spin texture characterized by an unchanging topological integer given by the wrapping of spins around a unit sphere [38]. Depending on the value of vorticity and helicity, there can be many possible types of Skyrmion structures [42] and an equally numerous variety of mechanisms for generating them in magnetic systems [42]. Of these, the most well known relies on the competition between the direct exchange interaction and the DMI in non-centrosymmetric magnets [39,40]. Within this class of materials, one of the most extensively studied is the B20 transition metal compound, MnSi.

MnSi is a ferromagnetic metal belonging to a chiral $P2_13$ space group [43]. Much of the interest surrounding this material stems from its rich magnetic phase diagram, which includes a CHM ground state, a conical phase and a novel magnetic phase referred to as the A-phase [44]. Further investigations of the A-phase by small angle neutron scattering has revealed that it can be characterized by the superposition of three helical spin structures each separated by 120° from one another (Figure 2.1) [1]. Based on model calculations, such a finding was taken as evidence for the existence of a two-dimensional spin vortex—the Bloch Skyrmion [1,45]. Following the positive identification of Skyrmions in MnSi, other B20 compounds such as the semiconductor, $Fe_{1-x}Co_xSi$ [46,47], FeGe [48,49], and the multiferroic insulator Cu_2OSeO_3 [50], where likewise found by neutron scattering and real space imaging techniques to host a Skyrmion lattice phase. Of all these materials, the latter has proved to be especially appealing as it opens up the

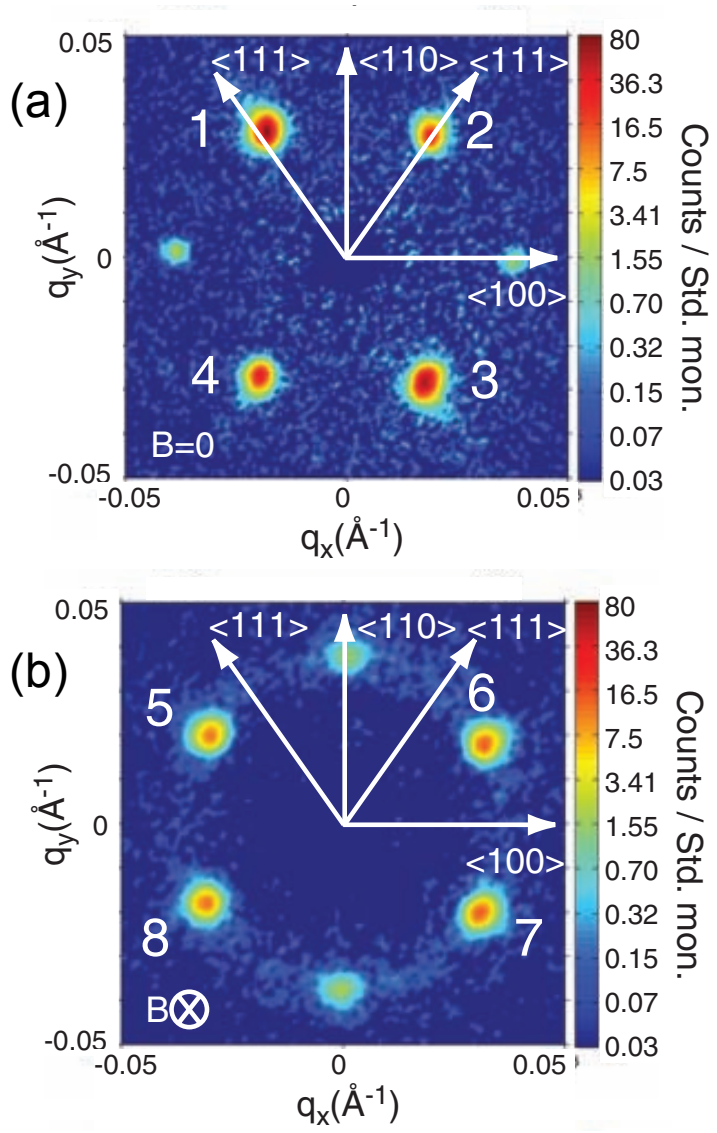

Figure 2.1: Small angle neutron scattering (SANS) performed on MnSi in (a) the helical and (b) the A-phase [1]. Signature of helimagnetic ordering along the 111 direction is given by the presence of satellite peaks at +/- Q = 0.036 Å^{-1}. SANS data collected in the A-phase shows superposition of three helical spin structures. Theoretical models showed this to be a signature of the Bloch Skyrmion

possibility for manipulating magnetic spin textures, like Skyrmions, through use of externally applied electric fields [51].

Since the discovery of a Skyrmion lattice phase in the B20 compounds, there has been a great incentive for the synthesis of novel non-centrosymmetric magnetic materials capable of hosting non-trivial spin textures. The main motivation for doing so stems from the technological appeal of Skyrmions as they are considered to be promising candidates for future magnetic storage devices [52]. Most notably, by exploiting the fact that Skyrmions couple strongly to conduction electrons, it has been found that ultra-low current densities and spin-polarized currents can be used to readily manipulate them on both a collective and individual level [53,54]. Ultimately, this can be attributed to the large length scales of Skyrmions relative to that of the lattice as these topological objects are only weakly coupled to lattice and are therefore not easily pinned by defects. As it turns out, this ability to manipulate Skyrmions using such low current densities is a consequence of the spin transfer torque effect and is intimately tied to the detailed interaction between itinerant electrons and Skyrmions.

One of the clearest examples that best illustrates the kind of strong coupling that exists between Skyrmions and itinerant electrons can be found in the so called topological Hall effect [2,55,56]. Here, the interaction between Skyrmion spin textures and conduction electrons can be described in terms of an emergent electromagnetic field that arises from a gauge field corresponding to the non-coplanar spin configuration of the Skyrmion. As shown in Figure 2.2, when an electron traverses a Skyrmion, it acquires a Berry phase due to the adjustment of its spin orientation to the local spin structure of the Skyrmion. The combined effect of both the Berry phase and interaction with the emergent electromagnetic field, results in the conduction electron experiencing an effective Lorentz force, which gives rise to a unique Hall effect referred to as the topological Hall effect. Taken together with the preceding paragraph, it is evident that itinerant electrons are not only be affected by Skyrmions, as in the topological Hall effect, but can also serve to directly affect Skyrmions as well. More explicitly, from the current driven motion of Skyrmions like that discussed in [53], it turns out that this will result in a temporal variation in the emergent magnetic field, which in turn produces an emergent electric field through induction [57]. Such an emergent field produces a Hall effect, known as the Skyrmion Hall effect, which actually serves as a counter to the topological Hall effect and thus leads to a suppression of the

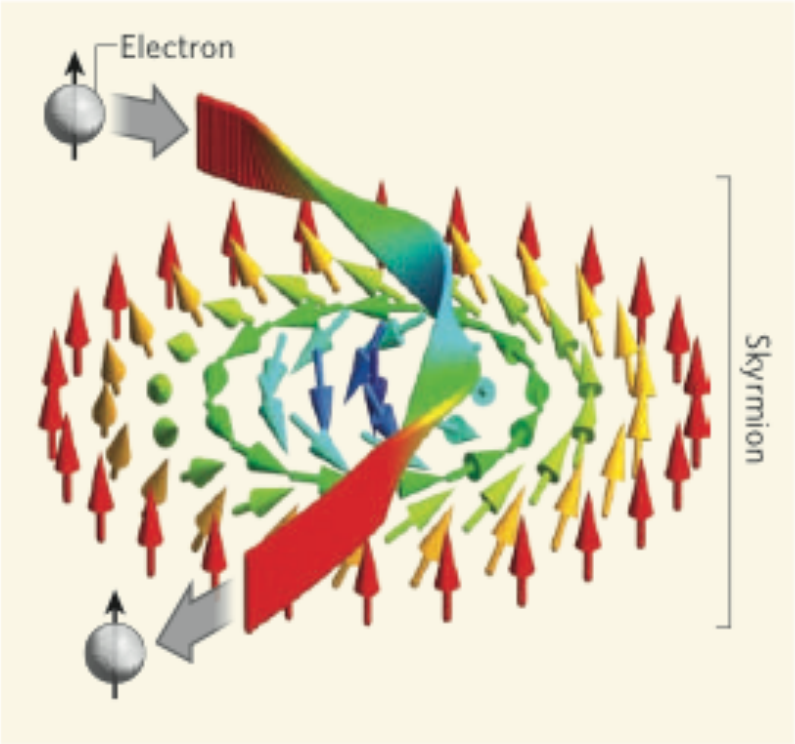

Figure 2.2: Schematic illustration of the topological Hall effect [2]. Effective Lorentz force experienced by the electron is a direct consequence of the type of strong interactions that exists between itinerant electron and Skyrmions

Hall response above some critical current density. Ultimately, it is because of the strong interaction that exists between the transport and spin DOF in this class of materials that there has been such an emphasis for the design and fabrication of new CHM materials.

2.3 The Chiral Soliton Lattice in $Cr_{1/3}NbS_2$

In the search for novel CHMs, the intercalacted transition metal dichalcogenide (TMDC), $Cr_{1/3}NbS_2$, has emerged as a promising material that possesses many of the same technologically appealing characteristics as the B20 compounds. Unlike the B20 compounds, however, $Cr_{1/3}NbS_2$ crystalizes in a more anisotropic Nb_3CoS_6 (hp20) structure type having a hexagonal $P6_322$ space group [5]. Here, the intercalated Cr atoms order in a $(\sqrt{3}\times\sqrt{3})R(30°)$ superstructure, occupying octahedral (O_h) sites within the van der Waals gaps of the 2H poly-type structure of NbS_2 (2H-NbS_2[58]) [59]. The unit cell of $Cr_{1/3}NbS_2$, with lattice constants a = b = 5.741Å and c = 12.101Å, contains 20 atoms, with twelve S atoms occupying the general site, and six Nb atoms in two inequivalent positions [5].

As far as the magnetic structure is concerned, local, Cr-derived spin moments order ferromagnetically in the ab-plane below a Curie temperature T_C = 116-132 K [5,60,61]. Static susceptibility measurements demonstrate a Curie-Weiss behavior in which the effective moment is consistent with that of a local, spin derived moment originating from Cr being in a Cr^{3+} oxidation state [5]. This is further supported by the saturation of the magnetization at 3 μ_B/Cr, suggesting that the Cr atoms adopt a high spin configuration in its trigonally distorted O_h crystal field [5]. Noting that inversion symmetry is broken only along the c-axis, a helical spin structure having a period of 480Å, determined by small angle neutron scattering [30] and Lorentz force microscopy [3], is found to develop parallel to this axis.

Most recently, a renewed interest in $Cr_{1/3}NbS_2$ has developed thanks to the discovery of a unique, one-dimensional solitonic excitation in this material known as a chiral soliton lattice (CSL) [3]. As can be seen in Figure 2.3, the CSL is a non-linear magnetic superstructure consisting of forced ferromagnetic domains that are periodically partitioned by 360° domain walls. Much like Skyrmions, the CSL is a topological object that can be manipulated by way of an external magnetic field. Namely, for a modest H > 0.2T magnetic field applied perpendicular to the helical axis, it has been shown that the size of the ferromagnetic domains in the CSL phase

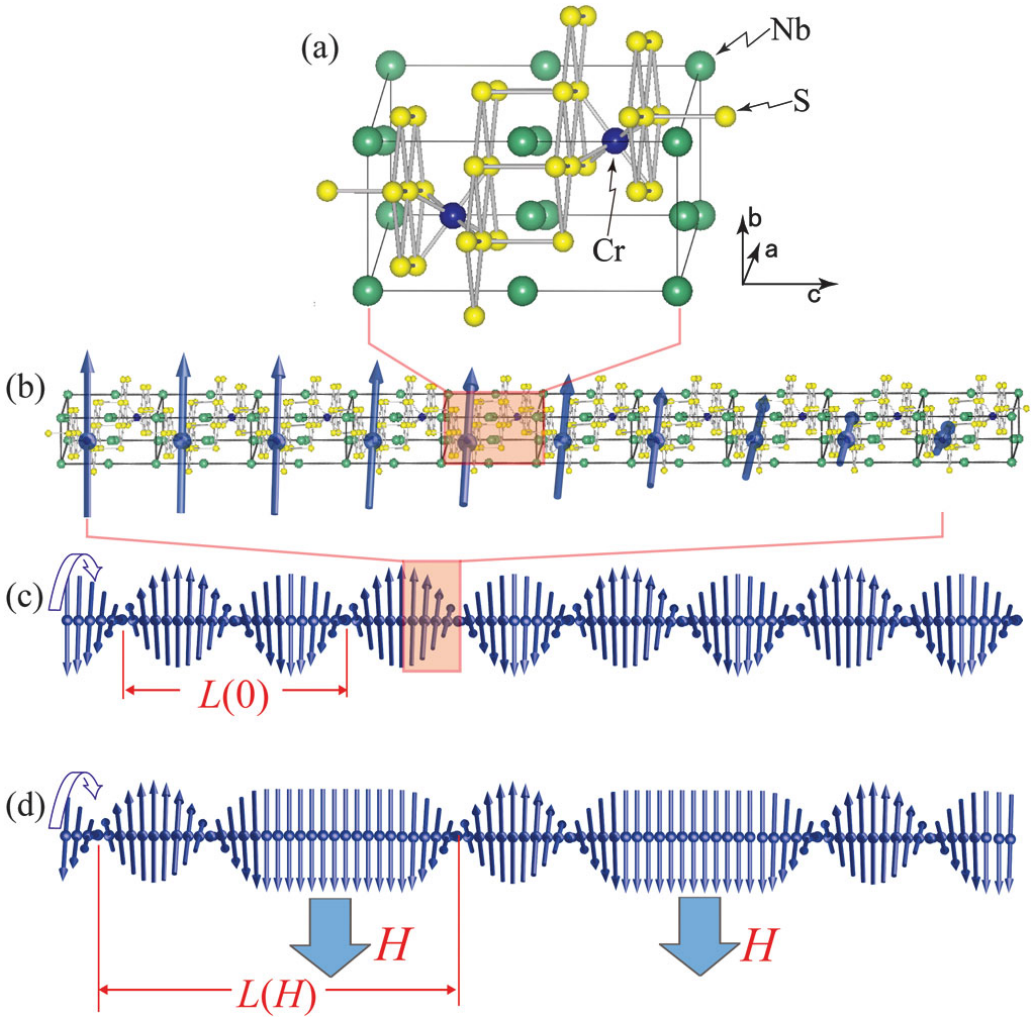

Figure 2.3: Schematic illustration of (a) crystal structure, (b) and (c) the CHM ground state and (d) the CSL phase taken from [3]. Note that the CSL comes about when field is applied in the easy plane perpendicular to the helical axis.

can be continuously tuned [3]. From a technological viewpoint, this finding is particularly significant as the CSL can act as a tunable effective potential for itinerant electron spins,allowing for the possibility to exercise precise control over the transport properties of itinerant spin carriers [62]. Additionally, the high stability and robustness of the CSL phase can pave the way for other spintronic functionalities such as spin current induction [63], soliton transport [64], and current driven collective transport [65]. Moreover, due to the fact that $Cr_{1/3}NbS_2$ crystallizes in a more anisotropic layered structure, this material has also been recognized as an ideal system for the study of spin-textures in magnetic thin films, devices fabricated on a substrate, and spin-orbit coupling effects in magnetic multilayers where the larger anisotropy provides for a greater opportunity for utility and control [66].

As previously mentioned, a major technological appeal of $Cr_{1/3}NbS_2$ lies in the tunability of the magnetic superstructure in the CSL phase. Based on this tunability, it was proposed that a possible origin for the inter-layer magnetoresistance (MR) as measured with the field applied along the *ab*-plane could be a result of Bragg scattering of conduction electrons by the chiral soliton kinks [67]. In other words, through changing the periodicity of the CSL by way of varying the strength of the applied field, the location of the superstructure zone boundary, and thus the condition for Bragg scattering along the k_z axis, will also change. From this change, one would expect the inter-layer MR to decrease as a stronger applied field causes a drop in the soliton kink density. Interestingly, measurements of the inter-layer MR in $Cr_{1/3}NbS_2$ have provided evidence for a direct correlation between magneto-transport and soliton lattice density [4]. Notably, as shown in Figure 2.4, the normalized, inter-layer MR was found to track the soliton density remarkably well. Such findings suggest a simple origin for the MR that is rooted entirely in scattering arguments.

Recent intra-layer transport and magnetotransport experiments depicted in Figure 2.5, however, have provided indication that the strong coupling that exists between the magnetic and transport DOF in this material could arise from more than what can be rationalized by spin ordering arguments alone. Most notably, as $T < T_C$, an abrupt, ten-fold drop in the resistivity is found to occur concomitant with the onset of magnetic order [5]. In a similar fashion, intra-layer MR data taken with a 140 kOe field applied parallel to the *ab*-plane shows a prominent, negative MR of approximately 55% at T_C. Moreover, as compared to the inter-layer MR presented in [4], the in-plane MR likewise exhibits a 5.5% drop occurring at the CHM to CSL transition [5].

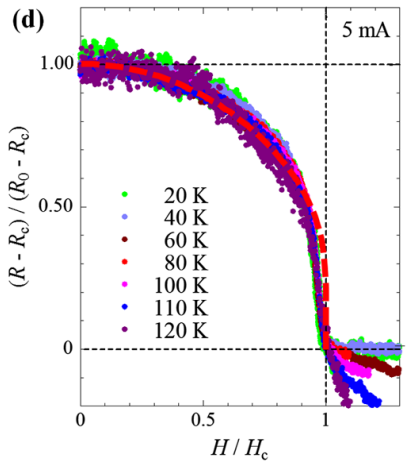

Figure 2.4: Normalized inter-layer magnetoresistance measured for $T < T_C$ and plotted as a function normalized field. As pointed out in [4] the inter-layer magnetoresistance is found to track the soliton kink density remarkably well.

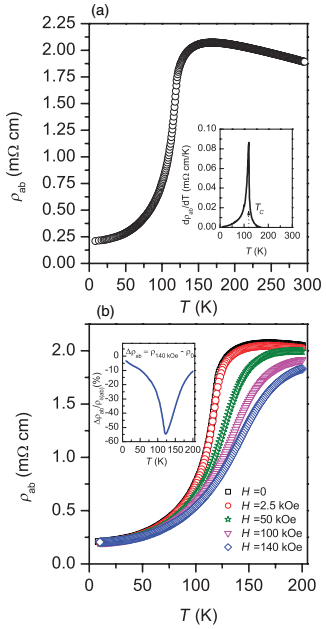

Figure 2.5: Intra-layer (a) transport and (b) magnetotransport measurements taken from [5]. Note the sharp drop in resistivity and large negative magnetoresistance occurring at T_C. Given these measurements to be taken in the ab-plane, such results cannot be rationalized on basis of Bragg scattering by soliton kinks.

Based on such findings, it is not readily obvious how the modulation of the CSL state along the c-axis could have such a strong impact on the in-plane transport properties. Ultimately, this suggests that the electronic structure may be playing more than a passive role in determining the magneto-transport properties of this material.

Evidence in support of this claim comes from insights gained by first principal calculations used to interpret the dependence of the intra-layer MR on the applied magnetic field direction [68]. Namely, for T < 50K, a three-fold drop in the MR is seen when a 7T field is applied parallel to the crystallographic *c*-axis as opposed to the *ab*-plane. Unlike other 3d intercalated TMDCs, like $Fe_{1/4}TaS_2$ [69], this finding shows that a larger drop in the MR occurs when the field is applied along a hard magnetization axis. Aside from this finding, the MR shows similar behavior to that reported in [4] and [5], where it likewise exhibits a sharp drop at the CHM to CSL transition. However, the critical field (H_C) at which this transition occurs shifts towards higher values as the angle at which the field is applied becomes increasingly normal to the current containing plane. For sufficiently strong magnetic fields (H > 3T), the magnetization will saturate regardless of the applied field direction, and the corresponding normalized MR turns out to be 10% lower when the field lies along the hard magnetization axis. Based on considerations from electronic structure calculations, the dependence of the MR on applied field direction can be attributed to changes in density of states near the Fermi level that depends sensitively on the spin orientation [68]. Taken together with the intra-layer MR measurements previously discussed, there is then sufficient motivation to investigate what role the electronic structure plays in the magneto-transport properties of this material.

2.4 Motivation for Measuring Electronic Structure

Aside from gaining deeper insights into the origin of the strong coupling that exits between the magnetic and transport DOF, a more general motivation for studying the electronic structure of $Cr_{1/3}NbS_2$ stems from the potential that this material has in being a model system for studying the role played by spin-orbit interaction in the DMI, and thus chiral helimagnetism in general. Although magnetic excitations such as Skyrmions, and CSL kinks, which are at the heart of the functionalities for CHMs, will manifest on the nanoscale to mesoscale level, their microscopic origin is found in the fundamental interactions allowed in a crystalline lattice lacking inversion symmetry. With the DMI being rooted in the relativistic spin-orbit interaction

[26, 27, 28], a detailed knowledge of the electronic structure of available CHMs is necessary in order to elucidate the microscopic interactions underpinning their functional properties. For this, 3d intercalated TMDCs are ideal systems as they represent a potential workbench for tuning the strength of the spin-orbit interaction through substitution of other TM elements that are either heavier or lighter than Nb [70]. In doing so, it is expected that such a substitution would result in a respective strengthening or weakening of the DMI, which in turn alters the properties of the CHM state.

In this same manner, beyond its importance as a model CHM material, a detailed knowledge of the electronic structure of $Cr_{1/3}NbS_2$ is further motivated by the fact that this material is a compelling example of a TMDC intercalated with a 3d magnetic element (Cr). Recently, group VI TMDCs have generated a great deal of interest in the community thanks to the possibility of manipulating valley spin or pseudo-spin using circularly polarized light [71,72,73,74]. Part of the broad appeal of layered TMDCs is that they are amenable to additional modification of their electronic structure [75]. One way this can be accomplished is through intercalation of a variety of electron donor species ranging from alkali metals [76] to large organic molecules [77]. This drastically changes the carrier concentration of the host TMDC material and results in many non-trivial effects including metal-to-semiconductor transitions [78], or semiconductor-to-superconductor transitions [79]. Consequently, given the potential technological application of layered TMDCs, it is important to develop a systematic understanding as to how intercalation serves to modify the electronic structure of the host material. In this regard, $Cr_{1/3}NbS_2$ serves as a prototypical case study of intercalation of TMDCs with 3d magnetic atoms.

2.5 Electronic Structure of Intercalated TMDCs

Much of what is known about the electronic structure of intercalated TMDCs, stems from the general interpretation that the added electronic charge introduced by the intercalant changes the total number of carriers, without altering the local bonding of the host material [59]. Consequently, it is believed that intercalation does not change the Fermi surface (FS) or band topology of the host TMDC, as its only effect is to raise the chemical potential by an amount dependent upon the oxidation state of the intercalant [80]. Accordingly, Hall measurements for intercalated 2H-NbS_2 are typically interpreted in this light [81]. Namely, by assuming a single

carrier type, which is valid given the discussion below, an estimate of the carrier type and concentration can be determined from the Hall coefficient. For intercalated 2H-NbS_2, it was found that the total number of hole-like carriers decreases accordingly thanks to the added electronic charge introduced by the intercalant (Figure 2.6). Given then the relevance of the host electronic structure in the description of intercalated TMDCs, it is necessary to first provide some essential background regarding the electronic structure of the parent TMDC compound. While few reports of 2H-NbS_2 have appeared in the literature, the iso-structural and iso-electronic compound 2H-$NbSe_2$ is in contrast very well studied. Thus, a description of the electronic structure of 2H-$NbSe_2$ will be presented below under the supposition that there are only minor differences as compared to that of NbS_2.

Ab initio density functional theory (DFT) calculations for 2H-$NbSe_2$ have shown a grouping of the Nb d-bands to be roughly consistent with that of a simplified ligand field model [82]. Here, the Nb atom ($4d^1$) sits in a trigonal prismatic environment (D_{3h}), in which the crystal field splits the five-fold degenerate Nb 4d states into one singly degenerate a_1' state with symmetry z^2, and two doubly degenerate e' and e'' states with symmetry x^2-y^2/ xy, and xz/yz, respectively [25]. The relative energies of these states is dictated by the overlap of the Nb 4d and the Se 3p states. Since the ligands are situated at the corners of the prism, a greater Coulomb repulsion results from an increased orbital overlap between the e'' states (d_{xz}/d_{yz}), with the ligand (Se) p states. Consequently, the e'' states are raised in energy relative to the e' ($d_{x^2-y^2}/d_{xy}$) and a_1' (d_z^2) states. Moreover, given the larger distance separating neighboring Nb atoms along the c-axis, the a_1' (d_z^2) states are lower in energy than the e' ($d_{x^2-y^2}/d_{xy}$) states. Therefore, based on ligand field arguments, the Nb d^1 electron should occupy a state of d_z^2 symmetry. Accordingly, it is common within the literature to see reference to a lower d_z^2 sub-band when discussing the Nb-derived bands in proximity of the Fermi level [59]. This label persists despite the fact that DFT calculations show the lower energy state to have exclusively d_z^2 character at the center (Γ), and $d_{x^2-y^2}/d_{xy}$ at the corners (K) of the Brillouin zone (BZ) [82].

Experimentally, the electronic structure of $NbSe_2$ has been investigated with de Haas van Alphen (dHvA) oscillations [83] and ARPES experiments [6, 84, 85]. These studies revealed the presence of a small, flat Se-derived, hole pocket centered at the Γ point, and two Nb-derived, cylindrical hole pockets at the Γ and K points. A much larger mass enhancement was found for the Nb-derived bands as compared to the Se-derived bands, suggesting a stronger electron-

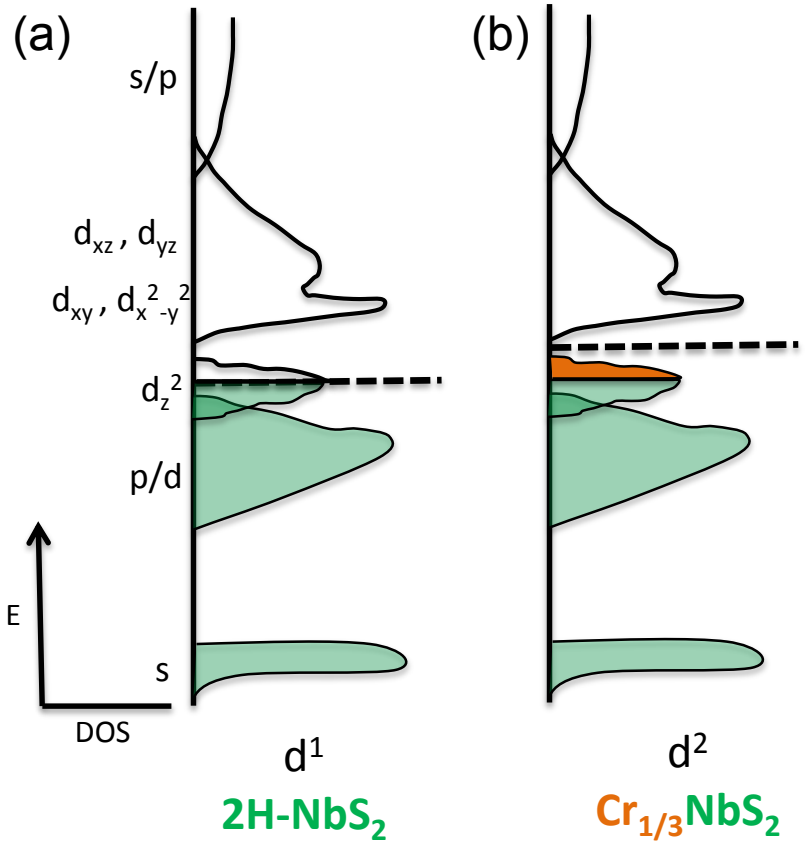

Figure 2.6: Schematic illustration of the valence band for (a) NbS_2 and (b) $Cr_{1/3}NbS_2$ under the supposition of a rigid band interpretation. Note that in the rigid band picture, the intercalant serves to donate electrons so as to fill d_{z^2} sub-band

phonon coupling. For the 2H poly-type, each band is actually doubled, since there will be two formula units per unit cell [58]. For this reason, interlayer coupling and spin-orbit interaction serves to lift the degeneracy of the Nb-derived bands, resulting in an energy splitting of the bands as can be clearly seen in Figure 2.7 [6,84,85]. This splitting is referred to as the bilayer splitting, where the upper and lower bands are denoted by the same labeling convention used for molecular orbitals. That is, the bonding and anti-bonding bands respectively. In contrast, based on the result of both dHvA and ARPES experiments, the Se-derived bands were found to be degenerate in energy. This difference highlights a key feature of TMDCs, which is the anisotropy arising from the low dimensionality in these materials [86]. In the end, such anisotropy results in many interesting features of the electronic structure including charge density waves, and a momentum dependence of the superconducting gap [87].

Based on the above understanding of the host electronic structure, arguments rooted in a rigid band interpretation can then be applied so as to understand how Cr intercalation is expected to modify the electronic structure of 2H-NbS_2. By invoking simple counting arguments, it is expected that $Cr_{1/3}NbS_2$ be semiconducting, as the intercalated Cr atom should donate a full electron to completely fill the d_z^2 sub-band of NbS_2. However, it is evident from transport measurements that this cannot be the case since $Cr_{1/3}NbS_2$ clearly displays metallic behavior [5]. While not entirely surprising that counting arguments fail to correctly predict the filling fraction for this material, such a failure does at the very least begin to arise suspicion in regards to the validity of the rigid band model. More recently, growing experimental evidence has actually begun to call the rigid band model into question. Most notably, several studies have shown that intercalation can alter the electronic properties of the host TMDC in non-trivial ways [7,78,79,88]. Two prominent examples include Cs and Rb intercalation of TaS_2 and $TaSe_2$, respectively. As shown in Figure 2.8, intercalating with alkali atoms had dramatically changed the charge density wave periodicity, and induced a metal-to-semiconductor transition. Moreover, an ARPES investigation directly comparing the electronic structure of $NbSe_2$, $Mn_{1/3}NbS_2$ and $Ni_{1/3}NbS_2$ has indicated that the added electronic charge introduced by the intercalant preferentially fills the hole pocket at the zone corner over that at the zone center [89]. Hence, it remains an important question to address whether or not the rigid band picture is valid for $Cr_{1/3}NbS_2$, and if not, then to what extent does it fail.

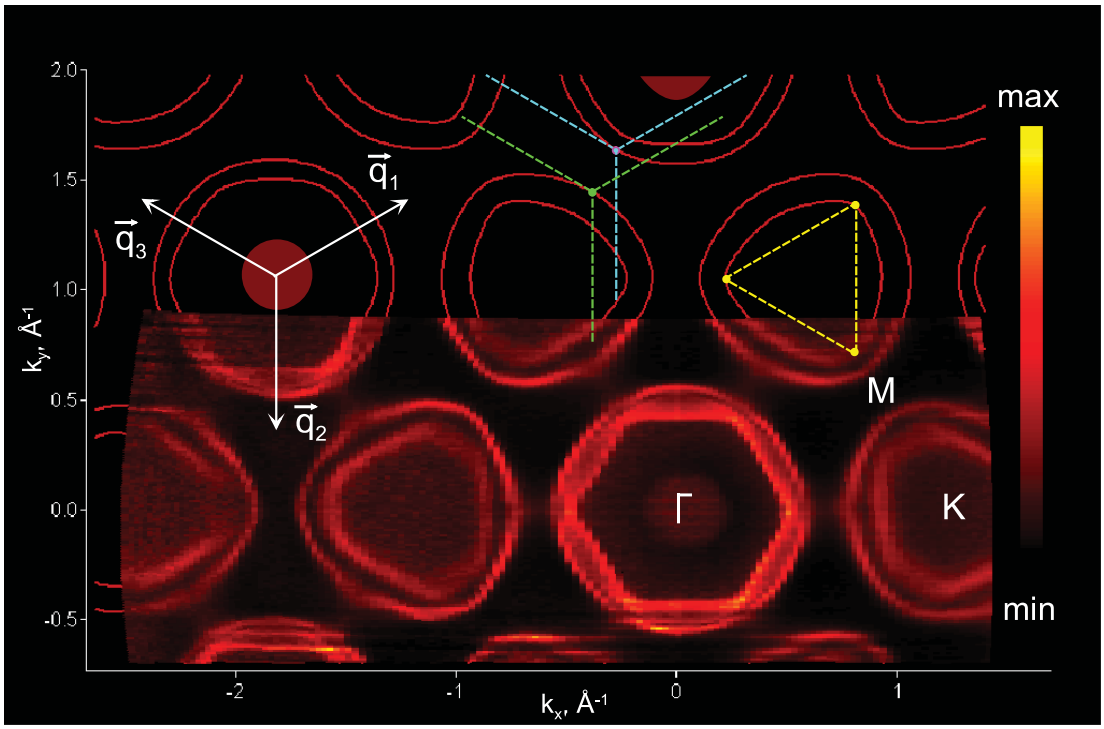

Figure 2.7: Fermi surface ARPES map of $NbSe_2$ taken from [6]. Note presence of small Se derived hole pocket at Γ and bilayer split Nd-derived hole pockets at Γ and K

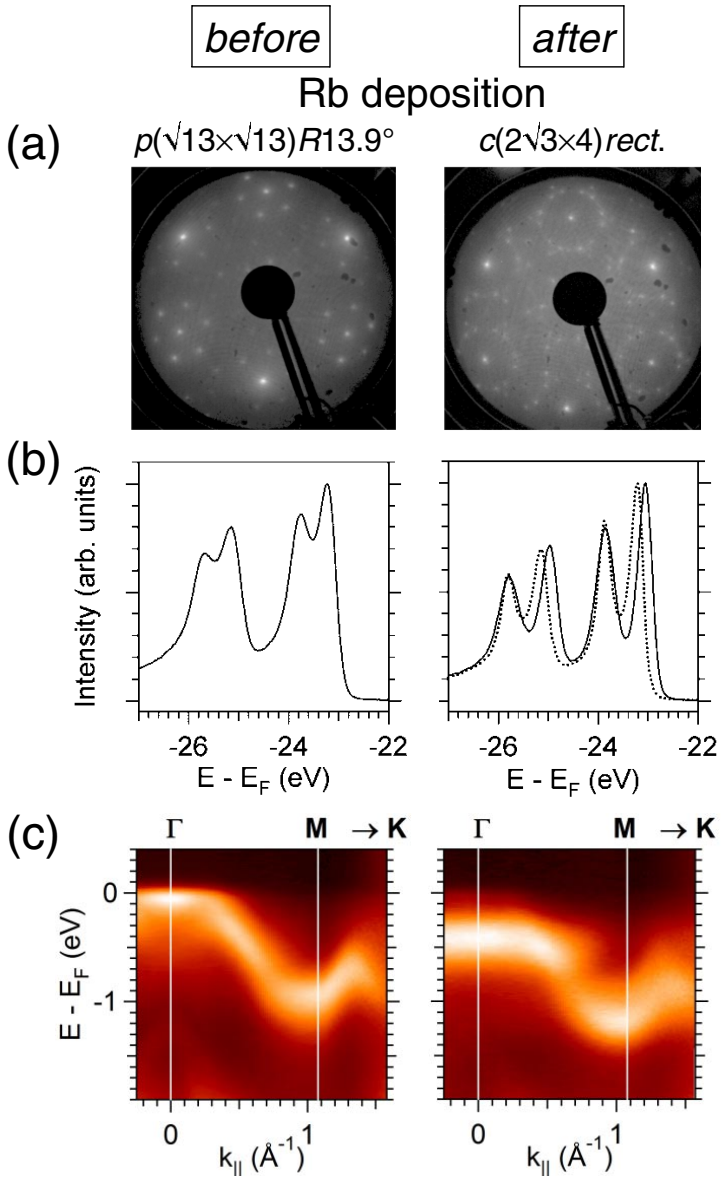

Figure 2.8: Effects of Rb intercalation on the electronic structure of TaS_2 taken from [7]. Here, Rb deposition alters the CDW periodicity as can be seen from LEED images in (a) and affects both the local electronic environment of the Ta 4f (b) and the size of the Mott-Peierls gap in the electronic structure (c)

2.6 Relating the Electronic Structure to the Exchange Interaction

Given that intercalation is accomplished by a 3d element, an additional question worth asking is what serves as the microscopic origin of the exchange interaction. More generally, this question can be extended to asking what exactly is the fundamental interaction between itinerant electrons and magnetism in this material. Such a question turns out to have little to do with the CHM and CSL states, as it has been previously discussed that non-trivial spin textures like Skyrmions exist in conductors, semi-conductors and insulators alike, but rather has specific implications for the magneto-transport properties of $Cr_{1/3}NbS_2$. In particular, based on DFT calculations, it was shown that the Stoner criteria is well satisfied in $Cr_{1/3}NbS_2$ [5], suggesting that this material is an itinerant ferromagnet in which magnetism emerges based on the spontaneous splitting of spin polarized bands [90]. However, in the more widely accepted context of the rigid band model, the typical origin for the magnetic exchange interaction for 3d intercalated TMDCs is taken to be a result of the Ruderman-Kittel-Kasuya-Yosida (RKKY) exchange.

Within the RKKY exchange, conduction electrons serve to mediate the interaction between local magnetic moments, which, due to their large separation distances, would otherwise be incapable of interacting through a direct exchange mechanism. In these materials, the rigid band model turns out to favor this type of exchange because it stipulates that following the donation of charge to Nb-derived bands; the electrons remaining on the intercalant site will be localized and give rise to a spin-derived magnetic moment. In such a case, given the details of the RKKY interaction, it is expected that the magnetic ordering switch between ferromagnetism and anti-ferromagnetism depending on the separation distance, and therefore concentration, of the intercalant. From a study examining magnetic ordering as a function of Fe doping in Fe_xTaS_2, such a ferromagnetic to anti-ferromagnetic phase transition was actually found to occur around $x\sim0.4$ [69,91]. In addition, some of the most convincing evidence in support of a RKKY exchange interaction in this class of materials comes from polarized neutron scattering experiments [92]. Here, a measure of the magnetization density of $Mn_{1/4}TaS_2$, revealed a spin polarization on the Ta, i.e. conduction electron, sites indicative of the kind of local spin polarization of the conduction electrons expected from RKKY.

Based on these two possible origins for the exchange interaction, one finds that the Cr-derived states will either play an active, or passive role in regards to the interaction between local magnetic moments and itinerant electrons. Therefore, in addition to understanding the validity of the rigid band interpretation in $Cr_{1/3}NbS_2$, it is likewise necessary to gain insights into interplay between local moments and itinerant electrons in $Cr_{1/3}NbS_2$ as such an interplay ultimately provides a fundamental understanding into the magneto-transport properties in this material.

Chapter 3: Experimental Techniques

3.1 Photoemission Spectroscopy

Modern photoelectron spectroscopy (PES) has established itself as a premier tool for studying the electronic structure of complex, many-body systems that are typical of condensed matter physics [9,10,13]. Initially described by Einstein in 1905, the basic premise behind PES is rooted in the production of photoelectrons by use of mono-energetic photons having an energy that is sufficiently high to excite an electron within a gas, liquid, or solid into a free-electron final state. Depending on the binding energy, E_B, of the electron, the resultant kinetic energy, E_{KE}, of the outgoing photoelectron is determined by

$$E_{KE} = h\nu - E_B^V \tag{3.1}$$

where E_B in this expression is referenced relative to the vacuum level. By recalling that the electron energy levels are quantized, it is evident from above that the kinetic energy distribution of photoelectrons will, to a first approximation, reflect the one-electron energy levels of the core subshells for the various atoms that comprise the solid. Herein lies the power of PES, as this technique is capable of providing a direct measure of the electronic structure both at the local, atomic level as well as over the whole valence band.

From a phenomenological perspective, the photoemission process can be described as comprising of three independent steps in which an electron is first excited by absorption of a photon, then transported to the surface, and finally ejected into vacuum [93]. While pedagogical, this model, known as the three-step model, turns out to be overly simplified as it neglects the possibility of there being interference between bulk and surface emission as well as from loss and no-loss transport. For this reason, a more proper, but less transparent description of photoemission treats the whole process as a single step consisting of just photoexcitation with an appropriate choice of initial and final states [94]. In particular, while the initial state can always be described in terms of a complete set of Bloch functions, the final state must account for the fact that the wavefunction of the outgoing photoelectron can freely propagate in vacuum but must then dampen at the surface interface. Such a state turns out to be best exemplified by that

of an inverse Low Energy Electron Diffraction (LEED) state, which has been subsequently used in the quantitative calculation of PES spectra [95]. With that being said, despite its shortfalls, the clear, intuitive picture provided by the three-step model makes it preferable to the one-step model in qualitatively describing the photoemission process. Consequently, for the sake of being instructive, the three-step model will continue to be used to develop a qualitative expression for the photocurrent measured in PES.

Namely, by recalling that the initial photoexcitation step will be governed by the transition rate probability $w_{f,i}$, one can expect that any expression for the photocurrent must ultimately contain some reference to Fermi's golden rule.

$$w_{f,i} = \frac{2\pi}{\hbar}|\langle f|\hat{H}'|i\rangle|^2 \delta\big(h\upsilon - (E_f - E_i)\big) \tag{3.2}$$

Put in a more usable form, through working in a semi-classical theory the interaction Hamiltonian, $\hat{H}'$, can be written as

$$\hat{H}' = \frac{e}{2m}\left(\vec{A}\cdot\hat{p} + \hat{p}\cdot\vec{A}\right) + \frac{e^2}{2m}\vec{A}\cdot\vec{A} \tag{3.3}$$

where the light-matter interaction term is expressed in the usual way by distributing the square over the conjugate momenta $\hat{p} \to \hat{p} + e\vec{A}$ in which $\vec{A}$ denotes the vector potential of the electromagnetic field. Using the fact that ${}^{e}/_{2m}\left(\vec{A}\cdot\hat{p} + \hat{p}\cdot\vec{A}\right) = {}^{e}/_{2m}\left(2\vec{A}\cdot\hat{p} - i\hbar(\vec{\nabla}\cdot\vec{A})\right)$ the above expression for the interaction Hamiltonian will simplify to

$$\hat{H}' = \frac{e}{m}\left(\vec{A}\cdot\hat{p}\right) \tag{3.4}$$

where an appropriate choice of gauge allows for one to define $\vec{\nabla}\cdot\vec{A} = 0$, while the diamagnetic term has been dropped as it represents the contribution coming from two photon processes, which turn out to be negligible at sufficiently low fluences. Moreover, given the wavelength of the typical excitation energies used in PES to be much larger than the atomic dimensions in the solid, the dipole approximation can be applied. By doing so,

$$\hat{H}' = \frac{e}{m}(A_0\hat{\varepsilon}\cdot\hat{p}) \tag{3.5}$$

making it such that the spatially varying vector potential can then be approximated as a constant whose direction is defined by the polarization $\hat{\varepsilon}$.

In regards to the photoexcitation step, it is important to note that this process involves the nearly instantaneous interaction between a single photon and a single electron. For this reason, it

is often assumed that the outgoing photoelectron can be treated as if it were decoupled from the remaining *N-1* electrons of the solid. This then allows for the final state to be written as

$$|f\rangle = |k_f\rangle \otimes |\Psi_s^{N-1}\rangle \tag{3.6}$$

in which the remaining *N-1* electron system will generally be left in some excited state *s* following the promotion of a photoelectron into the free electron state $|k_f\rangle$. Such an approximation, more commonly referred to as the sudden approximation, turns out to be fundamental to the physical interpretation of PES spectra. Notably, through invoking the sudden approximation, the transition rate probability defined above can then be rewritten as

$$I \propto w_{f,i} = \frac{2\pi}{\hbar}\sum_s \left|\left\langle k_f \middle| \frac{e}{m} A_0 \hat{\varepsilon}\cdot\hat{p} \middle| k_i \right\rangle\right|^2 |\langle \Psi_s^{N-1}|\Psi_0^{N-1}\rangle|^2 \times\delta(h\nu - E_{KE} - (E_s(N-1) - E_0(N))) \tag{3.7}$$

From this expression, it is evident that in addition to having a dependence on dipole selection rules, the transition rate will likewise be determined by the probability that upon removal of an electron, an *N* particle system in its ground state will be left in some excited state *s* of the *N-1* particle system. Put another way,

$$|\langle \Psi_s^{N-1}|\Psi_0^{N-1}\rangle|^2 = |\langle \Psi_s^{N-1}|c_k|\Psi_0^{N}\rangle| \tag{3.8}$$

meaning that the *N-1* overlap integral is nothing more than an expression for the probability of a hole being created in some eigenstate of the *N* particle system.

3.1.1 Corel Level Photoemission

For a photoelectron being ejected from the kth orbital of a system that is nearly in its ground state, the PES spectrum will consist of a single Lorentzian that can be attributed to the fact that the core-hole possesses a finite lifetime. In this case, the *N-1* overlap integral can be approximated as being equal to unity, meaning that the binding energy of the kth sub-shell as measured from PES will be given by

$$E_B^V = E_0(N-1) - E_0(N) \tag{3.9}$$

Such a supposition is referred to as the frozen orbital approximation as it neglects the effects of orbital relaxation and electron correlations in the photoemission process. By doing so, Hartree-Fock can be used to compute the binding energy of an electron in the kth sub-shell. In this way, the position of a core level in a PES spectrum can be reasonably given by the negative orbital energy defined by the Hartree-Fock eigenvalue. Such a result directly follows from Koopman's

theorem, which provides a physical interpretation for the Hartree-Fock eigenvalue as being the ionization energy of an electron residing in the k^{th} sub-shell. Remarkably, for binding energies computed in this way, predictions of core level positions turn out to be in fair agreement with experiments thanks largely to the fact that relaxation and correlations will have equal and opposite effects and will therefore negate one another [10]. In the end, by the direct measurement of electron binding energies from PES, valuable information concerning the local electronic environment of an atom can ultimately be made.

One of the best illustrations of the sensitivity of a core level position to its local electronic environment can be found in the so-called chemical shifts. Namely, for the same element being placed in different chemical environments, it has been shown that the binding energy of an atomic core level can experience a shift that is both systematic and reproducible. Typically this can be understood in terms of the availability of itinerant electronic charges capable of screening the resultant core-hole. Notably, the greater the number of bonds to an electronegative species, the weaker the screening of the core hole on the atomic site. Thus, as is shown in Figure 3.1, the binding energy of an electron from the k^{th} shell will shift towards higher values as compared to that of the pure elemental state. Quantitative predictions regarding the magnitude of core level shifts are not always straightforward, but in some instances an estimation based on thermodynamic variables can be successful.

From a more fundamental approach, the simplest model for chemical shift takes into consideration the potential felt at the atomic site due to all other atoms in the solid or molecule. For purely ionic compounds, this potential can be simply given by an electrostatic potential where neighboring sites are treated as point charges. In such a case, the attractive potential felt will be closely related to the Madelung energy. Furthermore, depending on the depth of the core level relative to that of the valence, it is possible that the chemical shift experienced by different atomic sub-shells may not actually be rigid. Namely, by considering a phenomenological explanation of core level shifts in which an atom is modeled as a sphere having a charge q and radius r_v determined by the Bohr radius of the valence. Then by representing a chemical shift as a change of q by an amount δq, only those core sub-shells having a radius $r < r_v$ will experience a rigid shift thanks to the fact that the electrostatic potential felt by such sub-shells will necessarily be constant. However, in the case where $r > r_v$, such as for the shallow core levels in 4f compounds, this will no longer be the case and the magnitude of chemical shift turns out to

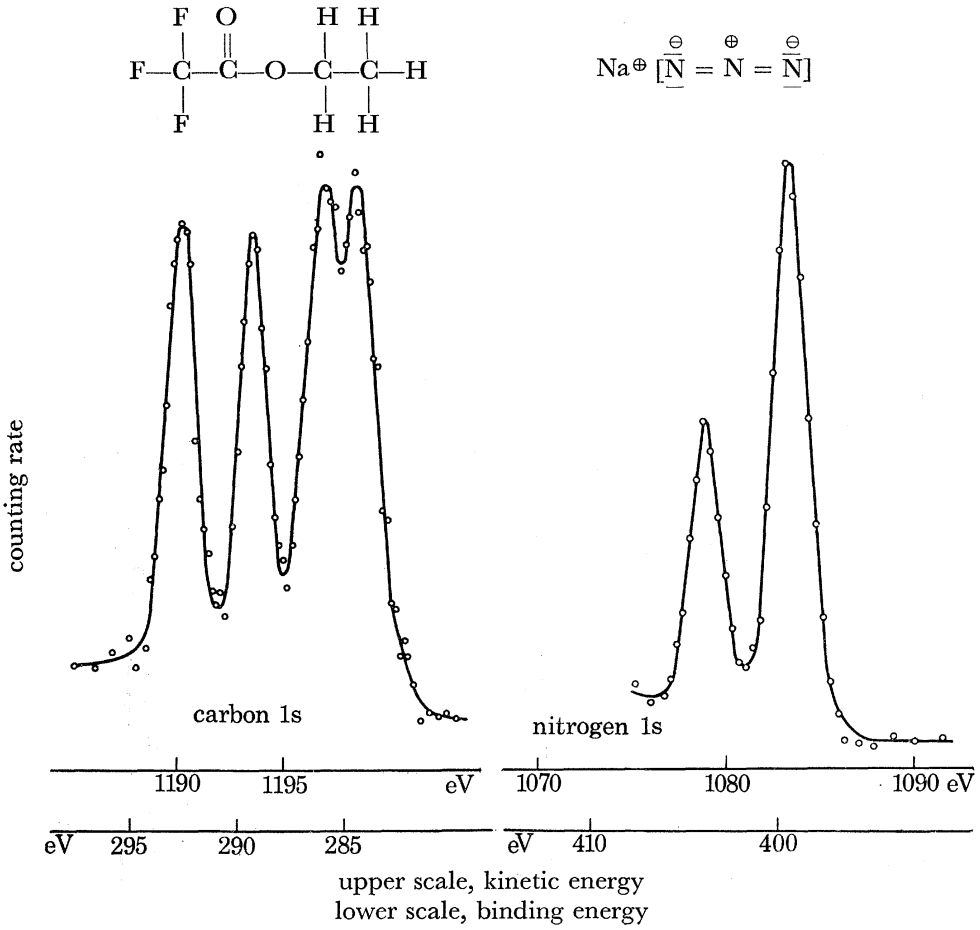

Figure 3.1: Core level PES spectra of (a) the Carbon 1s for ethyl trifluoroacetate and (b) the Nitrogen 1s of sodium azide. Note from the spectra the sensitivity of the core level binding energy to its particular chemical environment. Taken from [8]

depend sensitively on the particular sub-shell. In the end, it was in part because of the sensitivity of PES to the local electronic environment that this technique emerged as a powerful analytic tool that ultimately led to the recognition of Kai Siegbahn as the 1981 Nobel Prize recipient for his work in developing PES.

Up until this point, it has only been considered that a photoelectron ejected from the k^{th} orbital leave the system in an approximate ground state in which the *N-1* overlap integral can be taken as unity. However, as can be seen from equation 3.8, this is not the only possible final state, as there can be a finite probability that the system be left in an excited state *s* of the *N-1* particle system. In this way, the *N-1* overlap integral represents a kind of distribution of spectral weight, where a discrete or continuous number of loss features can accompany the main photoemission peak. Such loss features, commonly referred to as shake-up satellites, turn out to provide important insights into the many-body interactions present in a solid. Particularly, satellite peaks, known as charge transfer satellites, give one instance where especially relevant insights into the number of final states that can be reached following photoemission can be gained.

For systems having open *f* or *d* shells, the number of satellites, or final states, is often described in terms of the number of possible screening channels available for the core hole [13,96]. This viewpoint, described by the Kotani-Toyozawa model, comes about through noting that the creation of a core-hole produces a potential, U_c, which serves to lower the narrow, partially filled *d*- or *f*-bands below E_F. This will yield a two-hole state, in which the resultant hole in the *d*- or *f*- states can either be screened by the broad *sp* band of the metal ion, or be filled through a transfer of charge from the ligand. Typically, the latter screening process is favored, but details will depend on the strength of the core hole potential relative to the energy, Δ, necessary for such a charge transfer event to occur.

In the simplest case, consisting of just the two possible screening channels described above, the separation distance between the main and satellite peak can be determined by modeling the system as comprising of two levels $|d^n L\rangle$ and $|d^{n+1}L^{-1}\rangle$. Such a model turns out to be exactly analogous to that used in the description of bonding and anti-bonding molecular orbitals, allowing then for the following Hamiltonian to be constructed

$$\hat{H} \rightarrow \begin{pmatrix} 0 & T_m \\ T_m & \Delta - U_c \end{pmatrix} \tag{3.10}$$

By taking, $T_m = \langle d^n L | \hat{H} | d^{n+1} L^{-1} \rangle$ to denote the off diagonal, mixing matrix element while the charge transfer energy will be given by $\Delta = \langle d^{n+1} L^{-1} | \hat{H} | d^{n+1} L^{-1} \rangle - \langle d^n L | \hat{H} | d^n L \rangle$, the above Hamiltonian can be diagonalized to give an energy separation between the two peaks to be equal to

$$\Delta E = \sqrt{(\Delta - U_c)^2 + 4T_m^2} \tag{3.11}$$

In accordance with the Kotani-Toyozawa model, the presence of additional satellite peaks beyond that which can be described by a two level system must come about from additional screening channels, such as from non-local screening or charge transfer states like that of $|d^{n+2} L^{-2}\rangle$. As expected, this will increases the size and complexity of the Hamiltonian, making the analysis of the energy separation between satellite peaks more computationally involved, but essentially straight-forward.

In contrast to local, ionic systems, which exhibit shake-up features, like charge transfer satellites, that are discrete in energy, for sufficiently itinerant electron systems loss features owed to the creation of a core hole in an *N* electron system often manifest as an asymmetric tail in the spectrum's lineshape that extends towards higher binding energies. The presence of this tail in the lineshape can be attributed to an envelope of excitations arising from the creation of particle-hole pairs across the Fermi surface [97,98,99,100]. Noting there to be no energy gap between the occupied and unoccupied states in a metal, it costs the system virtually no energy to produce these pairs. As a consequence, in the limit of zero energy transfer, there will be a singularity, known as the x-ray singularity, which diverges according to $E^{1-\alpha}$. Here, the exponent, α, will depend on the phase shift arising from the scattering of conduction electrons by the transient core hole potential. Ultimately, the corresponding lineshape, famously described by S. Doniach and M. Sunjic illustrates the effect that the interaction between conduction electrons and the resultant core hole can have on the photoemission spectrum. This connection will be more explicitly made in Section 3.1.2 when discussing the utility of angle resolved PES as a probe of the many-body state.

Lastly, as discussed above, the presence of shake-up features in PES comes about as a consequence of the final state containing a core-hole. As it turns out, this is not the only final state effect that can arise. Notably for an element with a partially filled outer shell, the ejection of a core electron will result in an opening of its shell, which can give rise to an exchange splitting between the remaining spin of the core level and that of the valence of the emitter atom.

This effect, known as multiplet splitting, can be used as a measure of the local magnetic moment hosted on a particular atomic site. Typically, thanks to the fact that an *ns*-shell possesses no net angular momentum, a measurement of the multiplet splitting performed on this shell will reduces the number of possible final states to being no less than two. That is, in the absence of charge transfer satellites, the splitting of the *ns* core level into two multiplets corresponds to either a parallel or anti-parallel orientation of the remaining core electron spin with respect to that of the valence.

In accordance with the exchange energy, a parallel configuration will be more energetically favorable and will thus lead to an intensity ratio of $2S_v + 2 : 2S_v$ as compared to that of the anti-parallel orientation found at higher binding energies. Furthermore, for the orbital component of the magnetic moment being suppressed by crystal field effects, a simplified form of Van Vleck's Theorem can be used to define the energy separation between two multiplets to be given by

$$\Delta E_{ns} = (2S_V + 1)J_{ns-d}^{eff} \tag{3.12}$$

Here, the fact that the magnitude of the multiplet splitting is proportional to the exchange integral implies that a larger splitting will be observed for those core levels having a greater spatial overlap with the valance. Consequently, shallow core levels such as the 3s are typically used for the measure of the energy separation between multiplets. As this pertains to itinerant electronic systems, where a spin of the valence cannot always be clearly defined on a local atomic site, it is possible to extend van Vleck's theorem by extrapolating from values of the exchange splitting determined for ionic systems. However, as will be discussed in Chapter 6, this extension is not a trivial matter and is intimately related to the electron dynamics occurring on the timescale that is on the order of the core-hole lifetime [101,102].

3.1.2 Angle Resolved Photoemission Spectroscopy

When using excitation energies ideally suited for studying details in the valence band, PES spectra will generally be dominated by momentum conserving direct transitions. Consequently, by either varying photon energy or measuring the emission angle of an outgoing photoelectron, it is then possible to map the electronic band structure in a single crystalline metal. Specifically, by noting that the parallel component of the momentum for an outgoing photoelectron will be conserved, the fact that direct transitions dominate can be readily seen in

the relation between the final state, k_f, and initial state, k_i, crystal momentum in the extend zone scheme.

$$\vec{k}_f^{||} = \vec{k}_i^{||} + \vec{g}^{||} \tag{3.13}$$

From this expression, it is evident that a measurement of the electronic structure using PES can be carried out within a given k_xk_y-plane by keeping the excitation energy fixed and simply determining the angle at which the photoelectron was ejected. In this way, a simple relation between the emission angle, ϑ, measured relative to the sample normal and the final state crystal momentum can be given by

$$k_f^{||} = \frac{\sqrt{2mE_{KE}}}{\hbar}\sin\vartheta \tag{3.14}$$

where it is assumed that the final state will be that of a free electron. Hence, by rearranging the momentum conservation expression to read $k_i^{||} = k_f^{||} - g^{||}$, it is clear that the addition of angular resolution to PES, in what is known as ARPES, will allow for the capability of mapping both the electronic band structure and Fermi surface.

Much of the success of ARPES stems from its ability to measure the strength of electron correlations in complex, many-body systems. This is ultimately owed to the fact that experimental insights into the behavior of the electron self-energy can be obtained from ARPES spectra by way of the single particle removal spectral function. As it turns out, such a close relation between PES and the familiar quantities of many-body physics becomes natural when one begins to consider the physical interpretation of the many-body Green's function [103,104,105]. Namely, in defining $\hbar = 1$ the Green's function, or propagator, can be written as

$$G(k_2, t; k_1) = -i\langle\Psi_0^N\left|T\{c_{k_2}(t)c_{k_1}^\dagger\}\right|\Psi_0^N\rangle \tag{3.15}$$

where $|\Psi_0^N\rangle$ represents the fully interacting N particle ground state, while $T\{c_{k_2}(t)c_{k_1}^\dagger\}$ denotes the time ordered product of the annihilation and creation operators respectively. Upon explicitly writing out the time dependence of the operators for $t > 0$ it becomes evident that the Green's function is simply a probability amplitude that is determined by the commutativity between two processes. The first, denoted by $|A\rangle = e^{-iHt}c_{k_1}^\dagger|\Psi_0^N\rangle$, defines a state in which a particle is initially created in a single particle state $|k_1\rangle$ and then evolved with the whole system to some time t, while the second, given by $|B\rangle = c_{k_2}^\dagger e^{-iHt}|\Psi_0^N\rangle$, defines a state in which the many body system is first evolved to time t and then a particle is created in $|k_2\rangle$. By taking the inner

product, it becomes clear that the resultant probability amplitude will exactly define the single particle addition Green's function.

$$G^{+}(k_2, t; k_1) = -i\langle B|A\rangle \tag{3.16}$$

Despite the above interpretation for the propagator being more reminiscent of a Gedanken experiment, this actually is the very scenario that occurs in PES. Namely, through ejecting a photoelectron from a fully interacting *N* particle system, a hole will be introduced into a single particle state of the system. By treating this hole as if it were an anti-particle propagating backwards in time, the single particle, many-body Green function can then be written as

$$G^{-}(k, t) = i\theta(-t)\langle\Psi_0^N|c_k^{\dagger}c_k(t)|\Psi_0^N\rangle \tag{3.17}$$

If this hole is created in a stationary state of the many-body Hamiltonian, then after some time *t*, determined by the core-hole lifetime, it will necessarily remain in the same single particle state. However, as is generally the case, this hole will not be created in an eigenstate so there will be a certain probability that it will scatter into some other single particle state during the course of its lifetime. As it turns out, a measure of this probability can ultimately be found in an ARPES spectrum.

To establish a more rigorous connection between many-body physics and PES, the Green's function needs to be cast in the energy, as opposed to time, domain. To do so, consider inserting a complete set $\mathbb{I} = \sum_s|\Psi_0^M\rangle\langle\Psi_0^M|$ into the above expression for the hole propagator

$$G^{-}(k, t) = i\theta(-t)\sum_s\langle\Psi_0^N|c_k^{\dagger}|\Psi_s^M\rangle\langle\Psi_s^M|e^{iHt}c_k e^{-iHt}|\Psi_0^N\rangle \tag{3.18}$$

Noting that the only non-zero contribution will come from *M* = *N-1*, the evolution operator can then be distributed over the states $|\Psi_0^N\rangle$ and $|\Psi_0^{N-1}\rangle$ to yield

$$G^{-}(k, t) = i\theta(-t)\sum_s|\langle\Psi_s^{N-1}|c_k|\Psi_0^N\rangle|^2 e^{-i(E_0^N - E_s^{N-1})t} \tag{3.19}$$

which, by Fourier transforming to the energy domain ultimately gives

$$G^{-}(k, \omega) = \int_{-\infty}^{\infty} dt G^{-}(k, t)e^{i\omega t} = \sum_s \frac{|\langle\Psi_s^{N-1}|c_k|\Psi_0^N\rangle|^2}{\omega - (E_0^N - E_s^{N-1}) - i\xi} \tag{3.20}$$

where the infinitesimal ξ simply serves to shift the pole off the real axis. Once in the energy domain, many of the terms in the Green's function that factor into the expression for the PES photocurrent become apparent. This most notably includes the pole that defines the energy difference between the ground state energy of the *N* particle system and the excited state energy

of the *N-1* particle system, as well as the *N-1* overlap integral, which comes about in PES under the assumption of the sudden approximation.

As was briefly mentioned in developing an expression for the photocurrent, the *N-1* overlap integral is physically representative of the probability that the introduction of a hole into a *N* particle system subsequently leaves the system in a state, which is not necessarily the ground state, of the *N-1* particle system. Put in this way, the overlap integral then represents a kind of distribution of spectral weight in the PES spectrum that is more commonly associated with the single particle removal spectral function. That is, by defining

$$A^-(k,\omega) = \sum_s |\langle \Psi_s^{N-1}|c_k|\Psi_0^N\rangle|^2 \delta(\omega - \omega') \tag{3.21}$$

for $\omega' = E_0^N - E_s^{N-1}$, it is evident from equation 3.7 that the expression for the ARPES photocurrent at finite temperatures can then be given by

$$I \propto |M_{f,i}|A^-(k,\omega) f_{FD}(\omega) \tag{3.22}$$

where $|M_{f,i}|$ denotes the dipole matrix element, while $f_{FD}(\omega)$ represents the Fermi-Dirac distribution. By having a dependence on the single particle removal spectral function, the utility of ARPES extends beyond mapping the electronic band structure, as this technique will actually provide experimental insights into the many-body interactions. Chief among these being the dynamical electron self-energy $\Sigma(k,\omega)$.

Simply stated the electron self-energy is the corresponding energy felt by an electron due to its interaction with the surrounding medium. In considering how such an interaction will modify the propagation of a free particle, denoted here by $G_0(k,\omega)$, a self-consistent equation, known as the Dyson's equation, can be applied. Written out,

$$G(k,\omega) = G_0(k,\omega) + G_0(k,\omega)\Sigma(k,\omega)G(k,\omega) \tag{3.23}$$

it can be clearly seen how this equation forms the basis for diagrammatic perturbation as the solution can be found iteratively by first expanding

$$G(k,\omega) = G_0(k,\omega) + G_0(\mathrm{k},\omega)\Sigma(k,\omega)G_0(k,\omega) + \mathrm{G_0(k,\omega)}\big(\Sigma(k,\omega)G_0(k,\omega)\big)^2 + \cdots \tag{3.24}$$

and then summing over the geometric series

$$G(k,\omega) = \frac{G_0(k,\omega)}{1-\Sigma(k,\omega)G_0(k,\omega)} = \frac{1}{(G_0(k,\omega))^{-1}-\Sigma(k,\omega)} \tag{3.25}$$

Given the expression for the free particle propagator to be determined by $G_0(k,\omega) = (\omega - E_k + i\xi_\pm)^{-1}$, the fully renormalized, single particle Green's function can ultimately be shown as

$$G(k,\omega) = \frac{1}{\omega - E_k - \Sigma(k,\omega)} = \frac{1}{\omega - E_k - \Sigma_R(k,\omega) - i\Sigma_I(k,\omega)} \tag{3.26}$$

where both the real and imaginary components of the self-energy have been explicitly written out.

From the above expression for the renormalized Green's function, it is possible to determine how the same interactions, represented by the electron self-energy, manifest in experimentally relevant quantities like the single particle removal spectral function. Notably, this can be shown by equating 3.20 with an expression for the single particle removal Green's function as is written in the spectral, or Lehmann representation. Within such a representation, which is simply given by substituting 3.21 into 3.20, the propagator is expressed in terms of a distribution of spectral weight and poles that can be written in the form of excitations relative to the ground state. That is, by taking

$$G^{-}(k,\omega) = \int_0^\infty d\omega' \frac{A^{-}(k,\omega)}{\omega-\omega'-i\xi} = \frac{1}{\omega-E_k-\Sigma_R(k,\omega)-i\Sigma_I(k,\omega)} \tag{3.27}$$

it can be readily shown through invoking the Dirac identity that

$$A^{-}(k,\omega) = \frac{1}{\pi}\Im G^{-}(k,\omega) \tag{3.28}$$

making

$$A^{-}(k,\omega) = \frac{1}{\pi}\frac{\Sigma_I(k,\omega)}{\left(\omega-E_k-\Sigma_R(k,\omega)\right)^2+(\Sigma_I(k,\omega))^2} \tag{3.29}$$

The significance of this relationship is made apparent in Figure 3.2. Namely, in the absence of interactions, the spectral function will be given by a delta function whose center coincides with that of the bare band dispersion. However, with interactions, the band dispersion will then become renormalized, with the center shifting up by $\Sigma_R(k,\omega)$ relative to that of the bare dispersion and the corresponding bandwidth broadening by an amount determined by $\Sigma_I(k,\omega)$. In the simplest case of a Fermi liquid, a strongly interacting *N* particle system can be mapped onto a system of weakly interacting quasi-particles that can be approximated as free particle states. Here, the band renormalization will manifest in the form of a mass enhancement, which serves to flatten the band, while the width of the spectral function is found to scale with $\propto (E_k - E_F)^2$, for E_F denoting the energy at the Fermi level. For this reason, as is shown in Figure 3.2, it is expected that the quasi-particle peak sharpen as E_k approaches E_F as its lifetime will extend towards infinity.

Up until this point, it has been emphasized that by yielding a direct measure of the spectral function, ARPES can provide important experimental insights into the many-body interactions that are at play. However, it should be noted that unlike a Gadanken experiment in

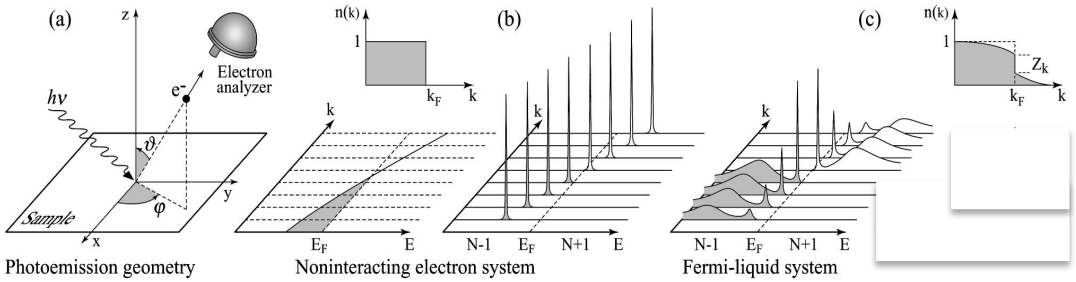

Figure 3.2: For the ARPES geometry shown in (a), (b) illustrates the electronic band dispersion and corresponding single particle removal spectral function for a non-interacting system characterized by a momentum distribution function $n(k) = \theta(k-k_F)$. In contrast (c) demonstrates the effect that electron correlations will have on an ARPES spectrum. Notably, the single particle removal spectrum takes on a characteristic peak-dip-hump structure with the coherent quasi-particle peak showing a broadening in accordance with $(E-E_F)^2$. Additionally, note how the momentum distribution function changes as compared to the non-interacting case. Here the magnitude of the step at k_F is defined by the quasiparticle renormalization factor Z_k. Taken from [9]

which a hole simply appears, in a real experiment, this hole has to be created by the absorption of a photon. Thus, as can be seen in equation 3.22 not only does the ARPES photocurrent depend on the spectral function, but another significant contribution comes from the dipole matrix element.

The importance of this term is made evident through considering the effect that photon energy and polarization have on the modulation of intensity in PES. Most notably, the dependence of the photocurrent on photon energy can be attributed to photoelectron cross-sections. Generally speaking, higher cross-sections, which translate to a greater number of photoelectrons, results from a high degree of overlap between the initial, atomic and final, free electron states. Ultimately, it is for this reason that photoelectron cross-sections drop precipitously in the hard x-ray regime, as the final state wavefunction is too rapidly varying for there to be any real overlap with that of the initial state. Consequently, special considerations, which are further discussed in section 3.1.3, must then be made so as to compensate for the low cross-sections in this regime.

While photoelectron cross-sections have a dependence on photon energy, the role played by the photon polarization in modulating the intensity of PES spectra can be owed to the dependence of the dipole matrix element on the symmetry of the initial state. As is illustrated in Figure 3.3, by having the detector slit contained in the mirror plane, this dependence can be exploited to allow for the majority orbital character of the initial state to be determined. Namely, with the detector in this particular geometry, the final state of the photoelectron wavefunction must necessarily be of even parity, otherwise there would be a node in the wavefunction at the position of the detector. Consequently, by symmetry constraints, a photoelectron can be detected only if the product of the dipole operator and the initial state wavefunction is of even parity. In using a photon polarization that is either even or odd with respect to the scattering plane, the initial state photoelectron wavefunctions must likewise exhibit the same respective parity in order for the dipole matrix element to yield a non-zero contribution. In this way, it becomes possible to identify the majority orbital character of the initial states.

3.1.3 Soft X-ray ARPES

While ARPES has established itself as a premier tool for studying the electronic structure of strongly correlated systems, the principal drawback of this technique is its inherent surface

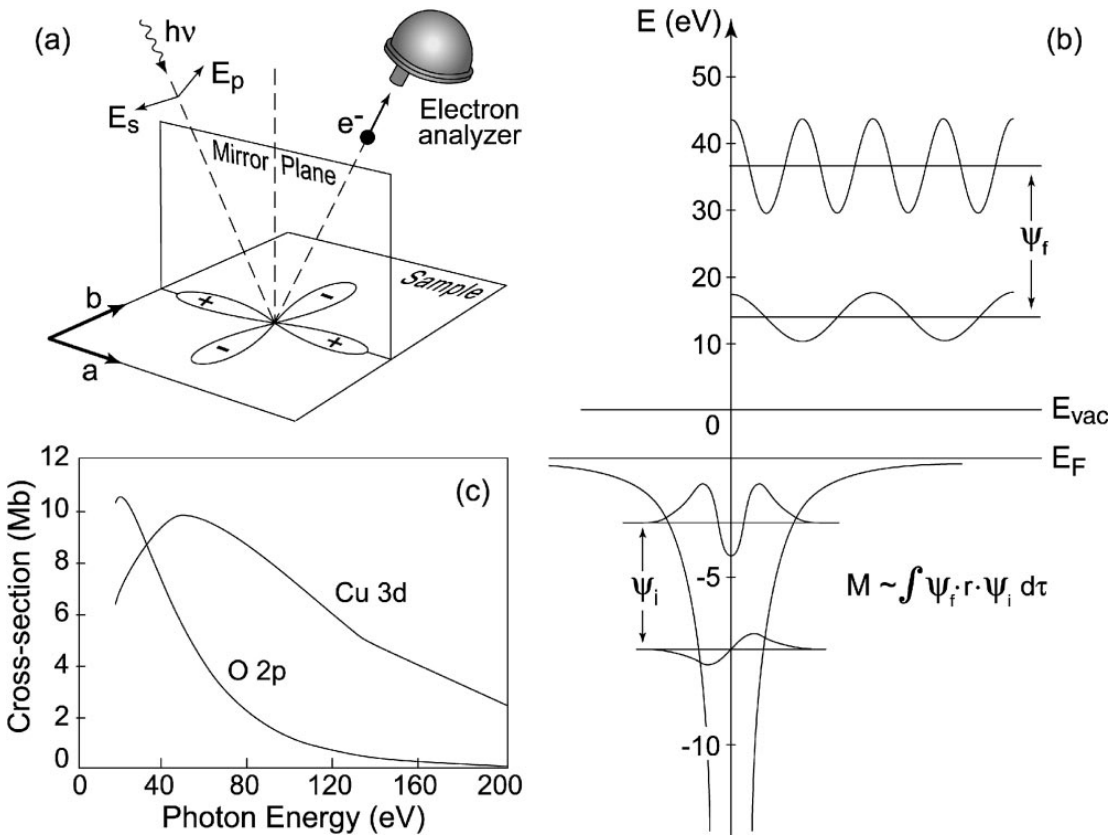

Figure 3.3: Dependence of ARPES intensity on (a) photon polarization and (b) photon energy, which manifests in (c) as the corresponding photoelectron cross-sections for a particular atomic sub-shell. Such dependencies comprise what is commonly referred to as matrix element effects in an ARPES spectrum. Taken from [9]

sensitivity. Ultimately, this arises from the fact that outgoing photoelectrons possess an electric charge and will therefore interact strongly via the Coulomb force with the remaining electrons in the solid. Most notably, as compared to the micrometer skin depth of vacuum ultraviolet or soft x-ray light, the probing depth of ARPES is limited to just the first few atomic layers. In order to understand why ARPES, as well as other electron spectroscopies, are characterized by such shallow probing depths requires one to first develop a more rigorous definition of this quantity by considering the probability distribution for inelastic scattering events experienced by an outgoing photoelectron. Seeing as such events, which occur within a given time τ, or equivalently length $l = v\tau$, are independent from one another, an outgoing photoelectron will experience inelastic collisions with a probability given by that of a Poisson distribution.

To demonstrate this fact, begin by defining the probability for a photoelectron to experience an inelastic collision within an infinitesimal length dl as dl/λ, where λ represents the inelastic mean free path (IMFP). Supposing at $l = 0$, the electron undergoes a scattering event in the form of absorption of a photon, then based upon the above definition, the probability that an electron will have traveled a distance $l = Ndl$ *without* experiencing any inelastic scattering events is given by

$$P[0,l] = \lim_{dl\to 0} = \left(1 - \frac{dl}{\lambda}\right)^{l/dl} = \lim_{N\to\infty}\left(1 - \frac{1}{N}\frac{l}{\lambda}\right)^{N} = e^{-\frac{l}{\lambda}} \tag{3.30}$$

for N denoting the number of steps of size dl taken within the length l. Such an expression defines the normalized probability distribution, $P(l) = \frac{1}{\lambda}e^{-\frac{l}{\lambda}}$, whose significance as it relates to photoemission lies in the fact that only those photoelectrons which *have not* undergone successive inelastic scattering events give rise to signal in a photoemission spectrum. All other electrons which have suffered from multiple inelastic scattering processes yet still possess a kinetic energy greater than the spectrometer work function provide for the background of the spectrum. As shown in Figure 3.4, the above probability distribution can be expressed in terms of a sampling depth z by substituting

$$P(z) = \frac{1}{\lambda\sin\theta}e^{-\frac{z}{\lambda\sin\theta}} \tag{3.31}$$

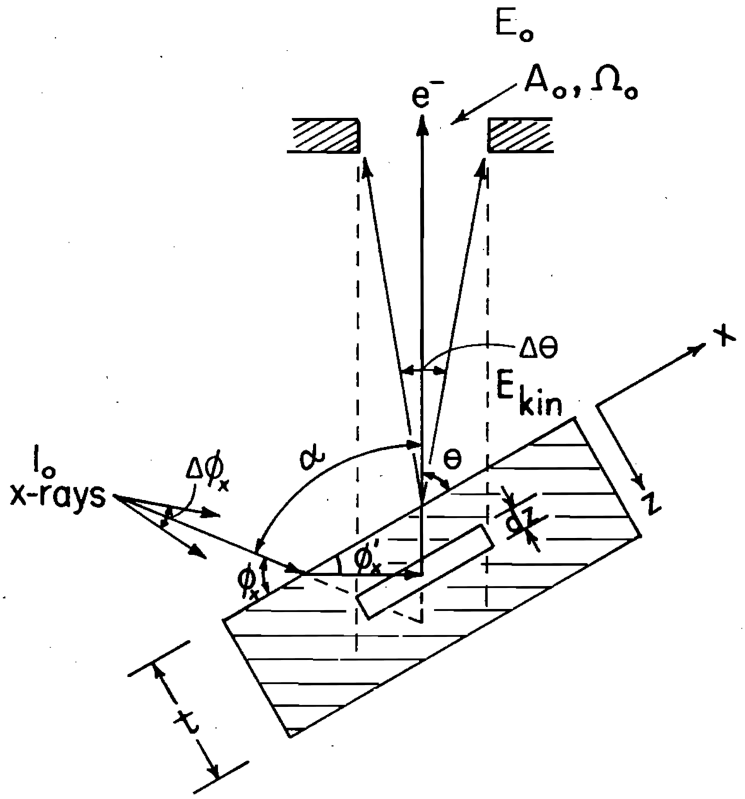

Figure 3.4: Schematic illustration of the experimental geometry for PES. Noting that the sampling depth is given here by $z = l/\sin\theta$, it is evident that a greater bulk sensitivity will be gained at normal emission, where $\theta = \pi/2$. Taken from [10]

where θ represents the angle between the mean emission direction and the sample surface. At normal emission ($\theta = \pi/2$), the probability that a photoelectron emitted from a depth of $z > 3\lambda$ will reach the detector without undergoing an inelastic scattering event is found to be less than 5%. In other words, 95% of the photoelectrons contributing to the signal in a photoemission spectrum come from a sampling depth of $0 < z < 3\lambda$. Thus, in having defined the sampling depth to be within $z < 3\lambda$, it is evident that the origin of the surface sensitivity of ARPES must be attributed to the short IMFP of photoelectrons within the 20 eV - 100 eV energy range.

Thanks in large part to its relevance in surface science, a great deal of work has gone into understanding the kinetic energy dependence of electron IMFP [11,106]. For the sake of this discussion, it is not necessary to explicitly develop the functional dependence of $\lambda(E_K)$, but rather worth mentioning just a few key insights gained from Refs. [11] and [106]. Most notably, a characteristic feature of the IMFP in metals is a broad minimum occurring within the very same energy range commonly used for high-resolution ARPES measurements (Figure 3.5). Ultimately, this minimum can be attributed to plasmon losses, which are found to be the predominant loss mechanism of photoelectrons especially in the 20 eV-100 eV kinetic energy range [107].

Consequently, in order to increase bulk sensitivity in an ARPES experiment, either very low or high excitation energies must be used. While the principal advantage of using low photon energies, such as those used in laser photoemission, is the high energy and momentum resolution, a critical disadvantage is that only those states in proximity to the zone center are accessible. As described in 3.1.2, this is due to the fact that the amount of k-space imaged by the detector is proportional to $\sqrt{E_K}$ for the outgoing photoelectron. Thus, a preferred means of increasing bulk sensitivity while still being able to measure over the entire Brillouin zone is to use excitation energies in the soft X-ray regime.

Aside from the increased bulk sensitivity, there are several other advantages in using soft X-ray excitation energies in an ARPES experiment. Most notably, a direct consequence of the increased probing depth is an improved momentum resolution perpendicular to the sample surface (Δk_z) [108,109]. To illustrate this fact, recall that the presence of a surface acts to breaks translational symmetry, making photoelectron momentum perpendicular to the surface a non-conserved quantity. Therefore, in order to estimate the smearing of the k_z dispersion thanks to

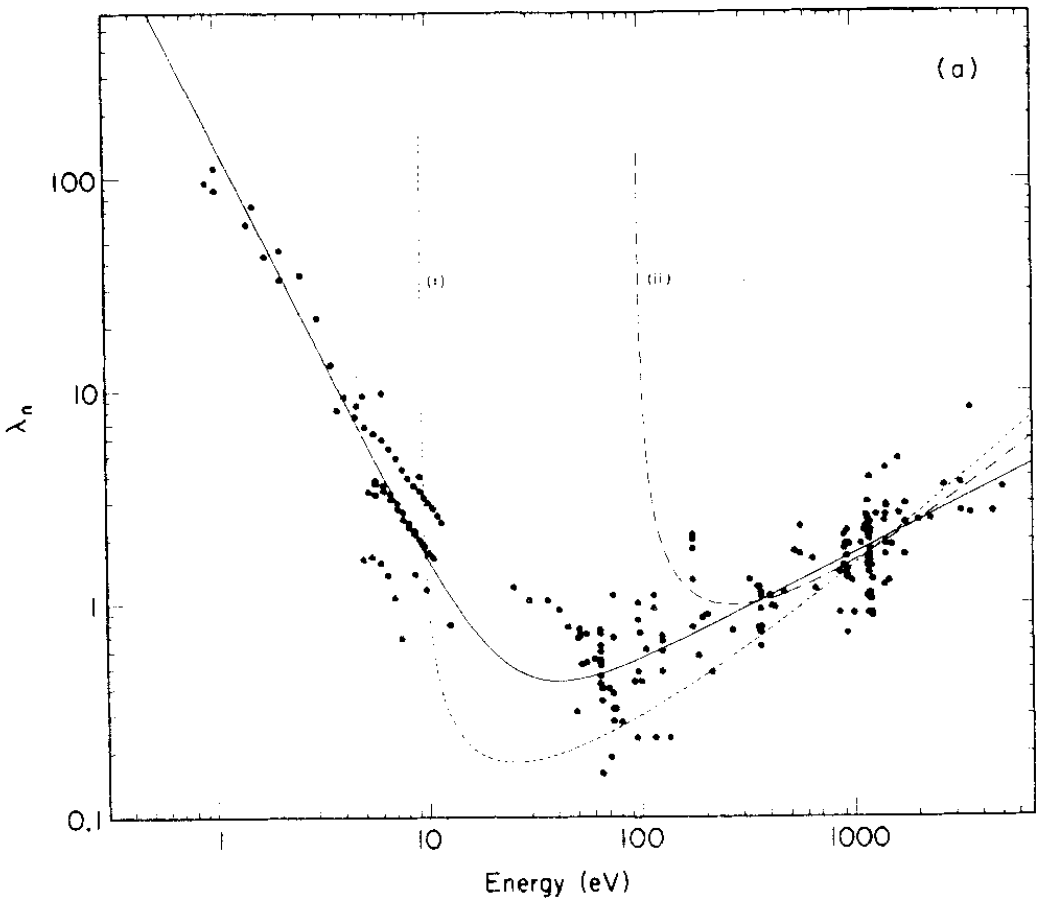

Figure 3.5: The so-called "universal curve" that phenomenologically describes the dependence of electron inelastic mean free path, λ, on kinetic energy. Taken from [11]

final state confinement effects, the Heisenberg uncertainty principal can be invoked in the form of $\Delta k_z \sim \lambda^{-1}$. Based on this argument, it is evident that with increased probing depth, an improved k_z resolution can be achieved. Using a more quantitative argument, based on the expression for the final state, k_z dispersion in the extended zone scheme,

$$k_z^f = \frac{\sqrt{2m_e}}{\hbar}\left(E_k \cos^2 \vartheta + U\right)^{1/2} \tag{3.32}$$

where U denotes the inner potential resulting from a break of translational symmetry at the surface, an expression for the k_z resolution at normal emission ($\vartheta = 0$) can be written as

$$\Delta k_z^f = \frac{1}{2}\frac{\sqrt{2m}}{\hbar}\left[\frac{\Delta E_K}{\left(E_K + U\right)^{1/2}}\right] \tag{3.33}$$

Noting that ΔE_K is determined by experimental parameters dependent on only the electron energy analyzer, it follows that $\Delta k_z^f \propto \left(E_K + U\right)^{-1/2}$. In other words, just as was shown above using uncertainty arguments, better momentum resolution perpendicular to the sample surface is achieved when the outgoing photoelectron possesses a higher kinetic energy and therefore deeper probing depth. With this improved resolution, it is then possible to identify subtle features in the k_z dispersion as is especially relevant for systems like VSe_2 in which the origin of the charge density wave can be attributed to the existence of a 3D nesting vector identified in the Fermi surface [110].

In addition to the improved momentum resolution along the k_z direction, carrying out an ARPES experiment in the soft X-ray regime allows for the possibility of tuning the excitation photon energy across the respective L- or M- absorption edges of transition metal and rare earth elements. In this way, ARPES spectra can be acquired on resonance allowing for the elemental character of the states that comprise the electronic band structure and Fermi surface to be identified. The principal advantage of doing so is that the behavior of correlated d- and f-dispersive states can then be highlighted. This in turn provides powerful insights into the physics of these materials especially as it pertains to dopant hybridization, as in the case of the dilute magnetic semiconductor $Mn_xGa_{1-x}As$ [111] or the nature of the Kondo resonance in heavy Fermions [112]. Unfortunately, because of the low photoelectron cross sections of d- and f-states at their resonant energies, high photon fluxes, which can be generated from insertion

devices in modern synchrotron radiation facilities, are necessary for the timely acquisition of spectra having adequate statistics.

In general, whether on resonance or not, compensation for low photoelectron cross sections in the soft X-ray regime represents one of a few challenges unique to soft X-ray ARPES (SX-ARPES). Another additional challenge critically important to the meaningful interpretation of ARPES spectra is that the probability of momentum conserving, direct transitions, which is what ultimately allows for band mapping to occur, decreases when using higher excitation energies [108,113]. This can be attributed to the creation and annihilation of phonons during the photoemission process resulting in a loss of momentum resolution as spectral features broaden to the point that they no longer appear to disperse [114]. At this limit, known as the XPS limit, transitions can occur over the whole Brillouin zone and the only information that can be obtained form an ARPES spectrum is that of the occupied density of states. While a rigorous inclusion of phonon effects has been carried out in a one-step theory calculation of photoemission [115], a semi-quantitate measure of the number of direct transitions can be given from the Debye-Waller (DW) factor.

Within scattering experiments, the DW factor accounts for the decrease in intensity of coherently scattered peaks due to thermal effects. From this perspective, it is less obvious how such a factor plays a role in determining the number of direct transitions in an ARPES spectrum. However, it should be emphasized that photoemission by its very nature is a scattering process as is best exemplified by its description in terms of an inverse LEED formalism. Therefore, in order to develop at least a conceptual understanding as to how the DW factor arises in the description of photoemission, it is helpful to begin with an expression for the transition rate $w_{f,i}$ from Fermi's golden rule,

$$w_{f,i} = \frac{2\pi}{\hbar}\left|\left\langle f\left|\hat{H}_{\text{int}}\right|i\right\rangle\right|^2 \rho \tag{3.34}$$

Here, by expressing the initial state, $|i\rangle$, in terms of a tight binding function, while the final state, $|f\rangle$, is the usual free electron state, the matrix element, $\langle f|\hat{H}_{\text{int}}|i\rangle$, can ultimately be written in terms of the photoabsorption cross section, σ and a scattering factor, *S(q)*.

In order to account for phonon excitations, the thermal average of the scattering factor must be computed. That is,

$$\langle S(q)\rangle = \frac{Tr\left(e^{-\beta\hat{H}}e^{i\vec{q}\cdot\vec{r}}\right)}{Tr\left(e^{-\beta\hat{H}}\right)} = \sum_j \frac{e^{-\beta E_j}}{Z}\langle j|e^{i\vec{q}\cdot\vec{r}}|j\rangle \tag{3.35}$$

where $\beta = 1/k_B T$, $\vec{q} = \vec{k}_f - \vec{k}_i$, and Z denotes the canonical partition function. Expressing the position vector r in terms of a displacement about an equilibrium site, $r = r_0 + x$, it follows that the displacement vector x can be written in terms of phonon creation and annihilation operators. This allows for one to express $e^{i\vec{q}\cdot\vec{r}} = e^{iq\cdot\sum_k \sqrt{\frac{\hbar}{2M\omega_k}}\left(a_k^+ + a_k\right)}$, which by invoking the Baker–Campbell–Hausdorff identity yields

$$\langle S(q)\rangle = \prod_k e^{-\frac{1}{2}\left(\frac{\hbar}{2M\omega_k}\right)q^2} \sum_j \frac{e^{-\beta E_j}}{Z}\langle j|e^{i\left(\sqrt{\frac{\hbar}{2M\omega_k}}q\right)a_k^+} e^{i\left(\sqrt{\frac{\hbar}{2M\omega_k}}q\right)a_k}|j\rangle \tag{3.36}$$

where the commutation relation, $\left[a_k, a_{k'}^+\right] = \delta_{k,k'}$ was used to generate this result.

Taking $|j\rangle = |N_1, N_2, N_3, ...\rangle = \prod_k |N_k\rangle$ to be in the Fock space of phonons having a particular k, then the energy, E_N and partition function, Z can be given by $E_{N_k} = \sum_k \hbar\omega_k N_k$ and $Z = \frac{1}{1 - e^{-\beta\hbar\omega_k}}$ respectively. Using these expressions, it is possible to expand the above exponentials in *S(q)*, keeping only those terms having an equal number of creation and annhilation operators. This will then results in

$$\langle S(q)\rangle = \prod_k \sum_{N_k} \frac{1}{Z} e^{-\beta\hbar\omega_k N_k}\langle N_k|1 - \frac{1}{2}\left(\frac{\hbar}{2M\omega_k}q^2\right)\left(2\hat{N}_k + 1\right) + \frac{1}{8}\left(\frac{\hbar}{2M\omega_k}q^2\right)^2\left(2\hat{N}_k^2 + 2\hat{N}_k + 1\right) + ...|N_k\rangle \tag{3.37}$$

where the number operator has been defined as $\hat{N}_k = a_k^+ a_k$. Finally, through making use of the fact that $\langle N_k\rangle = -\frac{1}{Z}\frac{\partial Z}{\partial\left(\beta\hbar\omega_k\right)} = \frac{1}{e^{\beta\hbar\omega_k} - 1}$ and $\langle N_k^2\rangle = \frac{1}{Z}\frac{\partial^2 Z}{\partial^2\left(\beta\hbar\omega_k\right)} = \langle N_k\rangle\left(1 + 2\langle N_k\rangle\right)$ a final expression for the scattering factor is ultimately given by

$$\begin{aligned}\langle S(q)\rangle &= \prod_k \left(1 - \frac{1}{2}\left(\frac{\hbar}{2M\omega_k}q^2\right)\left(2\langle N_k\rangle + 1\right) + \frac{1}{8}\left(\frac{\hbar}{2M\omega_k}q^2\right)^2\left(2\langle N_k\rangle + 1\right)^2 + ...\right) \\ &= e^{-\frac{1}{2}\sum_k\left(\frac{\hbar}{2M\omega_k}q^2\right)\left(2\langle N_k\rangle + 1\right)}\end{aligned} \tag{3.38}$$

in which the DW factor is defined as $W = \frac{1}{2}\sum_k \left(\frac{\hbar}{2M\omega_k} q^2 \right) \left(2\langle N_k \rangle + 1 \right)$.

As is written, it is difficult to develop a quantitative sense for the specific value taken on by the DW factor in real, physical systems. However, by converting the sum over *k* to an integral over ω, the DW factor can then be written in terms of known, calculable quantities such as the phonon density of states, *ρ(ω),* and the Debye frequency, ω_D.

$$W = \frac{1}{2}\left(\frac{\hbar}{2M} q^2 \right) \int_0^{\omega_D} d\omega \frac{\rho(\omega)}{\omega} \coth\left(\frac{\beta\hbar\omega}{2} \right) \tag{3.39}$$

As this specifically pertains to SX-ARPES, the most critical variables in determining the value of the DW factor are the excitation energy, which serves to define the *q* dependence, and the temperature. In light of this fact, constant probability contours of the DW factor can be computed in order to give a semi-quantitative measure for the probability of k-conserving direct transitions. As is shown in Ref. [114] for W(110), it is evident that when working at temperatures well below the Debye temperature, excitation energies greater than 5keV are needed before the DW factor drops below 50%. Interestingly, even when the number of direct transitions falls below 50%, band mapping can still be accomplished in the hard X-ray regime by properly normalizing spectra with respect to density of states and photoelectron diffraction effects [113]. Therefore, when collecting spectra at cryogenic temperatures using soft X-ray excitation energies, it is reasonable to consider oneself to be safely in the UPS limit where DW > 90%. Furthermore, it is important to note that momentum resolution cannot only be lost by phonon creation and annihilation but from recoil effects as well [108]. However, just as with the phonon broadening effects described above, the effect of recoil for transition metal systems only comes into play when excitation energies are well within the hard X-ray regime.

In having established the effects of phonon broadening and recoil to minimally alter the band mapping capabilities of SX-ARPES, there remains a critically important feature regarding the quantitative treatment of the data. This is the fact that the photon momentum $k_{h\nu}$, plays a non-negligible role in determining the initial crystal momentum k_i from the momentum of the outgoing photoelectron k_f. To understand why this is the case, begin by considering the expression for momentum conservation of the outgoing photoelectron.

$$\vec{k}_f^{\parallel} = \vec{k}_i^{\parallel} + \vec{g}_n^{\parallel} + \vec{k}_{h\nu}^{\parallel} \tag{3.40}$$

Here, the conservation equation has been written in the extended zone scheme and therefore includes a reciprocal lattice vector g_n. Furthermore, inclusion of the symbol || is meant to denote the fact that momentum is only conserved parallel to the sample plane. For high resolution ARPES experiments carried using $h\nu \sim$ 20 eV-100 eV, the contribution due to photon momentum can be neglected as it only represents a small fraction of the BZ. Notably, by using $Na_{0.75}CoO_2$ as an example, the photon momentum will account for a mere 0.4%-2% of the reciprocal lattice vector. Since such a small correction will be less than *k*-resolution of the analyzer, it is reasonable to simply equate the momentum of the outgoing photoelectron with that of the initial state crystal momentum. However, as higher excitation energies are used, the contribution resulting from photon momentum becomes increasingly significant. Returning to the example of $Na_{0.75}CoO_2$, it follows that the corresponding photon momentum for a 1 keV photon is ~20% of the reciprocal lattice vector. Consequently, at such high energies, the effect of photon momentum needs to be taken into consideration.

Developing an analytic expression that takes into consideration the photon momentum in the *k*-conversion, which relates the outgoing photoelectron momentum with the initial state crystal momentum, depends on the specifics of the experimental geometry [109]. For the derivation that follows, the experimental geometry sketched in Figure 3.6 is that found on Beamline 7.0.2 of the Advanced Light Source where the SX-ARPES experiment on Na_xCoO_2 was performed (Figure 3.7). Here, the incoming photon makes an angle $\alpha = 57°$ with respect to the axis of the analyzer. Furthermore, the entrance slit of the analyzer lies in the so-called scattering plane defined by the incoming photon and outgoing photoelectron. Within the fixed frame of the analyzer, the final state, photoelectron momentum and incoming photon momentum are defined as

$$\vec{k}_f^{\,\parallel} = \begin{pmatrix} \frac{\sqrt{2mE_K}}{\hbar}\sin\theta_A \\ 0 \\ \frac{\sqrt{2mE_K}}{\hbar}\cos\theta_A \end{pmatrix}; \quad \vec{k}_{h\nu}^{\,\parallel} = \begin{pmatrix} -\frac{2\pi\nu}{c}\sin\alpha \\ 0 \\ -\frac{2\pi\nu}{c}\cos\alpha \end{pmatrix} \tag{3.41}$$

where θ_A denotes the acceptance angle of the analyzer. As is often the case, the sample normal does not lie along the axis of the analyzer but is rotated by some angle ϕ and θ_M (Figure 3.6). Consequently, in order to develop a correspondence between the fixed analyzer frame and the

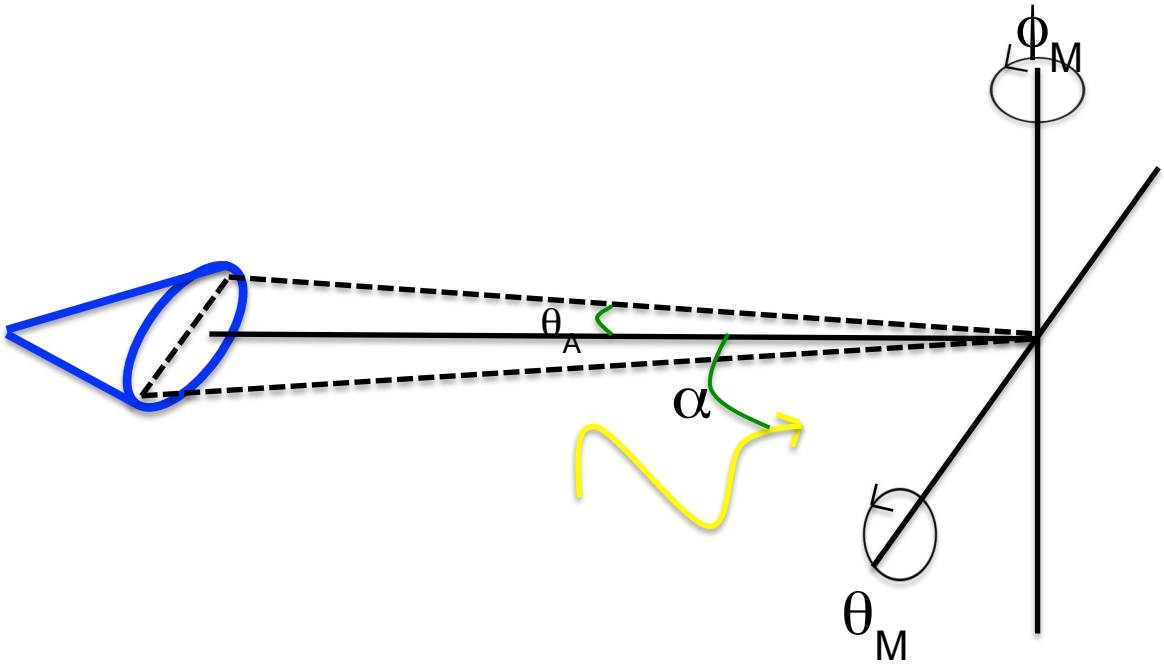

Figure 3.6: Schematic illustration of the experimental geometry of Beamline 7.0.2 at the Advanced Light Source. As compared to conventional ARPES, consideration of the angle at which the light impinges on the sample must be noted as the corresponding *k*-conversion will need to correct for the contribution coming from photon momentum.

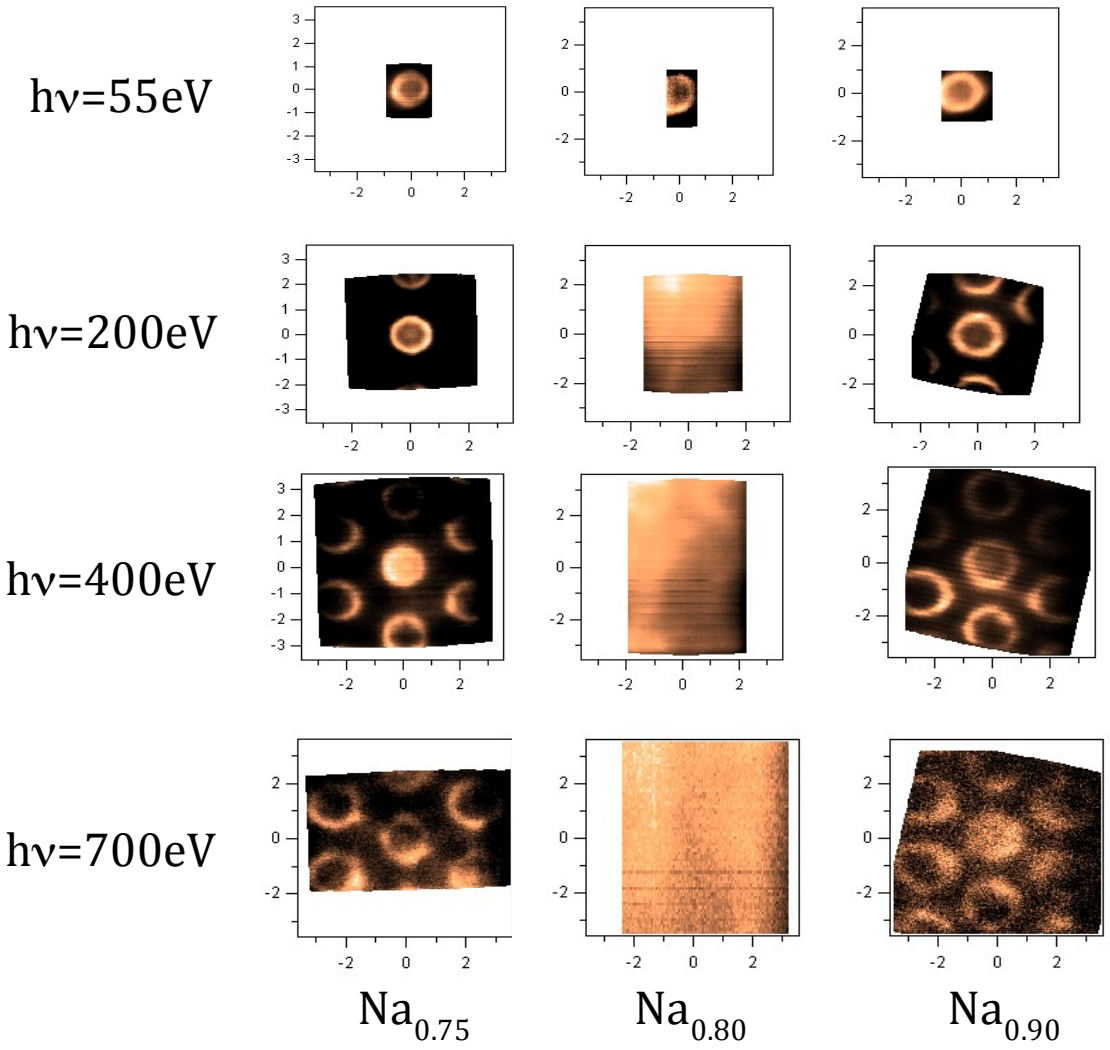

Figure 3.7: Fermi surface maps of $Na_{0.75}CoO_2$, $Na_{0.8}CoO_2$, and $Na_{0.9}CoO_2$, obtained as a function of increasing photon energy into the soft X-ray regime, where a correction for photon momentum has been applied.

rotated sample frame, it is necessary to perform an intrinsic Tait-Bryan transformation about the *y-x'* axis of Figure 3.6. The reason for doing so pertains to the fact that despite photoemission measurements being carried out in the fixed frame of the analyzer, what is ultimately desired is the initial state, crystal momentum of electron in the sample. Hence through relating these two frames by a Tait-Bryan transformation, the momentum of the initial state is given as

$$\vec{k}_i^{\parallel} = \hat{R}(\phi\hat{x}')\hat{R}(\theta_M\hat{y})\left(\vec{k}_f^{\parallel} - \vec{k}_{h\nu}^{\parallel}\right)$$

$$\begin{pmatrix} k_i^x \\ k_i^y \\ k_i^z \end{pmatrix} = \begin{pmatrix} 1 & 0 & 0 \\ 0 & \cos\theta_M & \sin\theta_M \\ 0 & -\sin\theta_M & \cos\theta_M \end{pmatrix} \begin{pmatrix} \cos\phi & 0 & \sin\phi \\ 0 & 1 & 0 \\ -\sin\phi & 0 & \cos\phi \end{pmatrix} \begin{pmatrix} \frac{\sqrt{2mE_K}}{\hbar}\sin\theta_A + \frac{2\pi\nu}{c}\sin\alpha \\ 0 \\ \frac{\sqrt{2mE_K}}{\hbar}\cos\theta_A + \frac{2\pi\nu}{c}\cos\alpha \end{pmatrix} \quad (3.42)$$

Recalling that momentum is only conserved parallel to the sample plane, the k_i^z component can be ignored, resulting in the following expression for the in-plane momentum that corrects for the contribution due to photon momentum:

$$\begin{aligned} k_i^x &= \frac{\sqrt{2mE_K}}{\hbar}\sin(\theta_A + \phi) + \frac{2\pi\nu}{c}\sin(\alpha + \phi) \\ k_i^y &= \frac{\sqrt{2mE_K}}{\hbar}\cos(\theta_A + \phi)\sin\theta_M + \frac{2\pi\nu}{c}\cos(\alpha + \phi)\sin\theta_M \end{aligned} \quad (3.43)$$

Importantly, the above expression for k_i^x highlights an additional complication that arises when performing an SX-ARPES experiment. This is the ambiguity in defining normal emission at higher photon energies. In particular, when taking θ_A, $\theta_M = 0$, k_i^x will take on a positive, non-zero value so as to compensate for the $-2\pi\nu/c\sin(\alpha+\phi)$ contribution from photon momentum. In other words, thanks to the effect of photon momentum, the true normal emission will shift down the slit position. As a result, sample alignment cannot be reliably carried out from a Fermi surface map at higher energies not only because of the poor $k^{||}$-resolution, $\Delta k^{||}$, but because of a tendency to overcompensate with the flip, ϕ. Therefore, in order to define the sample normal, alignment will need to be carried out either by performing a Fermi surface map at lower energies or by alternative means such as LEED or laser alignment. After having determined the sample normal, for the specific geometry outlined in Figure 3.6, a shift in the position of normal emission along the slit direction is expected and should not be corrected for mechanically as it is ultimately taken into account within the *k*-conversion.

As a final note, a brief explanation regarding the execution of the procedure for band and Fermi surface mapping in SX-ARPES is needed. In this case, just as for conventional ARPES, the conversion from angle to momentum takes place through the non-linear mapping of $I(E_K, \theta_A)$ to $I(E_B, k_x)$ or $I(\theta_A, \theta_M)$ to $I(k_x, k_y)$ with the only exception being the added contribution of photon momentum. Ultimately, such mapping is accomplished through computing the corresponding angles from an equally spaced momentum grid by calculation of the inverse of the expression for the in-plane momentum. By doing so, the intensity function $I(E_K, \theta_A)$ and $I(\theta_A, \theta_M)$ can be rewritten in terms of (E_B, k_x) and (k_x, k_y) via

$$\begin{aligned} I\left(E_K,\theta_A\right) &= I\left(E_B,\phi+\sin^{-1}\left(\frac{\hbar}{\sqrt{2mE_K}}\left(k_i^x-\frac{2\pi\nu}{c}\sin\left(\alpha+\phi\right)\right)\right)\right) \\ I\left(\theta_A,\theta_M\right) &= I\left(\phi+\sin^{-1}\left(\frac{\hbar}{\sqrt{2mE_K}}\left(k_i^x-\frac{2\pi\nu}{c}\sin\left(\alpha+\phi\right)\right)\right),\sin^{-1}\left(\frac{k_i^y}{\frac{\sqrt{2mE_K}}{\hbar}\cos\left(\theta_A+\phi\right)+\frac{2\pi\nu}{c}\cos\left(\alpha+\phi\right)}\right)\right) \end{aligned} \tag{3.44}$$

where the transformation relating a given (E_B, k_x) and (k_x, k_y) with its corresponding (E_K, θ_A) and (θ_A, θ_M) is used to map $I(E_K, \theta_A)$ and $I(\theta_A, \theta_M)$ onto $I(E_B, k_x)$ and $I(k_x, k_y)$. As is written this procedure will perform both the band and Fermi surface mapping given the expression for the *k*-conversion derived from the geometry of Beamline 7.0.2. Hence, the procedure will not be valid for SX-ARPES experiments performed on different beamlines. Fortunately, however, the same algorithm can still be used with appropriate substitution of the *k*-conversion for whatever the specific experimental geometry might be.

3.1.4 Resonant Photoemission Spectroscopy

As was discussed in 3.1.1, a core-hole created through absorption of a photon is characterized as having a finite lifetime, τ_C, associated with its subsequent decay. Regarding this eventual decay, it is found that the hole will typically fill through one of two competing processes: Auger electron emission or fluorescent x-ray emission. Generally speaking, for the relatively shallow core levels accessible by the photon energies used in X-ray Photoelectron Spectroscopy (XPS), Auger decays will dominate, as this process is favored over fluorescence for lighter elements having an atomic number $Z < 30$ [116]. Within an XPS spectrum, it is possible to identify Auger electrons as having a kinetic energy that is independent of the photon energy used in the initial core-hole formation. This can be attributed to the fact that the energy

of an Auger electron is entirely determined by the available energy levels in the atom. Namely for a core-hole being created in $|A\rangle$, an Auger decay will occur through an electron in $|B\rangle$ serving to fill this hole, allowing for the energy gained by such a relaxation process to be transferred to $|C\rangle$. Energetically, the corresponding kinetic energy of the outgoing Auger electron will be given by

$$E_{KE} = E_B(A) - E_B(B) - E_B(C) \tag{3.45}$$

where the electron binding energies can be referenced to either the vacuum or Fermi level. In the particular case where the states $|B\rangle$ and $|C\rangle$ are located in the valence of a solid, these discrete, atomic energy levels become bands, making it such that the kinetic energy of an Auger electron will fall within a distribution whose width, in the absence of correlations, is determined by

$$E_B(A) - 2\Gamma_{VB} < E_{KE} < E_B(A) \tag{3.46}$$

in which Γ_{VB} denotes the energy bandwidth of the valence band. Importantly, whether the line-shape reflects that of an atomic-like or band-like Auger electron emission the final state of the system following this decay process will always consist of two holes in $|B\rangle$ and $|C\rangle$. As is illustrated in Figure 3.8, such a final state is unique from that of direct photoemission, preventing the possibility that there be any energy coherence that develops between these two processes.

When the photon energy is tuned across an ionization edge of an inner atomic shell, a core hole will be created through the excitation of an electron above the Fermi level into an unoccupied energy state. Just as in photoemission, this core-hole eventually decays, but it can do so through two different auto-ionization channels, which can be distinguished by whether or not the excited electron directly participates in the decay process. Namely, within spectator decay (Figure 3.8), the electron promoted to the empty states is not directly involved in this process, and the decay of a core-hole proceeds through the emission of an electron similar to that for a normal Auger. However, as compared to a normal Auger, the so-called resonant Auger will be shifted towards higher kinetic energy, as the localized spectator electron will serve to screen the two-hole final state. Consequently, thanks to the fact that the excited electron can occupy different sites in the unoccupied states depending on the particular choice of photon energy tuned to across the absorption edge, the kinetic energy of a resonantly excited Auger electron is found to track the photon energy, giving it the appearance of being fixed in binding, as opposed to kinetic, energy. As shown in Figure 3.9, such behavior is a hallmark of a resonant Auger as it

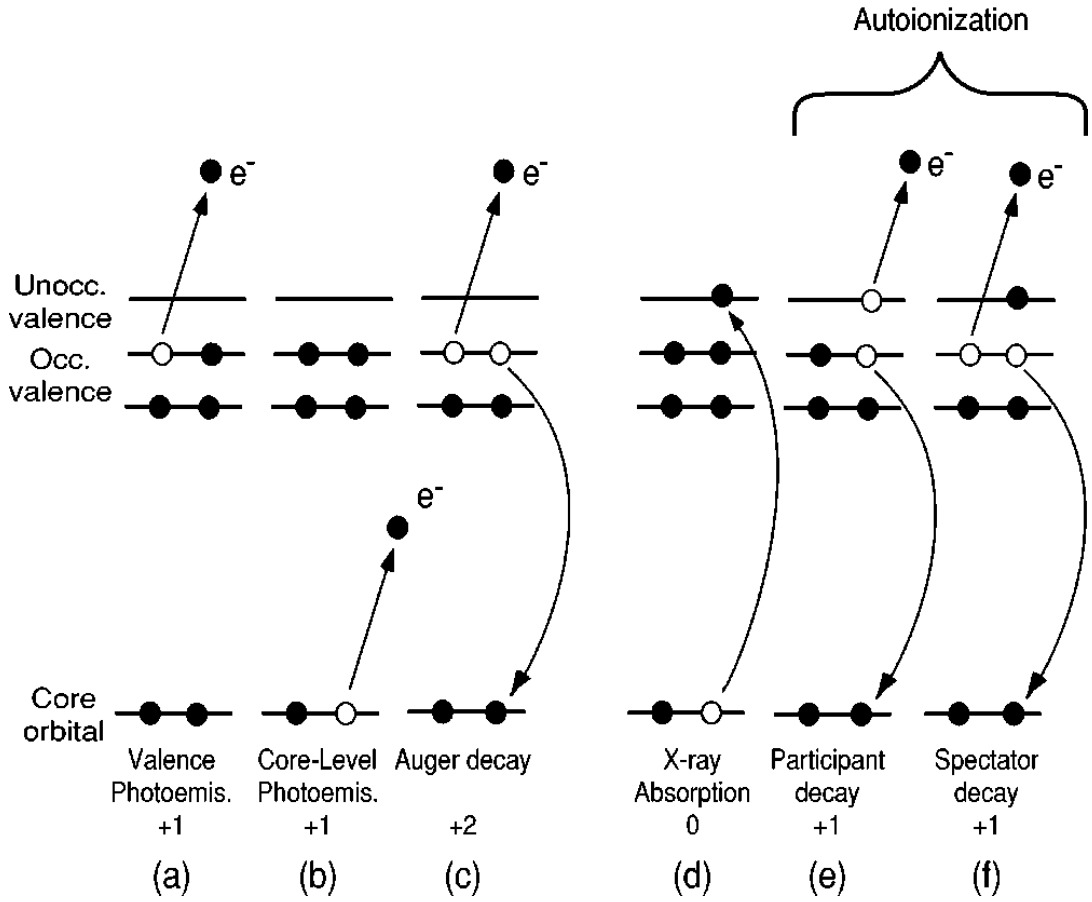

Figure 3.8: Schematic illustration of (a) valence and (b) core-level PES as well as (c) the non-resonant Auger decay of a core hole. With a resonant excitation, such as that shown in (d), the corresponding (e) participator and (f) spectator auto-ionization channels can then open up. Note how the final state in (e) and (a) are identical leading to a resonant enhancement of the valence band PES. Taken from [12]

will continue to track the photon energy until the excitation energy is tuned completely past the absorption edge, leading to a transition to a normal Auger.

In contrast to spectator decay, when the electron excited to the unoccupied state actually takes part in the decay of the core-hole, the particular auto-ionization channel that opens is that of the participator decay channel (Figure 3.8). Here, the final state of the system turns out to be identical to that produced by direct photoemission. Thus, in seeing that these two processes yield the exact same final state, the resultant energy coherence that develops will give rise to an interference in the PES spectrum that is a defining characteristic of Resonant PhotoEmission Spectroscopy (ResPES). Most notably, in considering the case where the incident photon energy is tuned across an *np* absorption edge(s), the decay of the core-hole through the participator auto-ionization channel can be described by

$$\mathrm{np^6 3d^N 4s^2 + h\nu \longrightarrow np^5 3d^{N+1} 4s^2 \longrightarrow np^6 3d^{N-1} 4s^2 + e^-} \tag{3.47}$$

where the resultant dipole allowed *np*-to-*3d* absorption serves to populate empty *3d* states located above the Fermi level. As compared to direct photoemission, in which

$$\mathrm{np^6 3d^N 4s^2 + h\nu \longrightarrow np^6 3d^{N-1} 4s^2 + e^-} \tag{3.48}$$

it is evident that both photoemission and the recombination of the core excited state, corresponding to the participator auto-ionization channel will leave the ion with a hole in the occupied 3d level. Thus, these two processes will produce indistinguishable final states. By noting that the intensity is proportional to the square of the summed probability amplitudes, when two processes result in the same final state, there will be an interference term that necessarily emerges. This manifests itself in a ResPES spectrum as a modulation in intensity whose dependence on photon energy can be described by the Fano profile [117].

As it turns out, the strength of the resonant response is strongly dependent on the orbital proximity of the two energy levels involved, as without such proximity, the coupling between these two channels via the Coulomb interaction becomes very small. With that being said, one of the greatest utilities of ResPES lies in the fact that it can be used to study the element specific contributions to the valence band. Such elemental sensitivity is attributed to the enhancement of the portion of the valence band spectrum associated with the resonating energy level(s) upon tuning the photon energy across the absorption edge of the particular element in question. In this way, it is possible to identify the contribution originating from a particular element, meaning that ResPES can be used as one type of element-specific probe of the valence electronic structure.

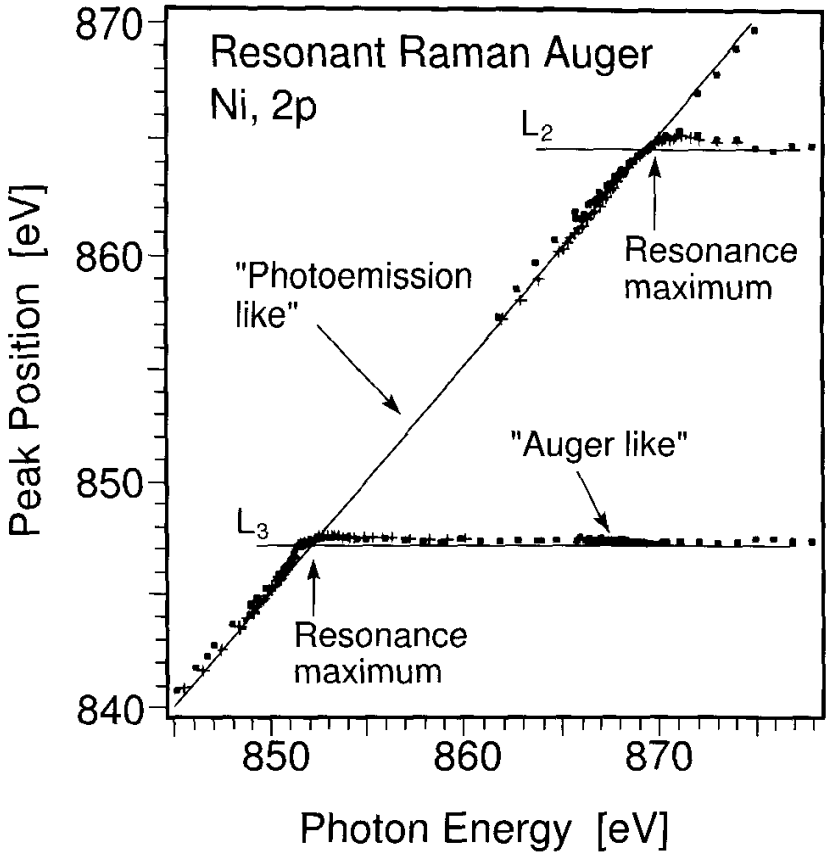

Figure 3.9: Illustration of the photon energy dependence of a resonant Raman Auger measured by tuning the photon energy across the Ni L_3 and L_2 edges. Taken from [13]

Beyond its utility in providing elemental character of the states comprising the valence band, resonant spectroscopies can be used to study ultrafast charge transfer dynamics with atomic specificity [12]. Ultimately, this is made possible by the fact that the intrinsic lifetime of the core-hole sets a natural timescales for these resonant processes in what is known as core hole clock spectroscopy. To better illustrate this point, consider the probability that a core-hole, having an intrinsic timescale τ_C, decays within a given time t according to the expression

$$P_C = \frac{1}{\tau_C} e^{-t/\tau_C} \tag{3.49}$$

Seeing as PES spectra are collected within the energy, as opposed to time, domain insights into the temporal dynamics will actually be given by consideration of the energy bandwidth in accordance with the time-energy uncertainty relation $\Gamma_C \tau_C \sim \hbar$. From this expression, by simply noting that the bandwidth and decay constant are inversely proportional to one another, a core-hole having a short intrinsic lifetime will necessarily be characterized as having a broad bandwidth. Thus, by recasting the probability for core-hole decay in terms of the energy bandwidth, it follows that

$$P_C = \frac{\Gamma_C}{\hbar} e^{-\Gamma_C/\hbar t} \tag{3.50}$$

where upon the typical widths of a core-level, which are on the order of a few eV, correspond to very fast timescales that will be $< 10^{-15}$s.

Within such a time scale, it can be asked what will be the probability that a resonantly excited electron will delocalize to a neighboring atomic site through a charge transfer process. Namely, given that charge transfer can be understood as a tunneling process described by an exponential probability

$$P^{CT} = \frac{\Gamma_{CT}}{\hbar} e^{-\Gamma_{CT}/\hbar t} \tag{3.51}$$

where Γ_{CT} denotes the hopping bandwidth, such a process can then be treated as being independent of the core-hole decay. Thus, by considering first the probability that *no* such charge transfer event occurs within the lifetime of the core hole, the consideration of both these channels simultaneously with independent rates yields to following conditional probability for the combined event.

$$P_C^{No\ CT} = \int_0^{T=\infty} dt' \frac{\Gamma_C}{\hbar} e^{-\Gamma_C/\hbar t'} \left[1 - \int_0^{t'} dt \frac{\Gamma_{CT}}{\hbar} e^{-\Gamma_{CT}/\hbar t}\right] = \frac{\Gamma_C}{\Gamma_C + \Gamma_{CT}} \tag{3.52}$$

Here, for Γ_{CT} being nothing more than the distribution of accessible empty states, in the limit where $\Gamma_{CT} << \Gamma_C$, there will be a higher likelihood that the core hole decays prior to the delocalization of the electron in the excited state. This can simply be attributed to the fact that the narrow bandwidth of the empty states implies that these states are well localized. Thus, in such a case the auto-ionization channels will remain open and the resonant spectra will reflect the fraction of spectral intensity stemming from decays where no charge transfer has occurred.

In contrast, if the excited state electron were to delocalize prior to the filling of the core-hole, then it can be similarly shown that

$$P_C^{CT} = \frac{\Gamma_{CT}}{\Gamma_C + \Gamma_{CT}} \tag{3.53}$$

Notably, for $\Gamma_{CT} >> \Gamma_C$, the increased probability for an excited state electron to hop to a neighboring atomic site implies that the auto-ionization channels become quenched and the core hole will then decay through a normal Auger process. Hence, a hallmark of ultrafast charge transfer is ultimately given by the suppression of the resonant response. Typically, charge-transfer dynamics are investigated in systems where an atom or molecule couples to some larger system through a weak coupling that can be treated as a perturbation. However, other important examples can be found in photovoltaics where exciton recombination has a deleterious effect on the efficiency of the solar cell [118].

3.2 Static and Ultrafast Optical Spectroscopy

3.2.1 Optical Pump-Probe Spectroscopy

As compared to core-hole clock spectroscopy, the recent development of turn-key femtosecond (fs) laser systems has opened up the possibility of measuring temporal dynamics in real time. Specifically, given the ultrashort duration of these light pulses, a temporal resolution on the order of the characteristic time-scales of electronic and atomic motion can now be achieved [14]. While such time-scales are arguably longer that that which can be captured by core-hole clock spectroscopy, a critical difference between these two techniques lies in the fact that a measurement of the dynamics in real time possesses a temporal coherence that is otherwise lacking when the time scales are inferred from energy bandwidths. This can be attributed to the

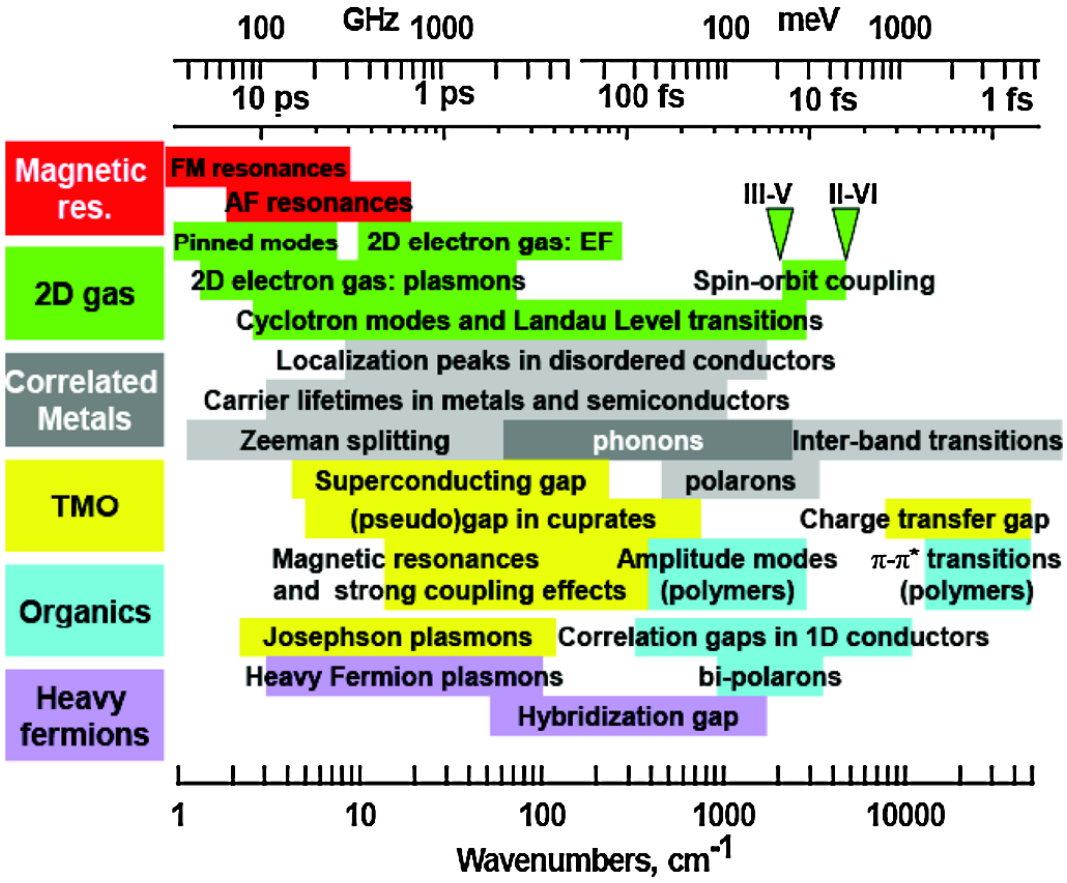

Figure 3.10: Respective time and energy scales of the various processes that can be found in strongly correlated systems. Taken from [14]

very nature of the pump and probe experiments used in ultrafast spectroscopy to measure the dynamical response of a system.

Here, an intense, perturbative pulse, known as the pump, impulsively creates a transiently excited, non-equilibrium state over some uniformly illuminated region of the sample. As the system begins to relax back down towards its ground state, snapshots of the time evolution for some observable are then made using a weak, non-perturbative probe pulse. In this manner, it is possible to disentangle the electron, lattice and spin dynamics, so as to establish a time hierarchy of events and crucially the coupling that arises between these various degrees of freedom (Figure 3.10). Therefore, interactions having similar energy scales can be a further elucidated by examining their respective time hierarchies. For this reason, ultrafast spectroscopy has emerged as a powerful technique capable of providing new insights into the behavior of strongly correlated materials [119].

At sufficiently low pump fluences, the subsequent recovery of a transiently excited state back towards equilibrium occurs in accordance with the same thermodynamic parameters that govern equilibrium properties. In such a case, a "hot" population of electrons created by the initial, impulsive excitation of the pump will decay through an exchange of energy with the lattice and spin degrees of freedoms. As previously mentioned, the recovery of the ground state can be unveiled by time resolved techniques in the form of different relaxation dynamics. Importantly, the stronger the coupling between the electronic degrees of freedom with that of the lattice or spin, the faster the relaxation dynamics will be. In an effort to describe such behavior, effective temperature models, such as that shown in Figure 3.11, can be employed [120]. Within this model, it is assumed that the microscopic processes that govern the relaxation of an out-of-equilibrium charge distribution will be the same as those that regulate the scattering processes in quasi-equilibrium conditions. Consequently, values for the electron-phonon or electron-magnon coupling parameters can be extracted from a fit of the relaxation dynamics using this model.

In many cases, an effective temperature model does well in reproducing the relaxation dynamics of a transiently excited state back down towards equilibrium. However, one of the underlying assumptions made in this model is that after an initial excitation, the non-thermal occupation of empty electronic states rapidly relaxes to a hot Fermi-Dirac population before any energy can be exchanged. While such an assumption is typically valid over long time delays

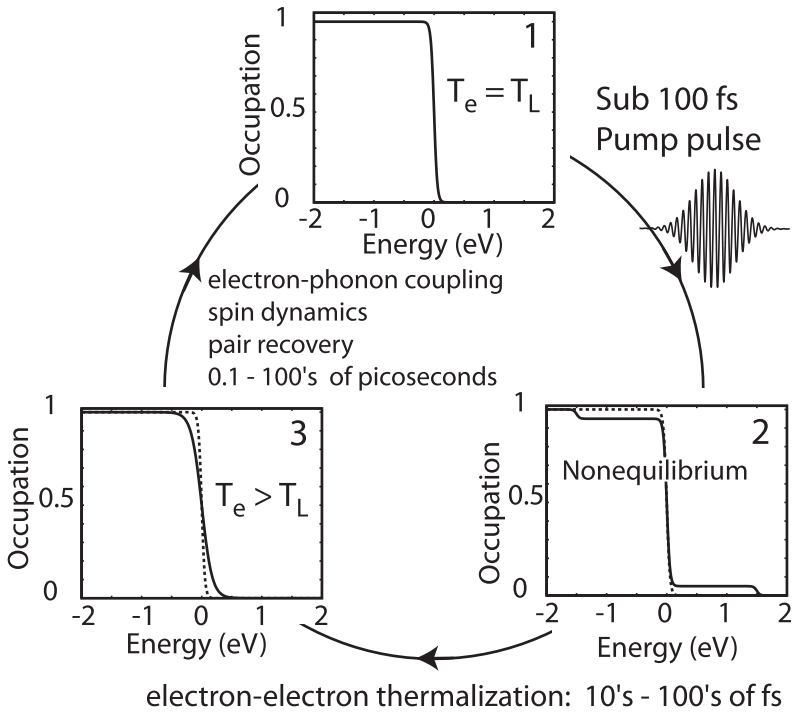

Figure 3.11: Schematic illustration of the effective temperature model used in the description of relaxation dynamics for an optical pump-probe experiment. Taken from [14]

($\sim 10^{-12}$s), it fails on sub-picosecond timescales as the initial non-equilibrium population of electrons established by impulsive excitation can exists for times long enough so as to begin exchanging energy with the lattice and spin degrees of freedom. Ultimately, the breakdown of the effective temperature model over the initial stages of the relaxation dynamics can be most clearly illustrated by time-resolved PES as such experiments provide a direct measure of the electron distribution as a function of time-delay [121]. Using simple arguments from Fermi liquid theory, the fact that a non-thermal distribution of electrons can exchange energy prior to thermalization can be rationalized by noting that the lifetime of a quasi-particle near the Fermi level can be orders of magnitude longer than the typical time scales associated with that of electron-phonon thermalization. Therefore, in order to accurately describe the relaxation dynamics, a proper treatment must necessarily requires a true non-equilibrium approach requiring the use of the Keldysh formalism [122].

Aside from providing insights into real time relaxation dynamics, optical pump and probe experiments can be used to study coherently excited collective modes arising from the impulsive excitation of an intense pump pulse [15]. While any bosonic mode having a frequency $\omega > 0$ in the optical limit of $q = 0$ is capable of being coherently excited, the most commonly observed collective modes are those deriving from optical phonons. Such coherent modes will be Raman active modes whose oscillations, measured in real time, will be at the same characteristic frequency of the phonon mode, while their relaxation will be determined by the dephasing time. Generally speaking, the launching of coherently excited optical phonons is typically a result of one of two processes distinguished by the temporal profile of the driving force.

Namely, when the pulse duration is short as compared to the vibrational period, it is expected that the driving force result in an impulsive change to the velocity of a harmonic oscillator without affecting its initial position. In such a case, the accompanying oscillation will be characterized as being sine-like which turns out to be a defining feature for coherently excited phonon modes arising from an impulsively stimulated Raman process. Here, in seeing that these modes must be launched by an excitation pathway mediated by some real, or virtual, electronic transition, the corresponding broad bandwith of a fs laser pulse will yield multiple combinations of two photon difference frequencies required for stimulated Raman scattering (Figure 3.12(a)). In contrast, it is also possible that the generation of photoexcited carriers by an ultrashort pulse can serve to suddenly shift the vibrational potential. That is, rather than producing an impulsive

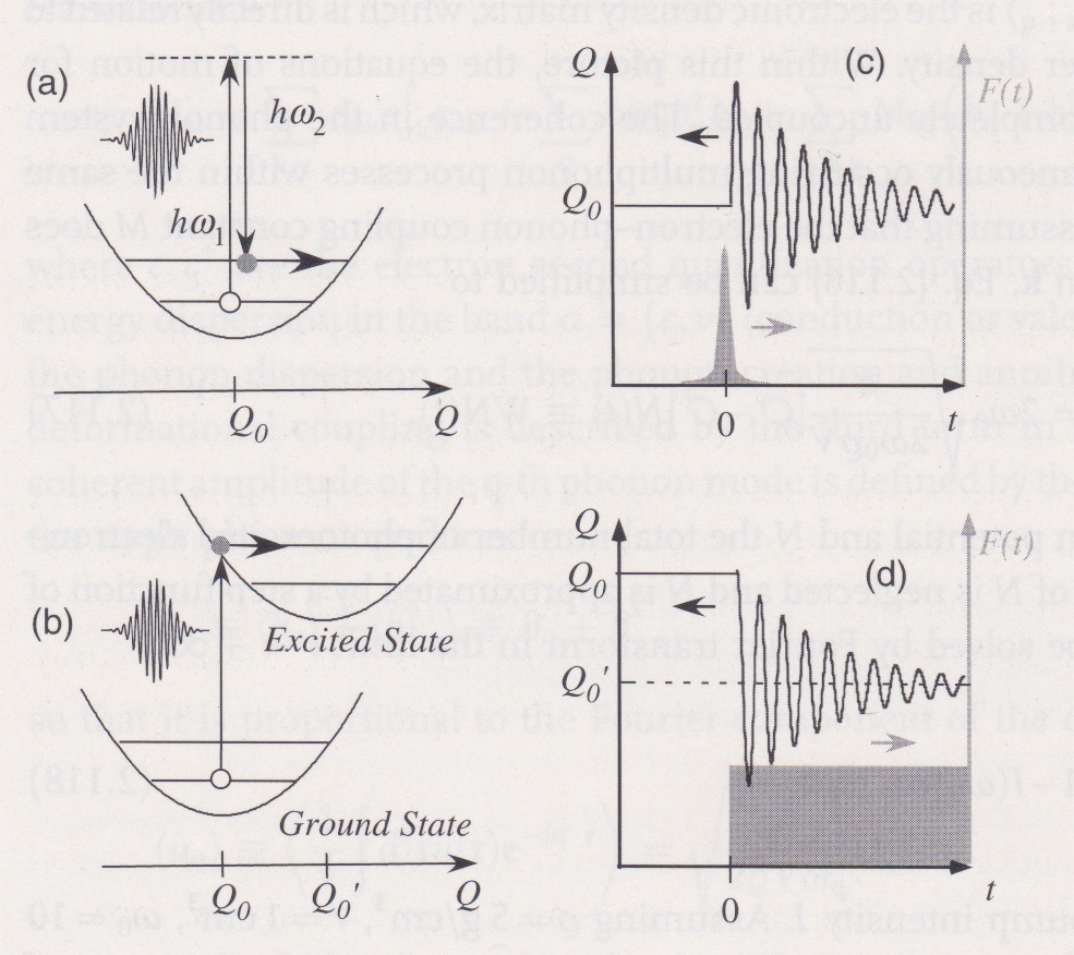

Figure 3.12: Illustration of the coherently excited collective modes that can arise from (a) an impulsively stimulated Raman process or (b) a displacive excitation. For both cases, the driving terms shown in (c) and (d) will yield different phases of the respective oscillations providing a means by which these two excitations can be distinguished. Taken from [15]

change, this type of displacive excitation will come about as a consequence of long-lived, pump induced changes to the equilibrium potential (Figure 3.12(b)). Thus, the corresponding driving force will take on the form of a step function, where the resultant coherently excited phonon modes can then be shown to exhibit a cosine-like behavior. Finally, in addition to the coherent excitation of optical phonons, it is possible to launch acoustic phonons through the introduction of stress due to the abrupt heating that occurs within the optical penetration depth of the pump pulse. In most instances detection of acoustical modes cannot be accomplished by optical techniques. However, when an additional superstructure periodicity is present, back-folding of the acoustic branches will subsequently allow for them to be observed in a transient reflectivity spectrum.

Up until this point, the discussion of ultrafast spectroscopy has been limited to the study of transient dynamics or coherently excited collective modes launched within a system as it relaxes back down towards its ground-state. However the primary attraction of performing this type of experiment, especially on strongly correlated electronic systems, lies in the fact that these systems are on the verge of multiple phase transitions. Therefore, it becomes possible to use ultrashort light pulses as an additional means to control physical properties on a transient timescale. This is particularly evident within the strong excitation regime, where ultrashort pulses can be used to trigger phase transitions that are otherwise inaccessible though adiabatic transformations. In this case, high pump fluences can be employed to prompt a photo-induced phase transition to non-thermally accessible metastable states, known as "hidden" phases [123]. This then result in a number of technologically appealing properties ranging from light induced insulator-to-metal phase transitions [124] to a proposed enhancement of superconductivity following illumination by an ultrashort light pulse [125].

3.2.2 Magneto-optical Kerr Effect

In optics, the response of a material to an electromagnetic wave can be described in the framework of linear response theory through the complex susceptibility function $\chi(r,t)$. For single crystals, it is often the case that this susceptibility function takes on the form of a tensor owing to the inherent anisotropy that can arise within a crystalline lattice. Typically, it is possible to define a principal axis within a crystal such that χ can be diagonalized. However, with the breaking of time-reversal symmetry, as occurs when applying an external magnetic

field, the susceptibility tensor will acquire an off-diagonal matrix element whose magnitude will be proportional to the strength of the applied field. To see how such a component arises, consider a simple expression for the polarization as derived from the equation of motion for a bound electron in presence of static *B*- and oscillating *E*-field [126].

$$\ddot{\vec{r}} + \omega_0^2 \vec{r} = -\frac{e}{m}\left(\vec{E} + \dot{\vec{r}} \times \vec{B}\right) \tag{3.54}$$

By expressing the optical field in terms of its typical time dependence, $E = E_0 e^{i\omega t}$, it follows that the displacement vector *r* will develop the same time dependence under steady state conditions. Therefore, in making use of the fact that the polarization, *P*, can be expressed as $\vec{P} = -Ne\vec{r}$, for *N* denoting the total number of electrons, it is possible to write the above equation as

$$(\omega_0^2 - \omega^2)\vec{P} = \frac{Ne^2}{m}\vec{E} + i\omega\frac{e}{m}\vec{P} \times \vec{B} \tag{3.55}$$

which can ultimately be put in a form of $\vec{P} = \varepsilon_0 \bar{\bar{\chi}} \vec{E}$ through solving in a component-wise fashion.

In the case where $\vec{B} = B_0 \hat{z}$, it can be shown that the susceptibility tensor will take on a form given by

$$\bar{\bar{\chi}} \longrightarrow \begin{pmatrix} \chi_{11} & i\chi_{12} & 0 \\ -i\chi_{12} & \chi_{11} & 0 \\ 0 & 0 & \chi_{33} \end{pmatrix} \tag{3.56}$$

where, as expected, the off-diagonal elements turn out to be proportional to the strength of the applied *B*-field. Noting that the form of this tensor exactly matches that found for optically active materials, the effect of the off-diagonal elements is to give rise to a circular dichroism resulting in a difference in propagation between right- and left-circularly polarized light. By recalling that linearly polarized light can be expressed as the superposition of right- and left-circularly polarized light, this difference in propagation ultimately serves to rotate the plane of polarization of such light by an amount determined by χ_{12}. Such a phenomenon, referred to as the Faraday effect in transmission and the magneto-optical Kerr effect (MOKE) in reflection, not only occurs through the external application of a *B*-field, but from the presence of an internal magnetization as well. Thus, by measuring the intensity and polarization state of reflected light from a ferromagnetic sample, a direct, real space measurement of the magnetization can be made.

As compared with other techniques, a measurement of the magnetization through MOKE offers a means of quantifying the degree of magnetic anisotropy in a single crystal or thin film [127]. As is shown in Figure 3.13, this is made possible by determining how the intensity and polarization state of light reflected from the sample changes based upon the direction that the magnetization makes relative to the scattering plane. More formally, this can be determined by the 2×2 scattering matrix $\bar{\bar{S}}$,

$$\bar{\bar{S}} = m_l^2\bar{\bar{L}} + m_t^2\bar{\bar{T}} + m_p^2\bar{\bar{P}} \tag{3.57}$$

where the reflection matrices, $\bar{\bar{L}}$, $\bar{\bar{T}}$, and $\bar{\bar{P}}$, are representative of the longitudinal, transverse and polar MOKE configurations, while the coefficients m_l, m_t, and m_p, define the normalized components of the magnetization projected along these same axes. Written out, the above reflection matrices will necessarily depend on the Fresnel coefficients, r, which can ultimately be determined by solving Maxwell's equations for a generalized form of the susceptibility tensor that is similar to that presented in equation 3.56 [16,127]. Thus, by expressing the reflection matrices in the form of [127], the scattering matrix can then be simplified to

$$\bar{\bar{S}} = \begin{pmatrix} r_{pp}(1 + m_t r_0^t) & m_l r_{ps}^l + m_p r_{ps}^p \\ -m_l r_{ps}^l + m_p r_{ps}^p & r_{ss} \end{pmatrix} \tag{3.58}$$

where the normalization condition $m_l^2 + m_t^2 + m_p^2 = 1$ has been used. Hence, when p-polarized light is incident on the sample, the effect of the MOKE scattering matrix will be to either change the intensity or rotate the plane of polarization of the reflected light in accordance with

$$\begin{pmatrix} E_p{}' \\ E_s{}' \end{pmatrix} = \begin{pmatrix} r_{pp}(1 + m_t r_0^t) & m_l r_{ps}^l + m_p r_{ps}^p \\ -m_l r_{ps}^l + m_p r_{ps}^p & r_{ss} \end{pmatrix} \begin{pmatrix} 1 \\ 0 \end{pmatrix} = \begin{pmatrix} r_{pp}(1 + m_t r_0^t) \\ -m_l r_{ps}^l + m_p r_{ps}^p \end{pmatrix} \tag{3.59}$$

where E_p', and E_s' denote the component of the electric field from the reflected light projected along the p- or s-polarization directions. Once reflected, an additional polarizer, which is more commonly referred to as the analyzer in a MOKE set-up, can be used to measure the subsequent changes that occur to the polarization state. Importantly, depending upon the orientation of this polarizer, it becomes possible to distinguish between the contributions coming from the longitudinal, transverse, and polar geometries of a MOKE signal.

Through rotating the analyzer by an angle θ_A with respect to the scattering plane, a measurement of the magnetization along the longitudinal, transverse, and polar axes can be made by noting that the intensity of light transmitted by the polarizer will be given by

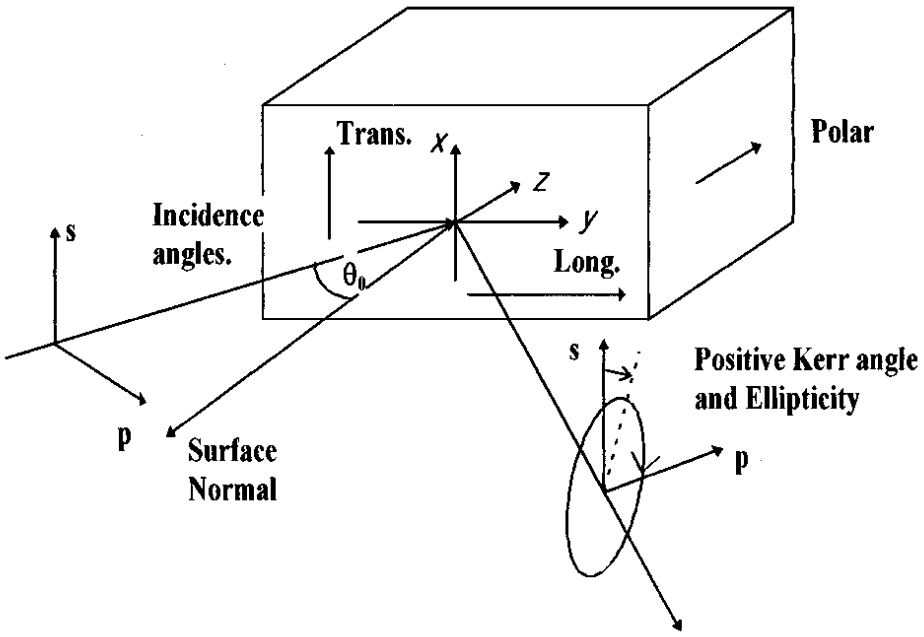

Figure 3.13: Schematic illustration of the relevant geometries for a MOKE experiment. Depending upon the direction of the magnetization relative to the scattering plane, the effect will be to vary the intensity and/or rotate the plane of polarization of the reflected light. Taken from [16]

$$I_T = |E_p' cos\theta_A + E_s' sin\theta_A|^2 \tag{3.60}$$

After substituting in for E_p' and E_s' from above, the square can be distributed in such a way that only those terms that are first order in the off-diagonal elements of the susceptibility tensor need to be kept. In doing so, the intensity of light passed through the analyzer becomes

$$I_T = r_{pp}^2(1 + (r_0^{t*} + r_0^t)m_t)cos^2\theta_A + \\ \left(-r_{pp}\left(r_{ps}^{l*} + r_{ps}^l\right)m_l + r_{pp}\left(r_{ps}^{p*} + r_{ps}^p\right)m_p\right)sin\theta_A cos\theta_A \tag{3.61}$$

which can ultimately be expressed in a more succinct fashion as

$$I_T = (A + Bm_t)cos^2\theta_A + (Cm_l + Dm_p)sin\theta_A cos\theta_A \tag{3.62}$$

Here, the ability to disentangle the contribution coming from the projection of the magnetization along the transverse, longitudinal and polar directions in a MOKE experiment lies in the symmetry of equation 3.62. Namely, by applying an H-field entirely within the sample plane, so as to have $m_p = 0$, the fact that the first term is even with respect to θ_A, while the second is odd implies that $m_t \propto I(\theta_A = 45°) + I(\theta_A = -45°)$, while $m_l \propto I(\theta_A = 45°) - I(\theta_A = -45°)$. Similarly, for an H-field being applied normal to the sample surface, m_p can likewise be found through again taking the difference $m_p \propto I(\theta_A = 45°) - I(\theta_A = -45°)$. Thus, by exploiting the angular dependence of the light's intensity passing through the analyzer, it is possible to isolate the contributions deriving from m_t, m_l, and m_p to the MOKE signal.

Lastly, despite the utility of MOKE in providing a measure for both the presence of ferromagnetic order, and the associated anisotropies that can result from such an ordering, special care needs to be taken in extracting quantitative information from this technique [128]. Namely, by recalling that light cannot directly couple to an electron's spin, the microscopic origin of the Kerr effect must then derive from a relativistic spin-orbit interaction. In seeing that the orbital component of the magnetization for most open-shell 3d systems will be quenched due to crystal field effects, the resultant magnetic moment for such systems will be entirely spin derived. Since 3d elements are characterized as having a relatively weak spin-orbit interaction, the Kerr rotations as measured in the polar or longitudinal configurations will necessarily be small (< 1°) and are likewise found to depend sensitively on changes occurring to the electronic band structure. Therefore, it is typical that a MOKE signal exhibit a pronounced wavelength dependence [128]. In the end, despite the presence of a Kerr signal being indicative of ferromagnetic ordering within a material, its amplitude cannot be taken as a reliable measure of the magnetic moment as there is no simple relation that exists between these two quantities.

Chapter 4: Experimental Apparatus

4.1 The ARPES Spectrometer

4.1.1 Ultra-high Vacuum

In the previous chapter, many of the experimental techniques discussed employ electron spectroscopies to directly measure the electronic structure of a material. While there are many advantages to such techniques, their principal drawback is the inherent surface sensitivity of the low energy electrons detected. As discussed in section 3.1.3, this is attributed to the fact that these electrons interact strongly with the material, leading to short inelastic mean free paths and therefore shallow probing depths. Ultimately, it is thanks to this surface sensitivity that the preparation of clean surfaces necessitates the use of ultra-high vacuum (UHV) conditions. By working under such conditions, fresh surfaces prepared by sample cleave, sputtering and annealing, or epitaxial growth, can be measured in a stable, controlled environment free from contaminants capable of being physisorbing or chemisorbing onto the surface. In order for this to be accomplished, pressures lower than 10^{-10} Torr are typically required.

To obtain such low pressures, specialized vacuum pumps capable of either removing or trapping residual gas molecules are needed [129]. Notably, beginning from ambient pressure, a preliminary vacuum, referred to as rough vacuum, is established by use of scroll or rotary pumps. Here, this initial stage of vacuum serves to lower the pressure in the chamber below the laminar to molecular transition, allowing for the operation of UHV specific pumps. Of these, turbomolecular pumps are the most widely used displacement pumps capable of bringing the chamber to the HV and UHV regimes. The operating principal of a turbo pump is rooted in the removal of gas molecules that strike a rapidly spinning rotor through imparting a component to its momentum that serves to direct it towards the pump exhaust. Given the velocity of a gas particle to be inversely proportional to $\sqrt{m}$, it is clear that the pumping speed of a turbo pump will be faster for heavier gas molecules as the rotor will be able to impart a larger component to their momentum. In seeing as turbo pumps serve to actively remove residual gas particles, their

greatest utility is in attaining UHV conditions. For this reason these pumps are most often used during "bake-out" conditions where the walls of the chamber are cooked up to 150 °C so as to predominantly remove adsorbed water.

While turbo pumps are best suited for attaining UHV conditions, to maintain vacuum, capture pumps such as ion pumps and Titanium sublimation pumps (TSP) are most often used. These pumps operate on the principal of using a chemically reactive element, Ti, as a getter material for any residual gas molecules remaining in the chamber. For a TSP pump, this is accomplished by simply subliming Ti onto a shroud so that any residual gas molecule that impinges on the shroud wall will then chemisorb to the surface. Here, pumping speeds naturally depend on the covered surface area and the sticking coefficient of the residual gas molecule. Consequently, speeds can be enhanced through a combined use of a mesh and liquid N_2 cooling shrouds so as to increase the surface area and sticking coefficient respectively.

In a similar manner, ion pumps possess Ti coated cathodes that will act as a getter material for ionized residual gas molecules accelerated under high voltage towards the Ti elements. Here, ionization is accomplished by a collision between residual gas molecules and electrons located near the pump anode. In order to increase the probability of such events, the path length of the electron is increased by externally applying a strong, permanent magnetic field. Thus, given the operating principal of ion and TSP pumps, it is evident these pumps will necessarily have a poor efficiency in removing inert gases such as noble gases and methane. However, as compared to turbomolecular pumps, capture pumps like TSP pumps are particularly well suited for removing H_2. Namely, thanks to the low molecular mass, and therefore high v_{rms}, H_2 is particularly difficult to be actively pumped out of a vacuum chamber and is therefore best removed through chemisorption. Finally, thanks to the fact that capture pumps contain no moving parts, they are ideally suited for maintaining vacuum in measurement chambers where high stability and low vibrations are especially important.

Within the Mannella lab, a sketch of the main and rough pumping configurations for the ARPES chamber is shown in Figure 4.1. Here, initial pump down is accomplished by use of dry scrolls and turbomolecular drag pumps, while UHV conditions are maintained by a 400L ion pump, and a titanium sublimation pump. Additionally, a large, magnetically levitated turbomolecular pump is mounted on the chamber, and put to use during operation of the vacuum ultraviolet (VUV) helium (He) light source as well as for bake-outs of the chamber. Generally,

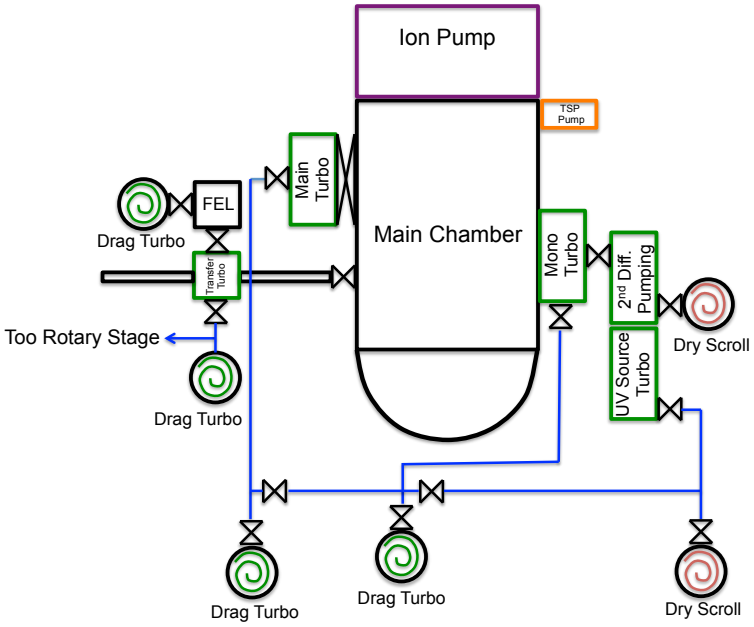

Figure 4.1: Sketch of the ARPES pumping configuration

following a bake-out, the typical base pressure reached will be better than 4×10^{-11} Torr, which is characterized by the residual mass spectrum shown in Figure 4.2. Moreover, aside from the pumps that serve to maintain vacuum in the chamber, there are also a series of differential pumps whose job is to correct for pressure gradients. The most notable is the differential pumping of the VUV He light source, where discharge occurs under a He pressure of a few mbar, but also the rotary stage of the manipulator and the sample fast entry lock are differentially pumped regions as well. In all cases, the purpose of differential pumping is to ensure that the pressure of the main chamber suffer only from minor changes when performing such necessary operations as starting the VUV source, rotating the manipulator or transferring a sample. By taking such care, the intent is to avoid any significant, that is spectroscopically identifiable, sample contamination during the course of an ARPES experiment.

4.1.2 Electron Energy Analyzer

When actually performing an ARPES measurement, what is as important as having a clean, single crystalline surface is the ability to precisely determine the kinetic energy and angle of emission of the outgoing photoelectron. To do so, an electron energy analyzer having a position sensitive detector must be employed [17,129,130,131]. Of the various analyzer designs, the most commonly used is the concentric hemispherical analyzer (CHA). This analyzer works as a band-pass filter allowing for only those photoelectrons within a specified energy range to reach the detector. The central energy of this range is referred to as the pass energy, E_p, as it defines the allowed kinetic energy for an electron to pass through the CHA without colliding on the walls of the hemispheres. This ability to discriminate between electron kinetic energies, which is essential for the determination of electron binding energy in the solid, is accomplished by precisely tuning the electrostatic potential placed on the inner and outer hemispheres.

Such potentials can be defined as [132]

$$V_{out} = V_0\left(\frac{2R_0}{R_{out}} - 1\right) < 0 \tag{4.1}$$

$$V_{in} = V_0\left(\frac{2R_0}{R_{in}} - 1\right) > 0 \tag{4.2}$$

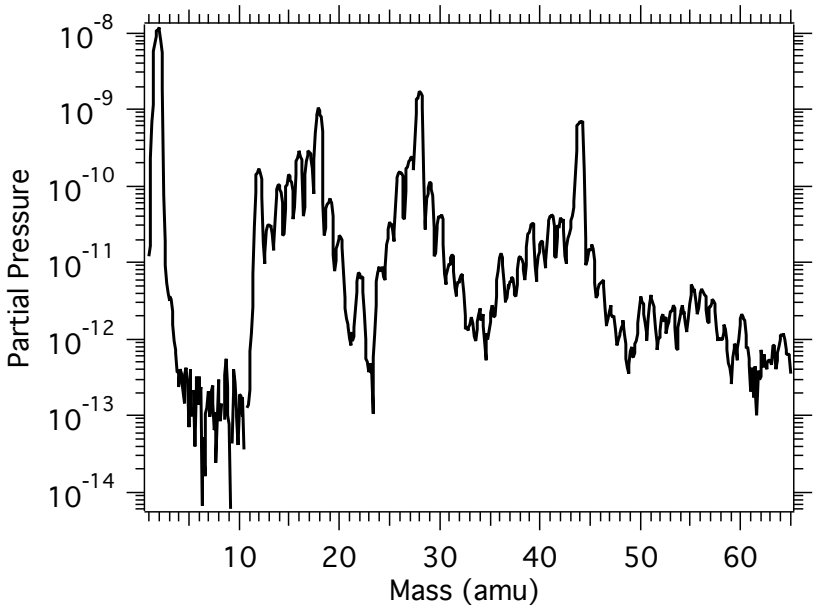

Figure 4.2: Mass spectrum of residual gas in ARPES chamber taken when the chamber base pressure is better than 6.0×10^{-11} Torr. Main peaks can be ascribed to H_2, C, H_2O, CO, and CO_2. Note that at such a pressure $P_{H2O} < P_{CO}$ indicative of a good bake-out.

where R_0 denotes the average radius between the two hemispheres, $R_0 = {}^1/_2\,(R_{out} - R_{in})$, and V_0 defines the corresponding potential for the pass energy, $E_p = eV_0$. By taking the potential difference between the two hemispheres to be,

$$\Delta V = V_0 \left(\frac{R_{out}}{R_{in}} - \frac{R_{in}}{R_{out}}\right) \tag{4.3}$$

it is possible to write an expression for the electric field between the hemispheres by assuming that the CHA can be modeled as a spherical capacitor. Such a simplifying assumption can be made thanks to the presence of a Herzog plate, which terminates the analyzer and serves to limit

any fringe fields resulting from the analyzer being hemispherical as opposed to spherical [17,133]. Consequently, by recalling the capacitance of a spherical capacitor to be given by, $C = 4\pi\varepsilon_0 \left(\frac{R_{out}R_{in}}{R_{out}-R_{in}}\right)$, Gauss' law can then be used to define the electric field between the two hemispheres as

$$\vec{E} = \Delta V \left(\frac{R_{out}R_{in}}{R_{out}-R_{in}}\right)\frac{1}{R^2}\hat{R} \tag{4.4}$$

By knowing the electric field, it is possible to determine the equation of motion for an electron traveling between the two hemispheres allowing for one to construct a ray-tracing diagram for all the possible trajectories [134]. Qualitatively, it is evident that such a central field will support stable orbits along the equipotential line R_0 for those electrons having an energy equal to E_p. Due to the fact that the analyzer is a band-pass filter, there will be a distribution of electrons whose energy is centered about E_p that are likewise capable of completing a full orbit and reaching the detector. For the Scienta R4000 CHA used in the Mannella lab [133], this distribution is roughly determined to be +/- 5% of E_p. Therefore, in order to narrow the band-pass, and subsequently increase the energy resolution of the analyzer, a smaller E_p must be used.

To select for a particular E_p of the analyzer, the simplest means of doing so is through continuously varying V_0 on the hemispheres so as to have E_p equal the corresponding photoelectron kinetic energy to be measured. However, seeing as an analyzer works with a fixed resolving power, $RP = {}^E/_{\Delta E}$, that depends entirely on geometric terms, by allowing for E_p to scale with the kinetic energy, the energy resolution, ΔE, will necessarily become poorer at higher energies. Since some of the most interesting features of the electronic structure are found in the valence band, i.e. at low binding energies/high kinetic energies, having a poor energy resolution

in this region is undesirable. To circumvent this problem, a tunable, preretarding potential can be applied to the photoelectron prior to reaching the entrance slit of the analyzer. In doing so, V_0 on the hemispheres can remain fixed allowing for E_p to remain constant, making it such that ΔE no longer depends on the electron kinetic energy.

For the Scienta R4000, a resolving power of up to $RP = 4000$ is claimed by the manufacturer [133]. In more familiar terms, such a resolving power translates to a lower limit of ΔE that is less than 1.0 meV! However, as is often the case, working with such high resolution is generally not necessary as it leads to poor statistics in the spectrum. Rather, by specifically choosing a fixed E_p, as well as width, w, to the entrance slit of the analyzer, a resolution given by [17,129]

$$\Delta E = \frac{w}{2R_0} E_p + O(\alpha^2) \tag{4.5}$$

allows for the user to work with a ΔE that is a compromise between energy resolution and good statistics. For the typical photoelectron kinetic energies observed in a VUV ARPES experiment, E_p = 5 eV and 10 eV, and w = 0.5 mm and 0.3 mm are the most commonly used settings. Given R_0 =200 mm for the R4000 analyzer [133], such values will yield the theoretical ΔE's presented in Table 4.1. Here, higher order effects due to the angle of incidence, α, that the photoelectron makes with the entrance slit of the analyzer have been neglected. As can be seen, negligible differences in energy resolution exist between w = 0.5 mm, E_p = 5 eV and w = 0.3 mm, E_p = 10 eV, making the choice between the two settings dependent on whichever pair yields the best statistics.

4.1.3 Electrostatic Lens

As was previously discussed, the electrostatic lens plays an important role in improving the energy resolution of a CHA by serving to preretard electrons to the pass energy of the analyzer. However, the lens also plays a much more critical role by acting as either a converging or collimating electron lens depending on the specific modality that is employed. In such a case, the ability to focus or collimate electron beams turns out to be exactly analogous to the situation found in optics. Here, the electrostatic potential satisfies the same role as the index of refraction by causing an electron beam to deflect when traversing across an "interface" defined by a potential difference [129]. This then allows for analogues expressions to Snell's law and the lens

Table 4.1: Calculated energy resolutions for the R4000 spectrometer given specific choice of pass energy and slit width.

E_p (eV) /w (mm)	5	10
0.3	3.75 meV	7.5 meV
0.5	6.25 meV	12.5 meV

focal length to be constructed where $\sqrt{V}$ can simply be substituted for the index of refraction, η. Thus, thanks to the ease of varying V over η, a series of electrostatic lens placed in a fixed geometry can be used to either focus or collimate an electron beam depending upon whether the lens is operating in a transmission or angular mode (Figure 4.3).

In transmission mode, electrons are collected over a wide solid angle and focused onto the entrance slit of the analyzer. Following the trajectory of the electrons through the hemispheres, it can be shown that these electrons will then refocus onto the exit slit of the analyzer and will therefore produce a narrow stripe down the center of the detector. Such a stripe accounts for the fact that there will still be a dispersion in energy attributed to the band-pass of the analyzer, but a focus in angle. In contrast, when the electrostatic lens is working in angular mode, electrons emitted over a solid angle of +/- 15 or +/- 7 degrees are collected by the lens and collimated onto the entrance slit of the analyzer. In this way, there will be no loss of angular information, as photoelectrons emitted over such an angular range will follow a trajectory about the CHA and be imaged on the detector in accordance with Figure 4.4. As can be seen from Figure 4.4, such imaging necessarily requires that the detector be a 2D spatial detector allowing for the simultaneous determination of both energy and angle. For this reason, the Scienta R4000 is equipped with a chevron multichannel plate coupled to a phosphor screen and CCD camera. Such a detector design allows for the precise determination of both the kinetic energy and emission angle of the photoelectron with an angular resolution that is better than $\Delta\theta = 0.2°$.

4.1.4 Sample Manipulator

Given the importance of determining the angular dispersion along a specified crystallographic direction, a critical component of an ARPES spectrometer is the sample manipulator. Notably, the manipulator design used in the Mannella lab is centered on a continuous flow cryostat having three translational and three rotational degrees of freedom (DOF). As discussed in section 3.1.3, these rotational DOF are essential for the *k*-conversion, which relates the outgoing photoelectron momentum with the initial state crystal momentum. Recalling that such a relation depends on the specifics of the experimental geometry, by using the fact that the entrance slit of the analyzer lies perpendicular to the scattering plane, an intrinsic Tait-Bryan transformation about the *y-x'* axis yields an expression for the conserved components of the initial state momentum to be

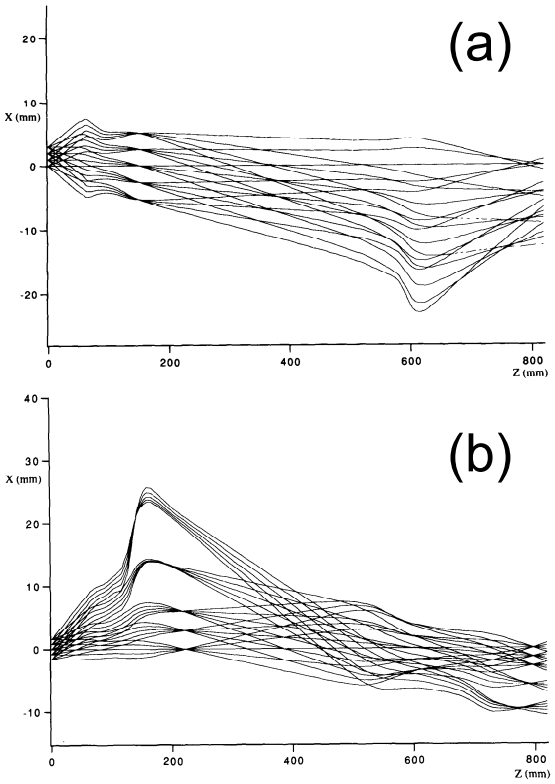

Figure 4.3: Ray tracing diagrams for an electrostatic lens working in (a) transmission and (b) angular mode. Taken from [17]

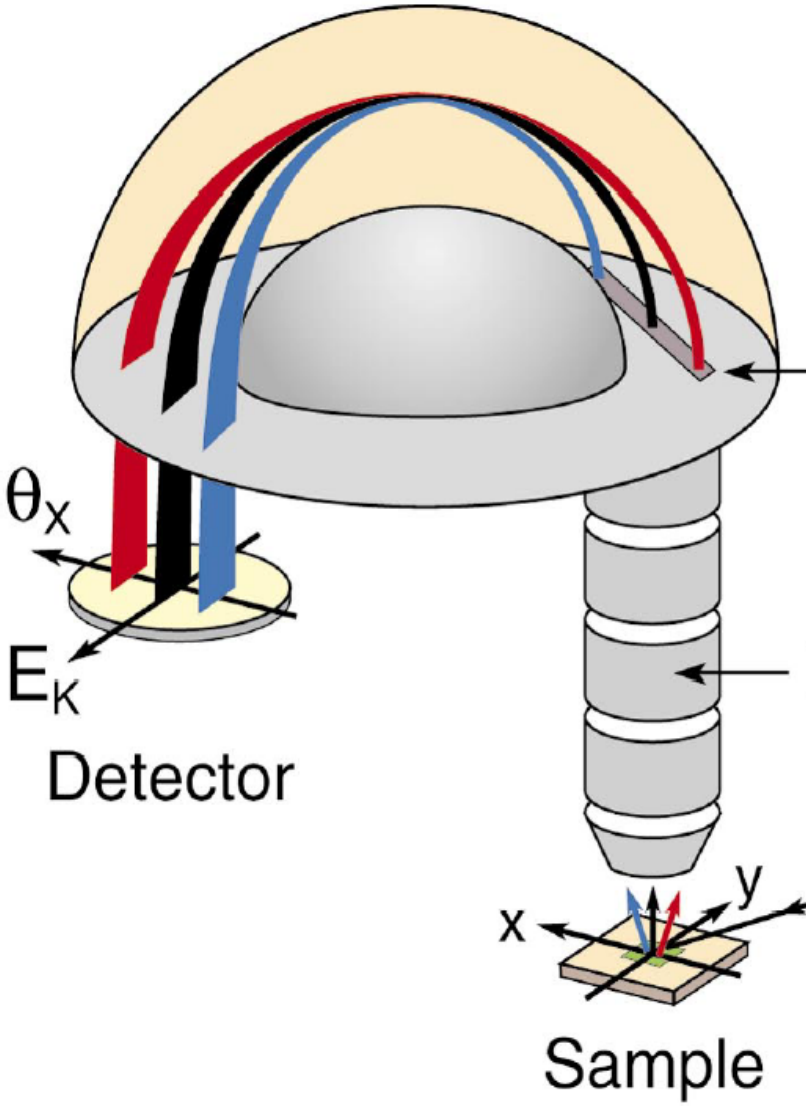

Figure 4.4: Schematic illustration of the trajectory taken by an electron emitted from the sample with a given E_K and θ_K as it passes through the CHA and strikes a 2D spatial detector. Figure reproduced here from NM

$$k_i^x = \frac{\sqrt{2mE_K}}{\hbar}\sin\left(\theta_A + \phi\right)$$
$$k_i^y = \frac{\sqrt{2mE_K}}{\hbar}\cos\left(\theta_A + \phi\right)\sin\theta_M \tag{4.6}$$

Such a relation is exactly analogous to that derived in section 3.1.3 but with no correction for photon momentum needed as its contribution at VUV energies is negligible. As can be seen from the above expression, the most critical angles used for ARPES experiments on this spectrometer are the flip, ϕ, and polar, θ_M, angles. In contrast, the azimuth, ω, is predominantly used for sample orientation prior to measuring, so it will remain constant over the duration of a band dispersion and Fermi surface scan and therefore will not factor into the *k*-conversion. While having a three-rotation axis manipulator allows for the sample to be aligned along its high symmetry directions, the manipulator itself also plays a subtle, yet important role in grounding the sample to the spectrometer. Considering the simplest case of a metallic sample, not only will any sample charging be avoided by grounding to the spectrometer, but the Fermi level between the sample and spectrometer will become equilibrated and serve as an absolute reference for the electron binding energies [10]. As shown in Figure 4.5, the work function of the sample, ϕ_s, can be different from that of the spectrometer, ϕ_{spec}, leading to a potential difference that will either accelerate or decelerate the outgoing photoelectron. This in turn acts to change the initial kinetic energy, E_{KE}', as measured at the sample surface by an amount given by

$$E_{KE} = E'_{KE} + \phi_s - \phi_{spec} \tag{4.7}$$

Here, the resultant kinetic energy, E_{KE}, is that which is measured by the spectrometer. Since determination of ϕ_s will be sample dependent, and also not a trivial measurement to perform, it is more favorable to work with E_{KE} and ϕ_{spec} as this work function will remain constant. Ultimately, this can be done because the Fermi levels equilibrate when a metallic sample is placed in electrical contact with the spectrometer. Therefore, by referencing the electron binding energy to the Fermi level,

$$E_B^F = h\upsilon - E_{KE} - \phi_{spec} = h\upsilon - E'_{KE} - \phi_s \tag{4.8}$$

making it such that a measure of E_{KE} and ϕ_{spec} yields the exact same information as a direct measurement of E_{KE}' and ϕ_s. For the ARPES spectrometer used in the Mannella lab, ϕ_{spec} was determined on a polycrystalline gold sample to be ϕ_{spec} = 4.856 eV for E_P = 10 eV.

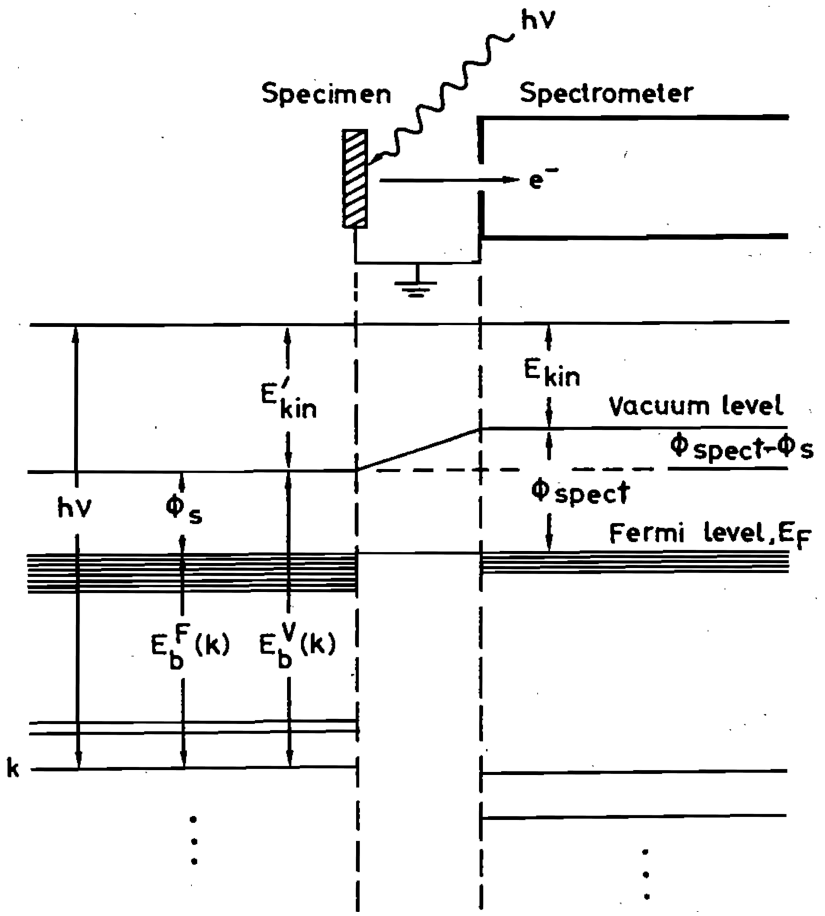

Figure 4.5: Energy level diagram taken from [10] showing the difference in work function that comes about from grounding the sample to the spectrometer

4.1.5 Helium Gas Discharge Lamp

Up until this point, the discussion has focused on how photoelectrons are detected, but no attempt has been made to describe how such photoelectrons are generated in the first place. From the preceding section, it is evident that this will require a light source capable of producing photons with an energy, $h\nu$, greater than the work function, ϕ_{spec}, of the spectrometer. Within the Mannella lab, this is accomplished by use of two different laboratory based light sources including a versatile He gas discharge lamp used for static VUV photoemission and an ultrafast laser source used for studying dynamics in the electronic structure.

The static He light source employed in lab operates on the basis of plasma generation by an electron cyclotron resonance technique [135]. Here, microwaves generated by a 300W klystron are fed into the discharge region of the source by a rectangular waveguide. Within the discharge region, electrons trapped by an inhomogeneous magnetic field are accelerated by the oscillating electric field of the microwave radiation. Since the 10 GHz frequency of the microwave radiation is on resonance with the electron cyclotron frequency, the effect is to considerably increase the free travel distance of an electron far beyond the dimensions of the cavity. For such a long travel distance, there will be a higher probability that an electron strike a passing He atom, and promote it to an excited state. The VUV radiation that then results is generated by the subsequent decay of this excited state by radiative emission.

As depicted in Figure 4.6, for the He gas discharge lamp employed in the lab, most of the emitted monochromatized UV light comes from the He Iα transition. This transition is defined by the 2p to 1s transition in neutral He, where the resultant radiative emission line is centered at hν = 21.2182 eV. However, another important emission comes from the same 2p to 1s transition, but in singly ionized He^+. This transition, known as the He IIα transition, will produce higher energy light centered at hν = 40.814 eV. Depending on photoelectron cross-sections or regions of reciprocal space to be explored, certain experiments will call for use of either the He Iα or He IIα emission line. Thus, by using a 1200 line/mm platinum coated, toroidal grating these two excitation energies can be separated and independently selected for static ARPES experiments.

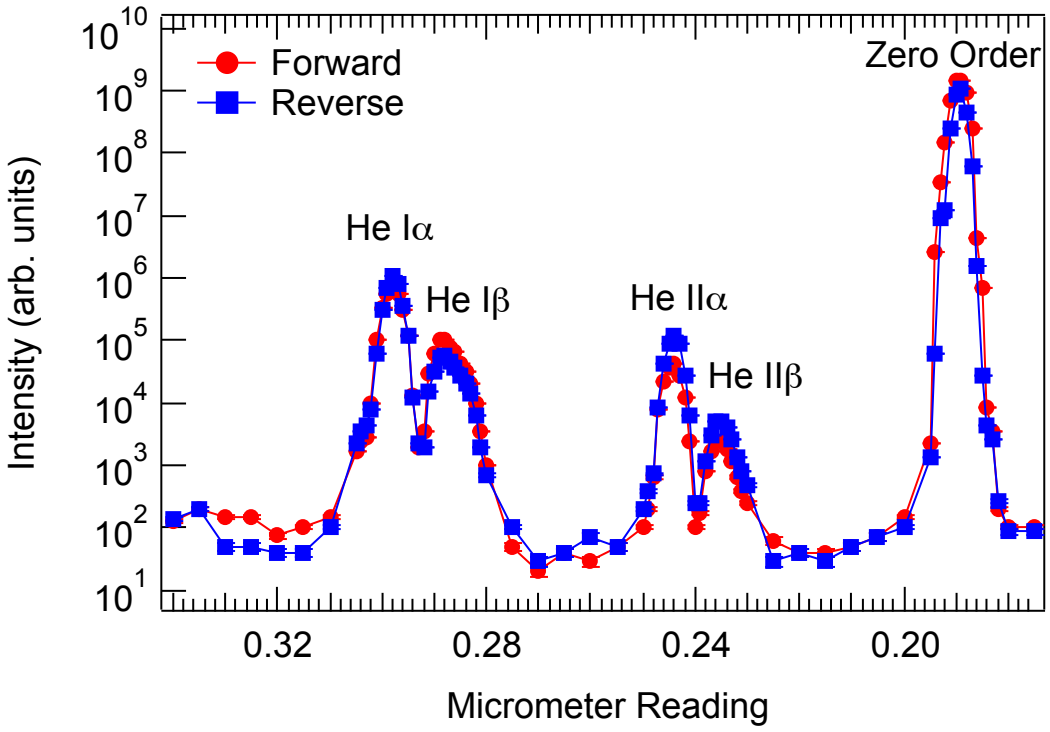

Figure 4.6: Intensity of photoelectron secondaries as a function of monochromator reading. Main lines are labeled with the zero order peak denoting specular reflection. Counts measured by sweeping monochromator in both a forward and backward direction for determination of backlash.

4.2 Ultrafast Laser System

In order to study electron and collective mode dynamics in real time, it is necessary to use an experimental technique capable of measuring on the intrinsic timescale of these interactions. Considering the lower limit of this timescale to be determined by electron-phonon or electron-impurity interactions, a rough estimation is given by the electron inelastic mean free path, λ_{IMFP}, and Fermi velocity, v_F, as the time between successive scattering events $\tau = \lambda_{IMFP}/v_F$ $\sim 10^{-15}$s. Thanks to the incredibly short duration between these events, any traditional means of measuring a temporal response, such as with an oscilloscope, turns out to be several orders of magnitude too slow. Most notably, at the time of this writing, the fastest commercial oscilloscope available boasts an impressive 100 GHz bandwidth [136]! However, even with such a broad bandwidth, in order to capture dynamics on the timescale of electron-phonon scattering events, a bandwidth greater than a THz is necessary. For this reason, measuring electron and lattice dynamics in real time is accomplished by use of ultrafast optical pulses, which are on the order of tens of femtoseconds (fs) in duration.

4.2.1 Modelocking

The generation of ultrashort optical pulses is often achieved through a process known as modelocking [137,138,139]. In essence, the fundamental idea behind this process is that a coherent sum of longitudinal cavity modes is used to create a wavepacket possessing a broad bandwidth and therefore short pulse duration. To understand how this process is accomplished, it is necessary to first recall a few fundamental concepts of lasing. Most notably, for any laser system the essential components are the pump, gain medium, and laser cavity. While the pump acts solely to create a population inversion in the gain medium, the main contribution to the creation of modelocked pulses comes from the amplification of a broad bandwidth gain medium over many longitudinal cavity modes. Such cavity modes arise from the presence of end mirrors in the laser that allow for multiple passes of light through the gain medium. However, because these end mirrors provide a boundary, only those wavelengths corresponding to the longitudinal modes of the cavity will be amplified. For this reason, the development of cavity modes in a laser is akin to the resonances that arise in a Fabry-Perot interferometer.

As is sketch in Figure 4.7 (a), a Fabry-Perot interferometer is comprised of two partially reflective surfaces that are oriented parallel to one another so as to form a cavity separated by distance d. When incoming light of amplitude E_0 is incident on one such surface, its amplitude is attenuated according to how much light is transmitted t versus reflected r with probability $|t|^2 = T$ and $|r|^2 = R$ respectively. Considering that the condition for resonance in the interferometer is determined by the difference in path length taken between the transmitted waves as sketched Figure 4.7 (b),

$$a + b = \frac{d}{\cos\vartheta}\left(1 + \cos\left(2\vartheta\right)\right) \tag{4.9}$$

Then not only will each subsequent reflection result in an attenuation of the initial amplitude E_0 by r, but an additional phase factor of $\phi = 2kd\cos\vartheta$ will also be added to the phase of each transmitted planewave. For the series of reflections shown in Figure 4.7 (a), this results in an expression for the transmitted planewave given by a geometric series

$$\begin{aligned} E_t &= E_0 t^2 + E_0 t^2 r^2 e^{i\phi} + E_0 t^2 r^4 e^{i2\phi} + \ldots + E_0 t^2 r^{2n} e^{in\phi} \\ &= E_0 t^2 \frac{1}{1 - r^2 e^{i\phi}} \end{aligned} \tag{4.10}$$

Writing out the intensity of transmitted radiation $I_t = |E_t|^2$, and making use of the identity $\cos\phi = 1 - 2\sin^2\left(\phi/2\right)$, one can ultimately express the intensity transmitted from the interferometer in the form of the Airy distribution.

$$I_t = I_0 \frac{T^2}{(1-R)^2} \frac{1}{1 + \frac{4R}{(1-R)^2}\sin^2\left(\phi/2\right)} \tag{4.11}$$

Here, the condition for resonance is determined by the minimization of the denominator. This occurs for $\phi = 2\pi m$, which as expected, is the exact same condition for constructive interference between the transmitted waves in Figure 4.7 (b). Taking $\theta = 0$ in the expression for the path length difference, it is evident that a resonance of the interferometer occurs when the cavity separation distance is given by $d = n\frac{\lambda}{2}$. Such an expression turns out to be quite familiar as this is the same condition that is required for standing waves to form in a cavity closed at both ends. Ultimately, it is these standing waves in the laser cavity, which are more commonly expressed in terms of their frequency ν_n

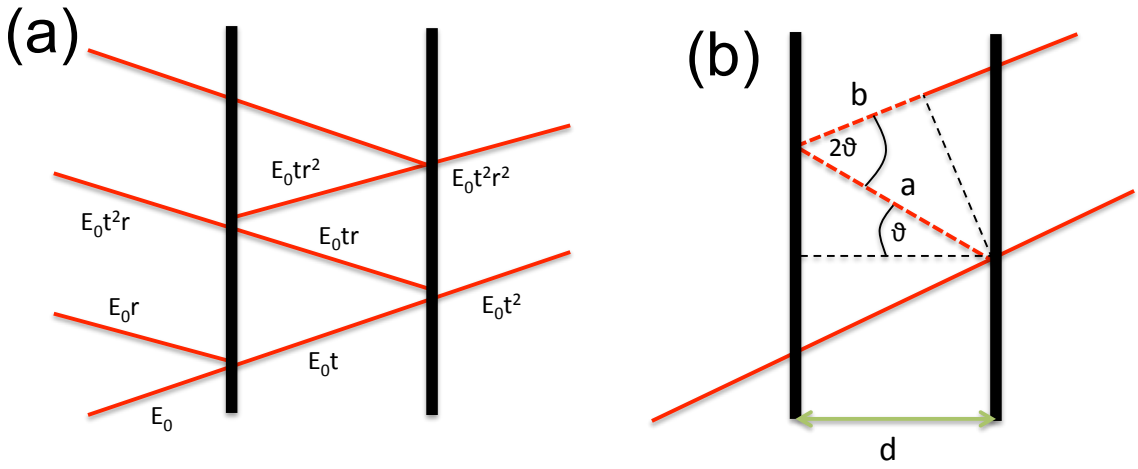

Figure 4.7: Illustration of a Fabry-Perot interferometer showing in (a) the attenuation of an incident E_0 by subsequent reflection and transmission through the etalon and (b) the difference in path length taken between two transmitted beams.

$$\nu_n = n\frac{c}{2\eta d} \tag{4.12}$$

where c denotes the speed of light in vacuum and η defines the refractive index of the medium, that are referred to as the longitudinal modes. As this relates to laser systems, despite the gain medium serving to emit light over a given bandwidth, it is only those frequencies that match the longitudinal modes of the cavity that ultimately become amplified.

As depicted in Figure 4.8, for a gain medium possessing a broad lasing bandwidth, it is evident that many longitudinal modes in the cavity can survive. In fact, for modelocked laser systems, it is the presence of so many of such modes that the origin of term "oscillator" comes about. Under normal circumstances, there is no phase relation that exists between these modes and the resultant superposition will yield an expression for the intensity given by

$$I(t) = \left|E(t)\right|^2 = N\left|E_0\right|^2 \tag{4.13}$$

where N denotes the total number of longitudinal modes that fall within the gain bandwidth. However, if, for any reason, a well-defined phase relation does develop between each of the amplified cavity modes, then the resultant waveform will be given by their coherent superposition

$$E(t) = E_0\sum_{n=0}^{N-1} e^{i(\omega_n t+\varphi_0)} = E_0 e^{i\varphi_0}\sum_{n=0}^{N-1} e^{i\omega_n t} \tag{4.14}$$

Such a process is referred to as modelocking. In this case, by defining $\omega_n = n\frac{\pi c}{\eta d} = \omega_{N-1} - n\Delta\omega$, the above summation can be computed by making use of the fact that $\sum_{n=0}^{N-1} e^{-in\Delta\omega t} = \frac{1-e^{-iN\Delta\omega t}}{1-e^{-i\Delta\omega t}}$.

From this result, the expression for the coherent superposition of longitudinal cavity modes will simplify to a form given by

$$E(t) = E_0 e^{i\left(\left(\omega_{N-1}/2\right)t+\varphi_0\right)}\frac{\sin\left(N\frac{\Delta\omega t}{2}\right)}{\sin\left(\frac{\Delta\omega t}{2}\right)} \tag{4.15}$$

which consequently yields an intensity of

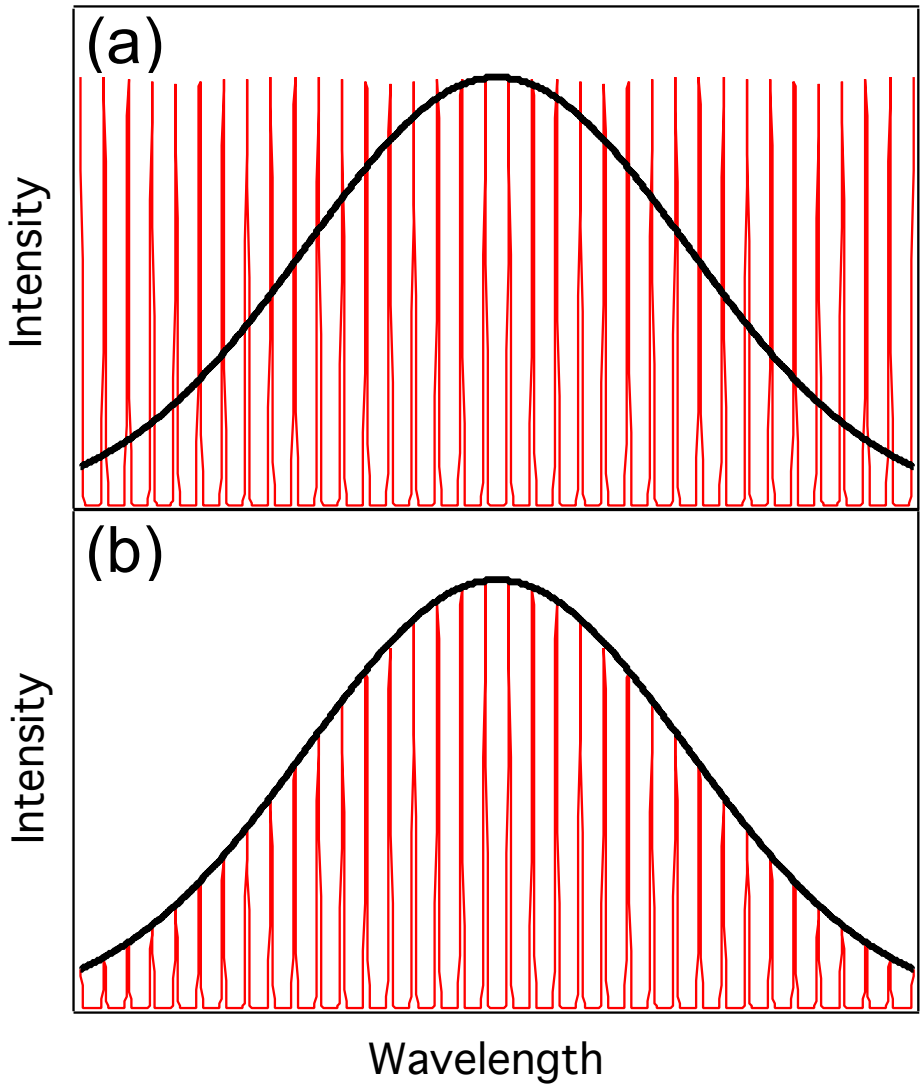

Figure 4.8: (a) The total number of longitudinal modes that can be stained in a laser cavity juxtaposed to the gain bandwidth of the active medium. Note in (b) how only the modes that fall in the gain bandwidth become amplified.

$$I(t) = |E_0|^2 \frac{\sin^2\left(N\frac{\Delta\omega t}{2}\right)}{\sin^2\left(\frac{\Delta\omega t}{2}\right)} \tag{4.16}$$

Comparing this intensity with that resulting from the summation of N incoherent, longitudinal modes, it is evident that such a form is akin to that of a wave packet. In addition, the intensity maximum for the above expression can be shown to behave as $I_{max} = N^2|E_0|^2$. As this compares to the case where each cavity mode possesses a random phase, one finds that a modelocked pulse has a max intensity that turns out to be greater by a factor of N. In order to better illustrate the differences that arise between coherently and incoherently summed waveforms, a side-by-side comparison is presented in Figure 4.9. Here, one of the more striking features is the clear formation of pulses in the intensity profile of Figure 4.9 (b) even for the coherent sum of relatively few sinusoidal functions. These pulses are characterized as having both a well defined separation difference $\Delta t = 1/\Delta\nu = 2\eta d/c$, as well as a temporal duration determined by

$$\Delta t_p = \frac{1}{N\Delta\nu} = \frac{1}{Bandwidth} \tag{4.17}$$

In other words, the broader the gain bandwidth, the shorter the pulse. Ultimately, such a finding is nothing more than a reiteration of the fundamental property of Fourier transforms. Thus, to make shorter and shorter pulses, one has to amplify over wider and wider bandwidths.

Figure 4.10 depicts a sketch of the Coherent Micra oscillator present in the Mannella lab [18]. Lasing occurs through excitation of a Ti:Sapphire (Ti^{3+}:Al_2O_3) crystal by a frequency doubled, Nd:YVO_4 pump laser centered at 532 nm. As expected from the above discussion, the broad gain bandwidth of the Ti:Sapphire allows for this system to be tuned from 680 nm to 1100 nm, making it ideal for the generation of ultrafast laser pulses. Given the typical repetition rate of this oscillator to be 80 MHz, the size of the cavity can be calculated to 1.87 m. From this length, it is then possible to provide an upper estimate for the number of longitudinal modes in the cavity. That is, by assuming a center wavelength of 800 nm, an impressive number of

$$n = \frac{2L}{\lambda} \approx 4.68 \times 10^6 \tag{4.18}$$

longitudinal modes will be simultaneously oscillating in the laser! In order to initiate

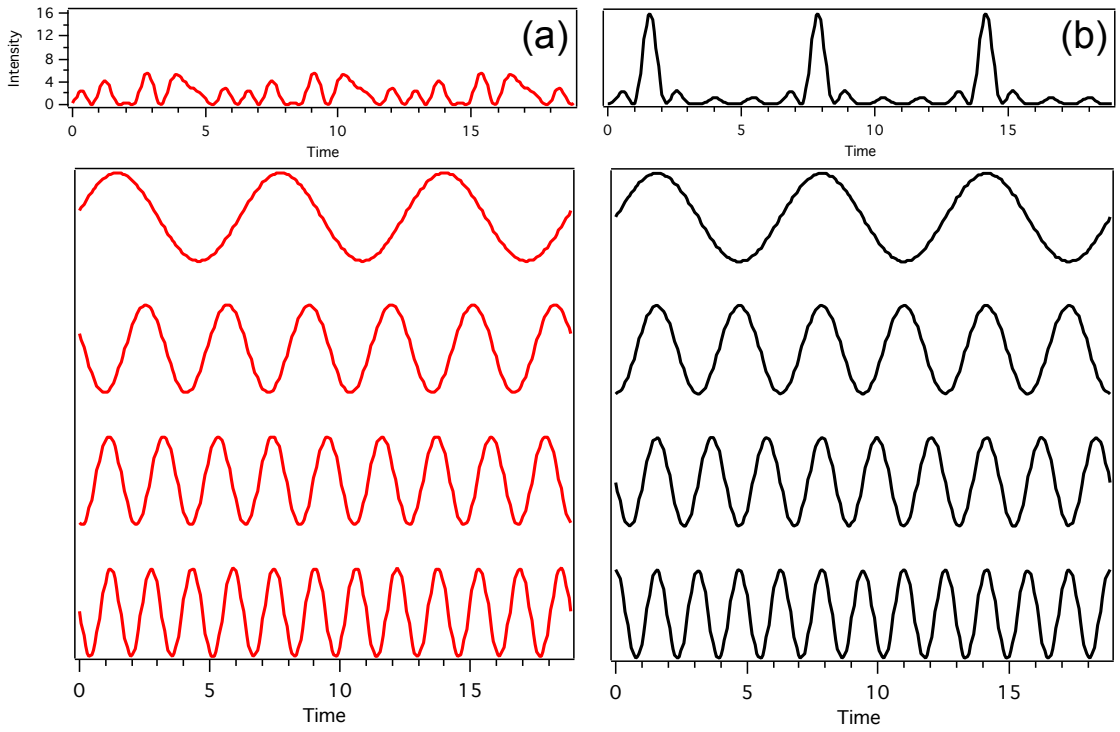

Figure 4.9: (a) incoherent and (b) coherent sum of N = 4 cavity modes. Note in (b) how even with relatively few number of modes a pulse starts to take shape

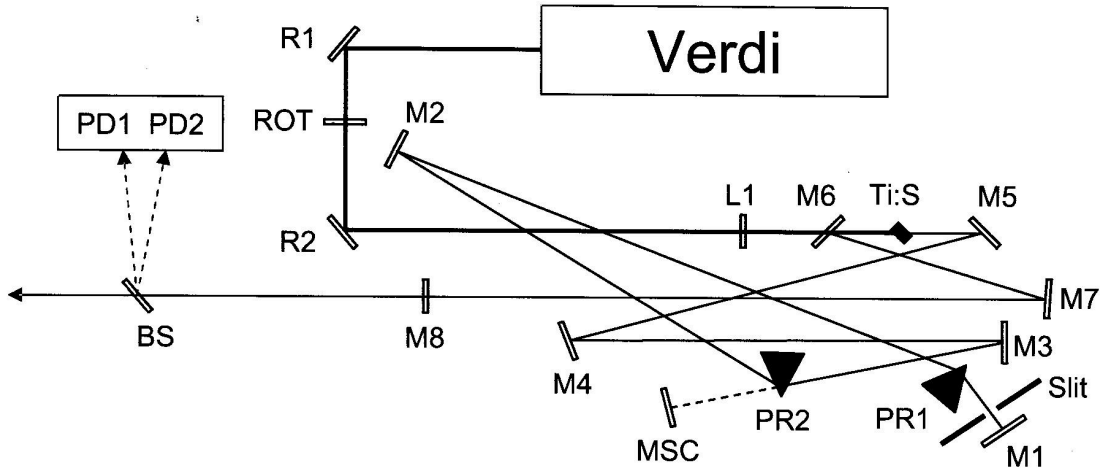

Figure 4.10: Schematic diagram of the Coherent Micra oscillator reproduced here from [18]

modelocking between these modes, the Micra takes advantage of a non-linear process known as the optical Kerr effect. Here, light of sufficiently high intensity can cause the refractive index $\eta(\omega)$ of a transparent optic to changes according to

$$\eta(\omega) = \eta_0(\omega) + \eta_2(\omega)I \tag{4.19}$$

where $\eta_2(\omega) > 0$. For a laser beam having a Gaussian profile, as in the TEM_{00} mode, the difference in intensity across the beam cross-section results in a self-focusing effect in which the higher intensity at the center induces a larger index of refraction as compared to that at the wings. This has the analogous effect as a biconvex lens. Recalling that the maximum intensity of a modelocked pulse to go as $I_{max} = N^2|E_0|^2$, as compared to $N|E_0|^2$ for incoherently summed cavity modes, this self-focusing effect will only occur for high intensity modelocked pulses. So, by placing an aperture after the Kerr lens that allows for the self- focused, modelocked beam to pass, but not a continuous wave (CW) beam, the laser cavity is then optimized for modelocking.

4.2.2 Pulse Compensation

Returning to Figure 4.10, one notes the presence of a pair of prisms whose role in the oscillator is to compress the pulse. In order to understand this detail it is worth noting that despite modelocking being a necessary condition for the generation of ultrafast laser pulses, it by itself is insufficient. That is, through modelocking, a pulse comprised of many wavelength components is produced, but ultimately what matters is that the timing between these components be precisely correct. Thanks to the wavelength dependence of the refractive index, when a broadband pulse travels through a transparent optical element the different wavelength components will travel with different group velocities. Such an effect, gives rise to a stretching of the pulse, which is commonly referred to as a chirp. To define a chirp more rigorously, consider the case where two separate light pulses, centered at ω_1 and ω_2, are directed towards a dispersive medium having $\eta(\omega_1)$ different from $\eta(\omega_2)$. If the two pulses are overlapped at $t = 0$, then their separation after time Δt will depend on the length L traveled through the medium and their difference in group velocities

$$\Delta t = \frac{L}{V_{G_1}} - \frac{L}{V_{G_2}} = L\left(\frac{dk}{d\omega_1} - \frac{dk}{d\omega_2}\right) \tag{4.20}$$

Expressed in another way, it is possible to write the time separation between the pulses in terms of the group velocity dispersion (GVD)

$$\Delta t = L\frac{d^2k}{d\omega^2}d\omega = L\frac{d}{d\omega}\left(\frac{1}{V_G}\right)d\omega = L\left(GVD\right)d\omega \tag{4.21}$$

Hence, the distance traveled through the optic and the GVD of the medium dictate what the separation difference between the two pulses will be. For most transparent optics, the refractive index follows a "normal dispersive curve" as shown in Figure 4.11. Such a curve corresponds to a positive GVD, which will produce a chirp in a broadband pulse resulting in the longer wavelengths leading the shorter wavelengths. By using predominately reflective optics, and ensuring all transparent optics to be thin, it is possible to avoid introducing more chirp into a compressed pulse. However, if the pulse is already stretched then the only way to remove a positive GVD is through the addition of a negative GVD. This is most commonly accomplished by the use of prism or grating compressors. As illustrated in Figure 4.12, a negative GVD can be introduced into the pulse by sending the leading wavelengths through a longer optical path. For a prism compressor, this is accomplished by sending the leading wavelength through more glass, and therefore a denser optical medium, while for a grating compressor it is the relative positioning of the gratings that is used to introduce a negative GVD. Within the Coherent laser system present in the Mannella lab, both prism and grating compressors are employed.

4.2.3 Chirped Regenerative Amplification

While the previous discussion focused on how to correct for chirping, there are actually certain circumstances where a chirped pulse is preferred. One such circumstance is in regenerative amplification. Here, the necessity of chirping the pulse prior to amplification stems from the fact that an ultrashort pulse has all its energy concentrated into fs packets. This can lead to a peak power as high as 10^{12} W, which is well above the damage threshold of most optics. Additionally, by having such high power per pulse, non-linear and multi-photon effects will likewise limit how much an ultrashort pulse can be amplified. Therefore, in order to amplify a fs pulse, a positive GVD that stretches the pulse to tens of picoseconds must first be introduced. Once the pulse has been stretched, it can then safely undergo amplification and be subsequently re-compressed to yield an ultrashort and intense light pulse.

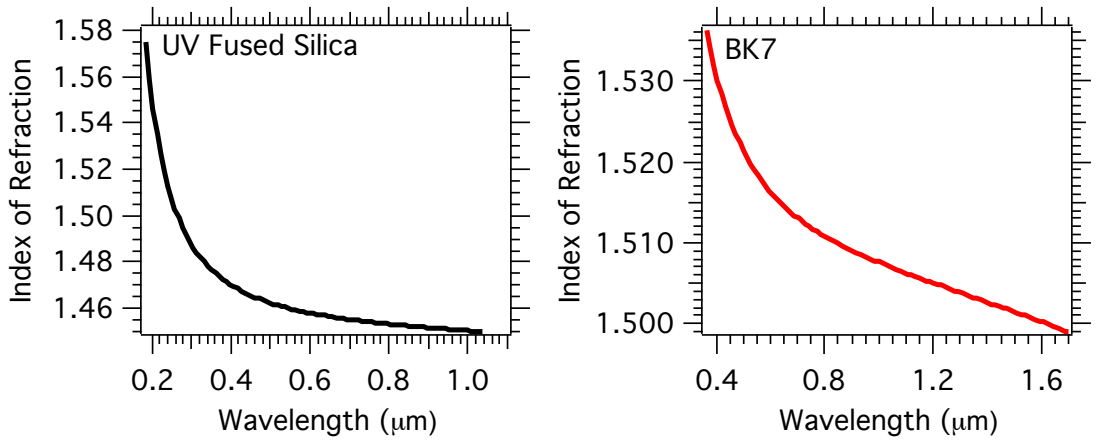

Figure 4.11: Normal dispersion curves of (a) UV used silica and (b) borosilicate glass plotted from data provided by Thorlabs website. Such glass is commonly used in optics and will introduce a positive chirp into an ultrashort pulse passing through the optic.

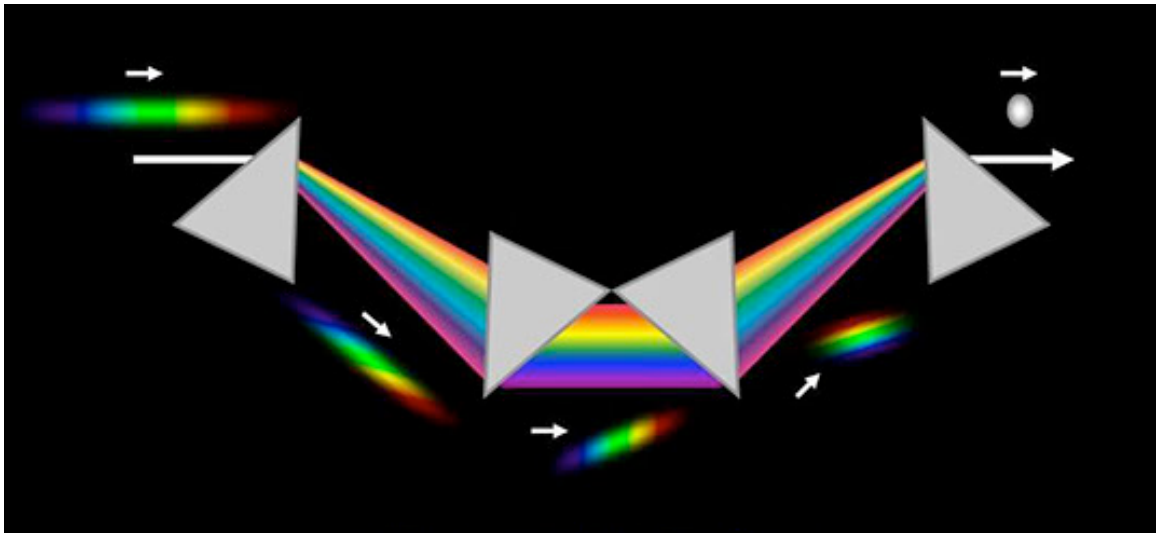

Figure 4.12: Simple illustration of a prism compressor reproduced here from [19]. In addition to prisms, pulse compensation can also be accomplished by use of other dispersive elements such as gratings

A diagram of the Coherent RegA 9050 amplifier found in the Mannella lab is shown in Figure 4.13 [20]. At the heart of this amplifier is a TeO_2 acousto-optical Q-switch. Prior to seeding with a chirped pulse, lasing inside the amplifier is held off so as to allow for a population inversion well above the lasing threshold to be reached. This is accomplished by keeping the amplifier cavity in a lossy, or low Q, state. To do so, a radio frequency generator is used to drive an ultrasonic wave in the TeO_2 glass. This wave will create a periodic strain in the medium, which, by the photoelastic effect, gives rise to a periodic modulation of the refractive index. Such a modulation will then act as a phase grating that serves to diffract the beam out from the cavity and therefore prevents lasing from occurring. While the cavity is in its low Q state, the Ti:Sapphire in the amplifier is being continuously pumped, which, thanks to the long lifetime of the upper state laser level (~2.5 μs), results in a significant population inversion in the crystal. Upon injection of the pulse, the radio frequency generator is cut off and the amplifier cavity is suddenly switched to a high Q state. This results in a high gain of the Ti:Sapphire medium and therefore allows for further amplification of the injected pulse with each pass through the amplifier. At peak amplification (22 round trips) the pulse is ejected from the amplifier by an acousto-optical cavity dumper and directed towards a grating compressor. After compression the final laser output is a 4 μJ, π-polarized pulse that is ~60 fs in duration.

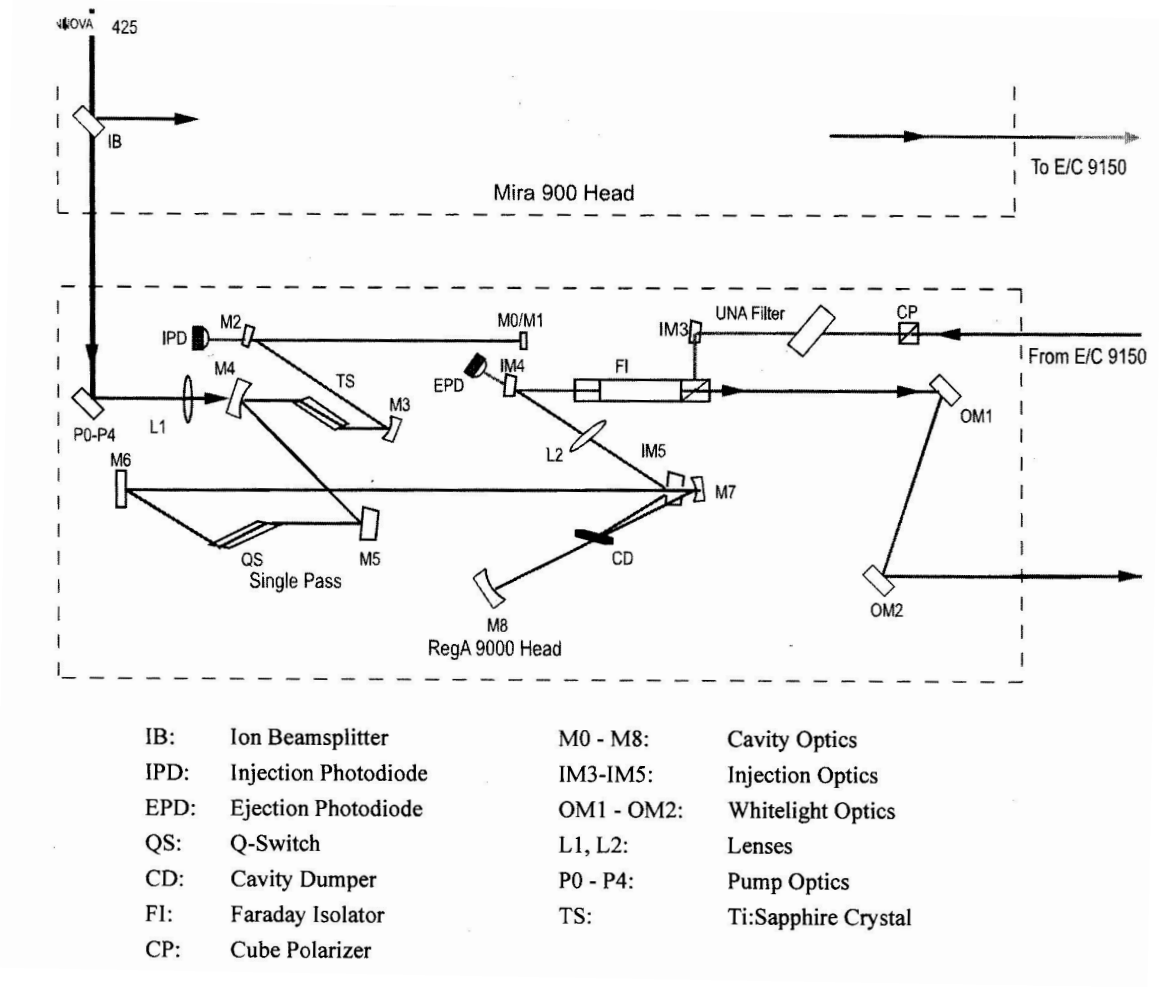

IB:	Ion Beamsplitter	M0 - M8:	Cavity Optics
IPD:	Injection Photodiode	IM3-IM5:	Injection Optics
EPD:	Ejection Photodiode	OM1 - OM2:	Whitelight Optics
QS:	Q-Switch	L1, L2:	Lenses
CD:	Cavity Dumper	P0 - P4:	Pump Optics
FI:	Faraday Isolator	TS:	Ti:Sapphire Crystal
CP:	Cube Polarizer		

Figure 4.13: Schematic diagram of the Coherent RegA 9050 chirped regenerative amplifier reproduced here from [20]

Chapter 5: Investigation into the Electronic Structure of $Cr_{1/3}NbS_2$

In Chapter 2, a clear motivation for studying the electronic structure of the chiral helimagnet and 3d intercalated transition metal dichalcogenide (TMDC), $Cr_{1/3}NbS_2$ was presented. While much of this discussion centered on broader concepts like the relation between spin-orbit coupling and the Dzyaloshinskii-Moriya interaction (DMI), such questions pertaining to the validity of the rigid band interpretation and the microscopic origin of the negative magnetoresistance can more readily be addressed. Therefore, it is the aim of this chapter to present results from electronic structure measurements on $Cr_{1/3}NbS_2$ that not only demonstrate the rigid band picture to be untenable, but provide evidence showing that spin ordering alone cannot explain the magneto-transport properties exhibited by this material. Seeing as such findings run counter to the more widely accepted understanding of this class of materials it is important to have in mind whether the surface measured reflects the electronic structure of the bulk crystal.

5.1 Surface Characterization

Generally speaking, it cannot be assumed that a surface cleaved *in-situ* will be representative of bulk. This can be attributed to the fact that surfaces will often relax or reconstruct so as to lower their free energy. Even without such processes, thanks to the fact that Cr atoms intercalate within the van der Waals gaps of NbS_2, through cleaving $Cr_{1/3}NbS_2$ it is entirely possible that both the ordering and stoichiometry of the remaining Cr atoms on the freshly exposed surface be different from that in bulk. Such a difference has important consequences on the electronic structure as it would imply a unique Brillouin zone or even doping of the topmost NbS_2 layer. Thus, before it can be reliably understood how Cr intercalation serves to modify the electronic structure of the parent NbS_2 compound, a complete characterization of the surface must first be performed. To do so, core level photoemission

(PES) is especially well suited as its sensitivity to the local electronic environment allows one to distinguish between spectroscopic features associated with surface verse bulk.

Keeping the crystal structure of $Cr_{1/3}NbS_2$ in mind, it is expected that a freshly cleaved surface be predominately S terminated with some residual Cr adatoms present. For this reason, we first investigated both the S 2p and Cr 2p core level PES spectra for signatures of different chemical environments associated with surface verse bulk. As can be seen from Figure 5.1 (a), the S 2p spectrum consists of three main structures, indicating the presence of more than one component. The spectrum is fit well by two doublets, where each doublet accounts for the spin orbit separation of the $2p_{1/2}$ and $2p_{3/2}$ core levels. From the fit, both the energy separation and the relative intensities of the peaks in each LS doublet were constrained to be the same. In seeing all S atoms lie in the same crystallographic site for the $x = {}^1/_3$ stoichiometry, the presence of two doublets cannot be attributed to inequivalent S sites. Rather, the large ($\approx$ 1eV) difference in binding energy between the pair of doublets suggests that the spectrum can be attributed to S having two distinct chemical environments associated with surface and bulk. Specifically, in seeing that the S 2p spectrum was measured at normal emission, the more prominent doublet at higher binding energy likely originates from S atoms bonded to the Cr intercalant as is expected from bulk. In contrast, due to a difference in coordination number, the lower binding energy doublet must then originate from surface S atoms possessing a lower coordination, thanks to an absence of surface Cr atoms removed by sample cleave. A similar assignment was made for the S 2p spectrum reported for Fe_xNbS_2 [140].

In much the same manner, it is expected that the Cr core level spectra likewise exhibit lower binding energy components owing to presence of surface Cr atoms having a lower coordination than in bulk. However, as shown in Figure 5.1(b), the Cr 2p core level spectrum does not exhibit a clear indication of such a surface component, despite the fact that this deeper core level was measured with the same photon energy as was used for the S 2p in Figure 5.1 (a). Put another way, for a fixed photon energy, the kinetic energy of a photoelectron coming from a deeper core level will be lower than that from a shallower core level making the former a more surface sensitive measurement. That being said, the spectrum in Figure 5.1(b) consists of three main peaks, labeled as A, B, and C. Peak C is a loss feature, and is observed in all of the other core level spectra measured in this study. Its value of 24 eV is consistent with the value assigned to a plasmon loss in Fe_xNbS_2 [140] and is therefore assigned as the same in this study. Peaks

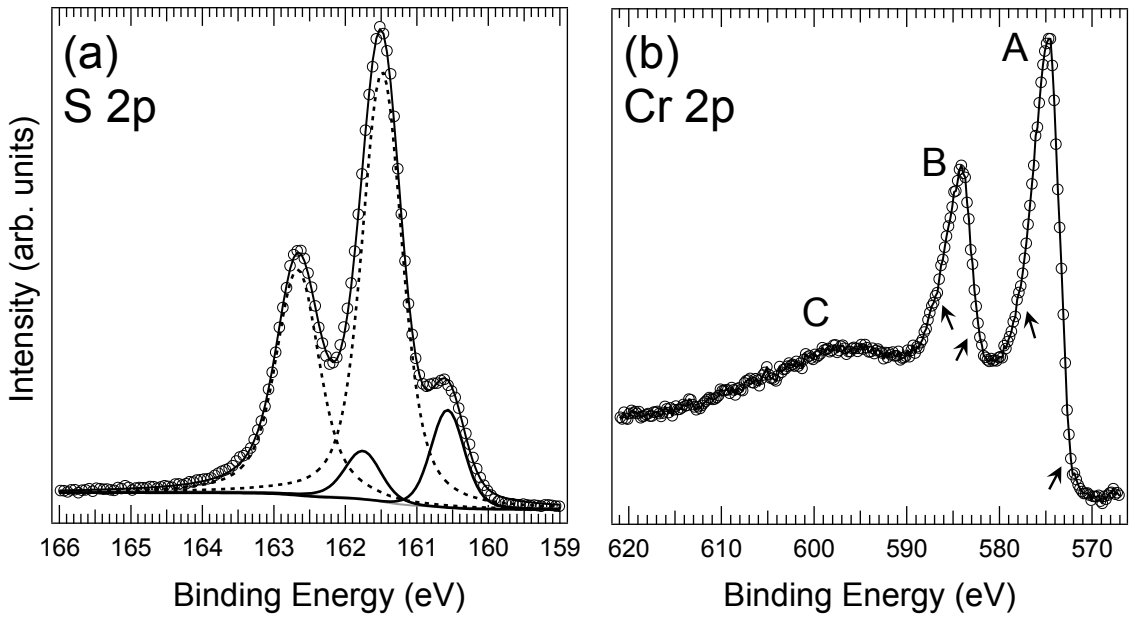

Figure 5.1: a) S 2p core level spectrum taken at normal emission from *in situ* cleaved $Cr_{1/3}NbS_2$ with hν = 918 eV. The BE separation between the doublet originating from the surface (solid line) and the deeper layers (dashed line) amounts to ~1 eV. (b) Cr 2p core level recorded at normal emission with hν = 918eV. Key features include a spin orbit split doublet (A, B), and a loss feature (C). The arrows indicate kinks in the line shape of features A and B.

A and B correspond to the spin-orbit split doublet of the Cr 2p core level.

While both peaks are intrinsically broad, owing to the fact that deeper core levels to have a shorter core hole lifetime, it is evident by the kinks in the lineshape that peaks A and B consist of more than one component. Addressing first the kinks at higher binding energies, such features are likely attributed to the presence of correlation satellites, such as charge transfer satellites, owing to the more localized environment of the Cr atom. This assignment was ultimately made based on consideration that no oxide contamination could be identified in the survey spectrum and that similar findings have been observed in the core levels of several other 3d intercalated 1T-TiS_2 compounds [141]. Conversely, by following similar arguments as above, the kinks in the lineshape on the low binding energy side of each peak are consistent with the presence of a surface component. Furthermore, based on the position of such kinks, there is the possibility that surface Cr have a lower valence as compared to bulk [142]. Unfortunately, due to the fact that the Cr 3s multiplet sat on a nearby loss feature of the Nb 4s, it was difficult to assign the particular valence of surface verse bulk from fitting. For this same reason, no attempt was made to fit the Cr 2p spectrum due to its complicated nature.

On the basis of core level PES, there is a clear indication that the *in-situ* cleaved surface of $Cr_{1/3}NbS_2$ is predominately S terminated. However, on the basis of these measurements, it remains unclear as to how much Cr remains on the surface following sample cleave, let alone if such Cr is atomically ordered. Thus, to gain additional insights both Low Energy Electron Diffraction (LEED) and Scanning Tunneling Microscopy (STM) experiments were performed. The STM image shown in Figure 5.2(a) reveals two distinct surfaces types. While some locations on the terraces are atomically flat, most of the areas have a much higher corrugation. We refer to these two types of terraces as smooth and rough, respectively. The difference in corrugation between the two distinct areas is best illustrated by the line profile corresponding to the dashed line in Figure 5.2(a). Here, the line profile shown in Figure 5.2(b) reveals a terrace step height of 0.61nm, with lower corrugation seen on the left (smooth area), and higher corrugation on the right (rough area). Based on the crystallographic lattice parameters of this material [5], such a step height is consistent with the separation distance between NbS_2 planes.

While both the rough and smooth areas share the same base line, the rough area exhibits spikes of several angstroms. Atomic scale images of the two areas shown in Figures 5.2(c),(d) reveal a hexagonal period in the atomic resolution image of the smooth area that is around 0.566

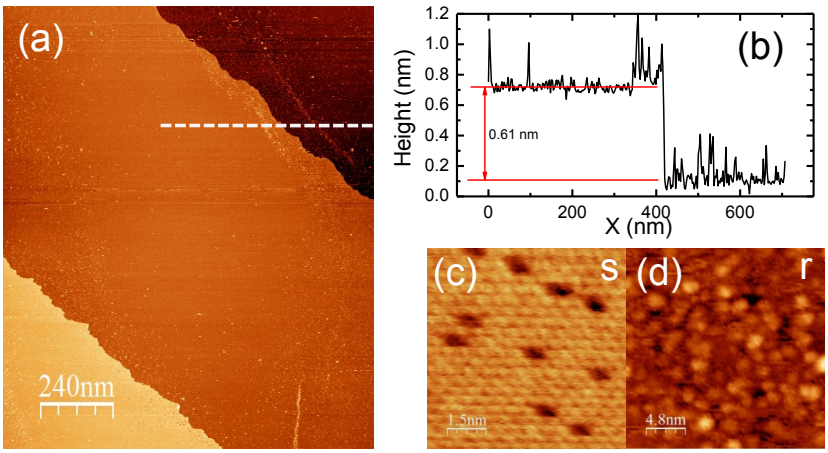

Figure 5.2: (a) STM image of *in situ* cleaved $Cr_{1/3}NbS_2$ single crystals taken with a bias voltage of -0.4V illustrating the large-scale surface morphology. (b) Line profile along the broken line in a) reveals a terrace step height of 0.61 nm with high corrugation near the step edge. (c,d) Atomic resolution images of the (c) "smooth" and (d) "rough" areas denoted by s and r respectively.

nm (Figure 5.2(c)). This value is consistent with the unit cell dimension of bulk $Cr_{1/3}NbS_2$, where Cr atoms order in a ($\sqrt{3}a \times \sqrt{3}a$) superstructure. In contrast, the atomic resolution image of the rough area shows no such periodic order (Figure 5.2(d)). Hence, based on what is known from core level PES and crystal structure, we identify the rough areas as comprised of disordered, residual Cr adatoms remaining on the surface following sample cleave, while the smooth areas are Cr free, S terminated planes. From this assignment, the fact that lattice constant measured corresponds to that of $Cr_{1/3}NbS_2$ and not the 0.333 nm expected for NbS_2 can be attributed to the fact that Cr ordering below the surface NbS_2 plane can produce a superstructure contrast in STM images of the surface through charge transfer modification of the local density of states [143]. Thus, despite the ordered Cr residing beneath the surface in the van der Waals gaps, the presence of the intercalant can still influence the local electronic environment at the surface. Taken as a whole, the results from real space imaging show that on average, there is a Cr deficiency on the surface as compared to the completely filled ($\sqrt{3} \times \sqrt{3}$)*R*30° Cr superlattice in bulk, and what Cr that does remain is loosely bound possessing no periodic order.

These STM results are corroborated by the findings from LEED collected with a systematic variation of electron beam energy. Notably, the LEED data are consistent with the absence of a ($\sqrt{3} \times \sqrt{3}$)*R*30° Cr superstructure at the surface of cleaved $Cr_{1/3}NbS_2$. Here, a representative LEED pattern taken with a beam energy $E_B = 215$ eV is shown in Figure 5.3. From this image, the intense spots corresponding to the 1×1 periodicity of the NbS_2 lattice, and weaker ($\sqrt{3} \times \sqrt{3}$)*R*30° superstructure spots attributed to Cr ordering can be seen. Given the ($\sqrt{3} \times \sqrt{3}$)*R*30° spots to possess a smaller reciprocal lattice vector compared to the 1×1, it is expected that these spots enter the field of view of the screen well before the 1×1. However, the opposite behavior is observed. Namely, while the 1×1 spots can be found at the border of the screen for $E_B = 60$ eV, the ($\sqrt{3} \times \sqrt{3}$)*R*30° spots do not become visible with any significant intensity until $E_B > 80$ eV. This observation can be rationalized by recognizing that with increasing electron beam energies the probing depth of the LEED experiment is increased. That is, for low beam energies the experiment is more surface sensitive and only the 1×1 NbS_2 termination is observed, whereas at higher beam energies the electron beam diffracts off of structures deeper below the surface, such as the ($\sqrt{3} \times \sqrt{3}$)*R*30° Cr superstructure present in the bulk. Hence we conclude that the observed ($\sqrt{3} \times \sqrt{3}$)*R*30° superstructure is located below the

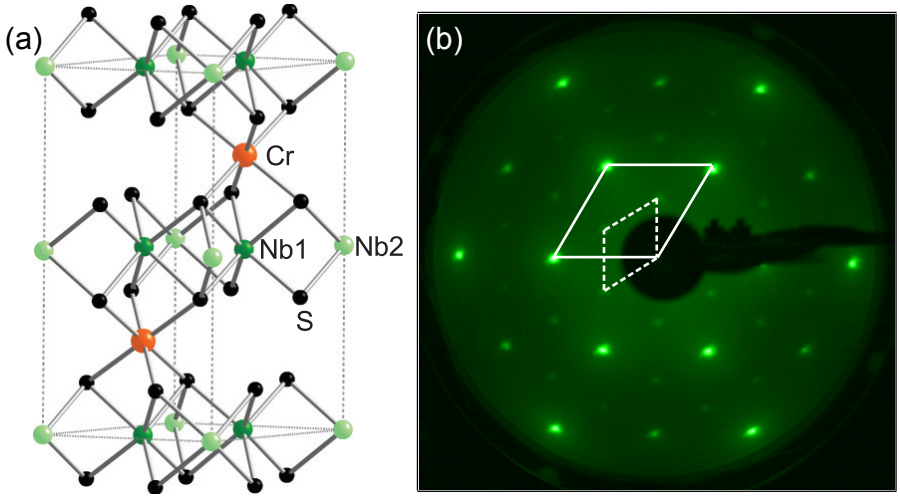

Figure 5.3: (a) Unit cell of $Cr_{1/3}NbS_2$ taken from [5]. (b) Representative LEED image obtained from $Cr_{1/3}NbS_2$ with an electron beam energy of 215 eV. The unit cell of the 1×1 (solid) and $(\sqrt{3}\times\sqrt{3})R30°$ (dotted) reciprocal lattice are indicated.

surface plane and is representative of Cr ordering in the bulk.

As this finding relates to measurements of the electronic band dispersion using surface sensitive techniques like Angle Resolved PhotoEmission Spectroscopy (ARPES), it is clear from Figure 5.4 that despite the presence of disordered Cr adatoms on the surface, the ARPES data are of high quality, and reveal the presence of dispersing bands. However, a closer inspection of the image plot in Figure 5.4(a) reveals several non-dispersing states with approximate energies of 1.5 eV, 1.0 eV, 0.5 eV and 0.25 eV below E_F. These states can be more clearly seem in Figure 5.4(b) from the stacked Energy Distribution Curves (EDC), which show photoelectron intensity plotted for fixed momenta as a function of energy. Based upon the findings of core level PES, STM and LEED, these non-dispersive states likely originate from the remaining Cr adatoms randomly distributed on the surface. As would be expected, such states are found to show no dispersion with photon energy—a characteristic indicative of surface states—and are enhanced under certain measuring conditions such as when the photon polarization is contained in the sample plane, or when the photon energy is tuned across a Cr resonance.

Further confirmation that the non-dispersive states observed in ARPES originate from residual surface Cr atoms comes from Resonant PhotoEmission Spectroscopy (ResPES). In a ResPES experiment, the incident photon energy is tuned across the absorption edge of a deeper core level of an atom [17,118,144]. As discussed in section 3.1.4, from such a measurement PES spectra of the valence band (VB) develop an elemental sensitivity as the portion of the VB associated with the resonating energy level(s) is enhanced. In this way, it is possible to identify the contribution originating from a select element in the total VB structure. As shown in Figures 5.5(b),(c), when the photon energy is tuned across the Cr L_3-edge there is a marked enhancement of a narrowly defined state in the VB $\approx$ 1.5 eV below E_F. From selection rules, by tuning the energy across a 2p absorption it follows that the corresponding resonant channel must then belong to the Cr 3d manifold. Importantly, this resonance was observed for the photon polarization being parallel to the sample plane, and with the photon energy tuned in proximity of the shoulder located on the low energy side of the XAS spectrum (Figure 5.5(a)). From our previous findings, this would suggest that the low energy shoulder in the Cr XAS spectrum originates from non-periodically ordered Cr at the surface. Consequently, the resonance of the narrow state 1.5 eV below E_F most likely corresponds to the same non-dispersive states seen in

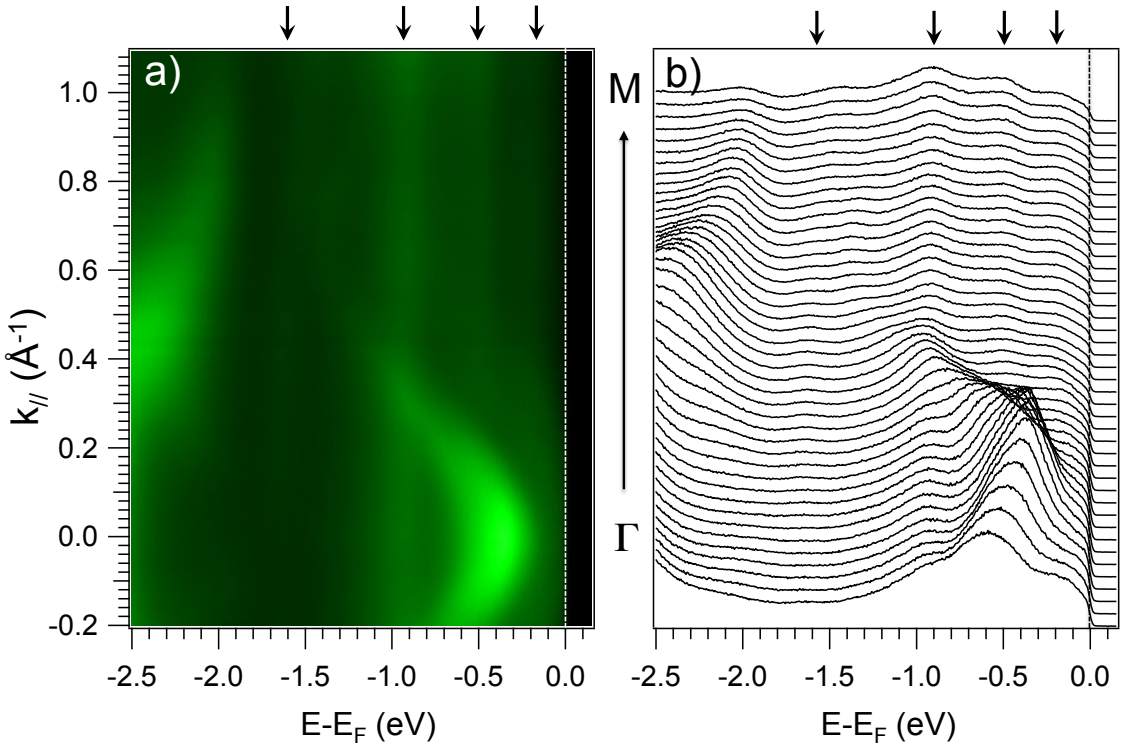

Figure 5.4: High resolution ARPES spectra taken from $Cr_{1/3}NbS_2$ with σ-polarized photons of energy hν = 48eV. Non-dispersive surface states are indicated by arrows in both the a) image plot and b) stacked EDCs.

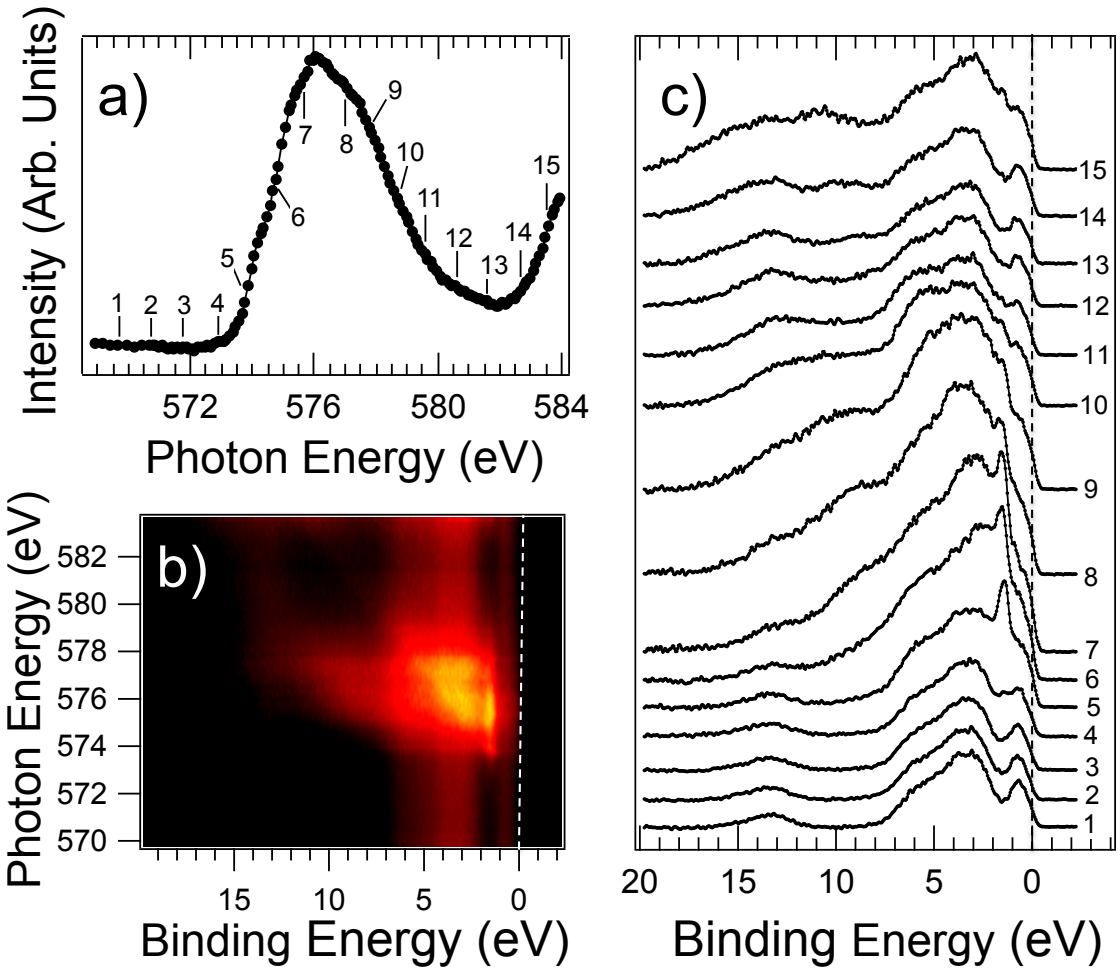

Figure 5.5: ResPES measured from $Cr_{1/3}NbS_2$ across the Cr L_3 absorption edge with photon polarization contained entirely in the sample plane. (a) Cr L_3 XAS measured in total electron yield. (b) ResPES image plot and (c) representative line profiles extracted at the corresponding photon energies labeled in (a).

the ARPES spectra. In fact this has been subsequently confirmed by collecting ARPES spectra across the Cr L_3 resonance.

From Figure 5.4, it appears that the only affect that the presence of non-periodically ordered Cr adatoms has on the ARPES spectra is in giving rise to non-dispersive surface states. However, by removing a fraction of Cr atoms by cleaving, it is possible that not only the ordering, but also the stoichiometry at the surface be different from that in the bulk. Seeing as the Cr intercalant serves to donate electrons to Nb-derived bands, having a difference in surface Cr could lead to a doping in the top-most NbS_2 layer that is different from that in the bulk. Thus, in order to address whether conventional ARPES experiments can be used to study the true bulk electronic structure of $Cr_{1/3}NbS_2$, a direct comparison between spectra collected at different probing depths must be made. Ideally this could be assessed by performing a Luttinger count on Fermi surface (FS) maps taken at increasingly higher photon energies into the soft-X-ray regime. Unfortunately, due to the low photoelectron cross-sections at such high photon energies, a full FS map having adequate statistics cannot be feasibly measured. As an alternative, we report here, cuts of the band dispersion measured from $h\nu$ = 40 eV through $h\nu$ = 736 eV with the hope of determining whether changes in the Fermi crossing points can be taken as indication for a difference in doping at the surface.

The results of this experiment are presented in Figure 5.6, which shows a comparison between ARPES image plots taken along the ΓK direction using conventional ($h\nu$ = 40 eV, Figure 5.6(a_1)), and soft x-ray photon energies ($h\nu$ = 196 eV, 401 eV, 736 eV in Figures 5.6(a_2), 5.6(a_3), and 5.6(a_4), respectively). In this case, after having measured an inner potential of 14 eV, such energies were chosen so as to yield the same $k_z = 0$ value in the reduced zone scheme. By doing so, any difference observed in the dispersion can be attributed to changes occurring with probing depth and not simply a consequence of k_z dispersion. With that being said, the estimated probing depths that will correspond to the above photon energies are computed to be 23 Å, 32 Å, and 44 Å. Unfortunately, such an increase in probe depth comes at the price of a poorer energy and momentum resolution. Namely, the overall energy resolution can be estimated to be ≈ 53 meV, 139 meV, and 250 meV, while the corresponding momentum resolution will be ≈ 0.18 $Å^{-1}$, 0.27 $Å^{-1}$, and 0.36 $Å^{-1}$, respectively. To a first approximation, the worsening of the energy and momentum resolution at higher photon energies manifest in the image plots as a smearing of spectral features. This is especially true for the spectrum obtained

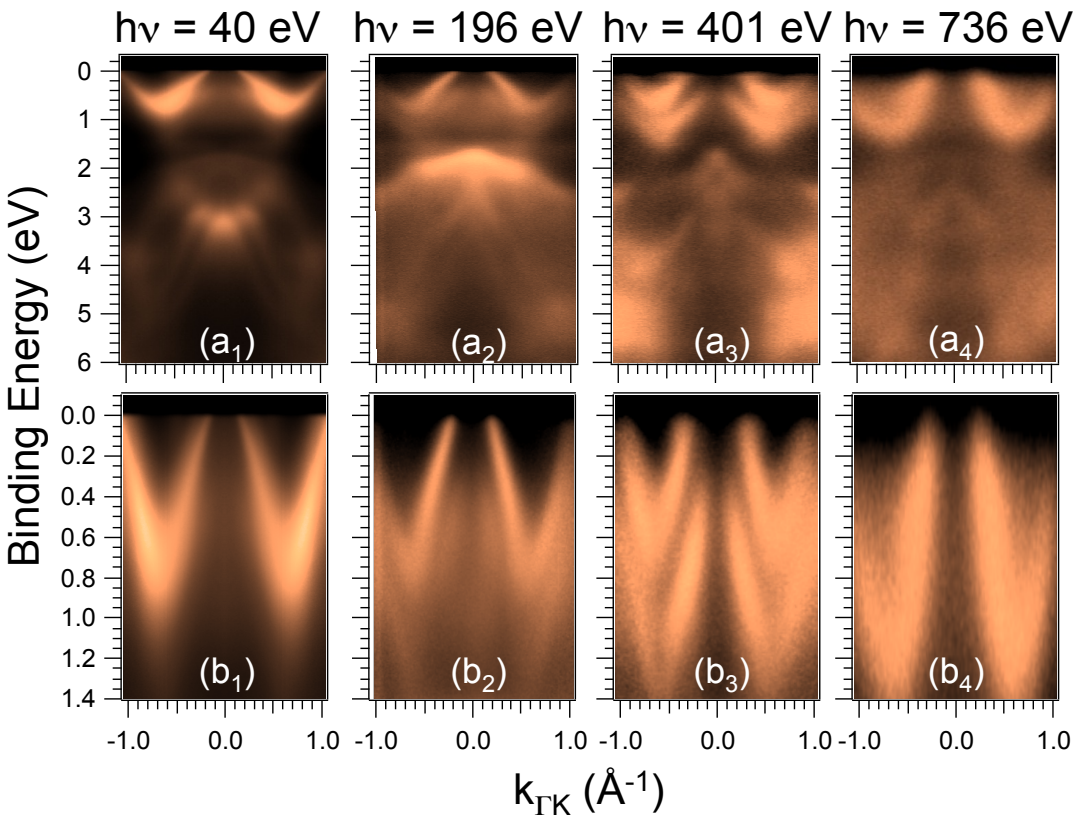

Figure 5.6: ARPES spectra measured from $Cr_{1/3}NbS_2$ along the ΓK direction over a wide (a_1-a_4) and narrower (b_1-b_4) binding energy range using photon energies hν = 40 eV (a_1, b_1), hν = 196 eV (a_2, b_2), hν = 401eV (a_3, b_3) and hν = 736 eV (a_4, b_4). Spectra at hν = 40 eV has been symmetrized with respect to the Γ point.

at hν = 736 eV (Figures 5.6(a_4),(b_4)), where the poorer energy resolution has the effect of smearing the image especially along the energy axis, giving the appearance of only a single broad band near E_F. However, despite this worsening in resolution it is important to note that it is still possible to identify the same dispersing features in the spectra irrespective of the photon energy used.

That is, while the resultant smearing due to poor resolution renders a comparison between the image plots not immediate, inspection of the corresponding EDC and MDC stacks shown in Figure 5.7 reveals there to be similar spectral features in all the data collected at high energies. Most notably, two bands are clearly seen in the EDC stacks taken at hν = 40 eV (Figure 5.7(a_1)), hν = 196 eV (Figure 5.7(a_2)) and hν = 401 eV (Figure 5.7(a_3)), while the asymmetric lineshape of the EDCs in Figure 5.7(a_4) indicates that the signal originating from this spectra is comprised of the same bands observed at lower energies, but smeared due to a loss of resolution. As can be seen from both the image plot and EDC stack in Figures 5.6(b_3) and 5.7(a_3), the relative intensity of the lower lying band increases for the spectra taken with hν = 401 eV as compared to that obtained with conventional ARPES energies. Noting, however, by inspection of the EDC stacks in Figure 5.7(a_1) that this lower band is still present in the hν = 40 eV spectra, it is likely that the progressive increase in relative intensity of this band at higher photon energies comes about due to matrix element effects, rather than being indicative of differences in the electronic structure corresponding to different sampling depths. Therefore, on the basis of these findings, it appears at least qualitatively there is no significant differences in the electronic structure as a function of probe depth.

More rigorously, if there is a difference in stoichiometry of the surface Cr that would lead to a doping in the top-most NbS_2 layer that is different from bulk, then it is expected that the Fermi crossing points determined from the MDCs show some kind of systematic trend with increased probing depth. In this case, thanks to a slight but noticeable sample misalignment, we specifically focus on the band crossings in proximity to the Γ point. As shown in Figure 5.8, from the MDCs extracted at E_F, there are three main structures, labeled as α, β_1, and β_2, that can be identified in the low energy data (hν = 40 eV). The curves become much broader for higher photon energies, consistent with the worsening of momentum resolution. Taking the latter into account, the data taken with hν = 196 eV are in good agreement with the hν = 40 eV data as far as structures α and β_1 are concerned. On the contrary, structure β_2 is not visible. Its presence is,

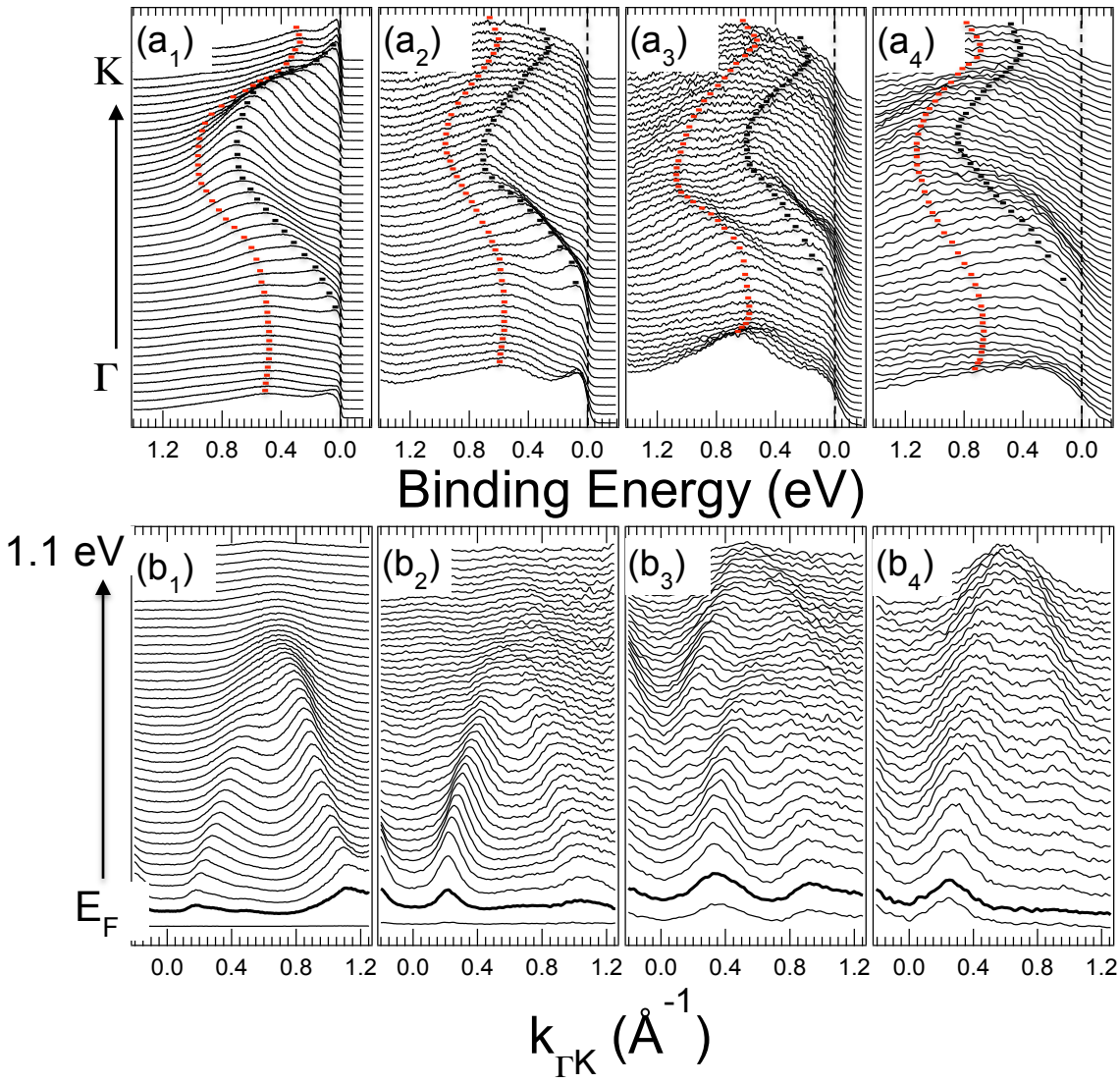

Figure 5.7 Stacked EDCs (a_1-a_4) and MDCs (b_1-b_4) along the ΓK direction extracted from the corresponding image plots depicted in Figure 5.6 b_1-b_4. Tick marks tracing the dispersion of the two bands in proximity to E_F have been added to the EDC stacks in a_1-a_4 as a guide to the eye. In the MDC stacks, the MDC at E_F is denoted with a thicker line.

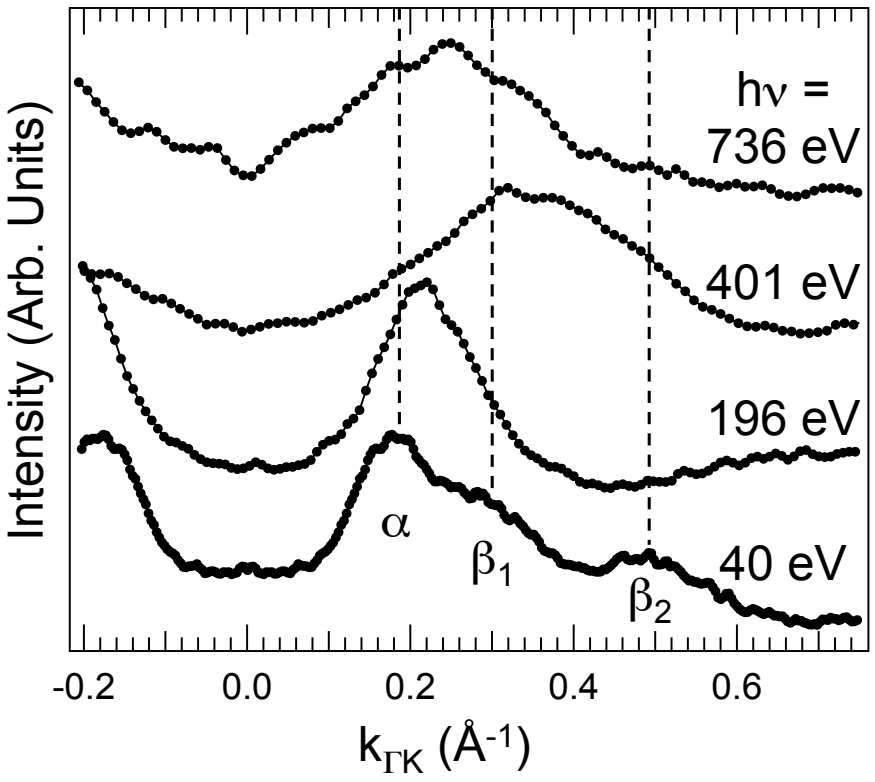

Figure 5.8: Direct comparison of MDCs extracted at E_F for hν =40 eV, 196 eV, 401 eV and 736 eV depicting k_F crossings about Γ. Features from the hν = 40eV spectra are labeled α, β_1, and β_2 for the purpose of comparisons. For a description of this notation, see text.

however, fully consistent with the data taken with hν = 401 eV. At this energy, the intensity at the momentum corresponding to structure β_2 is comparable to that of structures α and β_1, and cannot be accounted for by a broadening of the hν = 196 eV data. Conversely, the intensity of the data taken with hν = 736 eV is again higher for the momentum corresponding to structures α and β_1, while the intensity in at β_2 is now suppressed. From this, it is evident that the difference in spectral weight of the various crossing points shows no clear monotonic trend. Similarly, based on the location of the Fermi momenta assigned from the spectra collected with hν = 40eV, there is no significant shift in the Fermi crossing point occurring with increasing photon energy.

Consequently, despite a fraction of Cr being removed with the sample cleave, the fact that the Fermi crossing does not change with increasing probing depth implies a nominal half coverage on the topmost NbS_2 layer. While it has been established that such Cr is not periodically ordered, and will therefore give rise to non-dispersive surface states in the ARPES spectra, it is still capable of donating electrons to Nb bands. By doing so, under a nominal half coverage it is expected that there then be no difference in the doping of the topmost NbS_2 layer meaning that the salient features of the electronic structure revealed by low energy ARPES, such as bands dispersion and Fermi momenta, are not significantly modified as compared to the bulk.

5.2 Comparison of $Cr_{1/3}NbS2$ and NbS_2

In having established from the previous section that electronic structure measurements of *in-situ* cleaved $Cr_{1/3}NbS_2$ can be used to reliably measure how intercalation serves to modify the host NbS_2 compound, we turn our attention now towards addressing the validity of the rigid band picture in this class of materials. As was previously discussed, the rigid band picture is the most common interpretation used in rationalizing intercalant-induced modifications of the host electronic structure [59,80]. By testing the validity of this picture, new insights can be gained into not just the electronic structure but the magnetism and magneto-transport properties as well. Namely, the assignment of spin ordering as the origin of the negative magnetoresistance in this material turns out to be fully consistent with a rigid band interpretation. This is due to the fact that the rigid band picture stipulates that intercalant atoms act as a charge reservoir donating electronic charge, with the effect of raising the chemical potential, without altering the overall FS and band topology of the host material. Thus, following donation of electrons to Nb-derived

bands, the remaining electrons on the Cr site will simply form local spin moments that are coupled to neighboring sites through conduction electrons. By calling this picture into question, the whole microscopic basis for understanding the coupling between the magnetic and transport degrees of freedom in this material then changes. Thus, we begin with a direct comparison of core level PES and ARPES measurements taken on NbS_2 and $Cr_{1/3}NbS_2$.

The integrated VB, S 3s, and Nb 3d PES core level spectra are shown in Figure 5.9. The VB exhibits three main structures, which in $Cr_{1/3}NbS_2$ are shifted by ≈ 0.4 eV to higher binding energy. Seeing as the same shift occurs for the shallow S 3s core level (Figure 5.9(a)), this suggests that the chemical potential does increase in NbS_2 upon Cr intercalation. In contrast, the Nb 3d core level shows no such shift, but as can be seen from Figure 5.9(b), there is a change in its lineshape. Namely, the satellite peaks at higher binding energy present in the Nb 3d spectrum become strongly suppressed when Cr is intercalated. Noting such components to be absent from the Nb 3p spectrum, we exclude the possibility that they arise due to oxidation or contamination. Rather, the difference in the lineshapes indicates that Cr intercalation alters the local electronic environment of the Nb atoms. In agreement with the conclusions reported in similar studies on Fe_xNbS_2 [140], the two components in the spectra are indicative of different screening channels identified as the well-screened, and poorly-screened peaks. The suppression of the poorly screened satellite in favor of the well-screened main peak in $Cr_{1/3}NbS_2$ is then consistent with the fact that charge donation, resulting from intercalation, increases the number of available carriers capable of screening a resultant hole in the NbS_2 layer.

From the ARPES image plots depicted in Figure 5.10, there appears to be no significant difference in the band structure of NbS_2 and $Cr_{1/3}NbS_2$ beyond that of the same ≈ 0.4 eV shift. Using band structure calculations for bulk NbS_2 as a guide to compare with our ARPES results [145], it becomes evident from the EDC stacks in Figure 5.11(a_1),(a_2) that two bands are found to cross E_F at both the Γ and K points of the host compound. Based on what is known of the electronic structure for this compound, these two bands are identified as the bilayer split Nb 4d bands. Regarding $Cr_{1/3}NbS_2$, given its apparent similarity to the band structure of NbS_2, we can trace the same two bands in the EDC stacks of Figure 5.11(b_1),(b_2). Here, due to a shift in the chemical potential, the upper band is found to have a well-defined Fermi crossing in the vicinity of the Γ and K points, while the lower band sinks to ≈ 0.2 eV below E_F. In the rigid band

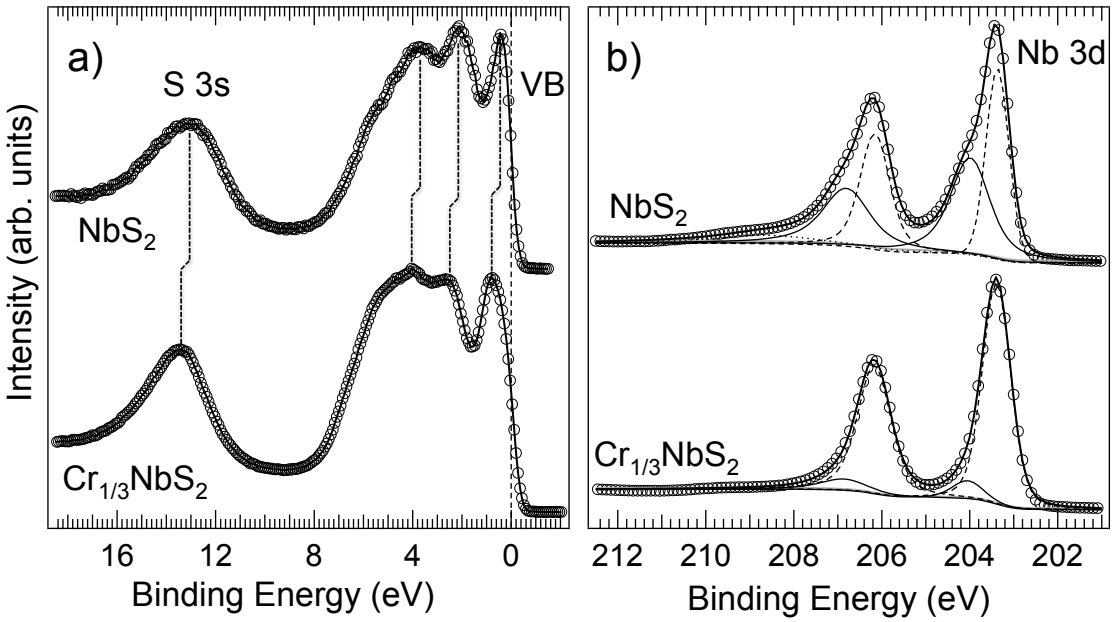

Figure 5.9: Comparison of (a) valence band and (b) Nb 3d PES spectra for NbS_2 (top) and $Cr_{1/3}NbS_2$ (bottom) as measured at normal emission with hν = 750 eV. From (a), a comparison of similar features in the VB as well as the shallow S 3s core level demonstrates a 0.4 eV shift towards higher binding energy. The suppression of the higher BE peaks of the Nb 3d doublet (solid line) observed in $Cr_{1/3}NbS_2$ is visible in (b).

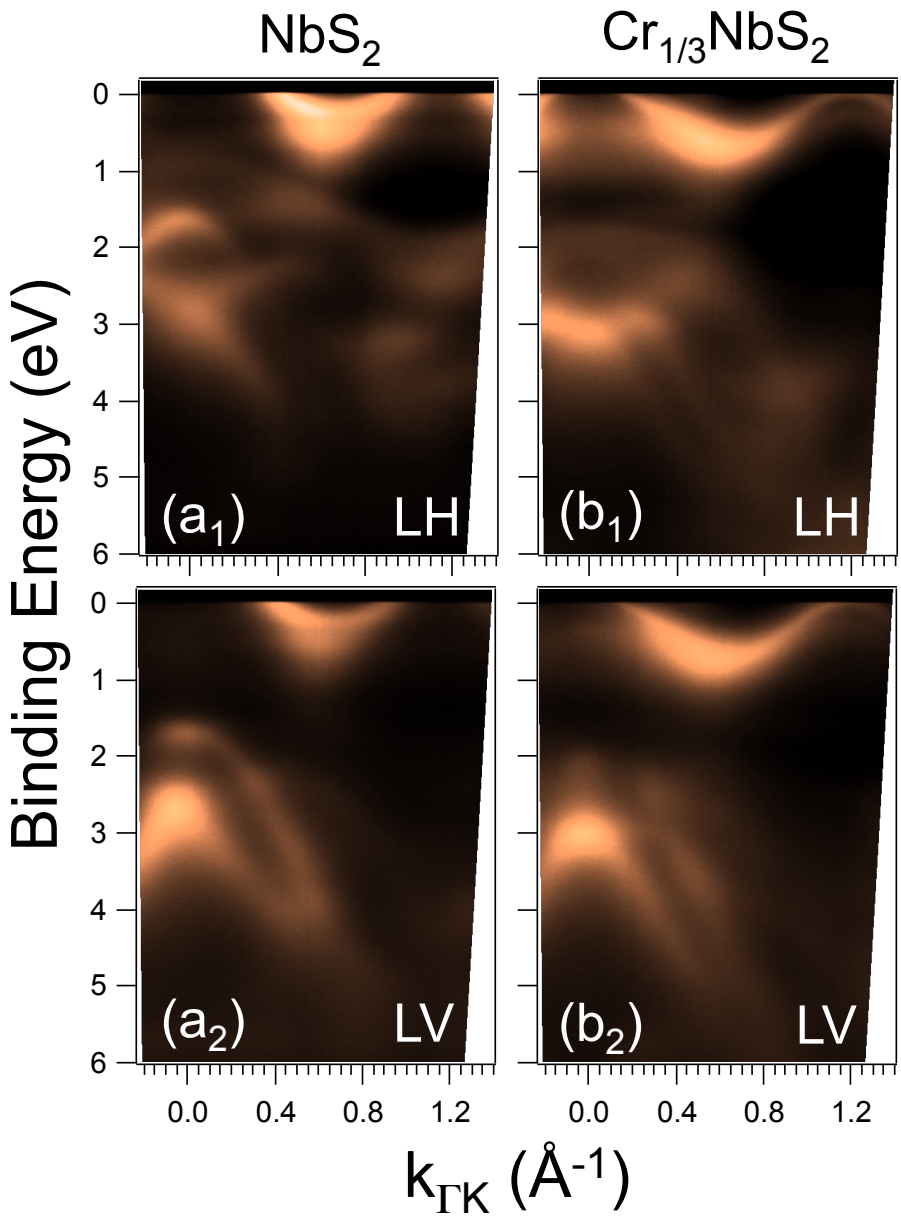

Figure 5.10: Band dispersion of ((a_1),(a_2)) NbS_2 and ((b_1),(b_2)) $Cr_{1/3}NbS_2$ measured along the ΓK direction over a wide BE range using hν = 40eV photons having a polarization horizontal ((a_1), (b_1)) or vertical ((a_2),(b_2)) with respect to the scattering plane.

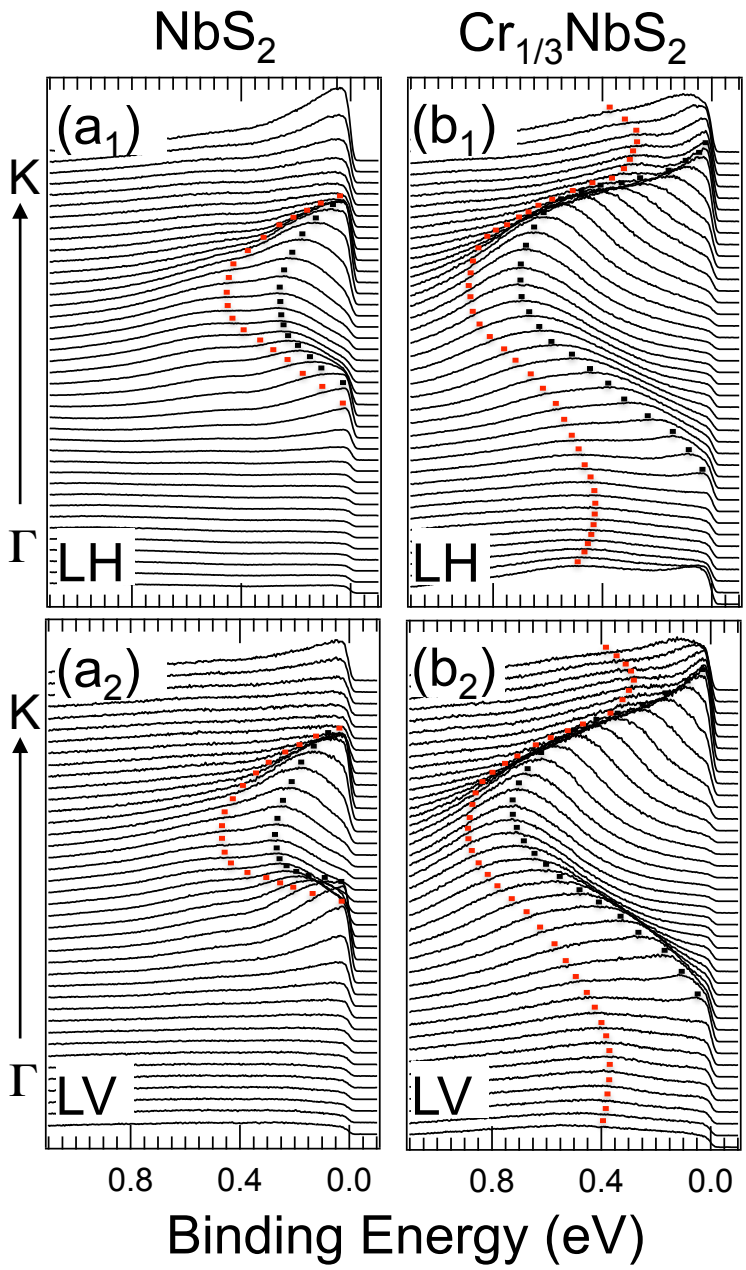

Figure 5.11: Stacked EDCs of the corresponding image plots in Figure 5.10 shown within ~ 1 eV from E_F. Tick marks tracing the dispersion of the "bonding" (red) and "anti-bonding" (black) bilayer split Nb-bands have been added as a guide to the eye. The Nb-derived "bonding" band is found to sink ~ 200 meV below E_F (b).

interpretation, this can be understood in terms of a filling of the bilayer split, bonding band due to the introduction of additional charge carriers from the Cr intercalant.

Based on the data presented thus far, it would appear that a rigid band picture nicely describes the changes occurring to the TMDC electronic structure through the introduction of an intercalant. However, closer inspection of the MDCs extracted at E_F provides the first indication for a breakdown of this picture. Namely, while the MDC shown in Figure 5.12(a_1) is nicely fit by two peaks representing the band crossings for the bilayer split NbS_2 bands, the situation for $Cr_{1/3}NbS_2$ is clearly more complicated. From Figure 5.12(b_1) three clearly identifiable structures near Γ, and a broad structure consisting of more than one component at K can be identified. The presence of these three structures in proximity of the Γ point indicates that there are three bands crossings near the zone center, denoted hereafter as α, β_1, and β_2. Since Cr intercalation has the effect of raising the chemical potential, one would expect for the Fermi crossings at Γ of the hole-like NbS_2 bands to move towards lower k_Fs. This is the situation for the α and β_1 bands, however the k_F of the β_2 band (0.5 $Å^{-1}$) is much greater than that of any NbS_2 derived band. By merely considering a raise in the chemical potential, this observation indicates that the β_2 band cannot originate from the band structure of NbS_2. In a similar manner, supposing that with Cr intercalation one of the bilayer split Nb bands sinks below E_F, on the basis of DFT calculations, a shift of the chemical potential compatible with our observations would indicate that just the α band of $Cr_{1/3}NbS_2$ can be attributed to the bilayer split, anti-bonding band of NbS_2. Therefore, in $Cr_{1/3}NbS_2$ the β_1 and β_2 bands do not originate from the NbS_2 band structure.

At the K point, the large intrinsic width of the structure in the MDC shown in Figure 5.12(b_1) is consistent with the fact that the set of hole-like bands at this point will approach each other due to the chemical potential being raised. A fit of the MDC in proximity of K reveals two peaks, labeled as γ_1 and γ_2, which are symmetrically located with respect to this point. We identify the position of these peaks as the k_F corresponding to that of the doped anti-bonding band of NbS_2. A third band denoted as δ crosses E_F at ≈ 0.95 $Å^{-1}$. Since the lower band in NbS_2 has been observed to sink below E_F upon Cr atoms intercalation, we likewise identify the δ band as being unique to $Cr_{1/3}NbS_2$ and therefore cannot be rationalized on the basis of a rigid band picture.

That is, despite the fact that Cr atoms effectively donate electrons to the NbS_2 layer,

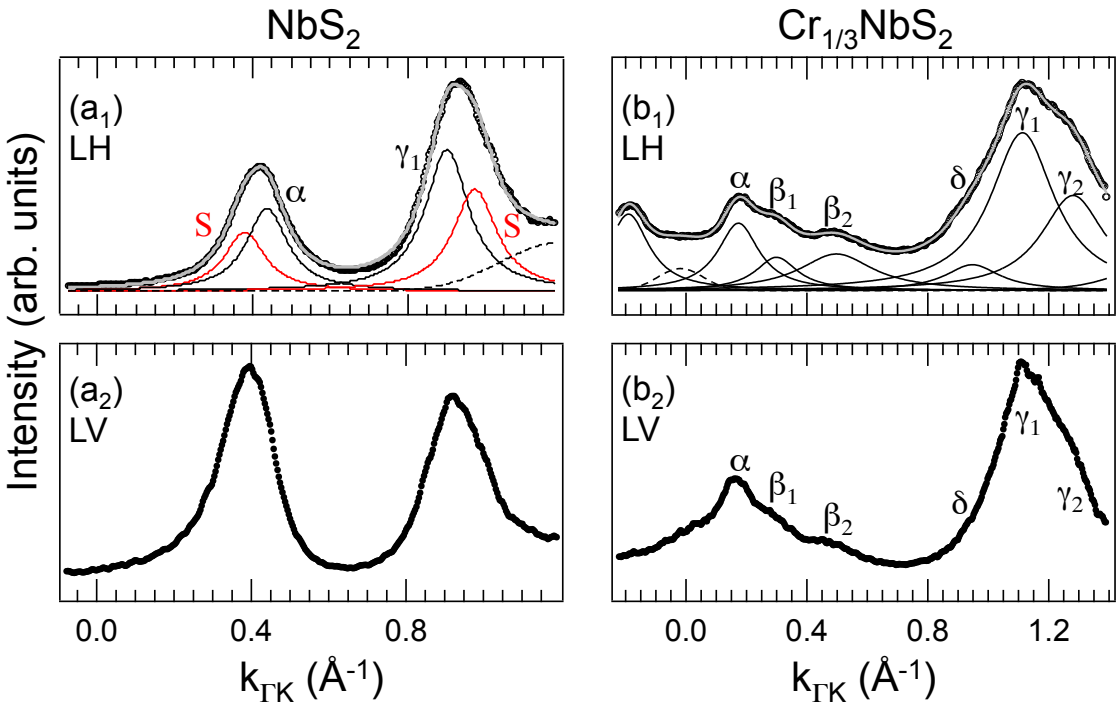

Figure 5.12: Direct comparison of MDCs at E_F extracted from the data shown in Figure 5.10. In the fit of the MDCs, shown in (a_1) and (b_1), the broken lines denote spectral weight originating from the background. The main features of the MDCs in $Cr_{1/3}NbS_2$ ((b_1), (b_2)) are likewise denoted in NbS_2 (a_1). In (a_1), peak S (red) sinks below E_F in $Cr_{1/3}NbS_2$. A slight misalignment of the sample is responsible for an asymmetry with respect to Γ of the MDCs in (a_2) and (b_2).

intercalation also appears to cause significant modifications to the electronic structure of the host compound. Such findings run contrary to the commonly held interpretation that the added electronic charge introduced by the intercalant changes the total number of carriers, without altering the band or FS topology of the host material. Rather, the two additional bands at Γ (β_1, β_2), and one additional band at K (δ) are found to arise solely as a result of Cr intercalation, and cannot be rationalized on the basis of a rigid band picture. Therefore it is natural to inquire as to the origin of these bands.

5.3 Polarization Dependence

Through use of polarization and temperature dependent ARPES, further insights into the origin of the β_1,β_2 and δ bands can be gained. Specifically, in $Cr_{1/3}NbS_2$, the bands forming the FS will derive from the d-orbitals of Nb and Cr. Recalling from section 3.1.2 that by exploiting the fact that the out-going photoelectron must necessary be even with respect to the scattering plane, the symmetry of the photoelectron's initial state can be determined through the particular choice of photon polarization with respect to this plane [9,13]. By selecting a photon polarization that is either odd (σ-) or even (π-) with respect to the scattering plane, symmetry constraints on the dipole matrix element will require that the respective initial state of the photoelectron likewise be odd or even. In this way, polarization dependent ARPES measurements like those depicted in Figure 5.13 can then be used to determinate the majority orbital character of the bands in this compound.

FS maps of $Cr_{1/3}NbS_2$ measured with the analyzer slit oriented along the ΓK and ΓM directions using both σ- and π- polarization geometries are shown in Figure 5.14. Here, the intensity of the features at Γ and K depends sensitively on the photon polarization used. Notably, for the bands crossing E_F in proximity to Γ, a marked enhancement in their intensity is observed with the use of a π-polarization. Furthermore, by observing that the intensity of these bands does not change appreciably when the mirror plane is oriented along the ΓK or ΓM directions, it is likely that they possess an even orbital character that is most consistent with that of a d_z^2 orbital. In contrast, the intensity of the bands crossing E_F in proximity to K is enhanced through use of a σ-polarization. While the symmetry of the states at K cannot be unambiguously determined, it is clear that these bands must have an odd orbital character, which is most

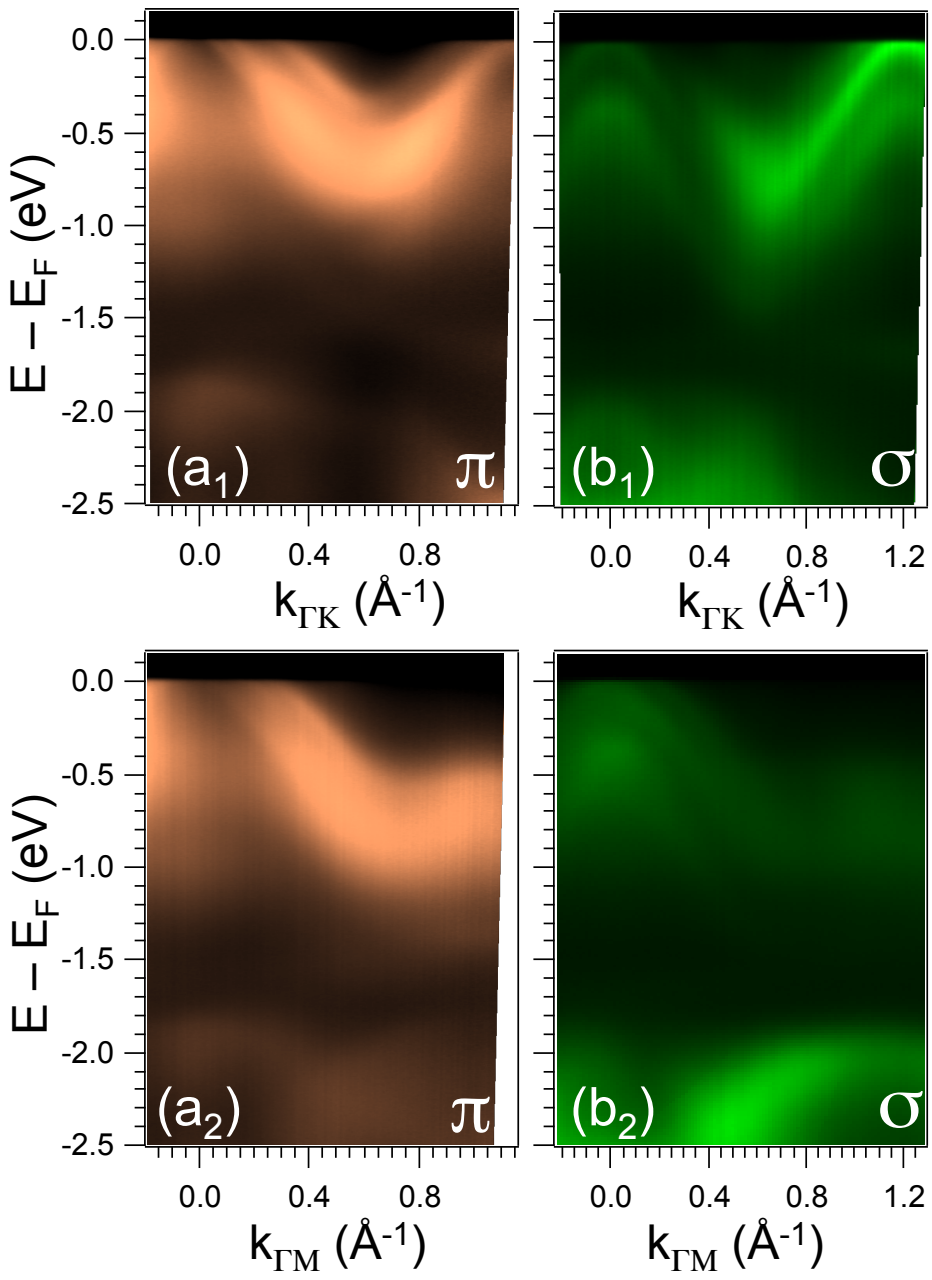

Figure 5.13: Band dispersion measured along the ((a_1), (b_1)) ΓK and ((a_2), (b_2)) ΓM direction using π-polarized ((a_1), (a_2)) and σ-polarized ((b_1), (b_2)) photons of energy hν = 40eV.

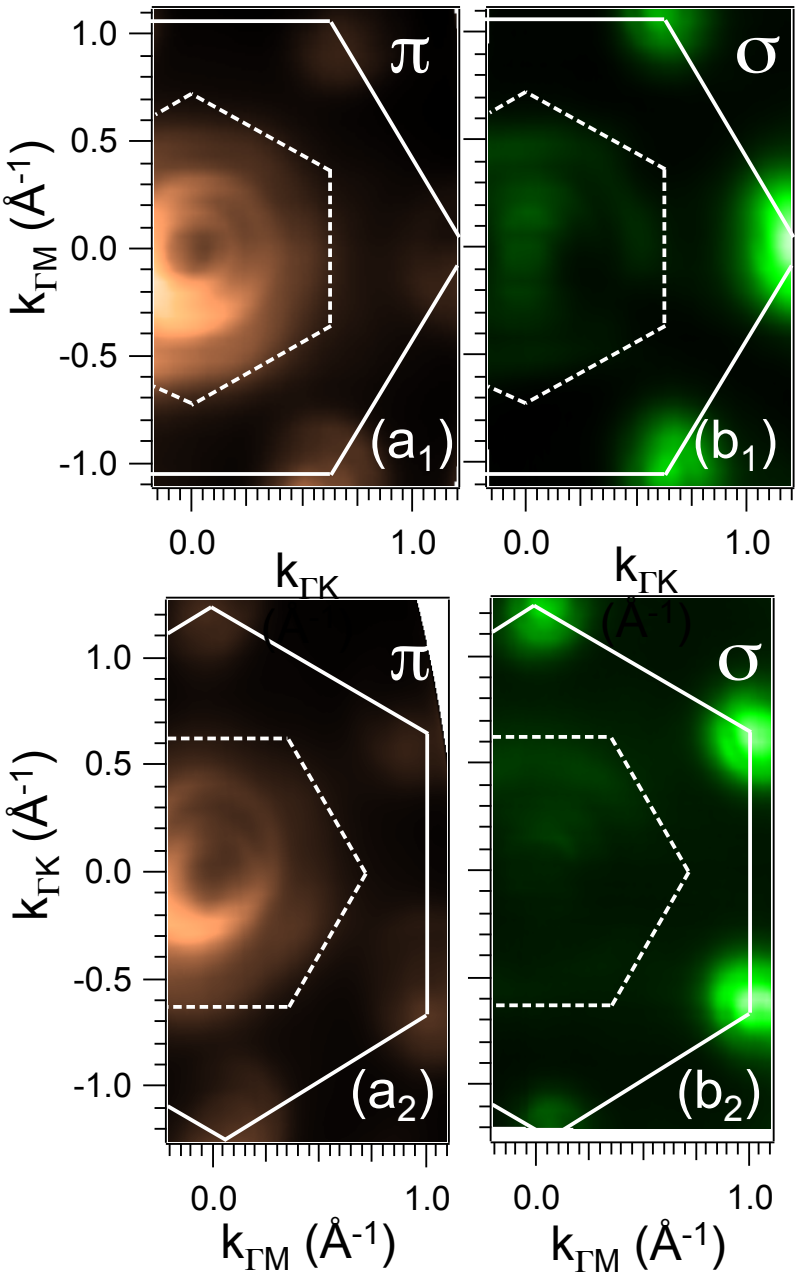

Figure 5.14: Fermi surfaces of $Cr_{1/3}NbS_2$ measured along the ((a_1), (b_1)) ΓK and ((a_2), (b_2)) ΓM direction using π-polarized ((a_1), (a_2)) and σ-polarized ((b_1), (b_2)) photons of energy hν = 40eV. Solid and broken lines denote the 1×1 and √3×√3 BZ, respectively.

consistent with that of the in-plane, $d_{xy}/d_{x^2-y^2}$ orbitals. As it turns out, the assignment of the above orbital character at Γ and K in $Cr_{1/3}NbS_2$ is fully consistent with that of *ab-initio* DFT calculations for 2H-$NbSe_2$ [82]. That is, despite the rigid band picture failing to describe the electronic structure of Cr intercalated NbS_2, the orbital character of the states at Γ and K seems to be retained. Thus, as can be seen in both Figure 5.13 and Figure 5.14, the β_1, β_2 bands at Γ and the δ band at K posses an orbital character that is likewise consistent with that of an out-of-plane d_{z^2}, and an in-plane $d_{xy}/d_{x^2-y^2}$ orbital respectively.

5.4 Temperature dependence

After having investigated the polarization dependence of the new states that emerge in the NbS_2 band structure from Cr intercalation, further insights can be gained by carrying out temperature dependent ARPES experiments through the helimagnet transition temperature, T_C (= 131K). While no change was observed for the δ band, from the image plots depicted in Figure 5.15, the band crossing of the outermost β_2 band is seen to shift towards Γ with increasing temperature. Closer inspection of the MDCs extracted at E_F from spectra measured along the ΓM direction as a function of temperature reveals that as temperature is raised above 50K, not only does the Fermi momentum (k_F) of the β_2 band begins to shift towards Γ, but a progressive decrease of the spectral weight of the same band is found to occur (Figure 5.16). For T > 120K, it becomes impossible to clearly distinguish the k_F of β_2 from that of β_1. Given the close proximity of this temperature to T_C, the relative shift of β_2 towards β_1 suggests that these bands arise from magnetic exchange splitting.

The assignment of the $\beta_{1,2}$ bands as magnetic exchange split bands suggests the presence of Cr-derived states at E_F. Indeed, this has been confirmed with ResPES, where excitation with photon energies tuned across the Cr L-edge makes it possible to identify Cr 3d states in the VB. Unlike the previous ResPES results presented in Figure 5.5, those shown in Figure 5.17 where taken with a different photon polarization specifically chosen so as to emphasize the Cr-derived states having an out-of-plane orbital character. In such a case, a direct comparison of the ResPES spectra taken across the Cr L- and the Nb M-edges reveals a clear resonance of the state ≈ 0.6 eV below E_F. Recalling from literature that this state is known to be the Nb "d_{z^2} sub-band"

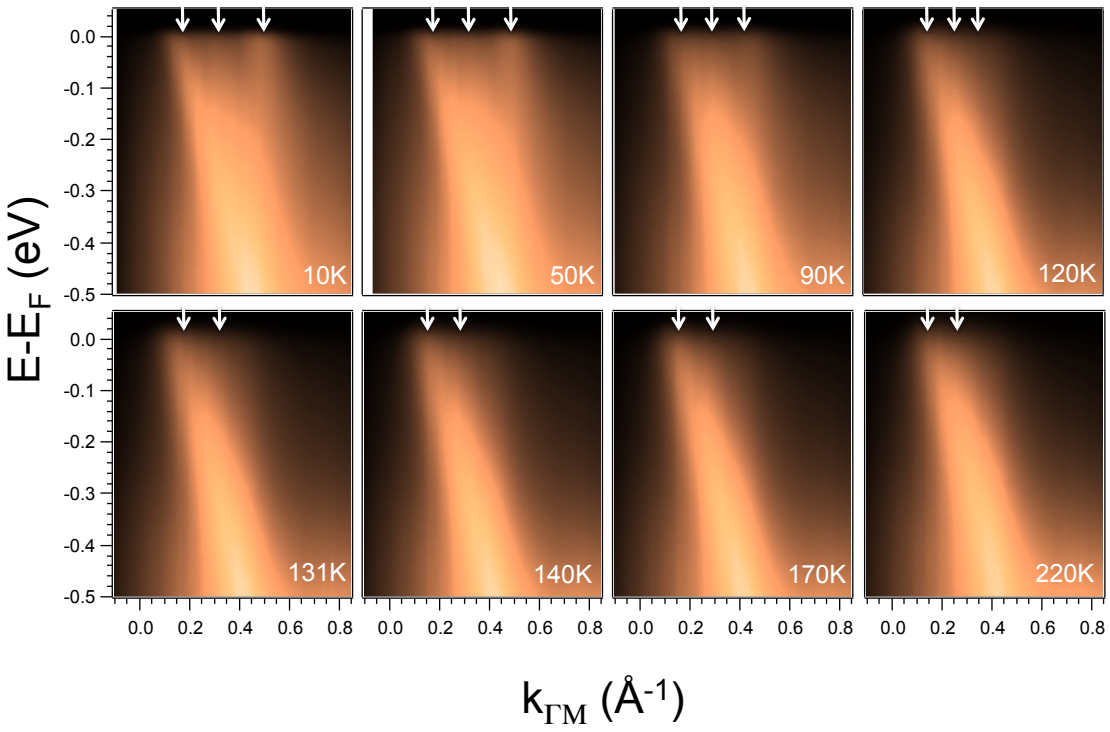

Figure 5.15: Temperature dependent ARPES image plots obtained along the ΓM direction using π-polarized photons of hν = 48 eV. Here, all band crossing points are denoted by white arrows.

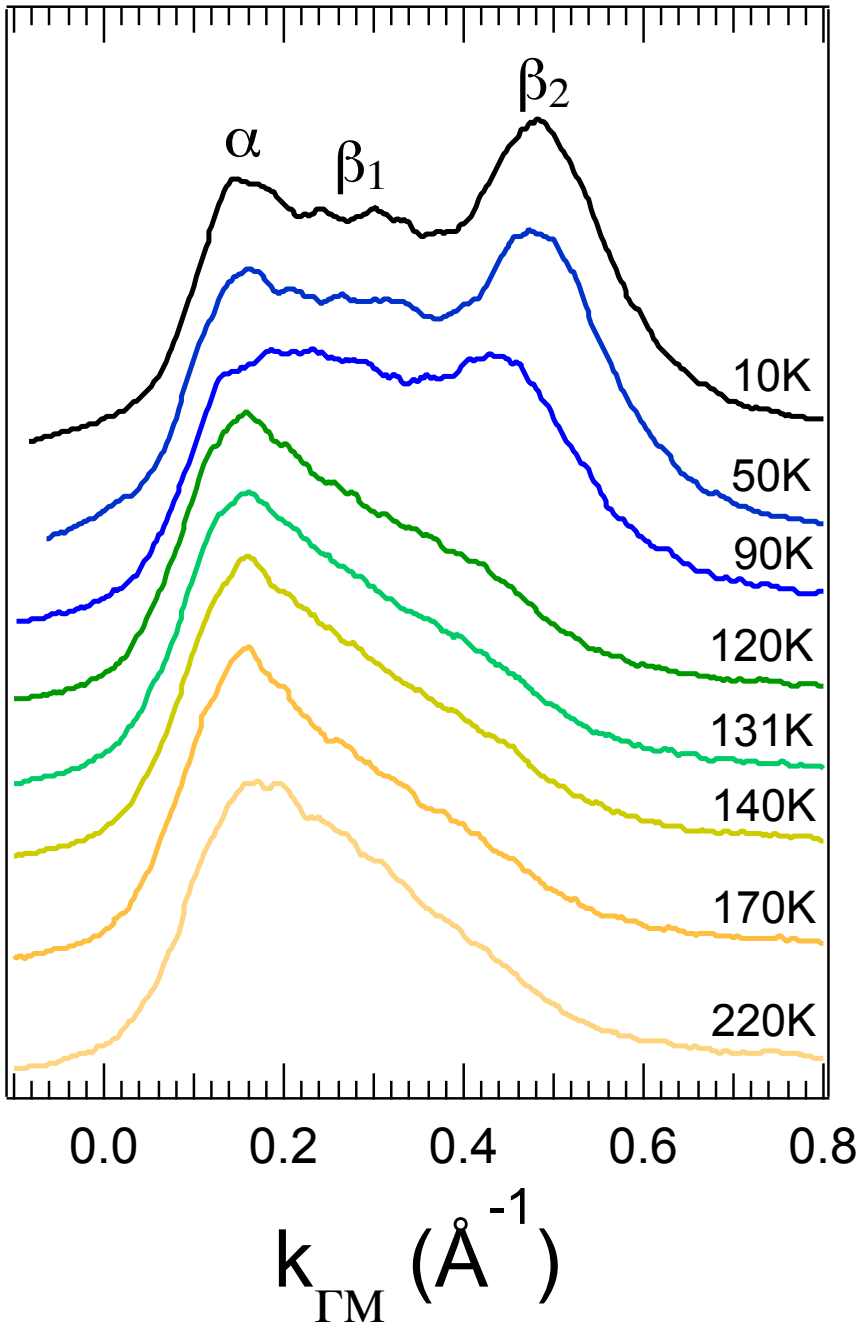

Figure 5.16: MDCs extracted at E_F for spectra measured along the ΓM direction with photon energy hν = 48 eV. Note the emergence of the exchange split $\beta_{1,2}$ bands for T < 120K, and the loss of spectral weight for $T > T_C$.

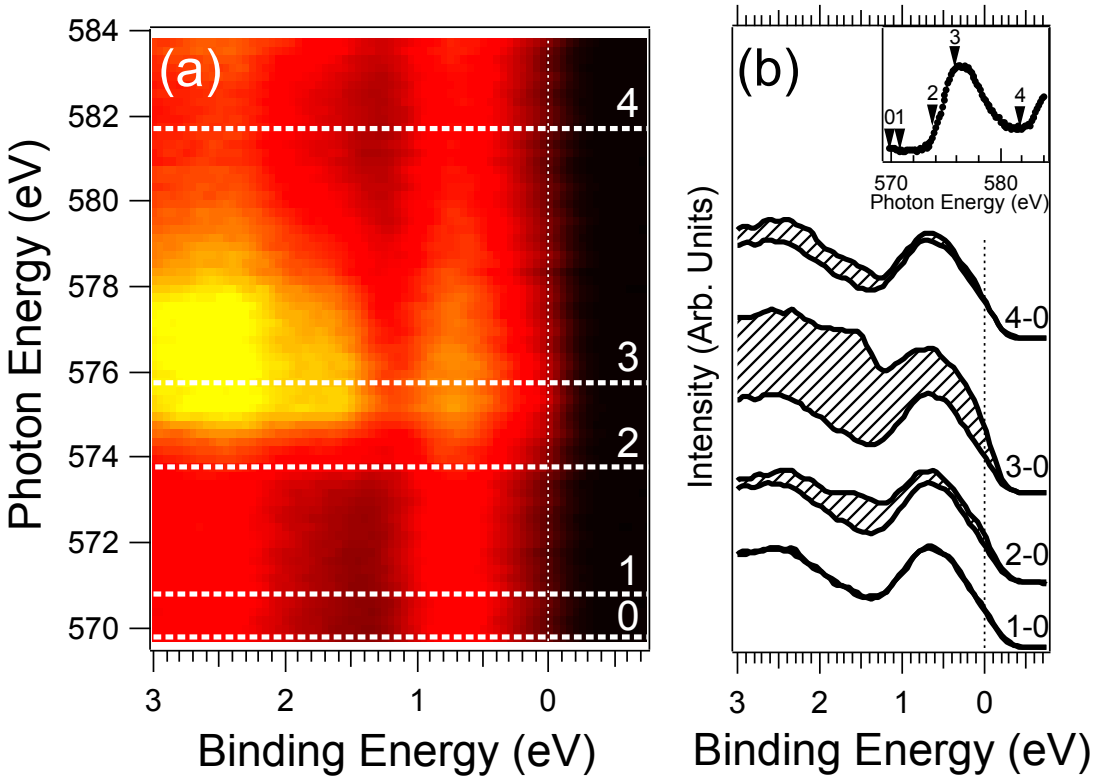

Figure 5.17: ResPES spectra obtained using a linear horizontal photon polarization. Here, photon energy was tuned across the Cr L_3 absorption edge where the corresponding x-ray absorption spectrum is shown as an inset in panel (b). Symbols on the XAS are used to denote the particular photon energy of the VB traces shown in (b). The spectra excited with different photon energies are compared to the spectrum excited off-resonance with photon energy hν = 570 eV. Note the clear indication of Cr resonance at E_F as hν is tuned to the peak of the XAS spectrum. This result clearly indicates that Cr-derived states participate in the FS of $Cr_{1/3}NbS_2$.

[59], a resonance across the Cr edge would then suggest there to be hybridization between the Cr- and Nb- states that comprise the VB. Furthermore, as shown in Figure 5.17(b), by comparing valence band traces taken through the Cr L_3 resonance, it found that the states at E_F are likewise observed to resonate. Taken together, these results demonstrate that both Cr- and Nb-derived states are hybridized, and participate in the formation of the FS.

As was previously mentioned, the presence of Cr-derived states at E_F has significant implications for a microscopic description of magnetism and its interplay with the transport degrees of freedom. Namely, the use of spin ordering arguments in the interpretation of the magnetoresistance for this material is fully consistent with a rigid band picture. Here, given the large separation distance between Cr atoms, it is generally believed that the Curie-Weiss local spin moments (LSMs) are localized to the Cr sites, and that the states at E_F, the ones responsible for transport, are Nb-derived [59,146]. This leads to the notion that ferromagnetism in $Cr_{1/3}NbS_2$ occurs via an RKKY exchange interaction between Cr LSMs and Nb–derived conduction electrons [91,92]. In such a case, when LSMs are formed from electrons with states *not* present at the Fermi level, and hence not rooted in transport, the magnetism can be discussed concentrating on the magnetic DOF alone. This is exactly the case for insulating transition metal oxides and rare earth metals, where at most, the interaction between LSMs and itinerant electrons can be considered as a weak perturbation resulting from an instability of the FS, as in the RKKY picture [147].

Based on the findings presented in Figure 5.17, for $Cr_{1/3}NbS_2$ the LSMs are formed from Cr 3d states, some of which are also present at the Fermi level. Consequently, a clear separation of magnetic and itinerant degrees of freedom does not occur, and the motion of the itinerant electrons and the LSMs are influenced reciprocally in a self-consistent fashion, as in itinerant 3d magnetic systems [148,149,150]. Evidence in support of such a strong interplay between the itinerant and magnetic degrees of freedom in $Cr_{1/3}NbS_2$ can actually be found in the temperature dependent ARPES data taken across T_C. As was shown in Figure 5.16 from the MDCs, the merging of the β_1 and β_2 bands as temperature is raised above 50K is also accompanied by a significant loss of spectral weight at E_F. This is better illustrated by the EDCs extracted from a momentum integration of the ARPES data over $k_{\Gamma M} = 0.24$ Å^{-1} to 0.8 Å^{-1} (cf. Figure 5.18(a)). Such a wide momentum range was chosen so as to encompass both crossing points of the exchange split $\beta_{1,2}$ bands and avoid any loss of spectral weight associated with the branching of

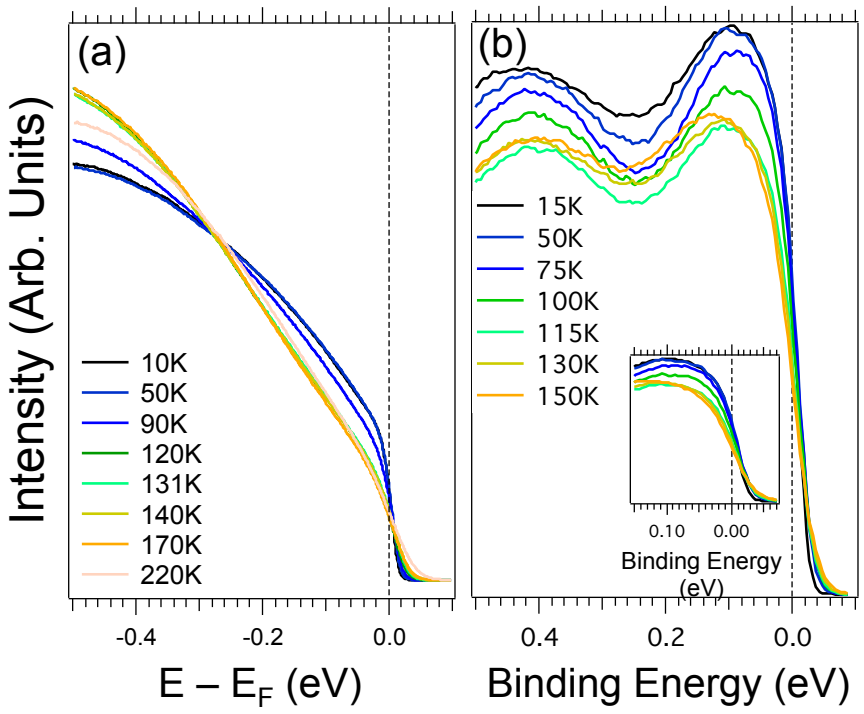

Figure 5.18: (a) EDC spectra integrated from $k_{\Gamma M}$ = 0.24 Å^{-1} to 0.8 Å^{-1} and normalized to photon flux. This data reveals an increase of spectral weight in proximity of E_F occurring for $T < T_C$. Similarly, (b) shows EDCs extracted at k_F of the α band as a function of temperature in which spectra have been normalized in a region absent of any dispersive features (1.4 eV). Note the monotonic increase of spectral weight as T is lowered below T_C. This behavior is more clearly highlighted by the inset in (b) showing the changes in spectral weight occurring within 150 meV from E_F.

the bands for $T < T_C$. From Figure 5.18(a), it is evident that as $T > 50K$, the spectral weight in proximity to E_F begins to drop until $T > 120K$, whereupon there is no longer any change.

Furthermore, while it appears from the image plots in Figure 5.15 that little to no change in the behavior of the α band is observed as temperature is varied across T_C, nevertheless the same monotonic drop of spectral weight with increasing T is exhibited by the EDCs extracted at the k_F vector of the α band (Figure 5.18(b)). This behavior can be more clearly illustrated by removing the Fermi-Dirac distribution through symmetrizing about E_F (Figure 5.19). Namely, through symmetrization, it is more clearly revealed that this drop in spectral weight occurring with increasing T can be solely attributed to the behavior of the single particle removal spectral function. Here, the choice of symmetrizing the data as opposed to a direct deconvolution of the Fermi-Dirac distribution stems from the relative ease of removing the Fermi function that symmetrization offers. Namely, rather than having to divide through by small numbers for $E > E_F$, as would be the case for a deconvolution, symmetrization takes advantage of the fact that $f(-\omega) = 1 - f(\omega)$. However, by doing so, it is assumed that the spectral function is necessarily even in proximity to E_F, making $A^{-}(k_F,\omega) = A^{-}(k_F, -\omega)$. Given the symmetrized spectra in Figure 5.19 to similarly shows a clear, monotonic drop in spectral weight as T is raised above T_C, these results complement that of Figure 5.18(b) as it demonstrates that the change in the EDC intensity is not a simply a consequence of Fermi broadening but the true underlying behavior of the spectral function. Importantly, we stress that the increase in spectral weight occurring in our data for $T < T_C$ is in contrast to both the behavior of a typical exchange split band in an itinerant ferromagnetic system [151], and the results of first principle Density Functional Theory calculations in $Cr_{1/3}NbS_2$ [5]. Rather, despite the latter predicting the existence of Cr-derived states at E_F, it also indicated a substantial reduction of spectral weight at E_F for $T < T_C$, consistent with the Stoner criterion. Furthermore, we note that the increase of spectral weight observed in our data occurs mostly in proximity to T_C, as temperature is lowered from T = 130 K to T = 90 K. This behavior cannot be accounted by thermal broadening effects, and suggests instead a close relationship to the drop of the in-plane resistivity occurring right at T_C.

We believe that these results provide relevant insights that assist in rationalizing at a microscopic level the interplay of the in-plane transport and magnetic degrees of freedom. This interplay, established by magneto-transport measurements and the behavior of the in-plane resistivity at T_C, indicate the occurrence of a mechanism that links electron itinerancy to the

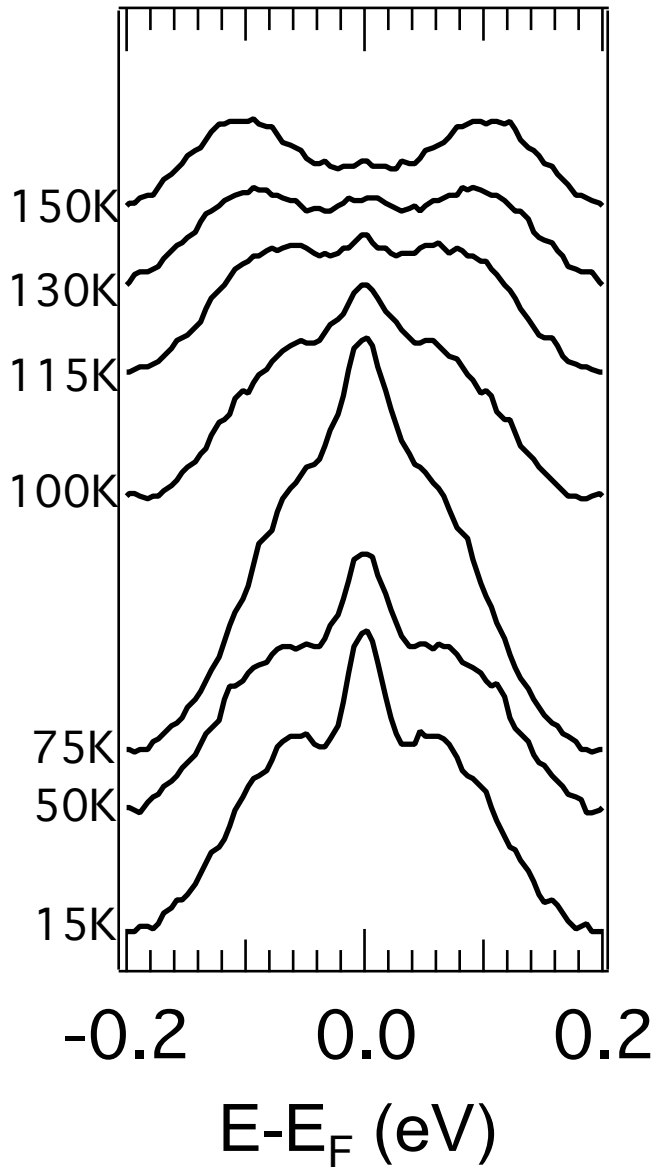

Figure 5.19: Symmetrized EDCs of the α-band displayed over +/- 200 meV binding energy range and stacked as a function of increasing temperature.

onset of ferromagnetism. Our findings lead naturally to the notion that such mechanism is rooted in the microscopic interaction between itinerant electrons and LSMs. This interaction is far richer than that contemplated in the conventional RKKY picture. In the latter, the interaction between itinerant electrons and LSMs is taken into account only as a weak perturbation. On the contrary, the presence of Cr-derived states at the FS provides evidence that itinerant electrons and LSMs are strongly coupled, as both are formed by Cr-derived states.

While not possible to fully elucidate the details of this interaction on the basis of this work, from the set of considerations valid for itinerant 3d magnetic systems [148,149,150], the ability of itinerant electrons and LSMs to influence each other self-consistently can have important implication on the mechanism leading to ferromagnetic order. On the one hand, ferromagnetic order can foster electron itinerancy by reduction of electron scattering with thermal fluctuations of the LSMs. On the other hand, due to their strong coupling, the interaction between itinerant electrons and LSMs is synergistic, characterized by a regenerative aspect of electron itinerancy: ferromagnetic order promotes electron itinerancy, while the latter in turn modulates indirectly the exchange interaction between LSMs, leading to order. In this scenario, electron itinerancy acquires a fundamental role in the attainment of ferromagnetic order, and the magnetic transition in $Cr_{1/3}NbS_2$ can be viewed as a cooperative phenomenon driven by the mutual interaction of itinerant electrons and LSMs. The concomitant increase of electron itinerancy and alignment of the LSMs provide a route for the minimization of the total energy of the system. Electron itinerancy also provides new degrees of freedom that relieve entropy by adding significant flexibility to how the LSMs can interact with itinerant electrons, and indirectly with each other. Based on this interpretation, important aspects of in-plane transport can be rationalized within this scenario. For example, the minimization of the energy of the system due to an increase of electron itinerancy provides a natural explanation for the drop of the in-plane resistivity occurring right at T_C, and for the negative in-plane magnetoresistance. Ultimately, this serves to motivate future studies with the goal of understanding to what degree this picture might complement, or even supplement, the mainstream RKKY mechanism in this material.

By revealing that the close interplay between macroscopic magnetic and transport degrees of freedom in $Cr_{1/3}NbS_2$ established by in-plane magneto-transport measurements is rooted in the detailed microscopic mechanisms underlying the interaction between itinerant

electrons and LSMs, our study underscores the relevance of microscopic length-scales and details of the electronic structure in the description of the in-plane magneto-transport properties. In $Cr_{1/3}NbS_2$, the elucidation of the mechanisms underlying both inter- and intra-layer magneto-transport acquires particular importance in light of the possibility of exploiting the significant magnetic and transport anisotropy for functionalities of technological relevance. Our results suggest that arguments based entirely on magnetic scattering are insufficient to explain all the magneto-transport properties observed in this material. Certainly, since photoemission measurements are sensitive to the first few atomic layers, our results are directly relevant to a microscopic description of the in-plane, and not the inter-plane, magneto-transport properties. Nevertheless, it is unlikely that the microscopic interaction between itinerant electrons and LSMs evidenced by our data would be entirely irrelevant for the inter-layer magneto-transport properties as well. In fact, any mechanism proposed to explain the inter-layer magnetoresistance must be rooted in a Hamiltonian that necessarily has to take into account the interaction of itinerant electrons with LSMs. Therefore we believe the strong coupling between itinerant electrons and LSMs revealed by our data is thus relevant for any first-principle formulation of magneto-transport properties in $Cr_{1/3}NbS_2$.

5.5 Insights from *ab initio* Calculations

Regarding the present state of *ab initio* calculations for this material, as has been briefly mentioned throughout this chapter, a poor comparison with electronic structure measurements is typically found. Initially, this was surprising given that several predictions made concerning the magnetic and electronic properties of $Cr_{1/3}NbS_2$ showed consistency with experimental results. This includes a saturated magnetic moment of 3.01 μ_B/Cr, fairly close to the experimental value of 3.2 μ_B/Cr [5], and a "bare" low-temperature density-of-states of 2.76/eV-unit cell, which is near the experimental value of 3.40/eV-unit cell [5]. Here, by considering that the latter value includes the effective mass enhancement due to such factors as the electron-phonon interaction, it is believed that this prediction is in fairly good agreement with experiment. Therefore, it is important to understand what the root cause of the discrepancy between our ARPES measurements and first principal calculations must be.

As it turns out, significant insights into this problem can be gained from a measurement of the k_z dispersion. Namely, from Figure 5.20, the MDCs extracted at E_F from ARPES spectra measured along the ΓK direction using π- and σ-polarized photons of varying energy are used to construct a FS map along k_z direction given an inner potential of 14 eV. For both polarizations the dispersion measured along k_z is overall very modest, with k_F's changing by ≈ 0.05 $Å^{-1}$ at most. Seeing that such a small change translates to ≈ 4% of the length of the ΓK vector, it appears that intercalation with Cr does not substantially alter the two-dimensional character of the NbS_2 band structure. Based on intuitive arguments, the extremely weak k_z dispersion is surprising in light of the notion that the introduction of an intercalant between NbS_2 layers should actually serve to increase the interaction between the layers. Based on DFT calculations, such an increased interaction is what then led to a prediction that overestimates the three-dimensionality of the FS in $Cr_{1/3}NbS_2$. In other words, by overestimating the three-dimensionality of this system, it appears that DFT assigns a greater degree of covalency along the Cr-NbS_2 c-axis bond than what is observed experimentally.

One significant consequence from the overestimation of the covalency along the c-axis is that the proper Brillouin zone for $Cr_{1/3}NbS_2$ turns out to be that of the (1×1) zone of the host compound. Namely, due to the (√3×√3) superstructure ordering of Cr atoms, DFT calculations for $Cr_{1/3}NbS_2$ are necessarily carried out in a reduced Brillouin zone defined by the dotted line in Figure 5.14. In such a case, if the electronic structure of this material were to be correctly described by the (√3×√3) zone, it is expected for the states at Γ and those at K to coincide. However, as is clearly observed from our ARPES results, the states at Γ and K are unique from one-another, with the bands having distinct topologies, Fermi crossings, and orbital character. Recalling from the discussion in section 5.1, the fact that the proper Brillouin zone for $Cr_{1/3}NbS_2$ is that defined by the (1×1) cannot be ascribed to the surface sensitivity of ARPES, as the superstructure ordering of Cr atoms is evident in the electronic structure by the presence of band backfolding (Figure 5.21). This is clear indication that the coupling between the NbS_2 and Cr layers is not strong enough to back-fold the electronic structure of $Cr_{1/3}NbS_2$ into the reduced (√3×√3) Brillouin zone. Such a claim as this is consistent with the weak intensity of the back-folded bands at Γ as the intensity of such bands should be proportional to the strength of the coupling to the superlattice potential [152]. In the case of $Cr_{1/3}NbS_2$, this coupling is that of the interlayer interaction between the NbS_2 and Cr layers.

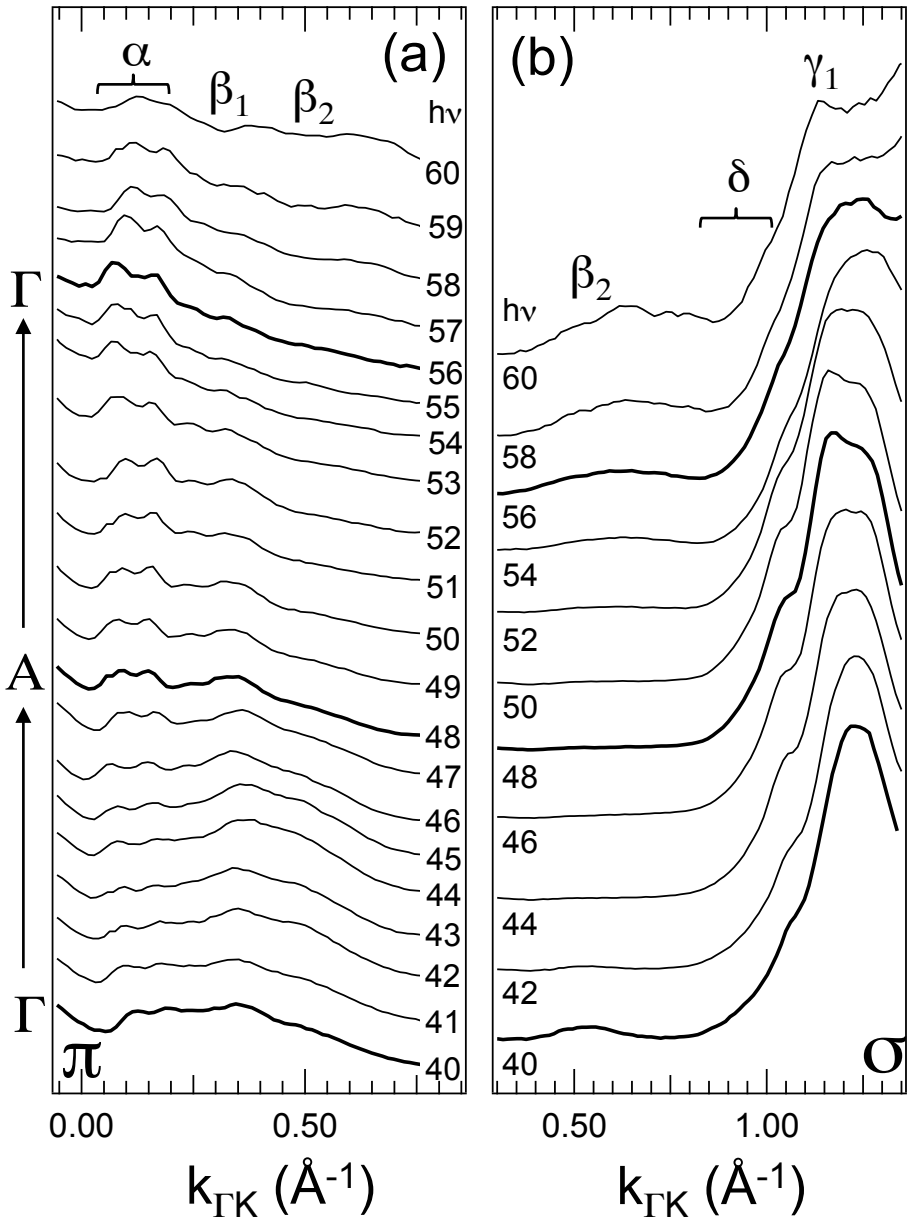

Figure 5.20: MDCs extracted at E_F along the ΓK direction using (a) π-polarized and (b) σ-polarized photons. The photon energy was varied from hν = 40eV to hν = 60eV in steps of 1 eV (a), or 2 eV (b).

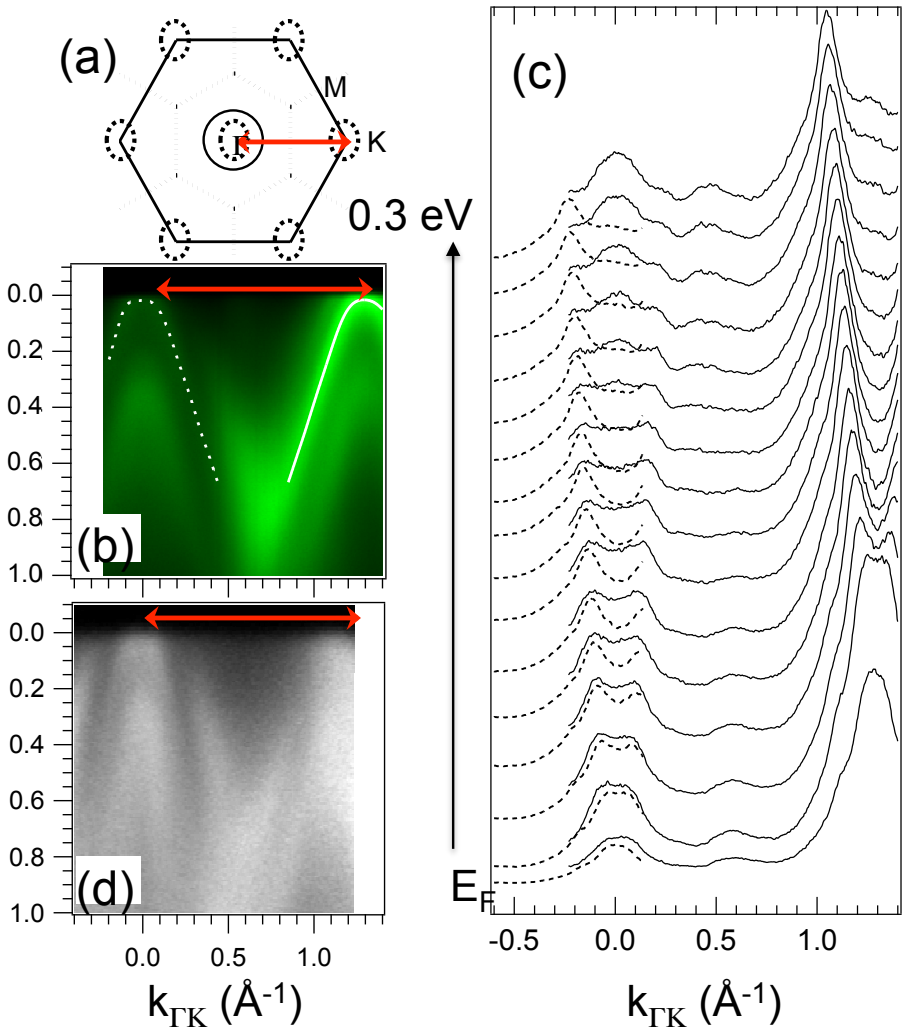

Figure 5.21: (a) Sketch of the 1×1 Brillouin zone illustrating how the hole-like band at K folds due to a √3×√3 super-lattice potential. (b) Band dispersion taken along the ΓK direction with σ-polarized photons of hν = 40eV. Superimposed on the image plot is a trace of the MDC peak positions of the band at K (solid) translated by a √3×√3 lattice vector (broken line). (c) MDC stacks having a negative offset taken from 300 meV to E_F from the image plot in (b). Broken lines have been translated by a √3×√3 lattice vector and rescaled so as to directly compare the dispersion. (d) Band dispersion measured along the ΓK direction with LV polarized photons of energy hν = 196 eV.

In light of this claim, by returning to the DFT calculation some basic considerations suggest a plausible explanation for the overstatement of the interlayer, Cr-mediated interaction to be rooted in the detailed mechanisms governing axial transport. Namely, the calculated plasma frequencies for $Cr_{1/3}NbS_2$ in the magnetic ground state are 0.95 eV (planar) and 1.12 eV (axial). This latter value is indicative of a strong three-dimensionality, as illustrated in the substantial c-axis dispersion of the calculation. From the calculated magnetic density-of-states of $Cr_{1/3}NbS_2$, it is found that nearly all the spectral weight at E_F is concentrated in the spin-up channel, and in fact the spin-down channel is gapped just above E_F. From these calculations one can also extract the plasma frequency squared Ω_p^2 for the separate channels. For the spin-up channel the planar value of Ω_p^2 is roughly an order of magnitude larger than for the c-axis, but surprisingly for the spin down channel it is the c-axis Ω_p^2 that is larger. If the interlayer interaction is just slightly overstated, as the Cr electronic wavefunctions is found to decay exponentially into the NbS_2 layers, it is quite possible that the gap in the spin-down DOS would extend to E_F, resulting in a strong suppression of the interlayer transport. Furthermore, this overstatement effect would only *increase* the anisotropy in the spin-up channel. In seeing as the Cr atom is the only "bridge" between otherwise well separated NbS_2 layers, all interlayer electronic transport must occur through this atom. Therefore, by suppressing the number of available states capable of participating in axial transport, the inter-layer coupling and thus three-dimensionality of the FS becomes significantly weaker.

Chapter 6: Spectroscopic Evidence for Strong Quantum Spin Fluctuations with Itinerant Character in YFe_2Ge_2

6.1 Introduction

The interplay between superconductivity and magnetism is one of the most interesting topics in condensed matter physics. While known that conventional, i.e. s-wave, superconductivity is damaged by nearness to magnetism [153], unconventional forms of superconductivity, such as that exhibited by the high-T_C cuprates, heavy fermions, and iron-based high temperature superconductors (Fe-HTSC), can be realized in proximity to magnetically ordered states [154,155]. In the case of Fe-HTSC, there is evidence for a close association between magnetism and superconductivity, and in particular an unconventional superconducting state mediated by spin-fluctuations is considered likely [156,157]. Two signatures are particularly indicative of the unusual magnetism found in the pnictide Fe-HTSC.

The first consists of large discrepancies between the experimental phase diagrams and density functional theory (DFT) calculations. For example, the measured antiferromagnetically ordered spin moments were found to be considerably smaller than those predicted from DFT calculations in the magnetic ground state. Such an overestimate is surprising as DFT typically underestimates the magnetic character in unconventional superconductors, like the high T_C cuprates, where strong electron correlations are at play. However, in the case of the pnictides, there is generally a good agreement between the measured electronic structure and DFT calculations, meaning that the opposite seems to occur. That is, DFT predicts a much larger spin moment of $\approx 2\mu_B$ on the Fe site that is mostly independent of doping [158].

The second signature of unusual magnetism in the pnictides is the presence of large, fluctuating spin moments in the normal, non-magnetically ordered states. As it turns out, such fluctuations can only be detected with fast measurement ($< 10^{-12}$s to 10^{-15}s) techniques, such as inelastic neutron scattering (INS), x-ray emission (XES) and core-level photoemission spectroscopy (PES) [102,159,160,161,162]. Of these techniques, it is found that the largest

magnitude of the spin moment measured for the pnictides is provided by soft x-ray spectroscopies. As will be discussed in detail below, this behavior is a signature of quantum spin fluctuations occurring on ultrafast timescales determined by the lifetime of the core hole.

Given the relevance of the Fe-HTSC in providing novel insights into the fundamental origin of unconventional superconductivity, there is a great incentive for the discovery of similar materials that exhibit much of the same physics. In this endeavor, by use of x-ray absorption and photoemission spectroscopy, we find that YFe_2Ge_2 possesses many of the same spectroscopic signatures as the Fe-pnictide superconductors. Most notably, this includes the occurrence of fluctuating spin moments on the Fe sites, as indicated by exchange multiplets appearing in the Fe 3s core level photoemission spectra, where the magnitude of the multiplet splitting is similar to that found in the normal state of the Fe-pnictide superconductor $CeFeAsO_{0.89}F_{0.11}$ [159]. These findings imply that magnetic behavior similar to the Fe-HTSC can be found in compounds containing neither pnictogens nor chalcogens, and suggest that perhaps unconventional superconductivity related to that in the Fe-pnictides could likewise be found in Fe-Ge compounds.

YFe_2Ge_2 is a Fe-containing compound that shows evidence for both bulk superconductivity with a critical temperature of $T_C = 1.8$ K, as well as for being in proximity to a magnetic quantum critical point [163]. Similarities with the Fe-pnictides stem from the fact that YFe_2Ge_2 crystallizes in the same $ThCr_2Si_2$ type structure (*I4/mmm*) as the 122 Fe-pnictide, and on the basis of electron counting, is electronically akin to KFe_2As_2, an Fe-based superconductor with a highly enhanced specific heat that is similarly seen in YFe_2Ge_2 [164]. The related compound $LuFe_2Ge_2$, which is isoelectronic and isostructural to YFe_2Ge_2, exhibits antiferromagnetic order below 9 K [165]. This magnetic order is continuously suppressed in $Lu_{1-x}Y_xFe_2Ge_2$ as the Y content is increased, with the quantum critical point occurring for $x \approx 0.2$ [166]. The proximity of the end series compound YFe_2Ge_2 to quantum criticality is consistent with the non-Fermi liquid behavior of the specific heat and resistivity [163].

Despite the fact that YFe_2Ge_2 is a metal that does not exhibit any magnetic order, DFT calculations have found a series of competing magnetic ground states [167,168]. Namely, the DFT calculations show a competition between different antiferromagnetic states, including an A-type antiferromagnetic structure consisting of ferromagnetic Fe-planes with antiferromagnetic stacking along the *c*-axis and, as shown by Subedi [167], a stripe-like structure similar to the Fe-

based superconductors. The overestimation of the magnetic tendencies within DFT is unusual, since in general DFT underestimates the magnitude of the ordered spin moment in correlated materials and normally gives reliable predictions in the absence of strong correlations. It is not, however, not unprecedented: It suggests proximity to, or incipient magnetism. In particular, besides the pnictide Fe-HTSC [155,158], it occurs in several compounds near quantum critical points associated with itinerant magnetism [169], as might be anticipated based on theoretical arguments [170,171,172]. In strong analogy to the pnictide Fe-HTSC, our x-ray spectroscopy data reveal in the normal state of YFe_2Ge_2 the presence of both itinerant electrons and large fluctuating spin moments on the Fe sites.

High quality crystalline samples were grown out of Sn flux. X-ray powder diffraction patterns were found to be consistent with that of the tetragonal crystal structure with space group *I4/mmm*. The PES and x-ray absorption (XAS) measurements were carried out on the BACH beamline at the Elettra Synchrotron Facility. Several samples have been measured at room temperature in a pressure better than 8×10^{-10} mbar. Surface cleanliness was assured by periodic (every 20 minutes) *in-situ* scraping with a diamond file [173]. Quantitative PES analysis of core-level spectra showed no surface contamination during spectra acquisition.

6.2 Fe 2p and $L_{3,2}$

The Fe 2p core level PES and the Fe L_{23} XAS spectra, shown in Figure 6.1, are remarkably similar to those excited in some of the pnictide Fe-HTSC such as $CeFeAsO_{0.89}F_{0.11}$ [159] and $Ba(Fe_{1-x}Co_x)_2As_2$ [174]. As in the pnictide Fe-HTSC, the Fe 2p PES and Fe L_{23} XAS spectra display signatures that are typical of delocalized, itinerant electrons, in agreement with other studies [175,176]. Specifically, the Fe 2p PES spectrum does not show the additional satellite structures indicative of the presence of strong electron correlation and localization effects, as for example found in the cuprates. Rather, the PES Fe 2*p* is akin to that of Fe metal and intermetallic compounds [177]. The Fe L_{23} XAS spectrum (Figure 6.1(b)) does not show the presence of well-defined multiplet structures. The broad and weak shoulder at ≈ 705 eV, also found in the Fe-HTSC, is most likely indicative of the covalent nature of the Ge and Fe conduction band states. Indeed, such structure is present in the Fe XAS spectra of Fe–X (X is an *sp*-element) compounds with strong Fe 3*d*-X n*p* hybridization such as Fe silicides [178].

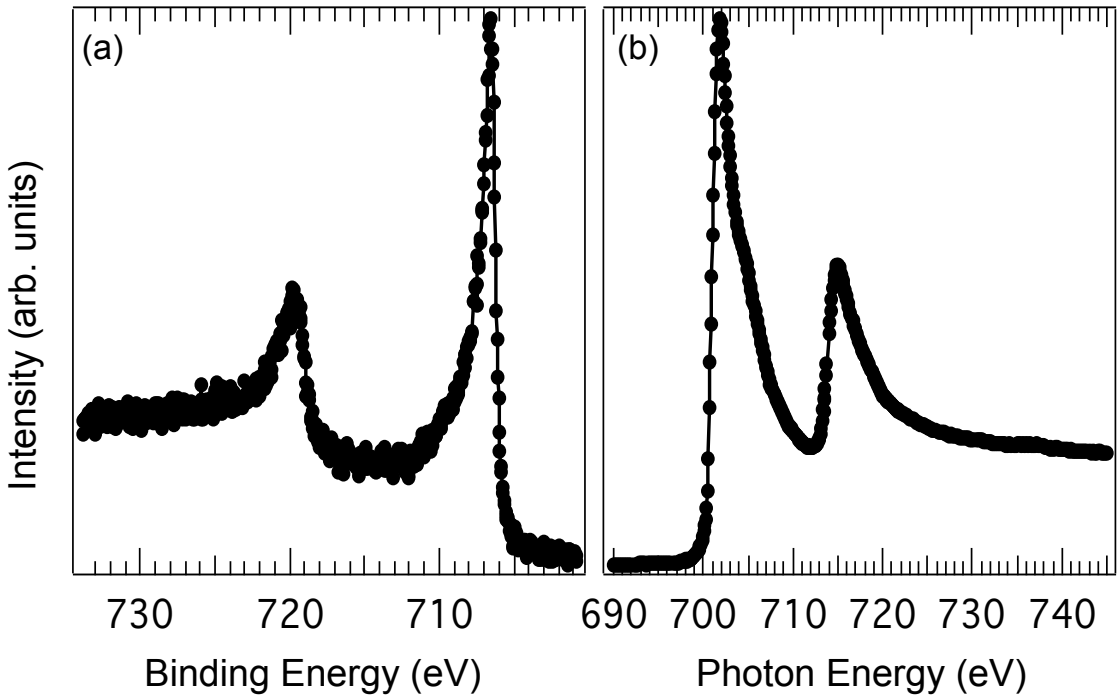

Figure 6.1: (a) Fe 2*p* core level PES spectrum excited with photon energy hν = 907.5 eV. (b) Fe L_{23} XAS spectrum. Note the marked similarities with corresponding spectra excited in Fe-based high temperature superconductors.

6.3 Valence Band

Figure 6.2(a) shows the valence band (VB) PES spectrum of YFe_2Ge_2. Given that the resulting samples are polycrystalline due to in-situ scraping of the surface, this spectrum provides a representation of the occupied density of states (DOS), modulated by atomic cross-section effects and instrumental resolution (≈ 500 meV). Similar to the Fe-HTSC, there is a high DOS at the Fermi level (E_F) primarily of Fe-derived character. This is consistent with the lineshape of the Fe 2p PES spectrum: The high Fe DOS at E_F is very effective in completely screening the Fe 2*p* core-hole excitation, leading to an absence in the core-level spectra of satellite structures. Overall, there is a very good correspondence of the main features in the VB with the total DOS and its decomposition into its main three components, i.e. Fe-3d, Ge-4p and Ge-4s, as calculated in Ref. [168]. A more detailed comparison requires including the proper orbital dependent cross-sections for the Fe-3d, Ge-4p and Ge-4s states. This task is complicated by the fact that the orbital decomposition in the LAPW method relies on projections onto the LAPW spheres. The Fe 3d states are almost entirely contained in the LAPW sphere, making this a good approximation. On the contrary, this is not the case for the Ge-4p and Ge-4s states, due to their extreme delocalization. This preempts the extraction of the precise Ge-4s and Ge-4p contribution to the DOS, which is prerequisite for including the cross-sections.

6.4 Fe 3s

The PES and XAS spectra shown in Figures 6.1 and 6.2 demonstrate that much like the pnictide Fe-HTSC, YFe_2Ge_2 does not seem to exhibit any spectroscopic signatures for strong electron correlations. Rather, in both classes of materials, the Fe states are found to have itinerant character with a very good correspondence between the measured electronic structure and DFT calculations. Moreover, just as seen in the pnictides, the Fe 3*s* core-level spectrum in YFe_2Ge_2 is found to exhibit a multiplet splitting (M-SP) in binding energy (BE) arising from the exchange coupling of the core 3*s* electron with the net spin S_V in the unfilled 3*d/4s* shells of the Fe emitter atom. Generally, the analysis of M-SP effects is considerably simplified by investigating shallower *ns*-core levels, like that of the 3s, as the core hole will have no net angular momentum, reducing the number of possible final states. Hence, given that M-SP occurs exclusively in atoms with the outer subshell(s) partially occupied with a non-vanishing net spin,

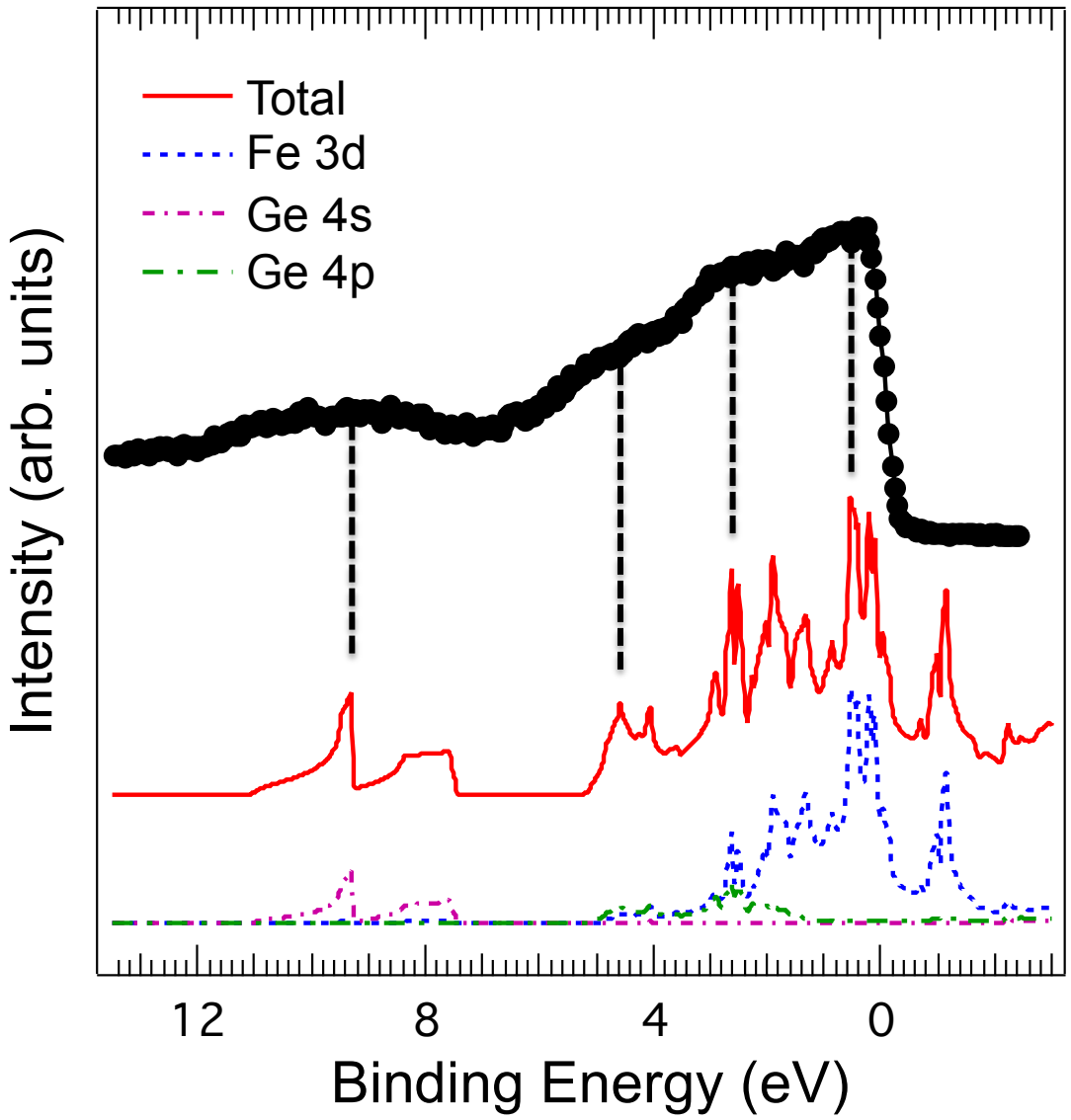

Figure 6.2: Valence band measured with photon energy hν = 907.5 eV. Note the high DOS at E_F, denoted with the vertical dashed line. Also shown are the calculated total DOS, and the Fe 3d, Ge 4s and Ge 4p partial DOS.

S_V, the Fe 3*s* spectrum in Figure 6.3(a) indicates the presence of spin moments on the Fe sites [159,162]. This finding is significant as YFe_2Ge_2 was found to exhibit simple Pauli paramagnetism [164], so it is not expected that a measurement of the Fe 3s spectrum would indicates the presence of a local magnetic moment on the Fe site. From the multiplet energy separation ΔE_{3s} an estimation of the effective net spin of the emitter atom, i.e., the local spin moment can be made. It has been shown that for itinerant systems the net spin S_V can be found by extrapolating the linear fit of the measured splitting ΔE_{3s} for ionic compounds versus $(2S_V + 1)$ [179,180]. This approach has been used for itinerant magnetic systems, including the pnictide Fe-HTSC [159,162]. Using this same approach, the value of the measured splitting $\Delta E_{3s} = 3.15$ eV obtained with a two-component fit of the Fe 3*s* spectrum (cf. Figure 6.3(a)) provides a value of the Fe spin moment $2S_V \approx 1.19\ \mu_B$ [181]. On the contrary, the Ge 3s spectrum does not seem to show any splitting, given the reasonably good fit obtained with a single Voigt function (cf. Figure 6.3(b)). A two-peaks fit would obviously give a better chi-squared, but the splitting turns out to be very small, indicating that, if any, the spin polarization of Ge is very small.

The extremely short time scales involved in the photoemission process (10^{-17}s to 10^{-16}s) can account for the disagreement with conventional static magnetic measurements, according to which Fe in YFe_2Ge_2 is non magnetic, with a Pauli paramagnetic susceptibility [164]. This indicates that, as in the pnictide Fe-HTSC, the value $\approx 1.19\ \mu_B$ extracted with PES is an estimate of the averaged magnitude of fast-fluctuating spin moments on the Fe sites. Additionally, just as observed in the Fe-HTSC, the best fit to the Fe 3*s* spectra is always obtained when using a Gaussian function to fit the peak at higher BE. From such a fit, the width of the Gaussian is found to be much larger than either that of the lower BE peak or that anticipated from experimental resolution. Indeed, a system with strong itinerant Fe-based spin fluctuations would locally mimic fluctuations in the magnitude of the moment on Fe sites, which should appear in an Fe 3*s* spectrum as sidebands at higher *BE* with the envelope of the peaks being a Gaussian, reflecting the normal character of their distribution (Figure 6.4). This is remarkably different from spin-fluctuations associated with paramagnetism due to local moments of fixed magnitude as found in most Fe compounds, since in this case all of the Fe local spin moments would exhibit the same constant value, with two peaks of similar width. Signatures of electron itinerancy and fluctuating Fe spin moments similar to those found here for YFe_2Ge_2 are also found in pnictide Fe-HTSC and other Fe-intermetallic compounds that are either near quantum critical points

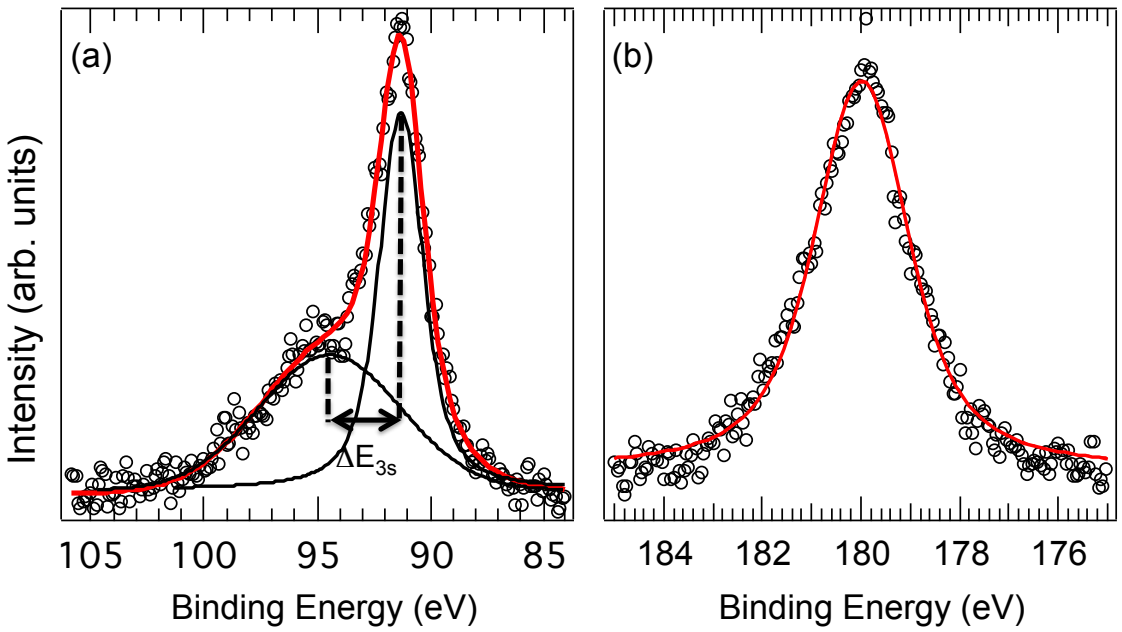

Figure 6.3: (a) Fe 3s and (b) Ge 3s core level PES spectra excited with photon energy hν = 907.5 eV. The value of the energy separation of the multiplet is ΔE_{3s} = 3.15 eV

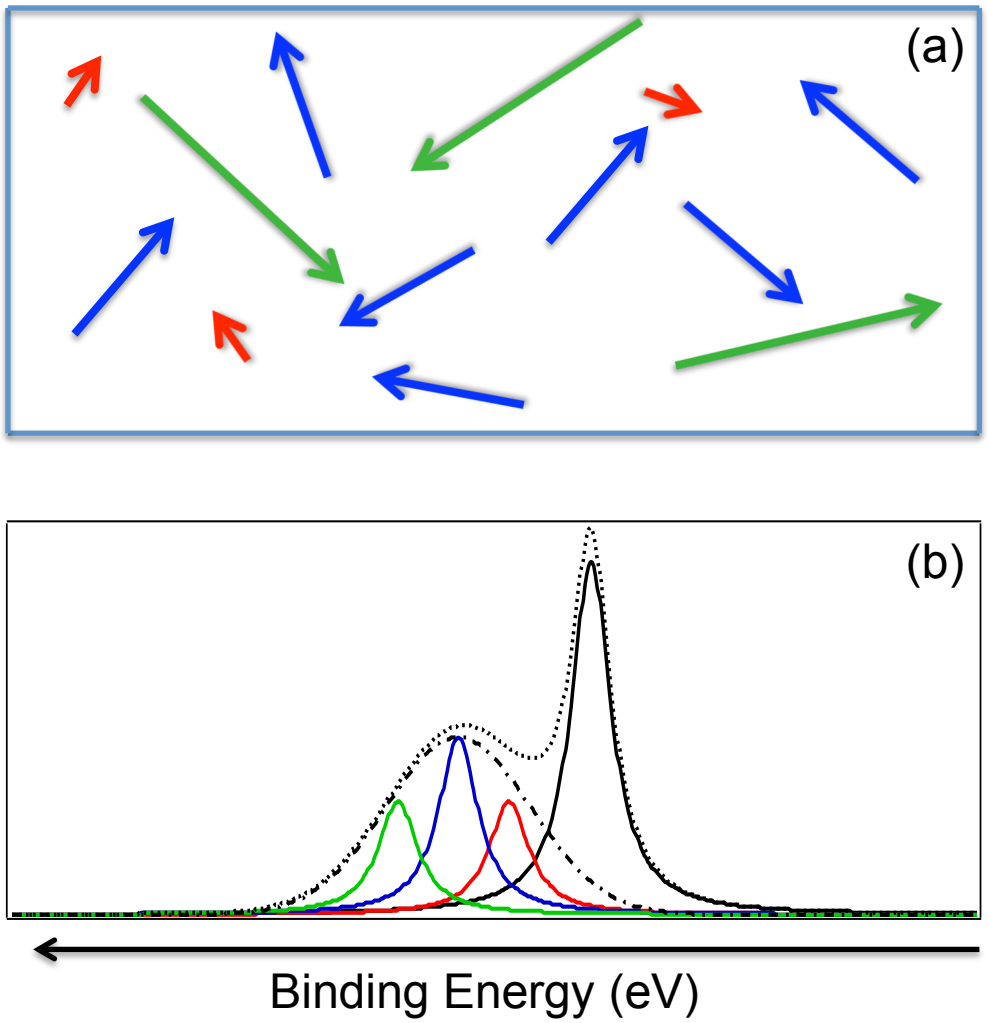

Figure 6.4: (a) Snapshot of a distribution of longitudinal spin fluctuations taken on a timescale that ranges between the electron hopping and spin procession lifetime. (b) The resultant M-SP 3s spectrum illustrating the wide Gaussian envelope of the higher BE component which is indicative of fluctuations in the magnitude of the magnetic moment

(FeAl [177], $NbFe_2$ [182]), and/or were subsequently found to have ordered magnetic ground states ($NbFe_2$,$TiFe_2$). [183,184,185].

One characteristic that may be expected for magnetism with itinerant character, as suggested for the Fe-based superconductors [186], is the presence of longitudinal spin fluctuations in the ordered state. We extended our previous calculations reported in Ref. [168], to include a stripe-like structure similar to the Fe-HTSC [167] and an additional order with the same in-plane arrangement, but antiferromagnetic stacking along the *c*-axis. The approach is the same as that used previously, i.e. a PBE generalized gradient approximation. Energies per formula unit relative to the non-spin-polarized state were calculated for ferromagnetic (-120 meV), A-type antiferromagnetic (-137 meV), C-type (-26 meV, (see ref. [168]), G-type (-4 meV), Fe-pnictide-like stripes with ferromagnetic stacking (-129 meV) and Fe-pnictide-like stripes stacked antiferromagnetically along *c* (-161 meV). These indicate, following the arguments of Ref. [167] and [168], that the magnetism has itinerant character. Additionally, there is a clear competition between the A-type and stripe-like states. Although the antiferromagnetic stacked stripe has the lowest energy, its origin in nesting of relatively small pockets as discussed by Subedi [167] means that it is a sharper feature in momentum space. As such, it may be more strongly influenced by scattering and more readily suppressed by spin-fluctuations. This is similar to a proposed scenario in the triplet superconductor Sr_2RuO_4 [187,188,189] where competition between different magnetic orders [190] is important for suppressing magnetism in favor of an unconventional superconducting state. Both the lowest energy *c*-axis stacked stripe order and the A-type antiferromagnetic orders couple strongly to electrons at the Fermi energy, as indicated by the DOS $N(E_F)$, which is reduced by magnetic ordering to 51% and 68% of the non-spin polarized value, respectively.

On the basis of the spectroscopic results presented here, the normal state of YFe_2Ge_2 is markedly similar to that of pnictide Fe-HTSC. It appears to be quite unique: It features i) no signatures of strong local Mott-Hubbard type correlations analogous to the cuprate HTSC (cf. Figure 6.1), ii) an itinerant Fe d-band character (cf. Figure 6.2), iii) a high DOS at E_F (cf. Figure 6.2), iv) an overestimation of the magnetic tendencies within DFT, and (v) the occurrence of quantum fluctuations of the Fe spin moment as revealed by multiplet splitting of the binding energy of Fe 3s core level PES spectra (cf. Figure 6.3). The 1.19 μ_B value of the Fe spin is similar to that found previously in the normal state of the pnictide Fe-HTSC $CeFeAsO_{0.89}F_{0.11}$

[159]. In the pnictide Fe-HTSC, it has been proposed that the occurrence of quantum fluctuations of the spin moment could be responsible for the DFT overestimation of the ordered spin moments [191,192,193]. There is growing evidence that strong fluctuations of the spin moment are an important defining characteristic of the normal state of the pnictides. Recent INS, XES, PES data have provided evidence of fluctuating Fe spin moments in both ordered and paramagnetic phases of several pnictide compounds. The values of the Fe spin moments are much larger than those previously found with conventional magnetic measurements such as nuclear magnetic resonance (NMR), muon spin resonance (μ-SR) and Mössbauer spectroscopy. The detection of fluctuating spin moments was possible because INS, XES and PES measurements occur on sub-picosecond time scales, much faster than the 10^{-8} s - 10^{-6} s time scales typical of NMR, μ–*S*R and Mössbauer.

In light of these facts, the apparent similarity of the magnetic (fluctuating moments), crystallographic, chemical, and electronic degrees of freedom of YFe_2Ge_2 to the Fe-HTSC is especially relevant as the Fe-HTSC are comprised of either pnictogen or chalcogen, and therefore do not contain any Ge. Consequently, the similarity of the PES and XAS spectra between YFe_2Ge_2 and the Fe-HTSC is therefore not necessarily expected. Although there are some important differences with respect to the pnictides, such as a nearby magnetic order of different nature and an unusually high specific heat, YFe_2Ge_2 is a compound that shares many of the characteristics found in the parent compounds of pnictides that were later found to host high temperature superconductivity. At this point, it should be noted that in addition to spin fluctuations, another characteristic feature of the Fe-HTSC, is that of nematicity. Within the Fe-HTSCs nematicity and its relationship to magnetism have also been discussed as being defining features in these compounds [194,195]. Furthermore, the interplay of spin and nematic fluctuations in the normal state may actually be central to high temperature superconductivity in the Fe-HTSCs [196,197,198]. With that being said, while there is no evidence as of yet for nematicity in YFe_2Ge_2, one might still speculate that high temperature superconductivity could be found in compounds based on Fe and Ge. Certainly, it will be of considerable interest to better elucidate the magnetic behavior of metallic Fe-germanide compounds and their similarities and differences from the Fe-based superconductors.

Chapter 7: Disentangling the Electronic, Lattice and Spin Dynamics in the Chiral Helimagnet $Cr_{1/3}NbS_2$

As discussed in Chapter 2, part of the main technological appeal motivating the study of $Cr_{1/3}NbS_2$ lies in the fact that the application of a modest magnetic field perpendicular to the helical axis opens up the possibility of tuning the size of the ferromagnetic domains in the chiral soliton lattice (CSL) phase [3]. In this way, the CSL acts as a tunable effective potential for itinerant electron spins, allowing for the precise control over the transport properties of itinerant spin carriers to be gained [62]. Furthermore, the high stability and robustness of the CSL phase can pave the way for other spintronic functionalities such as spin current induction [63], soliton transport [64], and current driven collective transport [65]. Consequently, the incorporation of this material into future technological devices should not only depend on the ability to manipulate the CSL spin texture in a controllable fashion, but the speed at which this manipulation can take place. As it stands, through the use of an externally applied field, this speed will be limited to the precessional time-scale of the spins. However, with the use of ultrashort laser pulses, it is oftentimes possible to manipulate the magnetic degrees of freedom on the sub-ps timescales of the spin-orbit or even the exchange interaction [199]. In this way, it may even be possible to induce the CSL transition using light.

One of the most noteworthy examples of intense, ultrashort light pulses being used to induce a magnetic transition is through the so-called inverse Faraday effect [200]. In contrast to the Faraday effect, where the plane of polarization is rotated for light transmitted through a magnetized medium, the basic premise behind the inverse Faraday effect is that the polarization of an intense, ultrashort laser pulse acts to induce a transient magnetic field in a material. This occurs when using circularly polarized fs pulses, which will produce a static magnetization along the direction of the photon helicity, allowing for the possibility to non-thermally excite and coherently control the spin dynamics without the absorption of a photon. Thus, for materials exhibiting a low absorption within the photon energy range of the pump, high fluences can be used to induce strong (> 1T) transient magnetic fields without causing significant damage to the material. For metals, however, such high fluences cannot be used, as their high absorption will

result in rapid laser heating that will ultimately lead to ablation. Consequently, even for low fluences, thermal effects, such as ultrafast demagnetization, will dominate the dynamics making the detection of any optomagnetic effect, like the inverse Faraday effect non-trivial [201].

Since $Cr_{1/3}NbS_2$ is metallic, it is expected that thermal effects dominate the magnetic dynamics in this material. However, as compared to a typical ferromagnet, the presence of a helical spin texture can lead to a coherent excitation of collective modes that are unique to helimagnetic systems. Such helimagnons have been investigated in the frequency domain using all electrical broadband spectroscopy and have been universally observed in metallic, semi-conducting and insulating chiral magnets alike [202]. Through a direct measurement of the magnetic dynamics by way of a time resolved magneto-optical Kerr effect (tr-MOKE) experiment, coherently excited helimagnon modes arising from impulsively stimulated Raman scattering were observed in the chiral helimagnet $Fe_{1-x}Co_xSi$ [203]. These strongly damped oscillations in the magnetization exhibit a characteristic scaling relation with respect to temperature and magnetic field, providing a clear signature for a helimagnon mode [36]. In such a case, launching a helical spin wave capable of being detected by optical techniques (i.e. $q = 0$) requires that a RF magnetic field be applied parallel to the helix direction so as to induce a conical state in the material. Unfortunately, as compared to $Fe_{1-x}Co_xSi$, the helical axis is the hard magnetization axis in $Cr_{1/3}NbS_2$ meaning that significantly stronger magnetic fields are needed to induce the conical phase. Consequently, despite the fact that helimagnon modes must be present in $Cr_{1/3}NbS_2$, it is unclear whether these can be coherently excited by pump-probe spectroscopies.

Given then the possibility of manipulating magnetic order on an ultrafast timescale, as well as the opportunity for studying collective modes in real-time within both the helimagnetic, and CSL phase, a characterization of the static and transient magneto-optical properties of $Cr_{1/3}NbS_2$ is first needed. In such a case, static MOKE, transient reflectivity and tr-MOKE measurements were carried out so as to disentangle the relevant contributions arising from electron, lattice and spin to the overall relaxation dynamics. It was confirmed that $Cr_{1/3}NbS_2$ possesses a magnetic easy plane as shown in [5], while single color optical pump-probe experiments reveal significant differences in the dynamics of NbS_2 and $Cr_{1/3}NbS_2$. Lastly, a long demagnetization dynamic was observed in the magnetic phase of $Cr_{1/3}NbS_2$ suggesting the spins to be thermally insulated from the electronic degrees of freedom. However, rather than being

indicative of a localized spin moment, the fact that the magnetic dynamic is not directly affected by optical excitations may simply imply spin flips occurring via Elliot-Yafet mechanism are inefficient due to an imbalance in the spin polarized density-of-states (DOS) in the ferromagnetic state.

7.1 Static MOKE

As was discussed in section 3.2.2, a measurement of the magnetization through MOKE offers a means of quantifying the degree of magnetic anisotropy in a single crystal or thin film [127]. Most notably, for an H-field applied within the ab-plane, the intensity and polarization state of light reflected from the sample will change based upon the direction that the magnetization makes relative to the scattering plane. Ultimately, by exploiting the angular dependence of the light's intensity as it passes through the analyzer used within a MOKE configuration (c.f. Figure 2.13), it is possible to isolate the contributions deriving from the transverse, longitudinal and polar magnetization.

Such a decomposition is shown for $Cr_{1/3}NbS_2$ in Figure 7.1. Specifically, for this measurement a 200 Oe field is applied parallel to the transverse direction (Figure 7.1(a)), while a 360 Oe field is applied along the polar direction (Figure 7.1(b)). From this it is evident that the large transverse component of the magnetization relative to that of the longitudinal implies that the magnetization vector will predominately align parallel to the applied field direction. This is most clearly illustrated by the inset in Figure 7.1(a) where the transverse and longitudinal magnetization are plotted relative to one another. Given that the magnetization seems to always align along the applied field direction regardless of sample orientation, such a finding suggests there to be no preferred magnetization direction within the ab-plane. In contrast, Figure 7.1(b) shows that the magnetization measured along the c-axis is significantly weaker despite a stronger applied field. Coupled with the absence of saturation along the polar direction, these findings are consistent with those from [5] indicating the c-axis to be the hard magnetization axis. Similarly, by correcting for induction effects through plotting the coercivity with respect to the strength of the applied AC magnetic field, an extrapolation to zero field reveals there to be only a small intrinsic hysteresis. This is likewise consistent with the results presented in [5], meaning that within the ~35 nm skin depth of our MOKE measurements, the findings are fully consistent with that of the bulk magnetization measurements made on $Cr_{1/3}NbS_2$.

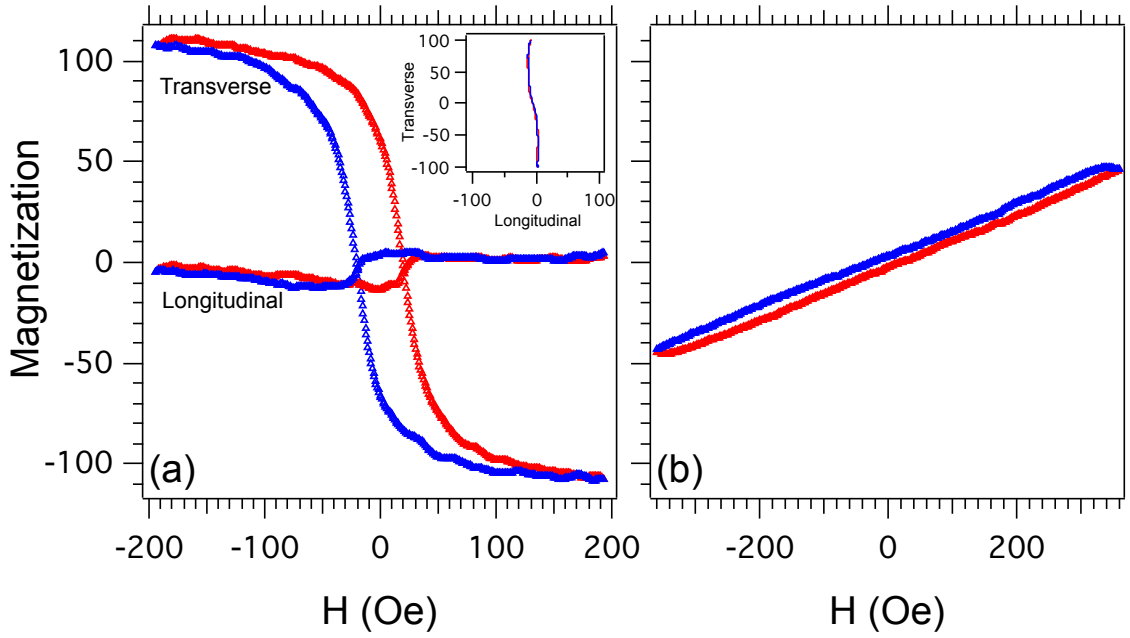

Figure 7.1: Decomposition of the magnetization along (a) transverse/longitudinal and (b) polar directions as measured by MOKE. A direct comparison of the transverse and longitudinal MOKE signal shown in the inset of (a) reveals that the magnetization predominately aligns parallel to the applied field direction within the ab-plane

7.2 Transient Reflectivity

To recognize the corresponding magnetic dynamic that arises within this material, it is important to first develop a systematic understanding of the dynamical response for the electronic and lattice degrees of freedom in the paramagnetic phase. Just as was done in section 5.2, such an understanding can be facilitated by directly comparing spectra collected from NbS_2 with those from $Cr_{1/3}NbS_2$. These results are presented in Figure 7.2, where transient reflectivity measurements following the excitation of a 1.0 mW (~3.0 mJ/cm^2) pump pulse centered at 1.55 eV provide a snapshot of the relaxation dynamics over both short (4.0 ps) and long (50 ps) time delays. Based on a qualitative assessment alone, it is evident that Cr intercalation of NbS_2 leads to significant changes in the dynamics. Most notably, aside from a change in sign, $Cr_{1/3}NbS_2$ exhibits two distinct coherently excited phonon modes (Figures 7.2(c) and 7.2(d)), as compared to the weaker more rapidly damped collective mode found in NbS_2 (Figure 7.2(b)). For both compounds, the period and phase of these coherent modes were found to exhibit no dependence on light polarization.

In order to better quantify the difference between the dynamical response of NbS_2 and $Cr_{1/3}NbS_2$, multi component fitting of the transient reflexivity spectra were performed so as to isolate the various relaxation processes that comprise the spectra. Noting that the creation of a transiently excited state results from a pump pulse having a finite temporal width σ, the subsequent relaxation dynamics for the i^{th} process can be modeled as the convolution of a Gaussian with an exponential decay. Here, each decay can be characterized by its own time constant τ_i, while the Gaussian serves to represent the temporal profile, and thus time resolution, of the pulse. The result of this convolution can be given analytically by

$$\sum_{i=1}^{N} A_i e^{\frac{1}{2}\left(\left(\frac{\sigma}{\tau_i}\right)^2 - \frac{2}{\tau_i}(t-t_0)\right)} Erfc\left(\frac{1}{\sqrt{2}\sigma}\left(\frac{\sigma^2}{\tau_i} - (t-t_0)\right)\right) \qquad (7.1)$$

where *Erfc(x)* denotes the complimentary error function, while A_i represents the amplitude of the i^{th} process in the reflectivity spectrum. From this expression, it is a simple manner to generalize to a description of coherently excited collective modes by substituting $e^{-(t/\tau - i(\omega t+\varphi))}$ for $e^{-t/\tau}$ in the convolution. In this way, important information regarding the frequency, and phase of the collective mode can be gained.

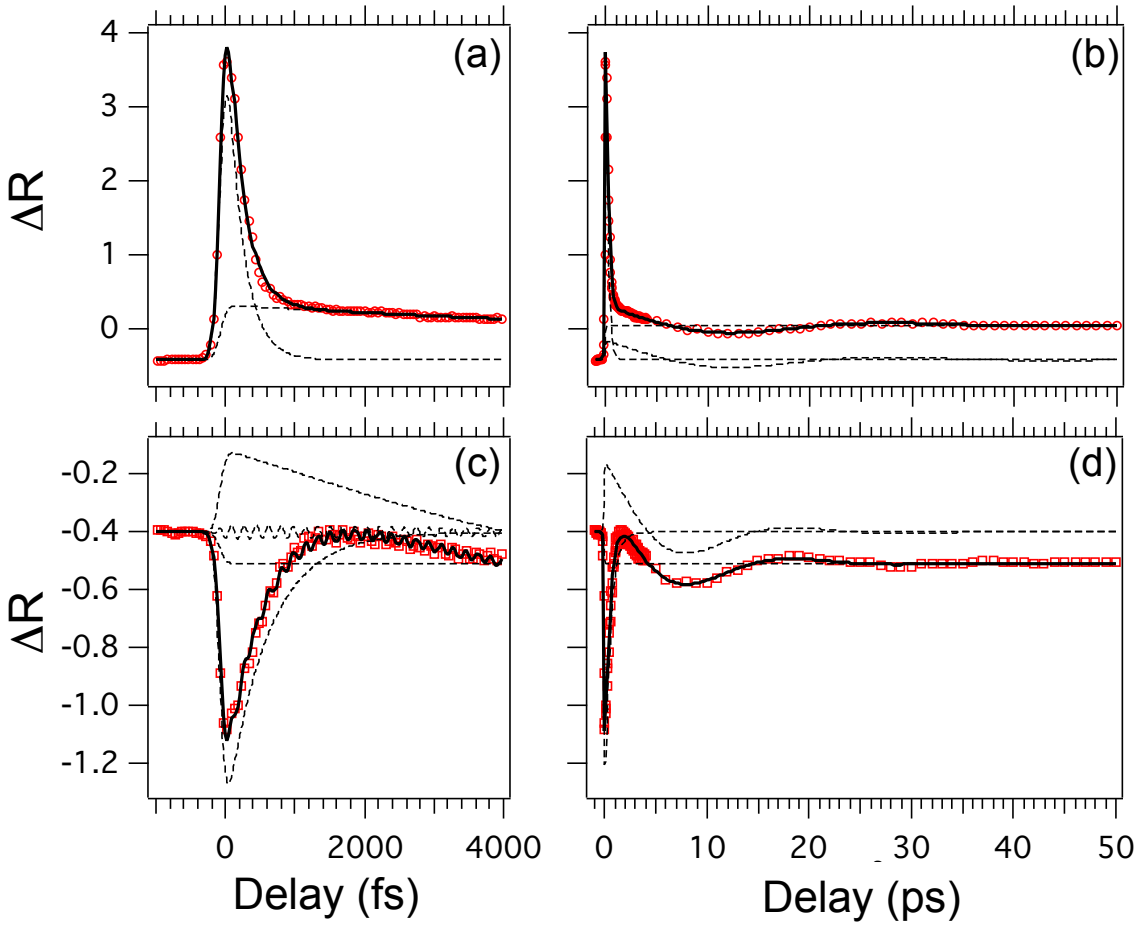

Figure 7.2: Transient reflectivity spectra of NbS_2 ((a) and (b)) and $Cr_{1/3}NbS_2$ ((c) and (d)) measured over short- and long-time delays. Spectra have been measured using an amplified Ti:Sapphire laser system operating a 1 kHz repetition rate

For the typical fits shown in Figure 7.2, the examination of systematic trends that develop as a function of pump fluence allows for greater insights into the relaxation dynamics and nature of the coherently excited phonon modes. Such trends are presented in Figure 7.3, where the focus remains on a comparison between the amplitude of the reflectivity change, electronic relaxation time, and low frequency collective mode common to both NbS_2 and $Cr_{1/3}NbS_2$. From such a comparison, it was found that NbS_2 and $Cr_{1/3}NbS_2$ similarly exhibit a saturation in their response for a pump power exceeding 1.0 mW. However, as is shown in Figure 7.3(a), the magnitude of the reflectivity change is an order of magnitude smaller for $Cr_{1/3}NbS_2$ as compared to that from NbS_2. Furthermore, the consistently longer electron relaxation times exhibited by $Cr_{1/3}NbS_2$ in Figure 7.3(b), suggests that Cr intercalation may actually weaken the coupling of the electronic degrees of freedom with that of the lattice and spin. Such a claim is implicitly rooted in an effective temperature model where a "hot" population of transiently excited electrons will necessarily decay through an exchange of energy with the lattice and spin. Thus, the stronger the coupling, the more efficient the energy exchange, the faster the decay rate will be.

Regarding the low frequency coherent phonon modes present in both the parent and Cr-intercalated compound, fits of the transient reflectivity spectra reveal such modes to display a cosine-like behavior indicative of a displacive excitation (Figure 7.2). In such a case, the excitation of a coherent phonon comes about as a consequence of long-lived, pump induced changes that serve to suddenly shift the vibrational potential. From a measure of the fluence dependence it is found from Figure 7.3(c) that the oscillation amplitude of the coherent mode in NbS_2 remains fairly constant after 0.5 mW, while the amplitude for the low frequency phonon mode in $Cr_{1/3}NbS_2$ continues to grow with increasing pump power. Interestingly, despite this increase in amplitude, the period shown in Figure 7.3(d) stays at a near constant 21 ps (48 GHz), meaning that such a mode is not driven out of the harmonic regime. In contrast, the period of the coherently excited mode in NbS_2 is found to change from 41 ps (24 GHz) to 30 ps (33 GHz) following an increase of pump power. However, rather than being a signature of anharmonicity, this is most likely an artifact from least squares fitting that comes about due to the strong dampening of this mode. Hence, given the low frequency, strong dampening and, in the case of $Cr_{1/3}NbS_2$, growth with increasing pump power, these low frequency coherent phonon modes found in NbS_2 and $Cr_{1/3}NbS_2$ most likely derive from interlayer breathing or shear modes.

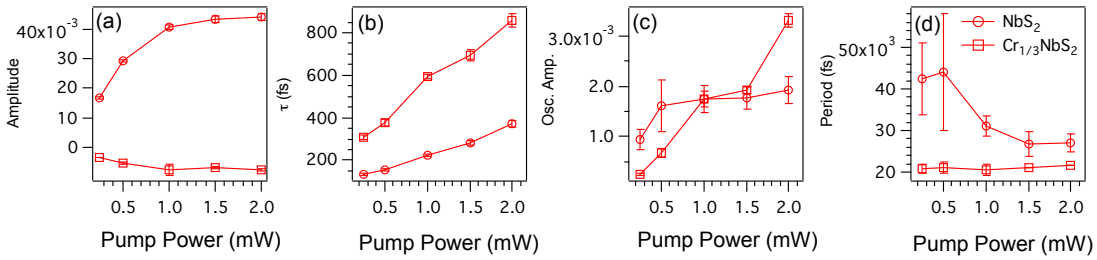

Figure 7.3: Summary of results from a room temperature fluence dependence comparing the fit parameters of NbS_2 (open circles) with $Cr_{1/3}NbS_2$ (open squares). Here, parameters for (a) the amplitude of the transient reflectivity, (b) electron relaxation time, (c) amplitude of low frequency coherent mode, and (d) period of low frequency coherent mode are plotted as function of pump power

In addition to the excitation of a low frequency coherent phonon mode, the impulsive nature of the pump pulse serves to likewise excite a high frequency coherent mode that is unique to $Cr_{1/3}NbS_2$. As is shown more clearly in Figure 7.4, the corresponding phase of this oscillation is characterized as being sine-like. Such a phase is a defining feature of coherently excited phonon modes arising from an impulsively stimulated Raman process. Within this process, the broad bandwith of an ultrashort laser pulse yields multiple combinations of two photon difference frequencies required for stimulated Raman scattering. In this way, when the pulse duration is short as compared to the vibrational period, it is expected that the driving force result in an impulsive change to the velocity of a harmonic oscillator without affecting its initial position. For phonon modes launched by such an excitation pathway in $Cr_{1/3}NbS_2$, a Fourier transform of the transient reflectivity shown in the inset of Figure 7.4 reveals a single mode having a frequency of 5.5 THz. By fitting the spectrum, this coherent mode was found to have a relatively long dephasing time of > 7 ps indicative of a longer phonon lifetime. Coupled to the fact that such a mode is unique to the Cr intercalated compound, the long dephasing time and high frequency leads to the most likely assignment for this mode as an intralayer, intercalate phonon.

Having fully characterized the relaxation dynamics within the paramagnetic phase of $Cr_{1/3}NbS_2$, a comparison of the transient reflectivity measured above and below the magnetic transition temperature ($T_C = 131$K) can reveal changes in the spectrum that arise due to a magnetic dynamic. As is shown in Figure 7.5, this can be identified by an exponential rise having a considerably longer characteristic timescale than that corresponding to the electronic and lattice degrees of freedom. Given this material to be metallic, it is expected that the excitation by an ultrafast laser pulse will give rise to a demagnetization dynamic in the reflectivity spectrum. The relevant timescale of this process will depend sensitively on the nature of the spin-flip mechanism. Chief among these being Stoner excitations, inelastic electron-spin-wave scattering or impurity/phonon mediated spin-flip events. Therefore, to gain further insights, tr-MOKE measurements were carried out so as to isolate the features in the reflectivity spectrum that specifically relate to the recovery of the magnetic state.

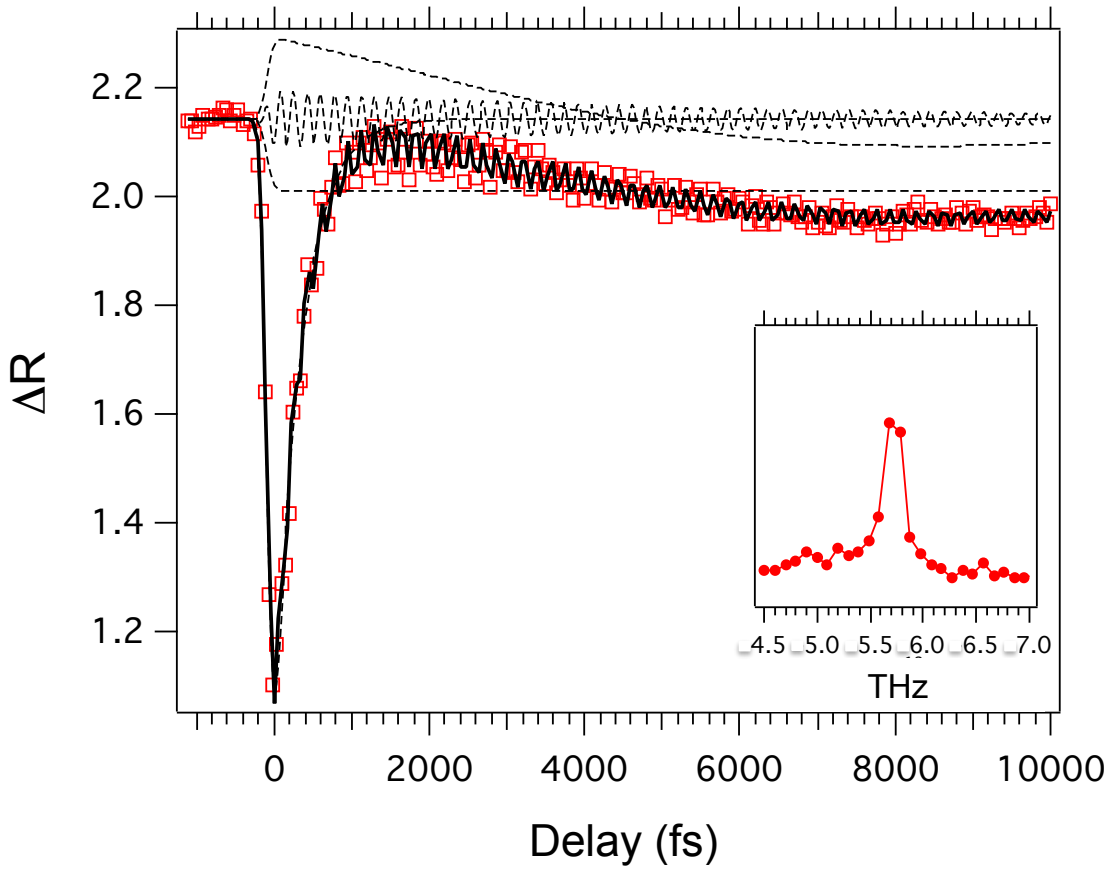

Figure 7.4: Transient reflectivity spectrum of $Cr_{1/3}NbS_2$ taken with a 50 fs step size over a 10 ps delay so as to better study the behavior of the high frequency coherent phonon mode. Fourier transform shown in inset reveals a single mode at ~5.5 THz, which is found from fitting of the real time dynamic to have a long dampening lifetime

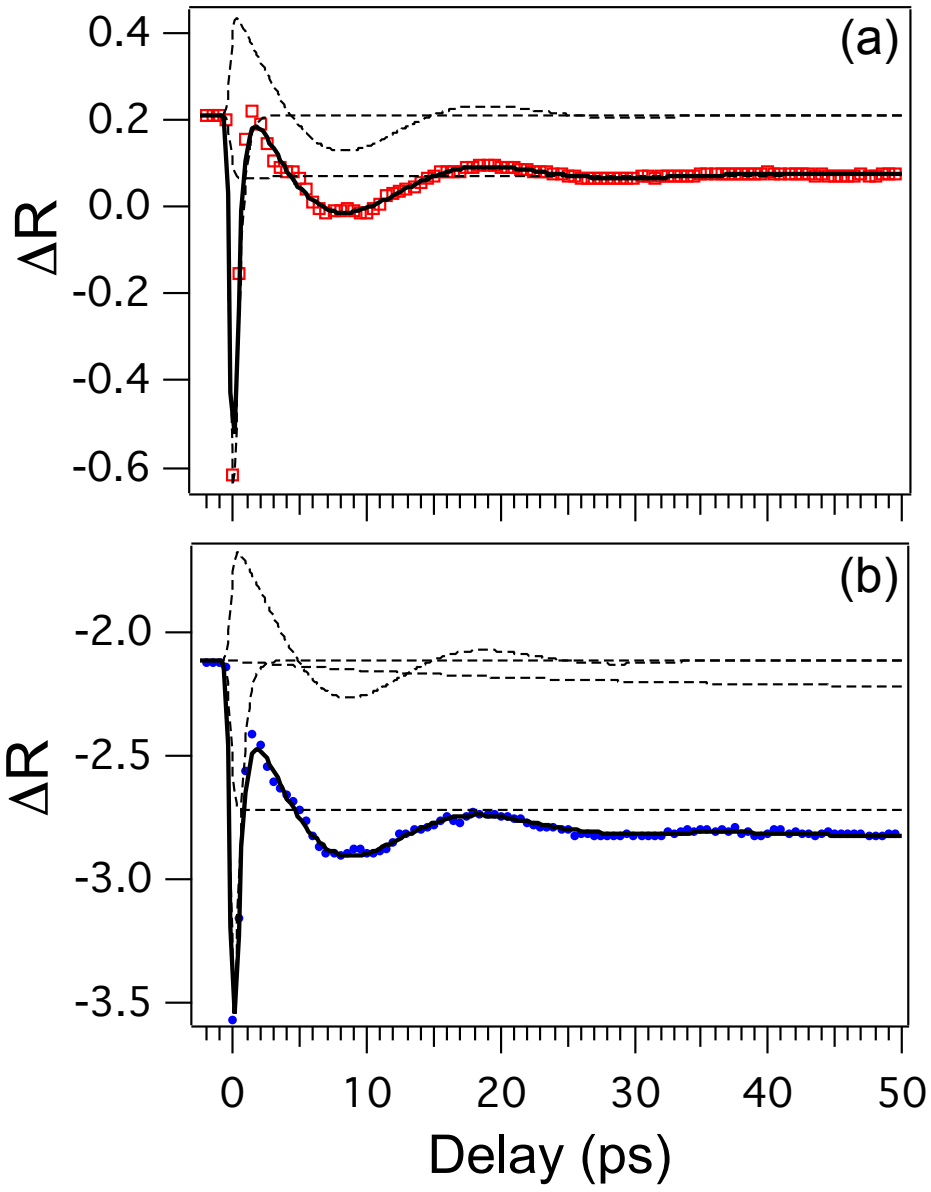

Figure 7.5: Comparison of (a) room temperature (300K) and (b) low temperature (77K) transient reflectivity spectra over a 50 ps delay. Note the presence of the long demagnetization dynamic in (b)

7.3 Time-Resolved MOKE

Figure 7.6 shows the transient reflectivity and tr-MOKE measurements performed on $Cr_{1/3}NbS_2$ in the magnetic phase using a non-collinear optical parametric amplifier (NOPA) centered at 680 nm. As compared to the reflectivity spectrum shown in Figure 7.5(b), these results demonstrate a more pronounced demagnetization dynamic, capable of being detected by tr-MOKE. In noting that a MOKE signal can depend sensitively on wavelength [128], the choice of using an NOPA stems from the fact that the wavelength can be tuned to exactly match that used for static MOKE measurements. This allows for a more direct comparison to be made between the transient and static MOKE signals.

A measure of the demagnetization dynamic as a function of pump power reveals a significantly long rise times ranging from 28 ps to 53 ps (Figure 7.6(b)). Given such a long buildup to this dynamic, it is evident that the demagnetization is not directly affected by the optical excitation itself. Thus, these results would seemingly imply that the electronic and spin degrees of freedom are thermally isolated from one another as is most often observed within magnetic dielectrics [204]. Here, localized electrons that serve to form the spin moments will rapidly relax following a transient excitation. This will then leads to a heating of the spin system that occurs as a result of an increase in lattice temperature. However, in regards to $Cr_{1/3}NbS_2$, the findings of ResPES and ARPES presented in Chapter 5 clearly illustrates a coupling between the electronic and spin degrees of freedom that is incongruous with a treatment of these being isolated from each other. Thus in an effort to rationalize the long demagnetization dynamic observed in $Cr_{1/3}NbS_2$, it may be that spin flips occurring via Elliot-Yafet mechanism are inefficient due to a significant imbalance in the spin polarized DOS in the ferromagnetic state.

The Elliot-Yafet mechanism describes a single-particle-like spin-flip scattering process from an impurity or phonon that is attributed to a band mixing of spin-up and spin-down states arising from the spin-orbit interaction [205,206]. For instances where there are significantly fewer available states in the minority spin channel, energy transfer between the electronic and spin degrees of freedom becomes blocked. This result in an analogous situation to that of magnetic dielectrics, where energy transfer will necessarily occur through the lattice. Since the lattice and spin degrees of freedom are only weakly coupled, this result in a long demagnetization dynamic. In the most extreme example where there are no available states for an electron undergoing a spin-flip event to scatter, such a characteristically long demagnetization

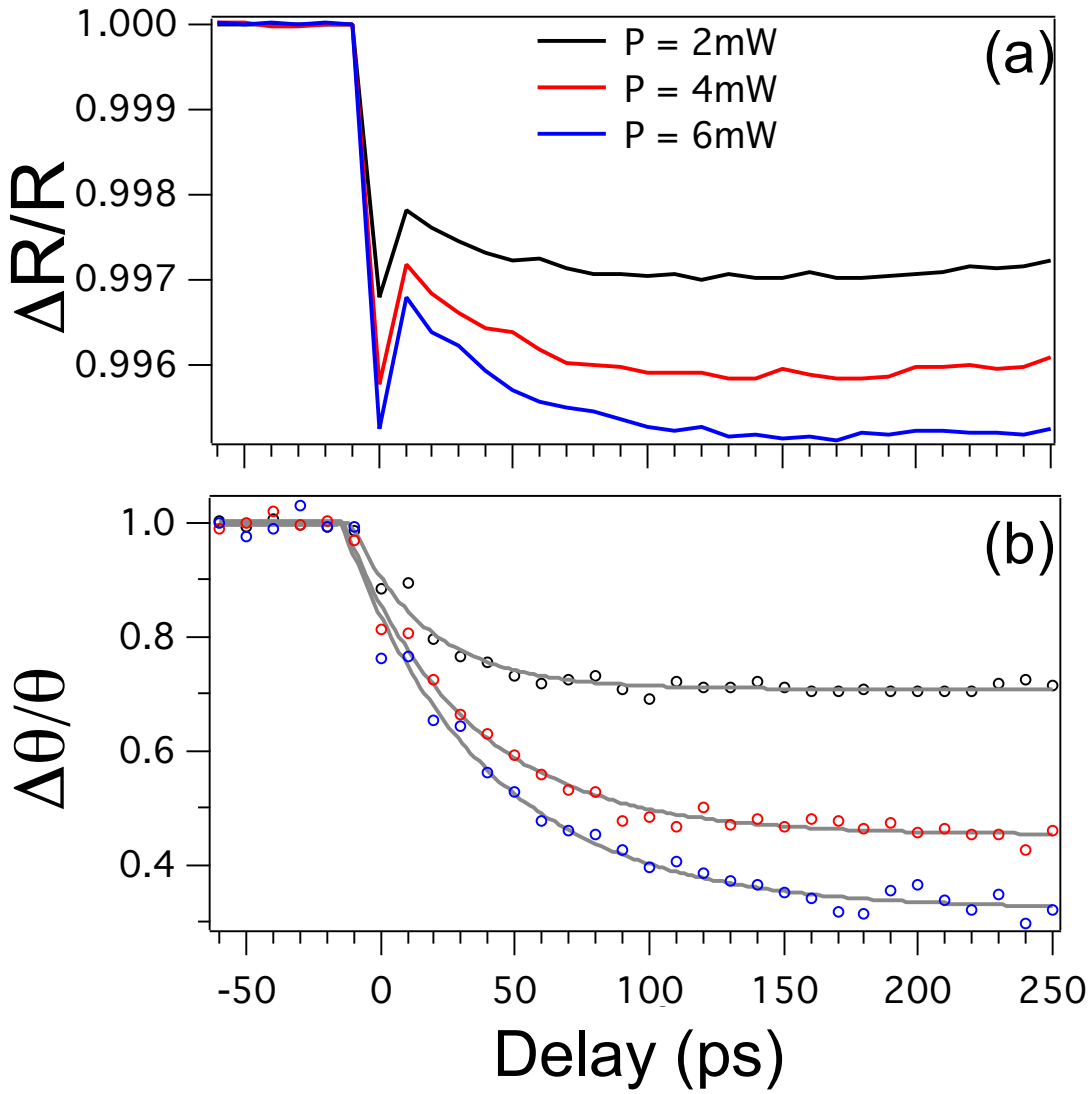

Figure 7.6: (a) Transient reflectivity and (b) time-resolved MOKE measurements made on $Cr_{1/3}NbS_2$ in the magnetic phase using a NOPA having an output centered at 680 nm

dynamic has been taken as a defining feature for half metallicity [207]. While a long demagnetization dynamic alone is insufficient for a claim of half-metallicity in $Cr_{1/3}NbS_2$, the imbalance of spin-up and spin-down states shown in the calculated DOS of Figure 7.7 supports the notion that spin-flip events will be inefficient within this compound. In this way, the results from optical pump and probe, ResPES and ARPES all yield a consistent picture regarding the physics of this material.

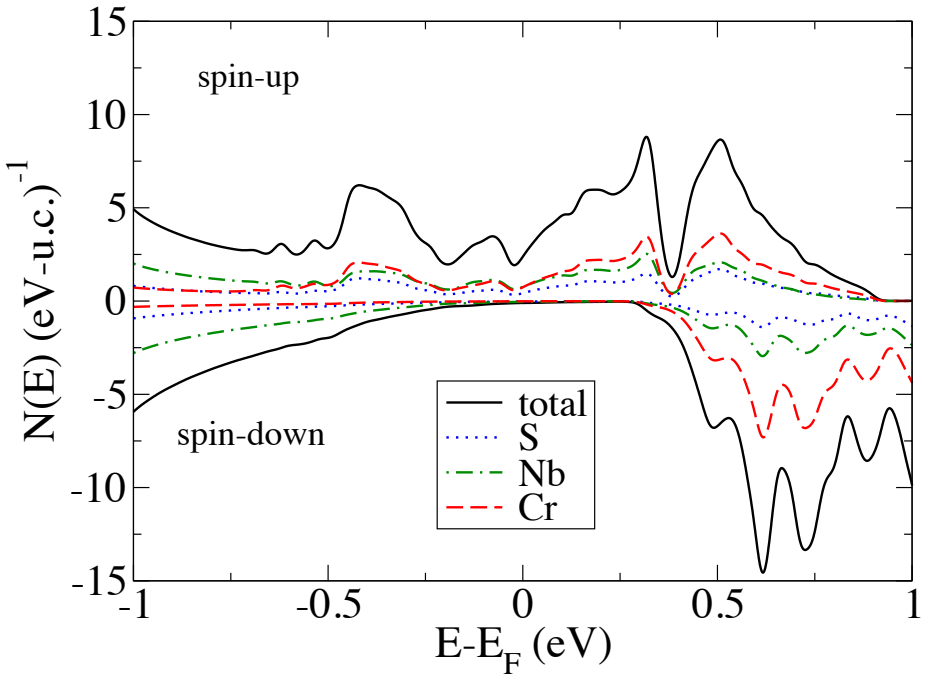

Figure 7.7: Calculated spin-polarized density-of-states of $Cr_{1/3}NbS_2$ in units of eV^{-1} per unit cell. Note the lower values of the DOS for the spin down channel for energies of ca. ± 250 meV from E_F

Chapter 8: Time-Resolved ARPES: Current Status and Future Directions

From the previous chapter, insights into the various interactions that exist between electron, lattice, and spin degrees of freedom were gained through a measure of the real-time relaxation dynamics using optical pump and probe spectroscopy. While such a technique has certainly proved its value, the fact that these experiments were performed using just the fundamental frequency of a Ti:Sapphire implies that only a temporal resolution can be achieved. In this way, an optical pump-optical probe experiment simply serves as a means of capturing the time evolution of the reflectivity, without providing any additional spectroscopic insights. Recalling from section 3.2.1, that within the initial stages of the pump excitation a non-equilibrium distribution of photo-excited electrons is created. Thus, without having any means of characterizing this transiently excited non-equilibrium state, there is a certain degree of ambiguity associated with what physically gives rise to a change in the transient reflectivity.

For this reason, a direct probe of the changes that occur within the electronic structure is needed so as to elucidate the role that an intense, optical pump pulse has particularly in regards the generation of photo-induced phase transitions or the creation of hidden states. In such a case, the ability of ARPES to not only provide a measure of the electronic structure with both an energy and momentum resolution, but also its capability of gaining valuable insights into the many-body interactions by way of the single particle spectral function makes this technique a premier tool for studying the time evolution of the electronic structure. However, in order to generate photoelectrons within a time-resolved ARPES scheme, the excitation radiation of the probe must be sufficiently energetic so as to overcome the work function of the spectrometer. Given a typical work functions to be on the order of 4-5 eV, this then requires a frequency quadrupling of the fundamental 1.55 eV of the Ti:Sapphire. Ultimately, such a process can be accomplished by the generation of the fourth harmonic through use of non-linear optics.

8.1 Non-linear Optics

Up until the advent of lasers, it was sufficient to describe the resultant polarization of a dielectric medium as being linearly dependent on the electric field of the incident light. Namely, this relation is simply given as

$$\vec{P} = \epsilon_0 \bar{\bar{\chi}} \vec{E} \tag{8.1}$$

where the response of the medium is dictated by the dielectric susceptibility, $\bar{\bar{\chi}}$, which takes on the form of a tensor so as to account for any anisotropies that may be present. More generally, the polarization should actually be expanded in terms of a power series,

$$P_i = \epsilon_0 \chi_{ij} E_j + \epsilon_0 \chi_{ijk} E_j E_k + \epsilon_0 \chi_{ijkl} E_j E_k E_l + \cdots \tag{8.2}$$

where the higher order terms make a non-negligible contribution only when the strength of the external field is on the order of that which corresponds to the interatomic electric field (~10^8 *V/m*) [137,208,209]. As mentioned, such field strengths cannot be achieved using conventional light sources, however with the high peak-power arising from a femtosecond laser pulse, these electromagnetic field strengths can ultimately be realized. Under such conditions, second and third order non-linear processes will start to occur, which, in turn, will give rise to a number of interesting phenomena including the generation of high harmonics.

To develop a conceptual understanding for how this comes about, consider a simple example, in which an oscillatory electric field is incident on an isotropic dielectric medium. Here, the resultant polarization will be given by

$$P = \epsilon_0 \chi^{(1)} E_0 cos(\omega t) + \epsilon_0 \chi^{(2)} E_0^2 cos^2(\omega t) + \epsilon_0 \chi^{(3)} E_0^3 cos^3(\omega t) + \cdots \tag{8.3}$$

which by making use of trigonometric identities allows for this expression to be re-cast in the form of

$$P = \frac{1}{2}\epsilon_0 \chi^{(2)} E_0^2 + \epsilon_0 \left(\chi^{(1)} + \frac{3}{4}\chi^{(3)} E_0^2\right) E_0 \cos(\omega t) + \frac{1}{2}\epsilon_0 \chi^{(2)} E_0^2 \cos(2\omega t) + \frac{1}{4}\epsilon_0 \chi^{(3)} E_0^3 \cos(3\omega t) + \cdots \tag{8.4}$$

Within this equation, the first term represents the direct current electric field response deriving from a second order effect known as optical rectification. While no further mention of this process will be made, it is worth noting that optical rectification is one of the primary means by which THz radiation can be generated from a laser source. Unlike the first term, the second term is linear in field. However, aside from $\chi^{(1)}$, there is an additional term deriving from a third order

process that is proportional to the intensity of the incident wave. Recalling that the refractive index is determined by $\eta = \sqrt{1+\chi}$, it is evident that this term ultimately serves as the origin for the optical Kerr effect discussed in section 4.2.1. Finally, the terms most relevant to the subsequent discussion of frequency addition are given by the third and fourth terms respectively. By examining the form of these two expressions, it is evident that for an incident wave of frequency ω, these terms imply that the resultant output will be either twice (2ω), or three times (3ω) the input frequency. For this reason, such a process is referred to as second (SHG) and third harmonic generation (THG).

In regards to such processes, due to the simplifying assumptions made in the derivation of equation 8.4, it is not evident that the generation of the second and third harmonic requires that certain constraints on the optical medium be in place. Most notably, thanks to the high peak power needed for these non-linear processes to occur, it follows that the medium will need to be hard enough so as to avoid damage by the intense beam. Furthermore, as it specifically pertains to SHG and THG, this medium will also need to be transparent to not only light at the fundamental frequency ω, but at 2ω and 3ω as well. Additionally, it can be readily shown based on symmetry arguments that the generation of even harmonics through SHG and FHG will only occur in crystals lacking inversion symmetry. Taken together, these constraints then serve to limit the available number of non-linear optics to insulating crystals having a space group that lacks in inversion symmetry. Of these, one of the most common employed is β-BaB_2O_4 (β-BBO), but many others can be used depending upon the spectral range that one wishes to access [137].

While the generation of the second harmonic requires an anisotropic crystalline medium to occur, the third harmonic turns out to be free from this constraint and can be generated in any medium, including an isotropic medium such as a gas or liquid. However, as compared to a second order process, producing the third harmonic in this way is inefficient and is for this reason not a common means of obtaining THG. Rather a more efficient means of producing the third harmonic can be accomplished through a process known as sum frequency generation. Here, a light pulse having a frequencies $\omega_1 = \omega$ is combined with another pulse whose frequency is $\omega_2 = 2\omega$ so as to yield $\omega_3 = \omega+2\omega = 3\omega$. Unlike, the THG process described in equation 8.4, sum frequency generation is a second order process that has the additional requirement that both light pulses need to be overlapped in time and space. As it turns out, sum frequency generation

is just one of many frequency mixing techniques that includes difference frequency generation and higher order four-wave mixing. Thus, given the possibility of having all manner of non-linear processes, there must then be a means by which one process can be enhanced over another. This can ultimately be accomplished through selecting the appropriate phase matching condition.

To do so, begin by returning to the expression for the wave equation in a dielectric medium

$$\vec{\nabla}\times\vec{\nabla}\times\vec{E} + \frac{1}{c^2}\frac{\partial^2\vec{E}}{\partial t^2} = -\mu_0\frac{\partial^2\vec{P}}{\partial t^2} \tag{8.5}$$

Typically, when rewriting $\vec{\nabla}\times\vec{\nabla}\times\vec{E} = \vec{\nabla}\left(\vec{\nabla}\cdot\vec{E}\right) - \vec{\nabla}^2\vec{E}$, the divergence term can be taken as zero since the medium is often assumed to be spatially uniform. In such a case, this then leads to a familiar form of the wave equation. However, at high field intensities, such as that achieved within the non-linear optical regime, this assumption will no longer be valid. Consequently, in considering the simplest example where two collinear beams having a frequency ω_1 and ω_2 are incident on a non-linear, lossless medium that serves to generate $\omega_3 = \omega_1 + \omega_2$, the wave equation then becomes

$$\frac{d^2E_3}{dz^2} + 2ik_3\frac{dE_3}{dz} = -\frac{{\mu_0}^2\chi^{(2)}\omega_3^2}{2\pi^2}E_1E_2e^{i(k_1+k_2-k_3)z} \tag{8.6}$$

Under the slowly varying envelope approximation, the first term can be neglected, leading to

$$\frac{dE_3}{dz} = i\frac{{\mu_0}^2\chi^{(2)}\omega_3^2}{4k_3\pi^2}E_1E_2e^{i\Delta kz} \tag{8.7}$$

where $\Delta k = k_1 + k_2 - k_3$. Finally, by solving for E_3 after integrating over a length L that the beam travels through the optics, the resultant intensity will be proportional to

$$I \propto \frac{sin^2\left(\Delta kL/_2\right)}{\left(\Delta kL/_2\right)^2} \tag{8.8}$$

This factor is referred to as the phase mismatch factor and will be sharply peaked at $\Delta k = 0$. In other words, the phase matching condition ensures that the intensity of light generated by the non-linear process $\omega_3 = \omega_1 + \omega_2$ is maximized when photon momentum is conserved. Using the photon dispersion relation, the expression for momentum conservation can be written as

$$\frac{\eta_1\omega_1}{c} + \frac{\eta_2\omega_2}{c} - \frac{\eta_3\omega_3}{c} = 0 \tag{8.9}$$

where η denotes the index of refraction. The effect of making such a change is to shift the perspective to that of a wave propagating through the medium. In then taking the generation of

the second harmonic ($\omega_1 = \omega_2$) as an example, the corresponding phase matching condition will dictate that

$$\omega_3 \eta_3 = 2\omega_1 \eta_1 \tag{8.10}$$

Recalling from section 4.2.2, that the refractive index is not constant in wavelength, the only way that this condition will be satisfied is through use of a birefringent crystal. This is attributed to the fact that the index of refraction depends upon the light's polarization and propagation direction within these crystals. For this reason, the most common way of achieving phase matching is through either angle or temperature tuning, whereupon the propagation of the incident and generated light can be directed along the ordinary or extraordinary axis of the crystal. Specifically, depending on the particular non-linear process to be enhanced, a certain type of phase matching may be preferably over another. Namely for type I phase matching, the polarization of both ω_1 and ω_2 incident on the optic will be the same, while the generated light will have an orthogonal polarization and will propagate along a different optical axis in the crystal. This type of phase matching is ideally suited for SHG. In contrast, when ω_1 and ω_2 are orthogonally polarized, each incident beam can be made to propagate along a different axis. In such a case, the type II phase matching condition, which is more favorable for sum and difference frequency generation, can then be met.

8.2 Optical Layout

Now that a sufficient background in non-linear optics has been developed, a detailed description of the optical layout for the time-resolved ARPES system (tr-ARPES) can be given. As is shown in Figure 8.1, this set-up consists of two optical tables—one located within the laser hutch where transient reflectivity measurements are performed, while the other is in front of the ARPES chamber where the generation of the fourth harmonic takes place. In all cases, reflective optics are used as much as possible so as to avoid loosing time resolution by way of chirping the pulse. Seeing as the beam is divergent as it exits the compressor, high reflective mirrors are used to direct the beam towards a reflective telescope comprised of two spherical mirrors having a focal length f = 100 mm. Here, care is made to ensure the beam strikes the center of the optic near normal incidence so as to avoid any unwanted aberrations such as astigmatism.
Once recollimated, an 80T/20R plate beam splitter transmits the intense pump beam to an optical delay stage having a 0.5 μm (3.33 fs) resolution, while the reflected probe beam is directed

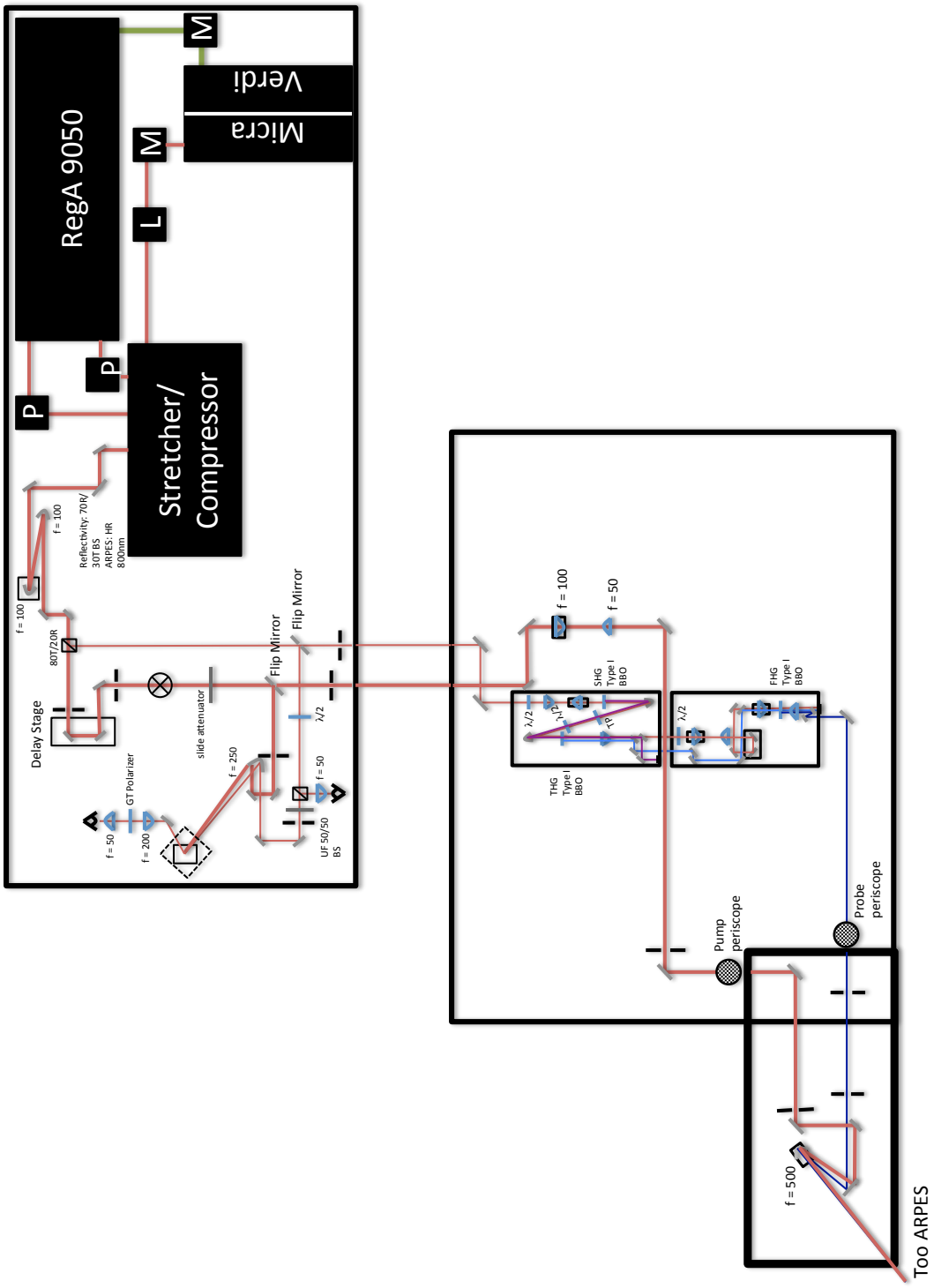

Figure 8.1: Schematic diagram of the optical layout for transient reflectivity and time-resolved ARPES

further downfield. From this beam splitter, it is necessary that the separate path lengths taken by pump and probe exactly match so as to maintain a well-defined temporal relation between the two pulses. With that being said, flip mirrors located at the end of the table can then be used to either direct the beams further downfield for optical pump-probe measurements or out of the laser hutch to the second optical table for tr-ARPES.

On the second table, the probe will undergo a frequency quadrupling through two separate stages. The first entails the generation of the third harmonic through summing the second harmonic and fundamental frequency, while the second serves to generate the fourth harmonic through a sum of the third harmonic and fundamental. The advantage of using the so-called "three plus one" scheme over simply frequency doubling the second harmonic is that light deeper in ultra-violet (UV) can be produced in this way. Namely, the resultant UV light generated will be π-polarized and centered at 195 nm (6.36 eV), which is just below the absorption threshold of the β-BBO used for the frequency conversions. As is built, all β-BBO crystals are cut for type I phase matching, with the incident light being σ-polarized and the phase matching condition achieved through angle tuning. Finally, while the generation of the fourth harmonic necessarily entails that the separate path lengths taken by the third harmonic and fundamental must match, the generation of the third harmonic makes use of a time-plate making it such that the second harmonic and fundamental can travel collinearly and no such separation is needed.

After having been frequency quadrupled, the probe is sent up a periscope, which changes height but not polarization, to an optical breadboard located directly in front of the ARPES chamber. This will then allow for the light to enter in the same plane containing the optical axis of the electron energy analyzer. Meanwhile, a telescope is used to reduce the beam diameter of the pump by half such that it equals that of the probe. The pump is then sent up a periscope that will likewise change height but not polarization and made collinear with the probe. Both beams are focused into the chamber by an $f = 500$ mm UV enhanced Aluminum, spherical mirror through a CaF_2 UHV viewport. Once in the chamber, a Mn doped Zn_2SiO_4 green fluorescence indicator is used to find the UV and spatially overlap pump and probe so that time resolved measurements can then be performed.

8.3 Time-Resolved ARPES

Within the literature, one can find a number of examples of laser based or time-resolved ARPES systems each of which is designed for studying some particular problem in condensed matter physics [210,211,212,213,214,215]. As this relates to the tr-ARPES constructed here at UTK, the choice of using a Coherent RegA 9050 laser source was rooted in a desire to strike a balance between the high repetition rate required by such experiments and a sufficient peak power needed to drive photo-induced phase transitions. Notably, unlike optical measurements, the importance of working at high repetition rates is not only limited to the accumulation of adequate statistics but ensures that the probe fluence is kept low enough so as to avoid space charge effects. Such an effect is a consequence of many low kinetic energies photoelectrons being produced within the brief timescale of ~100 fs pulse. The mutual repulsion from this cloud of slow-moving (~10^6 m/s) electrons can then have an adverse effect on the ARPES spectrum, causing distortions of the dispersion and a broadening of the Fermi edge. For this reason, repetition rates greater than 250 kHz are then used in the performance of laser based and tr-ARPES experiments so as to reduce the peak power of the probe pulse.

Before discussing some of the initial tr-ARPES spectra taken here at UTK, it should be noted that even without time resolution, there are many advantages to performing laser based ARPES experiments. Chief among these is the increased momentum resolution attributed to the wider dispersion in angle made by low energy photoelectrons. In other words, the inherent limitation of such electrons to yield information solely on those states centered at Γ implies that the whole detector can be used to image just a small region in *k*-space. Moreover, due to the fact that the beam can be focused, a higher fluence as compared to that of the He gas discharge lamp can be gained. While the ultrashort duration of the pulse will lead to an intrinsic loss of energy resolution especially as compared to the He lamp, this turns out to be on the order of 10 meV for a 100 fs pulse, which is comparable to that found in conventional ARPES. Lastly, due to the low kinetic energy of the outgoing photoelectrons, the longer inelastic mean free path will result in a reduced background and surface sensitivity in the ARPES spectrum.

Though there are many advantages to measuring laser based ARPES, a reliable measurement of such low energy electrons is complicated by the fact that they are highly susceptible to deflection by stray electric and magnetic fields. Furthermore, since the kinetic energy range of these photoelectrons is significantly lower than that typical for conventional

ARPES, the electrostatic lens table of the analyzer needs to be optimized to work at such low energies. Therefore, when calibrating the tr-ARPES system, spectra collected along the nodal direction of $Bi_2Sr_2CaCu_2O_{8+\delta}$ were used as this compound has been extensively studied in the ARPES literature and features only a single band crossing in this direction.

While optimization is still on going, Figure 8.2 shows the effect that a change in lens tables has on the spectra. Namely, Figure 8.2(a) illustrates the dispersion measured with a laser source using a lens table optimized for the He lamp, while Figure 8.2(b) shows the same dispersion when measured with the "small spot" lens table that is especially optimized for working at low kinetic energies. One particularly interesting feature of the small spot lens table is that it allows for the possibility of accelerating electrons to E_p without introducing distortions in the spectra like that shown in Figure 8.2(a). Generally, the disadvantage of working at higher E_p is a poorer energy resolution, but the intrinsic energy bandwidth of the laser pulse turns out to make this the limiting factor in the resolution even up to $E_p = 10$ eV. Hence, without there being any loss of resolution, it is often preferable to work at higher E_p as higher energy photoelectrons will be less susceptible to stray fields in the analyzer.

After having optimized the analyzer for detecting low kinetic energy photoelectrons, the optical pump beam can then be directed into the chamber so as to perform tr-ARPES experiments. To do so, both a spatial and temporal overlap between the pump and probe pulses must be found. While spatial overlap can be found relatively easily with the aid of a phosphor indicator, obtaining temporal overlap can be more challenging. For this reason, it is best to have a system that exhibits a fast, clearly identifiable electronic response followed by a slow relaxation dynamic. Furthermore, in seeing that the indication for temporal overlap is given by the presence of a transient population of electrons above the Fermi level, it is then important that there be available states in proximity to Γ that can be populated by an optical excitation.

Given these considerations, a good candidate for finding temporal overlap in the initial tr-ARPES experiments performed here at UTK was the topological insulator Sb_2Te_3. Most notably, as is shown in Figure 8.3, an optical excitation from the pump serves to populate the states of the Dirac cone located above E_F. Furthermore, in contrast to most metals, which can be characterized as having a fast relaxation dynamic on the order of a few hundred fs, the relaxation rate of the topological surface states is found to be considerably longer [216]. Namely, as can be seen in Figure 8.3(d), after a five ps delay, the bulk bands have largely depopulated, but the

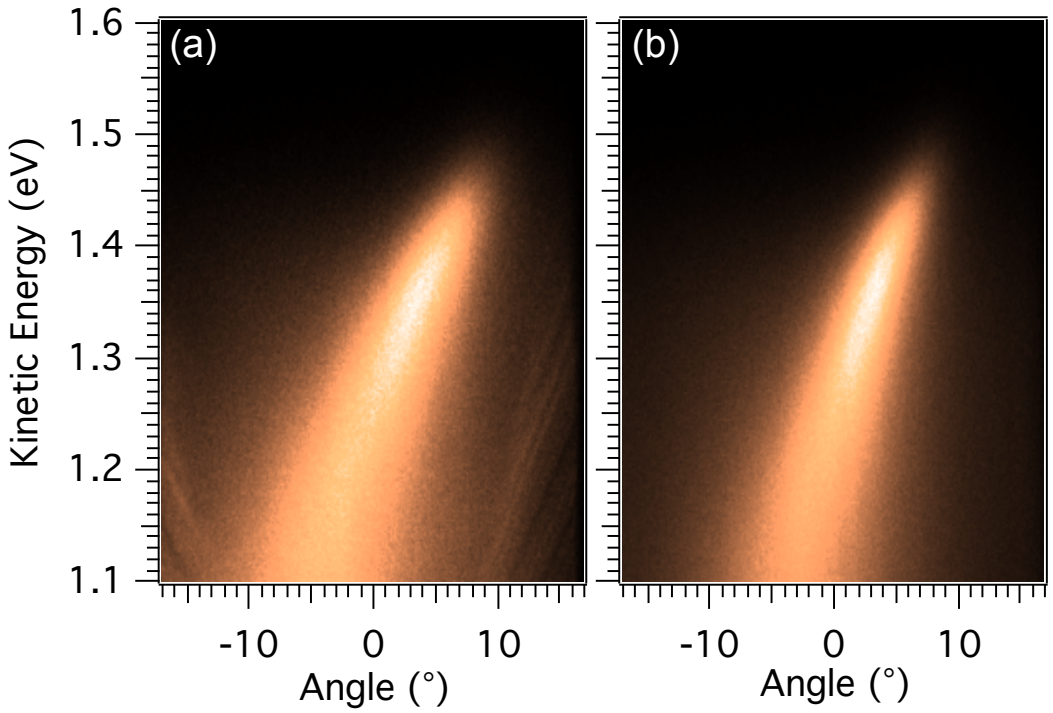

Figure 8.2: Electronic band dispersion of $Bi_2Sr_2CaCu_2O_{8+\delta}$ measured along the nodal direction using a laser excitation source ($h\nu$ = 6.34 eV). Spectra were obtained using a pass energy E_p = 5.0 eV for an electrostatic lens table optimized for (a) He gas discharge lamp and (b) laser source

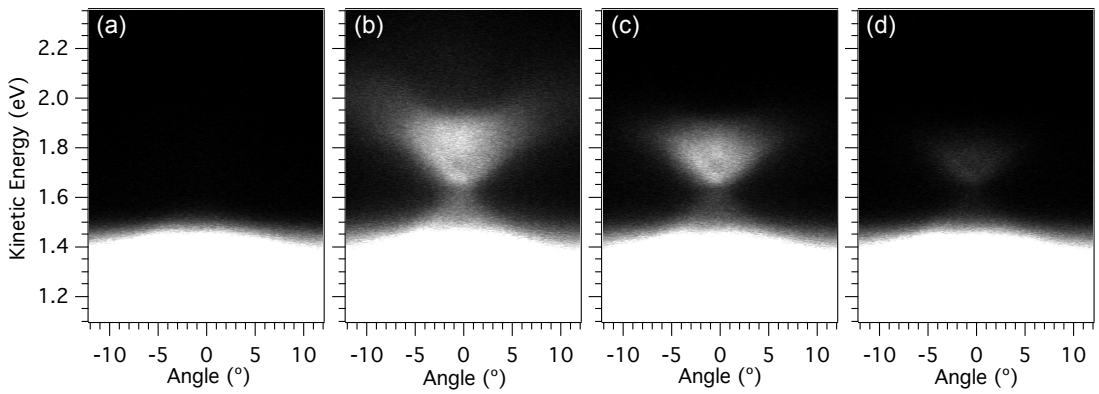

Figure 8.3: Snapshots of the time evolution of the transiently populated topological surface states in Sb_2Te_3 taken at (a) t = -2.0 ps, (b) t = 0 ps, (c) t = 2.5 ps and (d) t = 5.0 ps

topological surface states continue to remain at least partially occupied. Thus, after having found temporal overlap, the position on the delay stage was marked so as to have an absolute reference, allowing for additional characterization on other materials, including noble metals, to be performed. Chief among these is a measure of the temporal resolution. Generally this is accomplished by use of an autocorrelator, where the intensity of the third harmonic produced through difference frequency generation can be measured as a function of pump-probe delay. However, such a measurement requires a spectrometer capable of operating in the UV. Consequently, a more straightforward means of determining the time resolution will be given by a measurement of the rise time for a metallic sample. This is ultimately due to the fact that a fit of the rise time allows for the cross-correlation of the two pulses to be inferred.

8.4 Future Directions

Presently, the excitation energy of the pump within the tr-ARPES set-up is given by the fundamental frequency of the Ti:Sapphire. This energy corresponds to that of inter-band transitions, which are characteristic of the type of electronic excitations found in optics (see Figure 2.10). However, the ability to tune the excitation energy of the pump to other wavelengths, particularly within the infra-red (IR), would allow for the possibility of pumping on resonance certain excitations like optical phonon modes. Given the strong coupling that exists between electronic, lattice and spin degrees of freedom in strongly correlated systems, a resonant excitation of certain phonon modes can have profound implications on the electronic properties [217]. Notably, one intriguing possibility would be to examine the effect that a resonant excitation of the Oxygen optical phonon in Strontium Titanate ($SrTiO_3$) has on the superconducting transition of FeSe thin films [218]. To do so, this requires the construction of an optical parametric amplifier (OPA).

An OPA, like that that of the non-collinear OPA sketched in Figure 8.4, can provide a tunable source of fs pulses over a broad frequency, ranging from the visible to the near-IR [219]. Fundamentally, the basis on an OPA is rooted in the amplification of a weak signal pulse, possessing a variable frequency ω_s, due to an energy transfer from an intense pump, having a fixed frequency ω_p, while simultaneously producing an idle pulse of energy ω_i. From energy conservation, it is evident that such a non-linear process will differ from that of difference frequency generation only in the initial conditions. Namely, the amplification of the signal in an

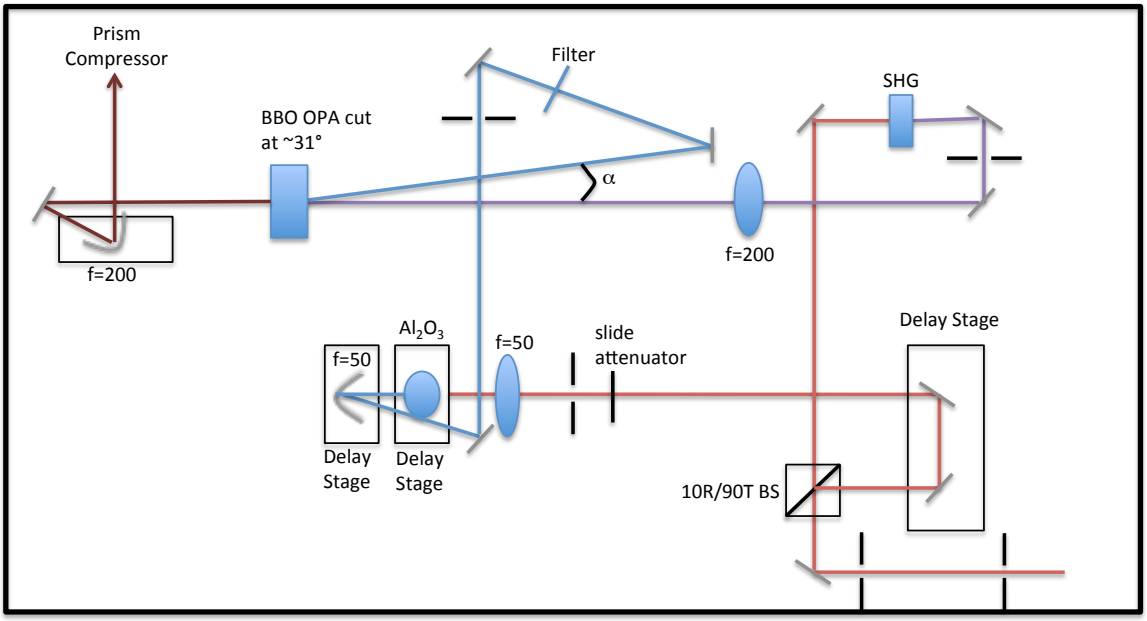

Figure 8.4: Schematic diagram of a visible/near IR non-collinear optical parametric amplifier

OPA results from a process in which $\omega_p \rightarrow \omega_s + \omega_i$, meaning that additional photons are added to the signal while the idle is produced simply as a consequence of energy conservation. In contrast, difference frequency generation will result in the production of the idle through $\omega_i \rightarrow \omega_p - \omega_s$ where the signal is subtracted, rather than amplified, from that of the pump

Given then the operating principal behind an OPA, it is clear that an essential task requires the generation of a signal, or seed, whose frequency must necessarily be less than that of the pump. Due to this constraint, the wavelength range of an OPA will be dictated by ω_p. Notably, for an OPA operating in the visible, the pump is most often given by frequency doubling the fundamental of the Ti:Sapphire, while those operating in the IR do not require such a conversion allowing for just the fundamental to be used. Since the pump will always be defined at a single frequency regardless of the wavelength range of the OPA, the tunability must therefore originate from the signal having a broad frequency bandwidth. This can be accomplished through generating a white light supercontinuum by focusing an intense ultrashort pulse on some transparent material, such as sapphire. In such a case, the continuum spectrum will extend from 420 nm to 1500 nm allowing for the possibility of amplifying over a 1080 nm bandwidth.

Recalling that the temporal duration of an ultrashort pulse is inversely proportional to the bandwidth, the ability of an OPA to amplify a signal over a broad frequency range not only allows for the photon energy to be tuned, but for the generation of pulses approaching the transform limit of ~4-5 fs. This is accomplished by making use of the non-collinear geometry shown in Figure 8.4, where the parametric amplification occurs on a type I β-BBO cut at 31° [219]. In such a case, the phase matching condition can be met over a broad frequency range, allowing for amplification to take place over the whole of the white light signal. Consequently, after compensating for chirp, resulting from both white light generation and parametric amplification, pulses of extremely short temporal durations can be produced. In this way, the time resolution can be pushed to the very limit of a tr-ARPES experiment, allowing for the most interesting initial stages of the dynamics to be investigated.

References

[1] S. Mühlbauer, B. Binz, F. Jonietz, C. Pfleiderer, a Rosch, a Neubauer, R. Georgii, and P. Böni. "Skyrmion lattice in a chiral magnet." *Science* **323**, 915 (2009). http://dx.doi.org/10.1126/science.1166767
[2] C. Pfleiderer and A. Rosch. "Condensed-matter physics: Single skyrmions spotted." *Nature* **465**, 880 (2010). http://dx.doi.org/10.1038/465880a
[3] Togawa, Y., Koyama, T., Takayanagi, K., Mori, S., Kousaka, Y., Akimitsu, J., Nishihara, S., Inoue, K., Ovchinnikov, a., and Kishine, J. "Chiral Magnetic Soliton Lattice on a Chiral Helimagnet" *Physical Review Letters* **108**, 107202 (2012). http://dx.doi.org/10.1103/PhysRevLett.108.107202
[4] Y. Togawa, Y. Kousaka, S. Nishihara, K. Inoue, J. Akimitsu, A. S. Ovchinnikov, and J. Kishine. "Interlayer Magnetoresistance due to Chiral Soliton Lattice Formation in Hexagonal Chiral Magnet $CrNb_3S_6$" *Physical Review Letters* **111**, 197204 (2013). https://doi.org/10.1103/PhysRevLett.111.197204
[5] N. J. Ghimire, M. A. McGuire, D. S. Parker, B. Sipos, S. Tang, J.-Q. Yan, B. C. Sales, and D. Mandrus. "Magnetic Phase Transitions in Single Crystals of the Chiral Helimagnet $Cr_{1/3}NbS_2$." *Physical Review B* **87**, 104403 (2013). http://dx.doi.org/10.1103/PhysRevB.87.104403
[6] S. V. Borisenko, A. A. Kordyuk, V. B. Zabolotnyy, D. S. Inosov, D. Evtushinsky, B. Büchner, A. N. Yaresko, A. Varykhalov, R. Follath, W. Eberhardt, L. Patthey, and H. Berger "Two Energy Gaps and Fermi-Surface 'Arcs' in $NbSe_2$" *Physical Review Letter* **102**, 166402 (2009)
[7] K. Rossnagel, E. ZTotenberg, H. Koh, N. V. Smith, and L. Kipp. "Continuous Tuning of Electronic Correlations by Alkali Adsorption on Layered 1T-TaS_2." *Physical Review Letters* **95**, 126403 (2005)
[8] K. Siebahn. "Electron Spectroscopy for chemical analysis (e.s.c.a)" *Philosophical Transactions of the Royal Society if London A* **268**, 33 (1970).
[9] A. Damascelli, Z. Hussain, and Z. –X. Shen. "Angle resolved photoemission studies of the cuprate superconductors" *Review of Modern Physics* **75**, 473 (2003).
[10] C.S. Fadley "Basic Concepts of X-ray Photoelectron Spectroscopy" from Electron Spectroscopy: Theory, Techniques and Applications Ed. C. R. Brundle and A. D. Baker. *Academic Press* (1978)
[11] M. P. Seah and W. A. Dench. "Quantitative electron spectroscopy of surfaces: a standard data base for electron inelastic mean free paths in solids" *Surface and Interface Analysis* **1**, 2 (1979)
[12] P. A. Bruhwiler O. Karis, and N. Martensson. "Charge-transfer dynamics studied using resonant core spectroscopies" *Reviews of Modern Physics* **74**, 703 (2002)
[13] S. Hufner. "Photoelectron Spectroscopy Principles and Applications" 3rd Edition. *Springer* (2003)
[14] D.N. Basov, R. D. Averitt, D. van der Marel, M. Dressel, K. Haule. "Electrodynamics of correlated electron materials" *Reviews of Modern Physics* **83**, 471 (2011).
[15]U. Bovensiepen, H, Petek, and M. Wolf "Dynamics at Solid State Surfaces and Interfaces" *Wiley-VCH* (2012).
[16] C.-Y. You and S.-C. Shin. "Derivation of simplified analytic formula for magneto-optical Kerr effects" *Applied Physics Letters* **69**, 1315 (1996)
[17] N. Martensson, P, Baltzer, P.A. Brujwiler, J.-O. Forsell, A. Nilsson, A. Stenborg, and B. Wannberg. "A very high resolution electron spectrometer" *Journal of Electron Spectroscopy and Related Phenomena* **70**, 117 (1994).
[18] Coherent Micra Operations Manual
[19] http://frog.gatech.edu/pulse-compression.html
[20]Coherent RegA 9000 Operation Manual
[21] I. Zutic, J. Fabian, and S. Das Sarma. "Spintronics: Fundamentals and applications" *Reviews of Modern Physics* **76**, 323 (2004). https://doi.org/10.1103/RevModPhys.76.323
[22] S. *Datta, and B. Das. "Electronic analog of the electrooptic modulator" Applied Physics Letters. **56**, 66 (1990).* http://dx.doi.org/10.1063/1.102730
[23] R. Rottmayer, and J. –G. Zhu, "A new design for an ultra-high density magnetic recording head using a GMR sensor in the CPP mode" *IEEE Transactions on Magnets* **31**, 2597 (1995) https://doi.org/10.1109/20.490065
[24] G. H. Wagniere. "On Chirality and the Universal Asymmetry" Wiley-VCH (2007)
[25] D. M. Bishop. "Group Theory and Chemistry" Dover (1993)
[26] I. Dzyaloshinsky. "A thermodynamic theory of weak ferromagnetism of antiferromagnetics." *Journal of Physics and Chemistry of Solids* **4**, 241 (1958). http://dx.doi.org/10.1016/0022-3697(58)90076-3
[27] T. Moriya. "Anisotropic superexchange interaction and weak ferromagnetism." *Physical Review* **120**, 91 (1960). http://link.aps.org/doi/10.1103/PhysRev.120.91
[28] C. D. Hu. "The Dzyaloshinskii-Moriya interaction in metals" *J. Phys.: Condens. Matter* **24** 086001 (2012)

[29] P. Bak and M. H. Jensen. "Theory of helical magnetic structures and phase transition in MnSi and FeGe." *J. Phys. C. Solid. St. Phys*. **13**, L881-5 (1980)
[30] T. Miyadai, K. Kikuchi, H. Kondo, S. Sakka, M. Arai, and Y. Ishikawa. "Magnetic Properties of $Cr_{1/3}NbS_2$" *Journal of the Physical Society of Japan* **53**, 1394 (1983)
[31] Y. Ishikawa, K. Tajima, D. Bloch, and M. Roth. "Helical spin structure in manganese silicide MnSi." *Solid State Communications* **19**, 525 (1976). http://dx.doi.org/10.1016/0038-1098(76)90057-0
[32] S.V. Grigoriev, D. Chernyshov, V.A. Dyadkin, V. Dmitriev, S.V. Maleyev, E.V. Moskvin, D. Menzel, J. Schoenes, and H. Eckerlebe. "Crystal Handedness and Spin Helix Chirality in $Fe_{1-x}Co_xSi$." *Physical Review Letters* **102**, 037204 (2009). http://dx.doi.org/10.1103/PhysRevLett.102.037204
[33] T. Moriya and T. Miyadai. "Evidence for the helical spin structure due to antisymmetric exchange interaction in $Cr_{1/3}NbS_2$." *Solid State Communications* **42**, 209 (1982). http://dx.doi.org/ 10.1016/0038-1098(82)91006-7
[34] Y. Kousaka, H. Ohsumi, T. Komesu, T-h. Arima, M. Takata, S. Sakai, M. Akita, K. Inoue, T. Yokobori, Y. Nakao, and E. Kaya. "Crystallographic Chirality of $CsCuCl_3$ Probed by Resonant Circularly-Polarized Hard X-ray Diffraction." *Journal of the Physical Society of Japan* **78**, 123601 (2009). http://dx.doi.org/10.1143/JPSJ.78.123601
[35] K. Ionoue, K. Kikuchi, M. Ohba, and K. Okawa. "Structure and Magnetic Properties of a Chiral Two-Dimensional Ferrimagnet with T_C of 38K." *Agnewandte Chemie, International Edition* **42**, 4810 (2003). http://dx.doi.org/10.1002/anie.200351888
[36] M. Kataoka. "Spin Waves in Systems with Long Period Helical Spin Density Waves Due to the Antisymmetric and Symmetric Exchange Interaction." *Journal of the Physical Society of Japan* **56**, 3635 (1987).
[37] K. Ho, T. Kirkpatrick, Y. Sang, and D. Belitz. "Ordered phases of itinerant Dzyaloshinsky-Moriya magnets and their electronic properties." *Physical Review B* **82**, 134427 (2010). http://link.aps.org/doi/10.1103/PhysRevB.82.134427
[38] H. –B. Braun. "Togological effects in nanomagnetism: from superparamagnetism to chiral quantum solitons" *Advances in Physics* **61**, 1 (2011). http://dx.doi.org/10.1080/00018732.2012.663070
[39] U. K. Rößler, A. N. Bogdanov, and C. Pfleiderer. "Spontaneous skyrmion ground state in magnetic metals." *Nature* **442**, 797 (2006). http://dx.doi.org/ 10.1038/nature05056
[40] A. Bogdanov and A. Hubert. "Thermodynamically stable magnetic vortex states in magnetic crystals" *Journal of Magnetism and Magnetic Materials* **138**, 255 (1994). http://dx.doi.org/10.1016/0304-8853(94)90046-9
[41] T.H.R. Skyrme. "A unified field theory of mesons and baryons." *Nuclear Physics* **31**, 556 (1962). http://dx.doi.org/10.1016/0029-5582(62)90775-7
[42] N. Nagaosa and Y. Tokura. "Topological properties and dynamics of magnetic skyrmions" *Nature Nanotechnology* **8**, 899 (2013). http://dx.doi.org/10.1038/nnano.2013.243
[43]Pierre Villars (Chief Editor), PAULING FILE in: Inorganic Solid Phases, SpringerMaterials (online database), Springer, Heidelberg (ed.) http://materials.springer.com/isp/crystallographic/docs/sd_0532789
[44] T. Thessieu, C. Pfleiderer, A.N. Stepanov, and J. Flouquet "Field dependence of the magnetic quantum phase transition in MnSi" *Journal of Physics: Condensed Matter* **9**, 6677 (1997)
[45] T. Adams, S. Muhlbauer, C. Pfleiderer, F. Jonietz, A. Bauer, A. Neubauer, R. Georgii, P. Boni, U. Keiderling, K. Everschor, M. Garst, and A. Rosch. "Long Range Crystalline Nature of the Skyrmion Lattice in MnSi" *Physical Review Letters* **107**, 217207 (2011)
[46] X. Z. Yu, Y. Onose, N. Kanazawa, J. H. Park, J. H. Han, Y. Matsui, N. Nagaosa, and Y. Tokura. "Real space observation of a two-dimensional skyrmion crystal." *Nature* **465**, 901 (2010). http://dx.doi.org/10.1038/nature09124
[47] W. Münzer, A. Neubauer, T. Adams, S. Mühlbauer, C. Franz, F. Jonietz, R. Georgii, P. Böni, B. Pedersen, M. Schmidt, A. Rosch, and C. Pfleiderer. "Skyrmion lattice in the doped semiconductor $Fe_{1-x}Co_xSi$." *Physical Review B* **81**, 041203 (2010). http://link.aps.org/doi/10.1103/PhysRevB.81.041203
[48] X.Z. Yu, N. Kanazawa, Y. Onose, K. Kimoto, W.Z. Zhang, S. Ishiwata, Y. Matsui, and Y. Tokura. "Near room-temperature formation of a skyrmion crystal in thin-films of the helimagnet FeGe." *Nature Materials* **10**, 106 (2009). http://dx.doi.org/10.1038/nmat2916
[49] H. Wilhelm, M. Baenitz, M. Schmidt, U. Rößler, a Leonov, and a Bogdanov. "Precursor Phenomena at the Magnetic Ordering of the Cubic Helimagnet FeGe." *Physical Review Letters* **107**, 127203 (2011). http://link.aps.org/doi/10.1103/PhysRevLett.107.127203
[50] Seki, S., Yu, X. Z., Ishiwata, S., and Tokura, Y. "Observation of Skyrmions in a Multiferroic Material." *Science* **336**, 198. http://dx.doi.org/10.1126/science.1214143

[51]J. S. White, I. Levatić, A. A. Omrani, N. Egetenmeyer, K. Prša, I. Živković, J. L. Gavilano, J. Kohlbrecher, M. Bartkowiak, H. Berger and H. M. Rønnow. "Electric Field Control of the Skyrmion Lattice in Cu_2OSeO_3" *Journal of Physics: Condensed Matter* **24**, 432201 (2012)
[52]N. Kiselev, and A. Bogdanov "Chiral Skyrmions in Thin Magnetic Films: New Objects for Magnetic Storage Technologies?" *Journal of Physics D: Applied Physics* **44**, 392001 (2011)
[53] F. Jonietz, S. Mühlbauer, C. Pfleiderer, A. Neubauer, W. Münzer, A. Bauer, T. Adams, R. Georgii, P. Böni, R.A. Duim, K. Everschor, M. Garst, and A. Rosch. "Spin transfer torques in MnSi at ultralow current densities." *Science* **330**, 1648 (2010). http://dx.doi.org/10.1126/science.1195709
[54] N. Romming, C. Hanneken, M. Menzel, J.E. Bickel, B. Wolter, K. von Bergmann, A. Kubetzka, and R. Wiesendanger. "Writing and Deleting Single Magnetic Skyrmions." *Science* **341**, 636 (2013). http://dx.doi.org/10.1126/science:1240573
[55] M. Lee, W. Kang, Y. Onose, Y. Tokura, and N. Ong. "Unusual Hall Effect Anomaly in MnSi under Pressure." *Physical Review Letters* **102**, 186601 (2009). http://link.aps.org/doi/10.1103/PhysRevLett.102.186601
[56] A. Neubauer, C. Pfleiderer, B. Binz, a Rosch, R. Ritz, P. Niklowitz, and P. Böni. "Topological Hall effect in the A phase of MnSi." *Physical Review Letters* **102**, 186602 (2009). http://link.aps.org/doi/10.1103/PhysRevLett.102.186602
[57] T. Schulz, R. Ritz, A. Bauer, M. Halder, M. Wagner, C. Franz, C. Pfleiderer, K. Everschor, M. Garst, and A. Rosch. "Emergent electrodynamics of Skyrmions in a chiral magnet" *Nature Physics* **8**, 301 (2012)
[58] M. Kertesz and R. Hoffmann "Octahedral vs. Trigonal-Prismatic Coordination and Clustering in Transition-Metal Dichalcogenides" *Journal of the American Chemical Society* **106**, 3453 (1984)
[59] R.H. Friend, and A. D. Yoffe, "Electronic-Properties of intercalation complexes of the transition-metal dichalcogenides." *Advances in Physics* **36**, 1 (1987). http://dx.doi.org/10.1080/00018738700101951
[60] F. Hulliger and E. Pobitschka. "On the Magnetic Behavior of New 2H-NbS2-Type Derivatives." *Journal of Solid State Chemistry* **1**, 117 (1970). http://dx.doi.org/10.1016/0022-4596(70)90001-0
[61] S. S. P. Parkin and R. H. Friend. "3d transition metal intercalates of the niobium and tantalum dichalcogenides. I. Magnetic Properties." *Philosophical Magazine B* **41**, 65 (1980). http://dx.doi.org/10.1080/13642818008245370
[62] C. Pappas. "Viewpoint: New Twist in Chiral Magnets" *Physics* **5**, 28 (2012)
[63] I. Bostrem, J. Kishine, and A. Ovchinnikov, "Transport Spin Current Driven by the Moving Kink Crystal in a Chiral Helimagnet" *Phys. Rev. B* **77**, 132405 (2008)
[64] A. Borisov, J. Kishine, I. Bostrem, and A. Ovchinnikov "Magnetic Soliton Transport over Topological Spin Texture in Chiral Helimagnet with Strong Easy-plane Anisotropy" Phys. Rev. B **79**, 134436 (2009)
[65] J. Kishine, A. Ovchinnikov, and I. Proskurin "Sliding Conductivity of a Magnetic Kink Crystal in a Chiral Helimagnet" *Phys. Rev. B* **82**, 064407 (2010)
[66] B.J. Chapman, A.C. Bornstein, N.J. Ghimire, D.Mandrus, and M. Lee. "Spin structure of the anisotropic helimagnet $Cr_{1/3}NbS_2$ in a magnetic field." *Applied Physics Letter* **105**, 072405 (2014). http://dx.doi.org/10.1063/1.4893567
[67] J. –I. Kishine, I. V. Proskurin, and A. S. Ovchinnikov. "Tuning Magnetotransport through a Magnetic Kink Crystal in a Chiral Helimagnet." *Phys. Rev. Lett.* **107**, 017205 (2011)
[68] A. C. Bornstein, B. J. Chapman, N. J. Ghimire, D. Mandrus, D. S. Parker, and M. Lee "Out-of-plane spin-orientation dependent magnetotransport properties in the anisotropic helimagnet $Cr_{1/3}NbS_2$" *Physical Review B* **91**, 184401 (2015). http://dx.doi.org/10.1103/PhysRevB.91.184401
[69] E. Morosan, H.W. Zandbergen, Lu Li, M. Lee, J. G. Checkelsky, M. Heinrich, T. Siegrist, N.P. Ong and R.J. Cava "Sharp Switching of the magnetization in $Fe_{1/4}TaS_2$" Phys. Rev. B **75**, 104401 (2007)
[70] L. M. Volkova, and D. V. Marinin. " Role of structural factors in formation of chiral magnetic soliton lattice in $Cr_{1/3}NbS_2$" *Journal of Applied Physics* **116**, 133901 (2014).
[71] W. Yao, D. Xiao, and Q. Niu. "Valley-dependent optoelectronics from inversion symmetry breaking." *Physical Review B* **77**, 235406 (2008). http://dx.doi.org/10.1103/PhysRevB.77.235406
[72] D. Xiao, G. –B. Liu, W. Feng, X. Xu, and W. Yao. "Coupled Spin and Valley Physics in Monolyers of MoS_2 and Other Group VI Dichalcogenides." *Physical Review Letters* **108**, 196802 (2012). http://dx.doi.org/10.1103/PhysRevLett.108.196802
[73] K.F. Mak, K. He, J. Shan, and T.F. Heinz, "Control of valley polarization in monolayer MoS_2 by optical helicity." *Nature Nanotechnology* **7**, 494 (2012).

[74] H. Zeng, J. Dai, W. Yao, D. Xiao, and X. Cui. "Valley polarization in MoS_2 monolayers by optical pumping" *Nature Nanotechnology* **7**, 490 (2012). http://dx.doi.org/10.1038/nnano.2012.95
[75] H. Wang, H. Yuan, S.S. Hong, Y. Li, and Y. Cui. "Physical and chemical tuning of two dimensional transition metal dichalcogenides." *Chemical Society Review* **44**, 2664 (2015). http://dx.doi.org/10.1039/C4CS00287C
[76] H. I. Starnberg. "Recent Developments in Alkali Metal Intercalation of Layered Transition Metal Dichalcogenides" Modern Physics Letters B **14**, 455 (2000). http://dx.doi.org/10.1142/S0217984900000628
[77] S. F. Meyer, R. E. Howard, G. R. Stewart, J. V. Acrivos, and T. H. Geballe. "Properties of intercalated $2HNbSe_2$, $4HbTaS_2$, and $1TTaS_2$." *Journal of Chemical Physics* **62**, 4411 (1975). http://dx.doi.org/10.1063/1.430342
[78] S. E. Stoltz, H. I. Starnberg, and L. J. Holleboom "Rb intercalation of 1T-TaS_2 studied by photoelectron spectroscopy." *Physical Review B* **67**, 125107 (2003).
[79] E. Morosan, H. W. Zandbergen, B. S. Dennis, J. W. G. Bos, Y. Onose, T. KLimczuk, A. P. Ramirez, N. P. Ong, and R. J. Cava. "Superconductivity in Cu_xTiSe_2" *Nature Physics* **2**, 544 (2006). http://dx.doi.org/10.1038/nphys360
[80] W. B. Clark "Structural and photoemission studies of some transition metal intercalates of NbS2" *J. Phys. C: Solid State Phys.* **9**, L693 (1976)
[81] R. H. Friend, A. R. Beal, and A. D. Yoffe. "Electrical and magnetic properties of some first row transition metal intercalates of niobium disulphides" *Philosophical Magazine* **35**, 1269 (1977)
[82] D. W. Bullett "Electronic band structure and bonding in transition metal dichalcogenides by atomic orbital methods" *J. Phys. C: Solid State Phys*. **11**, 4501 (1978)
[83] R Corcoran, P Meeson, Y Onuki, P -A Probst, M Springford, K Takita, H Harima, G Y Guo and B L Gyorffy. "Quantum oscillations in the mixed state of the type II superconductor 2H-NbSe2" *J. Phys.: Condens. Matter* **6**, 4479 (1994)
[84] Th. Straub, Th. Finteis, R. Claessen, P. Steiner, S. Hüfner, P. Blaha, C. S. Oglesby, and E. Bucher "Charge-Density-Wave Mechanism in 2H-$NbSe_2$: Photoemission Results." *Physical Review Lett*ers **82**, 4504 (1999)
[85] K. Rossnagel, O. Seifarth, L. Kipp, M. Skibowski, D. Voß, P. Krüger, A. Mazur, and J. Pollmann "Fermi Surface of 2H-$NbSe_2$ and its implications on the charge-density-wave mechanism" *Physical Review B* **64**, 235119 (2001).
[86] J. A. Wilson, F. J. Di Salvo, and S. Mahajan. "Charge-density-waves and superlattices in the metallic layered transition metal dichalcogenides" *Advances in Physics* **50**, 1171 (2001)
[87] T. Yokoya, T. Kiss, A. Chainani, S. Shin, M. Nohara, and H. Takagi. "Fermi Surface Sheet-Dependent Superconductivity in 2H-$NbSe_2$" *Science* **294**, 2518 (2001)
[88] H. J. Carawak, Y. Tomm and C. Pettenkofer. "Localization and Charge Density Wave Transformation in Cs-intercalated 1T-$TaSe_2$" *Surface Science* **465**, 301 (2000).
[89] C. Battaglia, H. Cercellier, L. Despont, C. Monney, M. Prester, H. Berger, L. Forro, M.G. Garnier, and P. Aebi. "Non-Uniform doping across the Fermi surface of NbS_2 intercalates" *European Physical Journal B* **57**, 385 (2007).
[90] S. Blundell. "Magnetism in Condensed Matter" Oxford University Press 2012
[91]K.-T. Ko, Kyoo Kim, Sung Baek Kim, H.-D. Kim, J.-Y. Kim, B. I. Min, J.-H. Park, F.-H. Chang, H.-J. Lin, A. Tanaka, and S-W. Cheong "RKKY Ferromagnetism with Ising-Like Spin States in Intercalated $Fe_{1/4}TaS_2$" *Phys. Rev. Lett.* **107**, 247201 (2011)
[92] S.S. P. Parkin, E. A. Marseglia, and P. J. Brown. "Magnetization density distribution in Mn1/4TaS2: Observation of conduction electron spin polarization" *Journal of Physics C: Solid State Physics* **16**, 2749 (1983).
[93] C.N. Berglund and W. E. Spicer. "Photoemission Studies of Copper and Silver: Theory" *Physical Review A* **136**, 1030 (1964)
[94] M. A. Hoyland, and R.G. Jordan. "An experimental and theoretical study of the photoemission from Ni(110)" *Journal of Physics: Condensed Matter* **3**, 1337 (1991)
[95] G. D. Mahan "Theory of Photoemission in Simple Metals" Phisical Review B 2, 4334 (1970)
[96] Frank de Groot and Akio Kotani. "Core-level Spectroscopy of Solids" *CRC Press* (2008)
[97] S. Doniach and M Sunjic "Many Electron Singularity in X-ray Photoemssion and X-ray line Spectra from Metals" *Journal of Physics C: Solid State Physics* **3**, 285 (1970).
[98] J. W. Gadzuk, and M. Sunjic "Excitation energy dependence of core-level x-ray-photoemission-spectra-line shapes in metals" *Physical Review B* **12**, 524 (1975)
[99] P. Nozieres, and C. T. De Dominicis "Singularities in the X-ray absorption and emission of metals. III. One body theory exact solution" *Physical Review* **178**, 1097 (1969)

[100] G. Mahan. “Many-Particle Physics” 2nd Edition Plenum Press (1990)
[101] N. Mannella “Measuring Spins in Photoemission Experiments: Old Challenges and New Opportunities” *Synchrotoron Radiation News* **27**, 4 (2014).
[102] N. Mannella “The magnetic moment enigma in Fe-based high temperature superconductors” *Journal of Physics: Condensed Matter* **26**, 473202 (2014)
[103] R.D. Mattuck, “A Guide to Feynman Diagrams in the Many-Body Problem.” *Dover Publications* (1976)
[104] A. M. Zagoskin, “Quantum Theory of Many-Body Systems” *Springer* (1998)
[105] W. Schattke, M. A. Van Hove, F. Garcia de Abajo, J. Diez, R. Muino, and N. Mannella. “Overview of core and valence photoemission” Solid State Photoemission and Related Methods: Theory and Experiment*. Wiley VCH* (*2003*)
[106] S. Tanuma, C. J. Powell, and D.R. Penn. “Calculation of electron inelastic mean free paths (IMFPs) VII. Reliability of the TPP-2M IMFP predictive equation” *Surface and Interface Analysis* **35**, 268 (2003).
[107] C. Caroli, D. Lederer-Rozenblatt, B. Roulet, and D. Saint-James. “Inelastic Effects in Photoemission: Microscopic Formulation and Qualitative Discussion.” *Physical Review B* **8**, 4552 (1973).
[108] C. S. Fadley. “Looking Deeper: Angle-Resolved Photoemission with Soft and Hard X-rays” *Synchrotron Radiation News* **25**, 26 (2012)
[109] V. N. Strocov, M. Kobayashi, X.Q. Wang, L. L. Lev, J. Krempasky, V. V. Rogalev, T. Schmitt, C. Cancellieri, and M. L. Reinle-Schmitt. “Soft-X-ray ARPES at the Swiss Light Source: From 3D Materials to Buried Interfaces and Impurities” *Synchrotron Radiation News* **27**, 31 (2014)
[110]V. N. Strocov, M. Shi, M. Kobayashi, C. Monney, X. Wang, J. Krempasky, T. Schmitt, L. Patthey, H. Berger, and P. Blaha. “Three-Dimensional Electron Realm in VSe_2 by Soft-X-Ray Photoelectron Spectroscopy: Origin of Charge-Density Waves” *Physical Review Letters* **109**, 086401 (2012)
[111] M. Kobayashi, I. Muneta, Y. Takeda, Y. Harada, A. Fujimori, J. Krempaský, T. Schmitt, S. Ohya, M. Tanaka, M. Oshima, and V. N. Strocov. “Unveiling the impurity band induced ferromagnetism in the magnetic semiconductor (Ga,Mn)As” *Physical Review B* **89**, 205204 (2014)
[112] T. Okane, T. Ohkochi, Y. Takeda, S.-i. Fujimori, A. Yasui, Y. Saitoh, H. Yamagami, A. Fujimori, Y. Matsumoto, M. Sugi, N. Kimura, T. Komatsubara, and H. Aoki. “4f-Derived Fermi Surfaces of $CeRu_2(Si_{1-x}Ge_x)_2$ near the Quantum Critical Point: Resonant Soft-X-Ray ARPES Study” Physical Review Letters 102, 216401 (2009)
[113] A. X. Gray, C. Papp, S. Ueda, B. Balke, Y. Yamashita, L. Plucinski, J. Minar, J. Braun, E.R. Ylvisaker, C. M. Schneider, W.E. Pickett, H. Ebert, K. Kobayashi, and C. S. Fadley. “Probing bulk electronic structure with hard x-ray angle-resolved photoemission” *Nature Material* **10**, 759 (2011)
[114] L. Plucinski, J. Minár, B. C. Sell, J. Braun, H. Ebert, C. M. Schneider, and C. S. Fadley. “Band mapping in higher-energy x-ray photoemission: Phonon effects and comparison to one-step theory” *Physical Review B* **78**, 035108 (2008).
[115] J. Braun, J. Minár, S. Mankovsky, V. N. Strocov, N. B. Brookes, L. Plucinski, C. M. Schneider, C. S. Fadley, and H. Ebert. “Exploring the XPS limit in soft and hard x-ray angle-resolved photoemission using a temperature-dependent one-step theory” *Physical Review B* **88**, 205409 (2013)
[116] D.P. Woodruff and T.A. Delchar, *Modern Techniques of Surface Science*, Cambridge University Press, (Cambridge, 1986), p. 126.
[117] (a) U. Fano, Physical Review **124**, 1866 (1961). (b) U. Fano and J.W. Cooper, Reviews of Modern Physics **40**, 493 (1968).
[118] P. Vilmercati, D. Cvetko, A. Cossaro, A. Morgante, “Heterostructured organic interfaces probed by resonant photoemission” *Surface Science* **603**, 1542 (2009).
[119] C. Giannetti, M. Capone, D. Fausti, M. Fabrizo, F. Parmigiani and D. Mihailovic. “Ultrafast optical spectroscopy of strongly correlated materials and high temperature superconductors: a non-equilibrium approach” *Advances in Physics* **65**, 58 (2016).
[120] P. B. Allen. “Theory of thermal relaxation in metals” *Physical Review Letters* **59**, 1460 (1987).
[121] L. Perfetti, P. A. Loukakos, M. Lisowski, U. Bovensiepen, H. Eisaki and M. Wolf. “Ultrafast Electron Relaxation in Superconducting $Bi_2Sr_2CaCu_2O_{8+\delta}$ by Time-Resolved Photoelectron Spectroscopy” *Physical Review Letters* **99**, 197001 (2007)
[122] Michael Sentef, Alexander F. Kemper, Brian Moritz, James K. Freericks, Zhi-Xun Shen, and Thomas P. Devereaux. “Examining Electron-Boson Coupling Using Time-Resolved Spectroscopy” *Physical Review X* **3**, 041033 (2013)

[123] L. Stojchevska, I. Vaskivsky, T. Mertelj, P. Kusar, D. Svetin, S. Brazovskii, and D. Mihailovic "Ultrafast Switching to a Stable Hidden Quantum State in an Electronic Crystal" *Science* **344**, 177 (2014).
[124] K. Miyano, T. Tanaka, Y. Tomioka, and Y. Tokura. "Photoinduced Insulator-to-Metal Tranistion in a Perovskite Manganite" *Physical Review Letter* **78**, 4257 (1997).
[125] D. Fausti, R.I. Tobey, N. Dean, S. Kaiser, A. Dienst, M. C> Hoffman, S. Pyon, T. Takayama, H. Takagi and A. Cavalleri. "Light-Induced Superconductivity in a Stripe Ordered Cuprate" *Science* **331**, 189 (2011).
[126] G. R. Fowles, "Introduction to Modern Optics" 2nd Edition *Dover Publishing* (1975)
[127] E. Carpene, E. Mancini, C. Dellera, E. Puppin and S. De Silvestri. "Three-dimensional magnetization evolution and the role of anisotropies in thin Fe/MgO films: Static and dynamic measurements" *Journal of Applied Physics* **108**, 063919 (2010)
[128] A. Delin, O. Eriksson, B. Johansson, S. Auluck, and J. M. Wills. "Calculated magneto-optical properties of cubic and tetragonal Fe, Co, and Ni" *Physical Review B* **60**, 14105 (1999)
[129] H. Luth. "Surfaces and Interfaces of Solid Materials 3rd Edition" *Springer* 1998
[130] D.P. Woodriff and T.A. Delchar. "Modern Techniques of Surface Science 2nd Edition" *Cambridge University Press* 1994
[131] S. Hufner. "Photoelectron Spectroscopy 3rd Edition" *Springer* 2003
[132] G.K. Ovrebo and J. L. Erskine. "Angle Resolving Photoelectron Energy Analyzer Designed for Synchrotron Radiation Spectroscopy" *Journal of Electron Spectroscopy and Related Phenomena* **24**, 189 (1981)
[133] Scienta R4000 User Manual
[134] E. M. Purcell "The Focusing of Charged Particles by a Spherical Condenser" *Physical Review* **54**, 818 (1938).
[135] P. Baltzer and L. Karlsson. "High-resolution extreme-ultraviolet spectrum of He between 35 and 55 eV" *Physical Review A* **38**, 2322 (1988)
[136] Teledyne LeCroy Labmaster 10-100Zi
[137] W. T. Silfvast. "Laser Fundamentals 2nd Edition" *Cambridge University Press* 2004
[138] O. Svelto. "Principles of Lasers 5th Edition" *Springer* 2010
[139] A. M. Weiner. "Ultrafast Optics" *John Wiley & Sons* 2009
[140] Y. Saitoh, K. Kobayashi, A. Fujimori, Y. Yamamura, M. Koyano, T. Tsuji, and S. Katayama. "Photoemission and core-level absorption spectroscopy of Fe_xNbS_2." *Journal of Electron Spectroscopy and Related Phenomena* **144**, 829 (2005).
[141] A. Fujimori, S. Saga, H. Negishi and M. Inoue. "X-ray photoemission and Auger-electron spectroscopic study of the electronic structure of intercalated compounds M_xTiS_2 (M=Mn, Fe, Co and Ni)" *Phys. Rev. B* **38**, 3676 (1988)
[142] W. Liu, D. West, L. He, Y.Xu, J. Liu, K. Wang, Y. Wang, G. van der Laan, R. Zhang, S. Zheng, and K. L. Wang. "Atomic-Scale Magnetism of Cr-Doped Bi2Se3 Thin Film Topological Insulators." *ACS Nano* **9**, 10237 (2015).
[143] Z. Dai, Q. Xue, Y. Gong, C. G. Slough, and R. V. Coleman. "Scanning-probe-microscopy studies of superlattice structures and density-wave structures in 2H-$NbSe_2$, 2H-$TaSe_2$, and 2H-TaS_2 induced by Fe doping." *Physical Review B* **48,** 14543(1993).
[144] D. Menzel, "Ultrafast charge transfer at surface accessed by core electron spectroscopies" *Chemical Society Reviews* **37**, 2212 (2008). http://dx.doi.org/10.1039/B719546J
[145] A. Kue, N. Zibouche, and T. Heine. "How does quantum confinement influence the electronic structure of transition metal sulfides TmS_2" *Physical Review B* **83**, 245213 (2011).
[146] (i) S.S. P. Parkin and R. H. Friend. "3d transition-metal intercalates of the niobium and tantalum dichalcogenides. I. Magnetic Properties. Philosophical Magazine 41, 65 (1980).
hhttp://dx.doi.org/10.1080/13642818008245370
(ii) S.S. P. Parkin and R. H. Friend. "3d transition-metal intercalates of the niobium and tantalum dichalcogenides. II. Transport Properties. Philosophical Magazine 41, 95 (1980). http://dx.doi.org/10.1080/13642818008245371
[147] L. M. Roth, H. J. Zeiger, and T. A. Kaplan. "Generalization of the Ruderman-Kittel-Kasuya-Yosida Interaction for Non-spherical Fermi Surfaces." *Physical Review* **149**, 519 (1966).
https://doi.org/10.1103/PhysRev.149.519
[148] J. Hubbard, "The magnetism of iron." *Physical Review B* **19**, 2626 (1979).
https://doi.org/10.1103/PhysRevB.19.2626
[149] J. Hubbard, "Magnetism of iron II" Physical Review B **20**, 4584 (1979).
https://doi.org/10.1103/PhysRevB.20.4584

[150] H. Hasegawa, "Single Site Functional Integral Approach to Itinerant-Electron Ferromagnetism." Journal of the Physical Society of Japan **46**, 1504 (1979). http://dx.doi.org/10.1143/JPSJ.46.1504
[151] P. Mohn. "Magnetism in the Solid State" Springer (2005)
[152] V. Brouet, W. L. Yang, X. J. Zhou, Z. Hussain, N. Ru, K. Y. Shin, I. R. Fisher, and Z. X. Shen. "Fermi Surface Reconstruction in the CDW state of Ce Te_3 observed by Photoemission" *Physical Review Letters* **93**, 126405 (2004).
[153] N.F. Berk and J.R. Schrieffer, *Phys. Rev. Lett.* **17**, 433 (1966).
[154] N.D. Mathur, F.M. Grosche, S.R. Julian, I.R. Walker, D.M. Freye, R.K.W. Haselwimmer and G.G. Lonzarich, *Nature (London)* **394**, 39 (1998).
[155] D.C. Johnston, *Adv. Phys.* **59**, 803 (2010).
[156] I.I. Mazin, D.J. Singh, M.D. Johannes and M.H. Du, *Phys. Rev. Lett.* **101**, 057003 (2008).
[157] A.D. Christianson, E.A. Goremychkin, R. Osborn, S. Rosenkranz, M.D. Lumsden, C.D. Malliakas, I.S. Todorov, H. Claus, D.Y. Chung, M.G. Kanatzidis, R.I. Bewley and T. Guidi, *Nature (London)* **456**, 930 (2008).
[158] I.I. Mazin, M.D. Johannes, L. Boeri, K. Koepernik and D.J. Singh, *Phys. Rev. B* **78**, 085104 (2008).
[159] F. Bondino, E. Magnano, M. Malevestuto, F. Parmigiani, M.A. McGuire, A.S. Sefat, B.C. Sales, R. Jin, D. Mandrus, E.W. Plummer, D.J. Singh and N. Mannella, *Phys. Rev. Lett.* **101**, 267001 (2008).
[160] M. Liu, L. W. Harriger, H. Luo, M. Wang, R. A. Ewings, T. Guidi, H. Park, K. Haule, G. Kotliar, S. M. Hayden, and P. Dai, *Nature Physics* **8**, 376-381 (2012).
[161] H. Gretarsson, A. Lupascu, Jungho Kim, D. Casa, T. Gog, W. Wu, S. R. Julian, Z. J. Xu, J. S. Wen, G. D. Gu, R. H. Yuan, Z. G. Chen, N.-L. Wang, S. Khim, K. H. Kim, M. Ishikado, I. Jarrige, S. Shamoto, J.-H. Chu, I. R. Fisher, and Young-June Kim, *Phys. Rev. B* 84, 100509(R) (2011).
[162] P. Vilmercati, A. Fedorov, F. Bondino, F. Offi, G. Panaccione, P. Lacovig, L. Simonelli, M. A. McGuire, A.S.M. Sefat, D. Mandrus, B.C. Sales, T. Egami, W. Ku, and N. Mannella, *Phys. Rev. B* **85**, 220503(R) (2012).
[163] Y. Zou, Z. Feng, P. W. Logg, J. Chen, G. Lampronti, and F. M. Grosche, *Phys. Status Solidi RRL*. **8**, 928 (2014).
[164] H. Chen, Y. Ren, Y. Qiu, W. Bao, R. H. Liu, G. Wu, T. Wu, Y. L. Xie, X. F. Wang, Q. Huang, and X. H. Chen, *Europhys. Lett.* **85**, 17006 (2009).
[165] T. Fujiwara, N. Aso, H. Yamamoto, M. Hedo, Y. Saiga, M. Nishi, Y. Uwatoko and K. Hirota, *J. Phys. Soc. Jpn*. **76**, 60 (2007).
[166] S. Ran, S.L. Bud'ko and Paul C. Canfield, *Phil. Mag.* **91**, 4388 (2011).
[167] A. Subedi, *Phys. Rev. B* **89**, 024504 (2014).
[168] D.J. Singh, *Phys. Rev. B* **89**, 024505 (2014).
[169] L. Ortenzi, I.I. Mazin, P. Blaha and L. Boeri, *Phys. Rev. B* **86**, 064437 (2012).
[170] A.J. Millis, *Phys. Rev. B* **48**, 7183 (1993).
[171] M. Shimizu, Rep. Prog. Phys. **44**, 329 (1981).
[172] I.I. Mazin and D.J. Singh, *Phys. Rev. B* **69**, 020402 (2004).
[173] Fe and Ge core level photoemission spectra did not exhibit changes before several hours. On the contrary, the Y 3d spectrum started to show additional peaks indicative of oxidation after 30-40 minutes.
[174] C. Parks Cheney, F. Bondino, T. A. Callcott, P. Vilmercati, D. Ederer, E. Magnano, M. Malvestuto, F. Parmigiani, A. S. Sefat, M. A. McGuire, R. Jin, B. C. Sales, D. Mandrus, D. J. Singh, J. W. Freeland, and N. Mannella, *Phys. Rev. B* **81**, 104518 (2010).
[175] W. L. Yang, A. P. Sorini, C-C. Chen, B. Moritz, W.-S. Lee, F. Vernay, P. Olalde-Velasco, J. D. Denlinger, B. Delley, J.-H. Chu, J. G. Analytis, I. R. Fisher, Z. A. Ren, J. Yang, W. Lu, Z. X. Zhao, J. van den Brink, Z. Hussain, Z.-X. Shen, and T. P. Devereaux, *Phys. Rev. B* **80**, 014508 (2009).
[176] E. Z. Kurmaev, J. A. McLeod, A. Buling, N. A. Skorikov, A. Moewes, M. Neumann, M. A. Korotin, Yu. A. Izyumov, N. Ni, and P. C. Canfield, *Phys. Rev. B* **80**, 054508 (2009).
[177] (a) M. Oku, T. Shishido, H. Matsuta, and K. Wagatsuma, *J. Elect. Spect. Rel. Phenom.* **153**, 75 (2006);
(b) M. Oku, N. Masahashi, S. Hanada, and K. Wagatsuma, *J. Alloys Comp.* **413**, 239 (2006).
[178] F. Sirotti, M. De Santis, and G. Rossi, *Phys. Rev. B* **48**, 8299 (1993).
[179] F.R. McFeely, S.P. Kowalczyk, L. Ley, and D.A. Shirley, *Solid State Commun.* **15**, 1051 (1974).
[180] D. G. Van Campen and L. E. Klebanoff, *Phys. Rev. B* **49**, 2040 (1994).
[181] In Fe-based magnetic systems hosting itinerant electrons, the relation between the multiplet splitting ΔE_{3s} vs. (2S+1) is found to be $\Delta E_{3s} = 0.94 + 1.01 \times (2S+1)$.

[182] J.F. van Acker, Z.M. Stadnik, J.C. Fuggle, H.J.W.M. Hoekstra, K.H.J. Buschow and G. Stroink, *Phys. Rev. B* **37**, 6827 (1988).
[183] P.J. Brown, J. Deportes and B. Ouladdiaf, *J. Phys. Condens. Matter* **4**, 10015 (1992).
[184] Y. Yamada and A. Sakata, *J. Phys. Soc. Jpn.* **57**, 46 (1988).
[185] A. Subedi and D.J. Singh, *Phys. Rev.* B **81**, 024422 (2010).
[186] D.J. Singh and M.H. Du, *Phys. Rev. Lett.* **100**, 237003 (2008).
[187] S.V. Halilov, D.J. Singh, J. Minar, A.Y. Perlov and H. Ebert, *Phys. Rev. B* **71**, 100503 (2005).
[188] K. Iida, M. Kofu, N. Katayama, J. Lee, R. Kajimoto, Y. Inamura, M. Nakamura, M. Arai, Y. Yoshida, M. Fujita, K. Yamada, and S.H. Lee, *Phys. Rev. B* **84**, 060402 (2011).
[189] J.E. Ortmann, J.Y. Liu, J. Hu, M. Zhu, J. Peng, M. Matsuda, X. Ke and Z.Q. Mao, *Sci. Rep.* **3**, 2950 (2013).
[190] I.I. Mazin and D.J. Singh, *Phys. Rev. Lett.* **82**, 4324 (1999).
[191] J. Dai, Q. Si, J.-X. Zhu, and E. Abrahams, *Proc. Nat. Acad. Sci. USA* **106** (2009), p. 4118.
[192] I.I. Mazin and M.D. Johannes, *Nature Phys*. **5**, 141 (2009).
[193] P. Hansmann, R. Arita, A. Toschi, S. Sakai, G. Sangiovanni, and K. Held, *Phys. Rev. Lett.* **104**, 197002 (2010).
[194] C. de la Cruz, Q. Huang, J. W. Lynn, J. Li, W. Ratcliff II, J.L. Zarestky, H.A. Mook, G. F. Chen, J.L. Luo, N.L. Wang and P. Dai, *Nature (London)* **453**, 899 (2008).
[195] C. Fang, H. Yao, W.F. Tsai, J.P. Hu and S.A. Kivelson, *Phys. Rev. B* **77**, 224509 (2008).
[196] S. Kasahara, H. J. Shi, K. Hashimoto, S. Tonegawa, Y. Mizukami, T. Shibauchi, K. Sugimoto, T. Fukuda, T. Terashima, Andriy H. Nevidomskyy and Y. Matsuda, *Nature* **486**, 382 (2012).
[197] J-.H. Chu, H-.H. Kuo, J. G. Analytis, and I. R. Fisher, *Science* **337**, 710 (2012).
[198] K. Nakayama, Y. Miyata, G. N. Phan, T. Sato, Y. Tanabe, T. Urata, K. Tanigaki, and T. Takahashi, *Phys. Rev. Lett*. **113**, 237001 (2014).
[199] A. Kirilyuk, A. V. Kimel, and Th. Rasing. "Ultrafast optical manipulation of magnetic order" *Reviews of Modern Physics* **82**, 2761 (2010)
[200]A. V. Kimel, A. Kirilyuk, P.A. Usachev, R.V. Pisarev, A. M. Balbashov and Th. Rasing. "Ultrafast non-thermal control of magnetization by instantaneous photomagnetic pulses" *Nature* **435**, 655 (2005).
[201] C. Stanciu, A. Tsukamoto, A. V. Kimel, F. Hansteen, A. Kirilyuk, A. Itoh, and Th. Raising. "Subpicosecond Magnetization Reversal across Ferrimagnetic Compensation Points" *Physical Review Letters* **99**, 217204 (2007).
[202] T. Schwarze, J. Waizner, M. Garst, A. Bauer, I. Stasinopoulos, H. Berger, C. Pfleiderer and D. Grundler. "Universal helimagnon and skyrmion excitations in metallic, semiconducting and insulating chiral magnets" *Nature Materials* **14**, 478 (2015).
[203] J. D. Koralek, D. Meier, J. P. Hinton, A. Bauer, S. A. Parameswaran, A. Vishwanath, R. Ramesh, R. W. Schoenlein, aC. Pfleiderer and J. Orenstein. "Observation of Coherent Helimagnons and Gilbert Damping in an Itinerant Magnet" *Physical Review Letters* **109**, 247204 (2012).
[204] T. Ogasawara, K. Ohgushi, Y. Tomioka, K. S. Takahashi, H. Okamoto, M. Kawasaki and Y. Tokura. "General Features of Photoinduced Spin Dynamics in Ferromagnetic and Ferrimagnetic Compounds" *Physical Review Letters* **94**, 087202 (2005)
[205] R. J. Elliot. "Theory of the Effect of Spin-Orbit Coupling of Magnetic Resonance in Some Semiconductors" *Physical Review* **96**, 266 (1954)
[206] Y. Yafet. "Solid State Physics" Academic Press (1963)
[207] G. M. Muller, J. Walowski, M. Djordjevic, G.-X. Miao, A. Gupta, A. V. Ramos, K. Gehrke, V. Moshnyaga, K. Samwer, J. Schmalhorst, A. Thomas, A. Hutten, G. Reiss, J. S. Moodera, abd M. Munzenberg. "Spin polarization in half-metals probed by femtosecond spin excitation" *Nature Materials* **8**, 56 (2009).
[208] B. B. Laud. "Lasers and Non-linear Optics" *John Wiley and Sons* (1985)
[209] R. W. Boyd. "Non-linear Optics 3rd Edition" *Academic Press* (2008)
[210] E. Carpene, E. Mancini, C. Dallera, G. Ghiringhelli, C. Manzoni, G. Cerullo, and S. De Silversti. "A versatile apparatus for time-resolved photoemission spectroscopy via femtosecond pump-probe experiments" *Review of Scientific Instruments* **80**, 055101 (2009)
[211] F. Boschini, H. Hedayat, C. Dalleram P. Farinello, C. Manzoni, A. Magrez, H. Berger, G. Cerullo, and E. Carpene. "An innovative Yb-based ultrafast deep ultraviolet source for time resolved photoemission experiments" *Review of Scientific Instruments* **85**, 123903 (2014)

[212] J. Faure, J. Mauchain, E. Papalazarou, W. Yan, J. Pinon, M. Marsi, and L. Perfetti. "Full characterization and optimization of a femtosecond ultraviolet laser source for time and angle resolved photoemission on solid surfaces" *Review of Scientific Instruments* **83**, 043109 (2012)
[213] C. L. Smallwood, C. Jozwiak, W. Zhang, and A. Lanzara. "An ultrafast angle resolved photoemission apparatus for measuring complex materials" *Review of Scientific Instruments* **83**, 123904 (2012)
[214] J. D. Koralek, J. F. Douglas, N. C. Plumb, J. D. Griffith, S. T. Cundiff, H. C. Kapteyn, M. M. Murnane, and D. S. Dessau. "Experimental setup for low energy laser based angle resolved photoemission spectroscopy" *Review of Scientific Instruments* **78**, 053905 (2007)
[215] R. Jiang, D. Moum Y. Wu, L. Haung, C. D. McMillan, J. Kolis, H. G. Biesber, J. J. Egan, and A. Kaminski. "Tunable vacuum ultraviolet laser based spectrometer for angle resolved photoemission spectroscopy" *Review of Scientific Instruments* **85**, 033902 (2014).
[216] J. A. Sobota, S. Yang, J. G. Analytis, Y. L. Chen, I. R. Fisher, P. S. Kirchmann, and Z. –X. Shen. "Ultrafast Optical Excitation of a Persistent Surface-State Population in a Topological Insulator Bi_2Se_3" *Physical Review Letters* **108**, 117403 (2012).
[217] M. Rini, R. Tobey, N. Dean, J. Itatani, Y. Tomioka, Y. Tokura, R. W. Schoenlein and A. Cavalleri. "Control of the electronic phase of a manganite by mode-selective vibrational excitation." *Nature* **449**, 72 (2007)
[218] J. J. Lee, F. T. Schmitt, R. G. Moore, S. Johnston, Y. –T. Cui, W. Li, M. Yi, Z. K. Liu, M. Hashimoto, Y. Zhang, D. H. Lu, T. P. Devereaux, D. –H. Lee, and Z. –X. Shen. "Interfacial mode coupling as the origin of the enhancement of T_C in FeSe films on $SrTiO_3$" *Nature* **515**, 245 (2014).
[219] G. Cerullo and S. De Silvestri. "Ultrafast optical parametric amplifiers" *Review of Scientific Instruments* **74**, 1 (2003).

Vita

Nicholas Sirica was born and raised in Richmond, VA to Dr. Alphonse E. Sirica and Annette M. Sirica. He attended Bridgewater College, a small liberal arts college nestled in the Shenandoah valley, where he graduated with a Bachelor of Science in Chemistry and Physics. He began his study at the University of Tennessee, Knoxville under advisement of Prof. Norman Mannella in 2010 and had the opportunity of being a visiting student at Politechnico di Milano in 2015. He lives with his wife Sarah, their dog Balou and cat Jay.